Experimental Studies of the Breakup Dynamics in Turbulent Multiphase Jets

Chin Hei Ng

A dissertation
submitted in partial fulfillment of the
requirements for the degree of

Doctor of Philosophy

University of Washington

2015

Reading Committee:

Alberto Aliseda, Chair

James Riley

Antonino Ferrante

Program Authorized to Offer Degree:
Department of Mechanical Engineering

University of Washington

Abstract

Experimental Studies of the Breakup Dynamics
in Turbulent Multiphase Jets

Chin Hei Ng

Chair of the Supervisory Committee:
Professor Alberto Aliseda
Mechanical Engineering

Breakup of a dispersed phase in a turbulent flow is a classical problem in multiphase flow with many applications in industrial and natural processes. Two different problems have been investigated.

The first problem focused on the atomization of a liquid jet. We investigated the effect of the high-speed spray-pattern-shaping air streams on the atomization of a coaxial twin-fluid atomizer. Our experimental data revealed that the pattern air streams contribute to the atomization process, providing the air streams impinge on the liquid jet close to the liquid nozzle (in our atomizer, it is 3.25 liquid nozzle diameter downstream). In comparison with the spray with no pattern air stream, the number density of the larger drops increases at the spray rim of the major axis and decreases at the spray rim of the minor axis. The transport of the larger drops is caused by the pattern air modified flow field. Finally, based on the two-stage instabilities mechanism, we developed a model to predict the drop size of the spray.

The second problem is the breakup of particles (air bubbles or oil drops) in a canonical turbulent round jet. Most turbulent breakup models are inspired by the Kolmogorov-Hinze theory, and assume the breakup is the result of the interaction between a particle and an eddy of similar length scale. We have shown that one of these models predicts the breakup of inviscid particles well, but it fails to predict the particle size of viscous particles.

High-speed image sequences of the viscous particles breakup event revealed three distinct stages of breakup: deformation, stretching, and disintegration. Quantitative data also supported these observations. The fluctuating behavior of the deformation factor (a particle shape indicator) in the deformation stage suggested that the deformation of a particle is caused by multiple series of eddy collisions. The stretching stage is unique and it is not observed in the breakup of inviscid particles. In this stage, a particle is stretched to multiple times its original size. This suggests the stretching mechanism is caused by the large scale fluid motion, so it contradicts with the Kolmogorov-Hinze theory where the deformation is caused by eddies in the inertial subrange. The disintegration of the stretched ligaments typically results in multiple daughter particles. This is also different from the breakup of inviscid particles, where binary breakup is the norm.

A breakup detection and particle tracking algorithm was developed to extract data of particles along their breakup paths. These data were used to develop models for important breakup parameters, such as the breakup probability and the breakup time. We found that the probability of breakup depends on the disruptive effect due to the colliding turbulent eddies, as well as the confinement effects due to the internal viscous stress and the surface restoration pressure. Although the stretching mechanism is due to the large scale turbulent eddy, the stretching/thinning time is dictated by the small scale eddies. This is because as the particle is stretched into a ligament, the ligament is still constantly collided by eddies with length scale similar to the thickness. These eddies are responsible for the thinning of the ligament that ultimately leads to disintegration.

The population balance equation describes the evolution of the particle size distribution in the breakup process. One of the closure functions required in this equation is the breakup frequency. The breakup frequency is obtained by combining the breakup time and breakup probability models. The prediction from the breakup frequency model compares favorably with the measured breakup frequency from the experimental data.

TABLE OF CONTENTS

Page

List of Figures iv

Chapter 1: Introduction 1
1.1 Breakup due to surface tension 1
1.2 Aerodynamic breakup of a liquid jet 2
1.3 Aerodynamic breakup of a spherical particle 3
1.4 Turbulent breakup 6
1.5 Motivation 6
1.6 Organization of the thesis 8

Chapter 2: Review of turbulent breakup 10
2.1 Background 10
2.2 Breakup frequency models 13
2.3 Daughter particle size distribution models 21

Chapter 3: Experimental setup for the study of particle breakup in a turbulent jet 31
3.1 Experimental facility 31
3.2 Imaging techniques 39

Chapter 4: Validation of jet properties 50
4.1 Mean velocity 51
4.2 Reynolds stresses 56
4.3 Turbulent dissipation rate 59

Chapter 5: Tracking algorithm for breakup events 62
5.1 Background 62
5.2 Ligament identification and back-tracking algorithm 64

5.3 Demonstration of LIBT 72
5.4 Daughter particles identification 75
5.5 Demonstration of daughter particle identification algorithm 78

Chapter 6: Breakup of inviscid particles 82
6.1 Bubble flux 82
6.2 Bubble size and size distribution 85
6.3 Evolution of the size distribution of air bubbles 85
6.4 Effect of Reynolds number and turbulent dissipation rate 90
6.5 Effect of air void fraction 94
6.6 Effect of initial size distribution 96
6.7 Comparison to an existing model 97
6.8 Visualization of bubble breakup 102

Chapter 7: Breakup of viscous particles: Particle size analysis 105
7.1 Dispersed phase fluid properties 105
7.2 Dimensionless quantity 107
7.3 Particle flux 108
7.4 Evolution of the particle size of viscous dispersed phase fluid 111
7.5 Comparison to an existing model 116
7.6 Frozen state particle size of viscous dispersed phase fluid 119
7.7 Effect of surfactant on particle size 122
7.8 Frozen state particle size prediction model 127

Chapter 8: Breakup of viscous particles: Breakup event analysis 134
8.1 Visualization of viscous particle breakup 136
8.2 Deformation to Stretching transition 139
8.3 Breakup time 144
8.4 Breakup probability 157
8.5 Breakup frequency 164

Chapter 9: Summary and Conclusions 178
9.1 Breakup of inviscid particles 178
9.2 Breakup of viscous particles 180

9.3 Future work 183

Appendix A: Aerodynamic breakup: Coaxial twin-fluid atomization with pattern air streams 186
A.1 Introduction 186
A.2 Experimental setup 188
A.3 Breakup mechanism of coaxial twin-fluid atomization 190
A.4 Prediction model of droplet size 197
A.5 Results 201
A.6 Summary 213

Appendix B: Phase Doppler particle analyzer 216
B.1 Laser beams generation 216
B.2 Size and velocity measurement of particles 217

Appendix C: Sauter mean diameter 221

Appendix D: Stokes number 223
D.1 PIV seeding particles 223
D.2 Dispersed phase fluid particles 225

Appendix E: Sample images of viscous particle breakup experiments 227

Appendix F: Equivalent particle size and shape 238
F.1 Equivalent ligament calculation 238
F.2 Equivalent particle diameter calculation 242

Appendix G: Sampling rate and phase shift study 246

Bibliography 250

LIST OF FIGURES

Figure Number		Page
1.1	Break mechanisms of a particle based on the Weber number [50].	5
2.1	Comparsion of Coulaloglou & Tavlarides' [13] and Prince & Blanch's [53] breakup frequency models. $\sigma = 0.072\ N/m$, $\rho = 1000\ kg/m^3$, $\epsilon = 1000\ m^2/s^3$.	16
2.2	Breakup frequency of Tsouris & Tavlarides' model [66] with different lower integration limits. $\sigma = 0.072\ N/m$, $\rho = 1000\ kg/m^3$, $\epsilon = 1\ m^2/s^3$.	17
2.3	Breakup frequency of Luo & Svendsen's model [36] with different upper integration limits. $\sigma = 0.072\ N/m$, $\rho = 1000\ kg/m^3$, $\epsilon = 1\ m^2/s^3$.	19
2.4	A summary of different approaches of modeling the breakup frequency.	21
2.5	A daughter particle size distribution predicted by Nambiar et al.'s model [45].	25
2.6	A daughter particle size distribution predicted by Tsouris & Tavlarides' model [66].	26
2.7	A daughter particle size distribution predicted by Luo & Svendsen's model [36]. $\epsilon = 1.0\ m^2/s^3$.	27
2.8	A daughter particle size distribution predicted by Martínez-Bazán's model [40].	29
2.9	A summary of different approaches of modeling the daughter particle size distribution.	30
3.1	A drawing of the octagonal acrylic tank.	32
3.2	A drawing of the nozzle showing the third order polynomial interior surface.	35
3.3	An example of the calibration target in the imaging field of view.	36
3.4	A schematic of the needle mount with the needle and spatial calibration target attached to it.	37
3.5	Schematic of the PIV setup for the cross-section of the turbulent jet.	40
3.6	Lense arrangement used to create the laser plane for illumination of the PIV images.	41
3.7	Image pairs of an lycopodium particle seeded jet ($Re = 25000$) before (top) and after (bottom) contrast normalization. Time delay between images is 20 μs.	43
3.8	Schematic of the high-speed imaging setup for the particle breakup experiment.	45

3.9 Illustration of different steps in the image processing sequence. 47
3.10 Illustration of the overlapping interrogation zones applied on an binary image. 48

4.1 An illustration of imaging multiple locations of the jet with different sizes of field of view. 51
4.2 Mean velocity field obtained by stitching multiple PIV results of different imaging windows. $Q_j = 2.5$ GPM and $d_j = 4$ mm. 53
4.3 A comparison of the normalized centerline velocity decay between our experimental results and the prediction from theory. 54
4.4 A comparison of the normalized velocity profile between our experimental results, previous results in the literature and the prediction from theory. . . . 54
4.5 Normalized turbulent viscosity of a self-similar jet. [52] 55
4.6 A comparison of the $\overline{u^2}$ between our experimental results and results in the literature. 57
4.7 A comparison of the $\overline{v^2}$ between our experimental results and results in the literature. 57
4.8 A comparison of the $\overline{uv}$ between our experimental results and results in the literature. 58
4.9 A comparison of the centerline turbulent dissipation rate between experiment and model. 60
4.10 A comparison of the normalized centerline turbulent dissipation rate between experiment and model. The red and blue lines represent the mean values of the experimental results for each location. 61

5.1 A visualization of a typical breakup sequence of viscous particle. $Re = 80000$ and $Q_p = 20$ mL/min. Needle positioned at $z/d_j = 20$. 100 cSt silicone oil. . 65
5.2 An illustration of a basic ligament. 67
5.3 Interrogation area for searching potential match. 68
5.4 Illustration of how particle overlapping affect the ligament's size, shape and bounding box area. 69
5.5 An illustration of a basic particle. 71
5.6 A visualization of the formation of daughter ligaments and their breakup. $Re = 60000$ and $Q_b = 20$ mL/min. Needle position at $z/d_j = 20$. Canola oil. 72
5.7 A demonstration of a breakup path overlaid on the breakup sequence. $Re = 80000$ and $Q_p = 20$ mL/min. Needle positioned at $z/d_j = 20$. Canola oil. . . 74
5.8 A demonstration of the daughter particle identification algorithm. $Re = 80000$ and $Q_p = 20$ mL/min. Needle positioned at $z/d_j = 20$. Canola oil. 80

5.8 A demonstration of the daughter particle identification algorithm. $Re = 80000$ and $Q_p = 20$ mL/min. Needle positioned at $z/d_j = 20$. Canola oil. 81

6.1 The number of bubbles per image over axial distance. $Re = 60000$ and $Q_b = 20$ mL/min. 83

6.2 Bubble flux over axial distance. $Re = 60000$ and $Q_b = 20$ mL/min. 84

6.3 Bubble flux over axial distance. $Q_b = 42$ mL/min. 84

6.4 The evolution of the size distribution (VPDF and CVPDF). $Re = 45000$ and $Q_b = 42$ mL/min. 87

6.5 The evolution of the size distribution (VPDF and CVPDF). $Re = 60000$ and $Q_b = 42$ mL/min. 88

6.6 The evolution of the size distribution (VPDF and CVPDF). $Re = 80000$ and $Q_b = 42$ mL/min. 89

6.7 A comparison of the CVPDF between $Re = 45000$, $Re = 60000$, and $Re = 80000$. $Q_b = 42$ mL/min. Dashed lines represents the size distribution from the last measurement location. 91

6.8 A comparison of the frozen state PDF between $Re = 45000$, $Re = 60000$, and $Re = 80000$. $Q_b = 42$ mL/min. 92

6.9 A comparison of the frozen state PDF (nomalized by D_{32}) between $Re = 45000$, $Re = 60000$, and $Re = 80000$. $Q_b = 42$ mL/min. 92

6.10 Sauter mean diameter vs Reynolds number for different experiments. 93

6.11 Sauter mean diameter vs initial turbulent dissipation rate for different experiments. 93

6.12 A comparison of the size distribution between test A and B over five different turbulent dissipation rate. 95

6.13 A comparison of the size distribution between test A and C over five different turbulent dissipation rate. 96

6.14 A comparison of the CVPDF between different nozzle diameters. $Re = 45000$ and $Q_b = 10$ mL/min. 97

6.15 A comparison of the CVPDF between the model and the experimental data. $Re = 45000$ and $Q_b = 42$ mL/min. 99

6.16 A comparison of the CVPDF between the model and the experimental data. $Re = 60000$ and $Q_b = 42$ mL/min. 100

6.17 A comparison of the CVPDF between the model and the experimental data. $Re = 80000$ and $Q_b = 42$ mL/min. 101

6.18 A comparison of the D_{32} between the model and the experimental data for three Reynolds numbers. $Q_b = 42$ mL/min. 101

6.19 A visualization of a sequence of bubble breakups. $Re = 60000$ and $Q_b = 42$ mL/min. Needle positioned at $z/d_j = 15$. 104

7.1 Particle flux over axial distance. 109

7.2 Ligament flux over axial distance. 110

7.3 The evolution of the size distribution (CVPDF) of set 1A (canola oil). $Re = 45000$. 112

7.4 The evolution of the size distribution (CVPDF) of set 1A (canola oil). $Re = 60000$. 112

7.5 The evolution of the size distribution (CVPDF) of set 1A (canola oil). $Re = 80000$. 113

7.6 The evolution of the size distribution (CVPDF) of set 1B (10 cSt silicone oil). $Re = 60000$. 113

7.7 The evolution of the size distribution (CVPDF) of set 1C (100 cSt silicone oil). $Re = 60000$. 114

7.8 The evolution of the size distribution (CVPDF) of set 1D (200 cSt silicone oil). $Re = 60000$. 114

7.9 Comparison of the evolution of D_{32} for sets 1A, 1B, 1C and 1D. $Re = 45000$ (red), $Re = 60000$ (green) and $Re = 80000$ (blue). 115

7.10 A comparison of the CVPDF between the model and the experimental data for sets 1A, 1B, 1C and 1D. $Re = 60000$. 117

7.10 A comparison of the CVPDF between the model and the experimental data for sets 1A, 1B, 1C and 1D. $Re = 60000$. 118

7.11 A comparison of the frozen state CVPDF for sets 1A, 1B, 1C and 1D. $Re = 45000$. 119

7.12 A comparison of the frozen state CVPDF for sets 1A, 1B, 1C and 1D. $Re = 60000$. 120

7.13 A comparison of the frozen state CVPDF for sets 1A, 1B, 1C and 1D. $Re = 80000$. 120

7.14 Weber number scaling of the frozen state D_{32} for sets 1A, 1B, 1C and 1D. . 122

7.15 A comparison of the particle size with different concentration of Triton X-100 in canola oil. Set 1A (solid line), set 2A (dashed line) and set 3A (dotted line). $Re = 45000$ (red), $Re = 60000$ (green) and $Re = 80000$ (blue). 124

7.16 A comparison of the particle size with different concentration of Triton X-100 in 100 cSt silicone oil. Set 1C (solid line), set 2C (dashed line) and set 3C (dotted line). $Re = 45000$ (red), $Re = 60000$ (green) and $Re = 80000$ (blue). 125
7.17 Weber number scaling of the frozen state D_{32}. 0 ppm (open symbol), 100 ppm (half filled symbol) and 1000 ppm (solid symbol) 127
7.18 D_c (viscous effect dominated case) scaling of the frozen state D_{32} for sets 1A, 1B, 1C and 1D. 131
7.19 Prediction of the frozen state D_{32} using D_c for all 10 experimental sets. . . . 132
7.20 Prediction of the frozen state D_{32} using D_c with Reynolds number scaling for all 10 experimental sets. 133

8.1 A visualization of a typical breakup sequence of viscous particle. $Re = 60000$ and $Q_p = 20$ mL/min. Needle positioned at $z/d_j = 20$. Canola oil. 138
8.2 Evolution of the deformation factor along the breakup path for two separate breakup events. 142
8.3 Evolution of the deformation factor along the breakup path for multiple breakup events. D-S transition of each path is shown as a red circle. 143
8.4 Critical capillary number vs viscosity ratio for simple shear flow [55]. 145
8.5 Measured stretching/thinning time vs modeled thinning time based on eddies collision. 149
8.5 Measured stretching/thinning time vs modeled thinning time based on eddies collision. 150
8.6 Measured stretching/thinning time vs modeled thinning time based on eddies collision with linear fit. 151
8.7 Illustration of the stretching and thinning of a cylindrical shape ligament. . . 152
8.8 Comparison of the thinning velocity between the shear and eddy collision mechanisms. 154
8.9 Measured deformation time vs modeled deformation time. 156
8.10 An image sequence showing a deformed drop reverted back to spherical shape. $Re = 80000$ and $Q_p = 20$ mL/min. Needle positioned at $z/d_j = 20$. 100 cSt silicone oil. 158
8.11 Breakup probability vs jet Reynolds numbers for different viscosity ratio. . . 161
8.12 Breakup probability vs viscosity ratio for different jet Reynolds numbers. . . 161
8.13 Breakup probability vs stress ratio. 163
8.14 Breakup probability vs stress ratio. Exponential fit. 164
8.15 Relationship between $b_{e,DS}^{2/3}$ and $b_{e,DS}^{2/3} - b_{e,BU}^{2/3}$. A linear fit is applied to the data. 165

8.16 Relationship between $D_o^{2/3}$ and $D_o^{2/3} - b_{e,BU}^{2/3}$. A linear fit is applied to the data. 166

8.17 Breakup time prediction model using simplified stretching/thinning model. A linear fit is applied to the data. 167

8.18 Deformation factor at the D-S transition for the 10 cSt, 100 cSt, 200 cSt silicone oils and canola oil. 168

8.19 Evolution of $N_p'(D \geq D_{v90})$ over axial distances. 100 cSt silicone oil + 1000 ppm Triton X-100. 171

8.20 Evolution of $N_p'(D \geq D_{v90})U_o$ over axial distances. 100 cSt silicone oil + 1000 ppm Triton X-100. 172

8.21 Comparison between measured and predicted breakup frequency. Canola oil with 0 and 1000 ppm of Triton X-100. $Re = 80000$. 175

8.22 Comparison between measured and predicted breakup frequency. 10 cSt silicone oil with 0 and 1000 ppm of Triton X-100. $Re = 80000$. 176

8.23 Comparison between measured and predicted breakup frequency. 100 cSt silicone oil with 0 and 1000 ppm of Triton X-100. $Re = 80000$. 177

A.1 Comparison between circular and elliptical spray patterns for the tablets coating process. A view from the cross-section of a rotating drum looking down on the tablet bed. 187

A.2 Cross-sectional view of the Schlick atomizer. 189

A.3 A comparison between the breakup of a drop (left) and the breakup of a jet (right) at high Weber number. Varga et al. [69]. 191

A.4 Illustration of liquid jet breakup due to Kelvin-Helmholtz and Rayleigh-Taylor instabilities. λ_{KH} is the wavelength of the Kelvin-Helmholtz instability. λ_{RT} is the wavelength of Rayleigh-Taylor instability. 192

A.5 Ratio of the wavelength of the primary instability to the boundary layer thickness of the gas phase as a function of gas velocity. ∘, $U_l = 0.45$ m/s; •, 0.94 m/s; □, 2 m/s. Marmottant and Villermaux [38] 194

A.6 Rayleigh-Taylor waves observed on the surface of a drop silicone oil drop exposed in high-speed air flow. (Joseph et al. [27]). 195

A.7 The effect of acceleration on dispersion relation. (Joseph et al. [27]). 197

A.8 Illustration of liquid ligaments thickness (b_l), velocity (U_c), and vorticity layer thickness (b_g). 198

A.9 High-speed image of the breakup process illustrating the scale of λ_{KH} (λ_1 in the image), λ_{RT}, and the resulting droplet size. $We = 153$. Aliseda et al.[2] . 203

A.10 Comparison between D_{32} prediction and experimental results for cases with no PA. . . . 204
A.11 Comparison between D_{32} prediction and experimental results for all cases. . 204
A.12 Size distribution at the center of the spray. . . . 206
A.13 Size distribution (D_{32}, [μm]) on cross-sections of the spray at $x/D_o = 48$. $Q_{AA} = 28$ LPM and $Q_{PA} = 0$. . . . 207
A.14 Size distribution (D_{32}, [μm]) on cross-sections of the spray at $x/D_o = 48$. $Q_{AA} = 28$ LPM and $Q_{PA} = 28$ LPM. . . . 208
A.15 Sauter mean diameter profile of the spray at $x/D_o = 48$. $Q_{AA} = 42$ LPM. . . 209
A.16 Size distribution at the spray rim of the major axis. $x/D_o = 32$. . . . 210
A.17 Size distribution at the spray rim of the minor axis. $x/D_o = 32$. . . . 211
A.18 Illustration of the droplets transport with (top) and without PA-modified flow field (bottom) . . . 213

B.1 Illustration of interference pattern (fringes) created by the laser beams. . . . 218

D.1 Stokes number of the seeding particle as a function of axial distance . . . 224
D.2 Stokes number of the dispersed phase particle as a function of axial distance 226

E.1 Sample images of experimental set 1A (Canola oil) . . . 228
E.2 Sample images of experimental set 1B (10 cSt silicone oil) . . . 229
E.3 Sample images of experimental set 1C (100 cSt silicone oil) . . . 230
E.4 Sample images of experimental set 1D (200 cSt silicone oil) . . . 231
E.5 Sample images of experimental set 2A (Canola oil + 100 ppm Triton X-100) 232
E.6 Sample images of experimental set 2B (10 cSt silicone oil + 100 ppm Triton X-100) . . . 233
E.7 Sample images of experimental set 2C (100 cSt silicone oil + 100 ppm Triton X-100) . . . 234
E.8 Sample images of experimental set 3A (Canola oil + 1000 ppm Triton X-100) 235
E.9 Sample images of experimental set 3B (10 cSt silicone oil + 1000 ppm Triton X-100) . . . 236
E.10 Sample images of experimental set 3C (100 cSt silicone oil + 1000 ppm Triton X-100) . . . 237

F.1 Illustration of a ligament converted into its equivalent ligament. . . . 239
F.2 Comparison between images before and after "Fit ellipse" is applied. . . . 240
F.3 The ligament length/thickness ratio vs circularity (for $CC \leq \pi/4$) . . . 241

F.4 Evolution of equivalent diameter for different breakup paths. 244
F.5 A comparison of the histograms of equivalent diameter standard deviation between the equivalent circle method and the equivalent ellipsoid method. . 245
G.1 Comparison of the evolution of the number of particles per frame for different sampling rates. 248
G.2 Comparison of the evolution of the number of particles per frame for different phase shifts. 249

ACKNOWLEDGMENTS

I am grateful to work with many wonderful people during my time in the University of Washington. I would like to thank the staff in the ME front office for all the administrative help. Thanks to Bill for resolving all kinds of technical issues I encountered in engineering the experiments. Thanks to Eamon and Kelvin for their help and expertise in fabricating the necessary components. I would also like to thank Prasad and Matthew from Professor Bergs lab for the fluid properties measurements.

I want to thank all my labmates. From hauling the giant tank to our lab to assisting all my experimental needs, they have continuously supported me throughout my time at the UW. Specifically, I would like to thank Ryan, my long time lab partner, whom I also considered as my mentor. Many skills I learned from him have been instrumental in my research. Thanks to Stephanie for devoting much of her time to the experiments. Thanks to Colin for laying all the ground works for the PDPA measurements. Thanks to Alicia for all the constructive discussions, work related or not. I would also like to express my appreciation to Ryan, Mike and Danny for keeping the computers and backup systems in working order.

My deepest gratitude goes to Professor Aliseda, my research advisor. Not only did he open the doors for all the interesting projects I have a chance to work on, but his mentorship is the central part of my personal and professional growth. I also want to thank all my committee members, Professor Riley, Professor Ferrante, Professor Dabiri and Professor Berg, for their time and all the constructive feedbacks. Also, this work would not be possible without the funding sources. Funding for the turbulent breakup project was provided by the National Oceanic and Atmospheric Administration. I would also like to express my gratitude for the funding for other projects (not shown in this work) I have worked on as a graduate student.

General Electric funded the liquid fuel atomization project and the Department of Justice funded the work on the turbulent jet measurement.

Finally, I want to thank my family and friends for their supports and encouragements. Special thanks go to my wife, Ivy, for everything she has done to get me through this journey. She was there in every step with me, patiently coped with me when I was frustrated, kept me motivated when I hit a roadblock and made this journey enjoyable. She truly deserves as much credit as everyone that has contributed to this work. I look forward to walking with her again in the journey of life.

DEDICATION

To my dear wife, Ivy

Chapter 1

INTRODUCTION

Breakup in multiphase flow occurs when a mass of one fluid, gas bubble, liquid drop or agglomeration of solid particles, commonly referred to as the disperse phase, disintegrates and disperses in another immiscible fluid, commonly referred to as the continuous or carrier phase. This process can be found in many industrial applications and in naturally-occurring phenomena. From important engineering processes, such as fuel injection in engines, spray coating for pharmaceutical tablets and liquid or gas extraction in dispersed phase reactors, to natural process that support our ecosystem, such as gas exchange at the ocean surface due to breakup of air entrained by surface waves [14], the effectiveness of these processes is often determined by the mass or heat transfer rate of the dispersed phase, which are ultimately controlled by the amount of surface area and the relative velocity between the dispersed and continuous phases, resulting from breakup. For example, the evaporation rate of fuel droplets in the combustion chamber controls the burning efficiency and pollutant formation. Similarly, the rate of gas dissolution in the ocean dominates ocean/atmosphere coupling that plays an important role in weather patterns and global circulation. In order to be able to predict or control these phenomena, through the size distribution of the dispersed phase which plays a dominant role, we need to understand the underlying mechanisms of the breakup process.

1.1 Breakup due to surface tension

There are many different mechanisms to disintegrate a fluid mass into smaller parcels. One of the simplest is the capillary breakup of a liquid jet. As early as the 19^{th} century, Plateau

[51] considered the breakup of a cylindrical jet. He found that the jet is inherently unstable because surface energy is not minimized for a cylindrical geometry. Any deformation on the shape of the interface will be amplified by surface-tension-induced pressure gradients and flow, thus becoming the driving force for breakup. Rayleigh [56] confirmed Plateau results by presenting the analytical solution to the instability analysis of the inviscid cylindrical liquid jet. Consequently, this kind of breakup mechanism is today known as the Plateau-Rayleigh instability.

Breakup dominated by the Plateau-Rayleigh mechanism occurs in low Reynolds and Weber numbers, considered by Reitz and Bracco [59] as the Rayleigh regime. In this regime, the size of the droplets can be predicted by the most unstable wavelength of the solution to the linear stability problem described by Rayleigh [56] in the late 19^{th} century, which is generally found to be larger than the jet diameter.

1.2 Aerodynamic breakup of a liquid jet

As Reynolds and Weber number increase, the breakup is no longer dominated by surface tension. The most unstable wavelength becomes shorter and the resulting droplets size does not follow the linear theory and starts to develop a dependency on the jet diameter. At high Reynolds number, the relative velocity between the injected liquid and the ambient fluid is too high and droplets are stripped off from the jet interface by aerodynamic forces. The instability that occurs at the interface has a much smaller wavelength, resulting in droplets with diameter much smaller than the nozzle diameter. This regime is frequently referred to as the atomization regime.

Many industrial applications require droplets sizes consistent with the atomization regime. To impart high velocity on the liquid jet, high pressures are required that may not be practical in some applications. In addition, the quality of the spray, in terms of the range of diameters achieved, created from the high-pressure nozzle is generally not very desirable. Therefore, specially-engineered atomizers, such as air-assisted atomizers, are used in these applications instead of high-pressure nozzles. Air-assisted atomizers introduce a high-speed

gas stream in contact with the liquid jet. The momentum difference between the gas and liquid phase is the source of the breakup. Although both the breakup of the high-speed liquid jet and the air-assisted atomizer are considered aerodynamic breakup, the underlying mechanisms are different. In the air-assisted atomization, it is considered to be a two-stage breakup involving two different instabilities, namely Kelvin-Helmholtz and Rayleigh-Taylor instabilities [33, 69].

1.3 Aerodynamic breakup of a spherical particle

The mechanism of the breakup of a spherical particle (i.e. a gas bubble or a liquid drop) is different than the breakup of a jet. Since a particle starts in a stable geometry given by minimum surface energy for the given volume, surface tension is a strong confinement force that resists breakup. For a stable particle, the difference between internal (P_i) and external pressure (P_e) is equal to a pressure differential imposed by surface tension ($P_\sigma = 4\sigma/D$). When the external pressure fluctuates, P_σ adjusts via geometrical changes in curvature. Large fluctuations in pressure lead to large deformations and eventually to breakup into smaller particles.

$$P_i - P_e = P_\sigma = \frac{4\sigma}{D} \tag{1.1}$$

where the Poison pressure, P_σ, is given by σ, the surface tension, and D, the spherical particle diameter.

In the aerodynamic breakup of a particle, the excess pressure acting on the exterior of the drop comes from the drag force. For a stable particle, equilibrium of stresses between drag and surface tension results in Equation (1.2) [35]. The left-hand side of this equation is the Weber number, which represents the ratio of the disruptive aerodynamic forces to the stabilizing surface tension force. In the context of Equation (1.2), a particle will be continuously disrupted out of equilibrium if the Weber number is greater than $8/C_D$, eventually resulting in break-up. In other words, $We_{crit} = 8/C_D$ is a critical Weber number for the aerodynamic breakup of a particle by a mean flow. The Weber number determines not only the onset

of the breakup, but also the leading mechanism responsible for it. Pilch and Erdman [50] observed five different breakup mechanisms based on different ranges in Weber number.

At the lowest Weber numbers, oscillations develop on the surface of the particle, grow in amplitude and eventually the particle breaks into a few large particles. Bag breakup is observed at $12 \leq We \leq 50$. In this case, a thin film is developed and attached to a ring. The thin film is blown downstream forming a bag shape. The bag eventually bursts and produces many small particles. The bag-and-stamen type of breakup is observed at a slightly higher Weber number. This mechanism is very similar to bag breakup, but in addition to the bag formation, a column of liquid is formed parallel to the flow. Larger particles are formed from the breakup of the stamen compare to the breakup of the bag. At a higher Weber number ($100 \leq We \leq 350$), the formation of the bag and/or stamen are not observed. Instead, particles are continuously stripped from the rim of a flattened drop, hence it was termed "sheet stripping". Finally for $We > 350$, the particle is first flattened, then short wavelength waves develop on the surface and small particles are stripped from these waves by the high speed freestream around the drop. At the same time, long wavelength waves penetrate through the particle and break it into large fragments. Secondary breakup for the fragments can then be observed. The combination of the small particles stripping and the breakup of the large fragments results in what has been termed "catastrophic breakup". An illustration of the different types of breakup mechanism is shown in Figure 1.1.

$$\frac{\rho_A U_R^2 D}{\sigma} = \frac{8}{C_D} \tag{1.2}$$

where ρ_A is the density of the ambient fluid, U_R is the relative velocity between the ambient fluid and the particle, σ is the surface tension, and C_D is the drag coefficient of the particle.

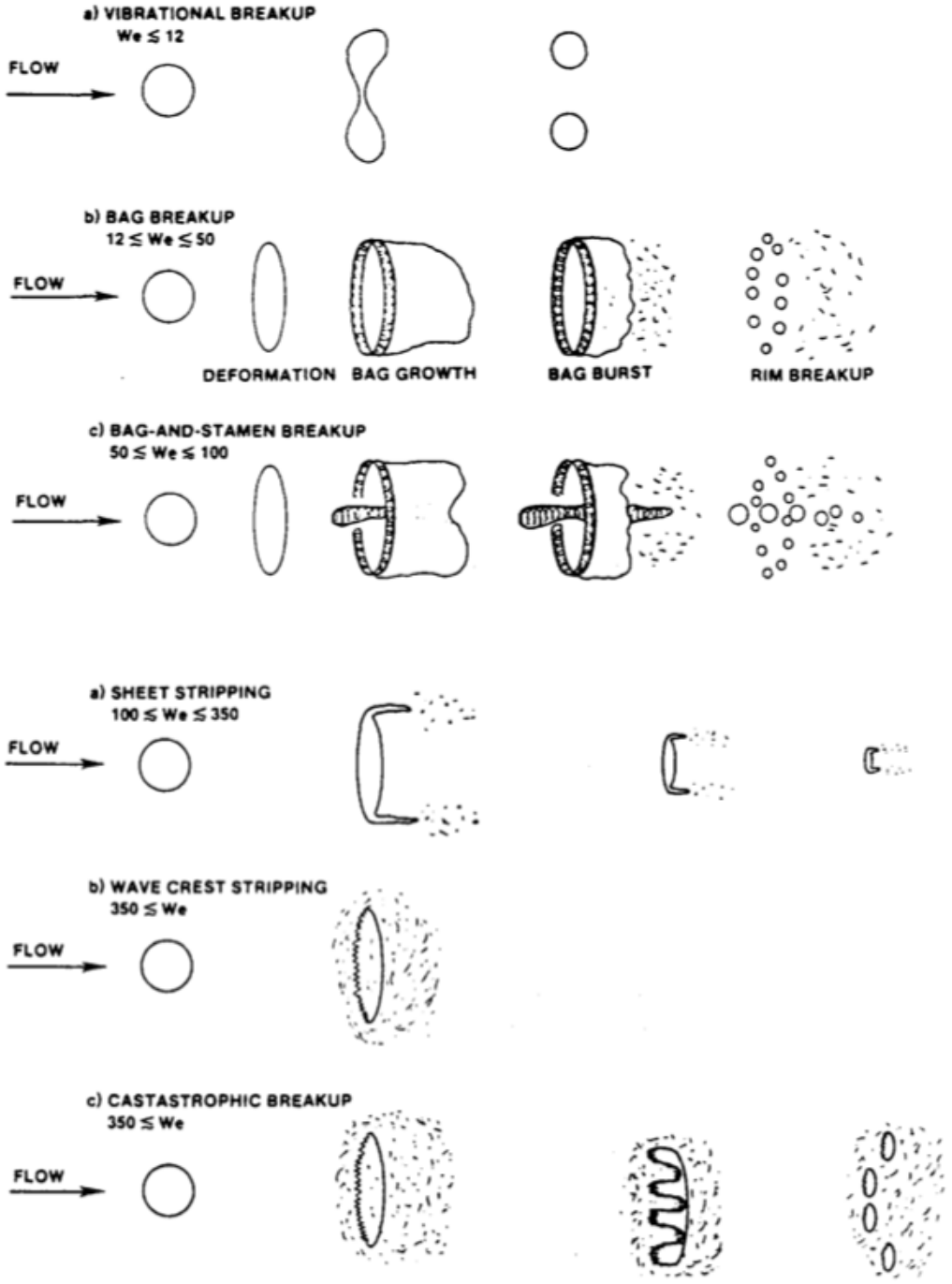

Figure 1.1: Break mechanisms of a particle based on the Weber number [50].

1.4 Turbulent breakup

The breakup mechanism described in the section above is considered to be driven by the aerodynamic effect of the mean flow: it requires the mean relative velocity between the ambient flow and the particle to be high. In a flow field where the mean relative velocity is low, the external stresses that cause breakup of a particle might be the result of turbulent ambient flow structures. In this alternative breakup mechanism, the general assumption is that the turbulent motions that contribute to the breakup have length scales similar to the particle diameter [22]. If the particle diameters are in the inertial subrange, the turbulence eddies acting on them can be considered to be locally isotropic and homogeneous according to Kolmogorov's first hypothesis [30]. In addition, the kinetic energy contained in these turbulent motions depends only on the turbulent dissipation rate providing a sufficiently high Reynolds number, according to Kolmogorov's second hypothesis [30]. Since the turbulent dissipation rate can be directly related to the velocity fluctuation rms (Equation (1.3)), it allows for the calculation of the turbulent kinetic energy responsible for the breakup in terms of the velocity spectrum and the particle size only. This becomes the basis for the modeling of the size distribution that uses an energy balance approach [13, 53, 66, 36]. On a different track, Martínez-Bazán et al. [39, 40] used a kinematic approach by balancing the stresses on a particle under turbulent fluctuations. Although the two approaches are fundamentally different, the assumptions used to obtain the turbulent stress is still based on the Kolmogorov's hypothesis.

$$\overline{\Delta u^2} = C(\epsilon D)^{2/3} \tag{1.3}$$

where $C = 2$ [22] is an empirical constant.

1.5 Motivation

Two separate studies, relating the breakup in multiphase flow, have been performed as part of this thesis. The first study is motivated by the tablet-coating process in the pharmaceu-

tical industry. The coating solution is injected and broken up into small droplets by using high-speed gas streams from a coaxial twin-fluid atomizer, so the mechanism is considered to be aerodynamic breakup. Typically, additional gas streams are introduced in order to modify the circular spray into an elliptical pattern for better coating efficiency. These additional gas streams are called pattern air jets. Unlike in previous studies in the literature [2], the momentum of the pattern air stream in this experiment is comparable to that of the coaxial air stream, so its contribution to the breakup process cannot be neglected. The effect of pattern air on both the breakup process and the subsequent transport of droplets was investigated experimentally in the preliminaries of this thesis. A droplet size prediction model that includes the effect of pattern air was developed and validated against the current experimental results and data from previous publications . This study is included in Appendix A.

The body of this thesis focuses on the second study: the breakup of particles in a turbulent round jet. This study was originally motivated by an oil spill event from a deep water well in the Gulf of Mexico. In recent years, exploration and production of oil and gas in deep water regions has become commonplace. Although discoveries of new ultra-deep water wells has prolonged oil and gas production that was once thought to be on a permanent decline, drilling into these wells have unforeseeable risks. In 2010, an explosion occurred on the Deepwater Horizon oil rig. The collapse of the drilling unit caused leakage of a gas-oil mixture at a water depth of about 5000 ft. Because of the inaccessibility of the well-head site, it took about 84 days to cap off and eventually permanently shut off the well. During that time, an estimated 5 million equivalent barrels of oil (STB) had flowed out of the well. One approach to attenuate the impact of the spill before the well was capped off was to inject chemical dispersants into the oil. This would reduce the surface tension between the oil and the seawater, and potentially result in the leaked oil breaking into smaller droplets. Unlike large oil droplets that can rise quickly to the surface due to buoyancy, small oil droplets can stay underwater for weeks or months [9]. More importantly, the rate of the biodegradation of the oil depends on the availability of the oil-water interface [70], so smaller oil droplets

can be degraded more easily by microorganisms before they reach the surface. In other words, the environmental impact of the oil spill was considered to depend highly on the size distribution of the oil droplets. A good understanding of the breakup mechanism is essential to obtain good estimates of the size distribution of droplets of immiscible fluids breaking under turbulence in the carrier flow. The experimental study and modeling of the breakup of inviscid (air) and viscous (oils with viscosities between 10 and 200 cP) fluids injected by a turbulent jet in an ambient immiscible liquid (water) that forms the core of this thesis was motivated by the need for better understanding and modeling capabilities of this complex turbulent multiphase process.

1.6 Organization of the thesis

In Chapter 2, a literature review of seminal work from previous research in turbulent breakup is presented. Specially, it focuses on different modeling of the particle size distribution. Since most previous works focused on chemical processes, the experiments were done using stirred vessels as the source of turbulence. As mentioned by Martínez-Bazán et al. [39], the turbulence in a stirred vessel is not well characterized. Also, the region near the surface of the impeller is highly anisotropic and tip vortices are shed from the impeller. Since we are interested in the breakup of oil drops by turbulent shear, this thesis uses a well-characterized turbulent round jet as the source of turbulence for breakup in the experiment. A detailed description of the experimental facility and the measurement technique are documented next, in Chapter 3. To ensure the turbulence created from our facility is well characterized, measurements of a pure jet (with no dispersed phase) were compared to published experimental data and well-established models. The validation of the turbulent round jet is described in Chapter 4. One major contribution in this thesis is the particle tracking algorithm that is specifically designed to track the breakup event of highly deformed viscous particles. This algorithm provides important breakup characteristics that are essential to the prediction of the size distribution. Chapter 5 provides a detailed description of the algorithm.

The study of turbulent breakup is broken up into two parts. The first part focuses on the

breakup of inviscid particles (air bubbles), which is presented in Chapter 6. In this chapter, the breakup dynamics of inviscid dispersed phase fluid (air bubbles) were investigated. Quantitative analysis on the effect of different parameters on the breakup dynamics are presented and the experimental size distribution is compared against the model developed by Martínez-Bazán et al. [39, 40].

Recent studies [4, 16, 19] have found that high viscosity and/or low surface tension dispersed phase fluid particles behave differently during breakup. To explore the effect of dispersed phase fluid properties, the second part of the results in this thesis consisted of experiments with various dispersed phase fluids. Chapter 7 provides the statistical analysis on the particle size of the breakup of drops of high viscosity fluids, and of high viscosity fluids covered with surfactants to isolate the effects of surface tension from that of viscosity. Some important parameters used in the population balance model, such as the breakup time and the breakup probability, are explored in Chapter 8, by using the new breakup tracking algorithm developed in this thesis. Finally, Chapter 9 summarizes the conclusions from this thesis, and discusses potential continuation of the experimental work as well as future modeling work that could support and close some aspects of the problem that this thesis did not address.

Chapter 2

REVIEW OF TURBULENT BREAKUP

2.1 Background

In most engineering applications and naturally-occurring processes involving the breakup of a fluid particle in turbulent flow, the major concern is the resulting particle size distribution. For example, in liquid mixture separation processes, the mass transfer rate is determined by the size distribution of the dispersed phase. In the process of gas exchange between the ocean and the atmosphere, the rate at which different gases (notably oxygen and carbon dioxide) dissolve depends on the size distribution of the entrained air bubbles, which result from the breakup of large air cavities entrained by breaking waves and broken-up by turbulence beneath the free surface.

Kolmogorov [31] and Hinze [22] started studying the process of breakup of a fluid particle, gas bubble or liquid drop, in a turbulent flow over fifty years ago. They proposed that the breakup of particles in a high Reynolds number flow is due to the dynamic pressure forces at the particle interface exerted by the carrier flow turbulent motion. These dynamic pressure forces are caused by the velocity fluctuations over length scales equal or smaller than the size of the particle. Since the kinetic energy of velocity fluctuations increases with increasing wavelength, the most energetic turbulent motions relevant to this process have the length scale of the particle size. Turbulent motions with length scales larger than the particle size only contribute to the transport of the particle.

By assuming the particle diameter, and therefore the characteristic turbulent length scale that dominates the process, is in the inertial subrange, Kolmogorov's second hypothesis of isotropic and homogenous eddies apply and the energy spectrum can be computed as follows:

$$E(k) \propto \epsilon^{2/3} k^{-5/3} \tag{2.1}$$

The characteristic velocity fluctuation can be obtained by integrating the spectrum over the length scale smaller than the particle size D.

$$\overline{\Delta u^2} = C_1(\epsilon D)^{2/3} \tag{2.2}$$

where $C_1 = 2$ [22], ϵ is the turbulent dissipation rate and D is the particle diameter.

Therefore, the Kolmogorov-Hinze theory suggested that the disruptive motions responsible for the breakup of particles in high Reynolds number turbulent flow depend solely on the turbulent dissipation rate. Many theoretical models [68, 13, 34, 66, 36, 39, 40] have been developed based on this theory. Some of these models [66, 39, 40] have been improved by comparison with experimental results.

All the literature reviewed in this chapter uses the population balance model, proposed by Hulbert and Katz [23], to describe the evolution of the droplet number density as the breakup process progresses. Considering situations where evaporation, condensation and dissolution are not important, meaning that the change in particle diameter is only due to breakup and coalescence, and that there is no external forces acting on the fluid particle, the population balance equation is written as follows:

$$\frac{\partial p}{\partial t} + \nabla_{\mathbf{x}} \cdot (\mathbf{v}p) = \dot{Q}'_b + \dot{Q}'_c \tag{2.3}$$

where p is the particle number density function that depends on particle diameter D, position $\mathbf{x}$, velocity $\mathbf{v}$, and time t. $\dot{Q}'_b$ and $\dot{Q}'_c$ are the rate of change of p due breakup and coalescence, respectively. The velocity dependence of the particle distribution function is not important in most applications, so a more practical form is derived by integrating Equation (2.3) over all velocities (Equation (2.4)).

$$\frac{\partial n}{\partial t} + \nabla_{\mathbf{x}} \cdot (\overline{\mathbf{v}}n) = \dot{Q}_b + \dot{Q}_c \tag{2.4}$$

where $n = \int p d\mathbf{v}$, $\overline{\mathbf{v}}$ is the mean velocity, $\dot{Q}_b = \int \dot{Q}'_b d\mathbf{v}$ and $\dot{Q}_c = \int \dot{Q}'_c d\mathbf{v}$.

In applications where n and $\overline{\mathbf{v}}$ are spatially uniform, as approximated in stirred tank experiments, the second term on the left hand side of Equation (2.4) can be eliminated. However, in turbulent jet experiments, this convective term must be considered. In order to solve this equation, models for $\dot{Q}_b$ and $\dot{Q}_c$ are necessary. Different variations of models for $\dot{Q}_b$ and $\dot{Q}_c$ are proposed by different authors. Generally, the following model is used:

$$\dot{Q}_b(D) = \int_D^\infty m(D_o) f(D, D_o) g(D_o) n(D_o, t) dD_o - g(D) n(D, t) \tag{2.5}$$

where $m(D_o)$ is the mean number of daughter particles that are broken up from the mother particle of size D_o, $f(D, D_o)$ is the daughter particle size distribution, and $g(D)$ is the breakup frequency.

$$\begin{aligned} \dot{Q}_c(D) = \int_0^V \lambda(V - V_1, V_1) h(V - V_1, V_1) n(V - V_1, t) n(V_1, t) dv_1 \\ - n(V, t) \int_0^\infty \lambda(V, V_1) h(V, V_1) n(V_1, t) dV_1 \end{aligned} \tag{2.6}$$

where $\lambda(V - V_1, V_1)$ is the collision efficiency between particles with volume of $V - V_1$ and V_1 and $h(V - V_1, V_1)$ is the collision frequency between the two particles.

Based on Equations (2.5) and (2.6), we know that the complete description of the breakup process comes down to modeling of $m(D_o)$, $f(D, D_o)$, $g(D)$, $\lambda(V - V_1, V_1)$, and $h(V - V_1, V_1)$. There are many practical applications where the number density of particles in the flow is very low and therefore coalescence can be considered negligible. Furthermore, in the effort to understand the process of turbulent break up of a fluid particle, not needing to derive models for $\dot{Q}_c$, that will impact the experimental results and obscure the theoretical analysis, is an important advantage. In this review, we will therefore focus on the modeling of the breakup frequency $g(D)$ and the daughter particle size distribution $f(D, D_o)$, as is relevant to the study described in this thesis.

2.2 Breakup frequency models

The modeling of breakup frequency began as early as 1966 when Valentas et al. [68] suggested that the breakage frequency could be dependent on the drop diameter, surface area, or volume. Thus, the following relationship is proposed:

$$g(D) = C_2 D^{C_2}, \qquad C_3 = 0, 1, 2, 3 \tag{2.7}$$

where the coefficient C_2 is determined experimentally.

Instead of a purely empirical model, a better approach for modeling breakup frequency is based on the eddy-particle collision idea. A variety of models have been developed based on this idea and, although the end results differ from each other, there are some common assumptions for all these models that emanate from the eddy-particle collision concept. First, particles break up when they collide with eddies with sizes comparable to or less than the particle diameter, providing the eddy have sufficient energy. Eddies with sizes larger than the particle only contribute to the transport (stirring) of the particle. Turbulence at the scale of the particle is assumed to be isotropic. Even in cases where turbulence is anisotropic, the structures responsible for breakup have length scales within the inertial subrange or smaller and can be considered to be locally isotropic, provided the Reynolds number is sufficiently high, according to Kolmogorov's hypothesis. To fit this hypothesis, the model can only be used to predict breakup of particles with sizes in the inertial subrange. Larger particles break through other mechanisms, interacting with the mean flow and the large coherent structures. These assumptions are made consistently with the Kolmogorov-Hinze theory. Consequently, the kinetic energy of the colliding eddies depends only on the turbulent dissipation rate.

Coulaloglou & Tavlarides [13] proposed a model based on an energy argument. With the assumption that drops are within the inertial subrange, viscous effects are negligible. So, the deformation of drops is only due to pressure fluctuations. The source of the pressure fluctuations on the drop surface stem from the collision of the drop with a turbulent eddy. If the turbulent kinetic energy of the eddy exceeds the drop surface energy, the surface of the

drop starts to oscillate causing the drop to deform and eventually break into smaller drops. They defined the breakup frequency as:

$$g(D) = \frac{1}{t_b}\frac{\Delta N(D)}{N(D)} \tag{2.8}$$

where t_b is the breakup time and $\frac{\Delta N(D)}{N(D)}$ is the fraction of drops breaking.

They assumed the velocity distribution of the turbulent eddies to be normal (see Equation (2.9)). This can be converted to a distribution of turbulent kinetic energy, as it is proportional to the square of the velocity fluctuations. The fraction of drops breaking is assumed to be proportional to the fraction of turbulent eddies with sufficient turbulent kinetic energy to overcome the surface energy of the drop. Thus, by integrating Equation (2.9) with respect to the turbulent kinetic energy for $E \geq E_c$, we have the relationship shown in Equation (2.10).

$$P(u_e)du_e = exp\left(-\frac{u_e^2}{\overline{u_e^2}}\right) d\left(-\frac{u_e^2}{\overline{u_e^2}}\right) \tag{2.9}$$

$$\frac{\Delta N(D)}{N(D)} = \int_{E_c}^{\infty} P(E)dE = exp\left(-\frac{E_c}{\overline{E}}\right) \tag{2.10}$$

where $E_c = C_4\sigma D^2$ is the surface energy of the drop, $\overline{E} = C_5\rho D^3\overline{u_e^2}(D)$ is the mean turbulent kinetic energy of the eddies, and u_e is the eddy velocity fluctuation. As discussed earlier, the eddy velocity fluctuation can be calculated using the Equation (2.2).

The breakup time can be estimated as the turbulent turnover time, i.e. $t_b \propto D^{2/3}\epsilon^{-1/3}$. Combining this with Equation (2.10) and the expression for E_c and $\overline{E}$, Equation (2.8) becomes:

$$g(D) = 2D^{-2/3}\epsilon^{1/3}exp\left(-\frac{C_6\sigma}{\rho\epsilon^{2/3}D^{5/3}}\right) \tag{2.11}$$

where C_6 are dimensionless empirical constants.

Prince & Blanch [53] proposed that the breakup frequency is related to the eddy collision frequency ω_{De} and collision efficiency $F(u)$ between particles and turbulent eddies. The collision frequency is related to the concentration of the eddies, the collision cross-sectional

area, and the average velocity of particles and eddies (Equation (2.12). The model of the collision efficiency is defined in a similar way as [13] (see Equations (2.9) and (2.10)).

$$\omega_{De} = n_e \left[\frac{\pi}{4} \left(\frac{D}{2} + \frac{\pi}{k} \right)^2 \right] (\overline{\Delta u_{tD}^2} + \overline{\Delta u_{te}^2})^{1/2} \tag{2.12}$$

where n_e is the concentration of eddies, obtained by integrating $dn_e/dk = 0.1k^2$ over the size range of interest (in terms of wavenumber). $\overline{\Delta u_{tD}^2}$ and $\overline{\Delta u_{te}^2}$ are the average turbulent velocity of particles and eddies, respectively. These velocities can be calculated by taking the square root of Equation (2.2), which is shown in the following equation [62]:

$$u_t = 1.4(\epsilon D)^{1/3} \tag{2.13}$$

where u_t is the turbulent velocity in the inertial subrange for isotropic turbulence. Combining the eddies collision efficiency and the collision frequency, the complete model is written as follows:

$$\begin{aligned} g(D) = \int_0^{10\pi/D} \frac{0.14\pi}{16} \left(D + \frac{2\pi}{k} \right)^2 \left[D^{2/3} + \left(\frac{2\pi}{k} \right)^{2/3} \right]^{1/2} \epsilon^{1/3} \\ \times exp \left[-\frac{1.18\sigma k^{2/3}}{(2\pi)^{2/3} \rho D \epsilon^{2/3}} \right] k^2 dk \end{aligned} \tag{2.14}$$

Note that the integration limits of this model, the lower and upper wavenumber k limits, must be defined according to the range of the size of eddies that would contribute to the breakup. However, Prince & Blanch [53] arbitrarily defined the lower integration limit as zero and the upper limit as $2\pi/0.2D$. They suggested that eddies with length scale smaller than 20% of the particle diameter do not contribute to the breakup. While it might be true that the model is insensitive to the lower limit of integration (zero wavenumber), it has been shown by [32] that the model is in fact sensitive to the maximum wave number ($10\pi/D$). A comparison between the models by Coulaloglou & Tavlarides [13] and Prince & Blanch [53] was provided by Eastwood et al. [16] and is re-plotted here in Figure 2.1.

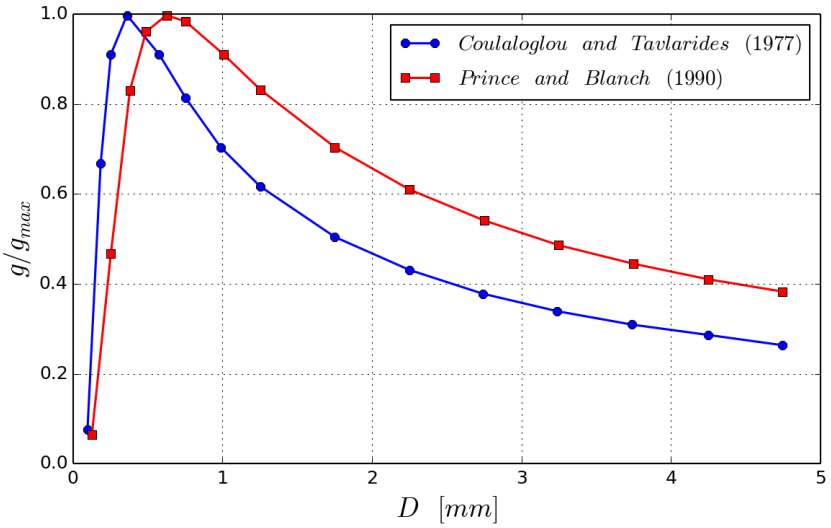

Figure 2.1: Comparsion of Coulaloglou & Tavlarides' [13] and Prince & Blanch's [53] breakup frequency models. $\sigma = 0.072\ N/m$, $\rho = 1000\ kg/m^3$, $\epsilon = 1000\ m^2/s^3$.

From figure 2.1, we see that the two models have the same general shape and that the predicted values are matching up well for small diameter particles, but for large particles they start to deviate. Another feature of these models is the appearance of a maximum breakup frequency at some critical diameter. Tsouris & Tavlarides [66] acknowledged that it is not realistic to have non-monotonic relationship between breakup frequency and particle size. They proposed an improved monotonic model as follows:

$$g(D) = C_7 F(\phi)\epsilon^{1/3} \int_{2/D}^{2/D_{min,e}} k^2 \left(D + \frac{2}{k}\right)^2 \left(1.07D^{2/3} + \frac{8.2}{k^{2/3}}\right)^{1/2} \times exp\left[-\frac{C_8\pi\sigma}{2} \frac{\left[2\left(\frac{D}{2^{1/3}}\right)^2 + D_{max}^2 + D_{min}^2 - 2D^2\right]}{0.43\rho\pi(2/k)^{11/3}\epsilon^{2/3}}\right] dk \tag{2.15}$$

where $F(\phi)$ is a turbulence damping factor with the introduction of the disperse phase. Similar to [53], this model depends on the integral limits. However, Tsouris & Tavlarides [66] claimed that, provided the particles are within the inertial subrange ($L_e > D > \eta$),

the model is independent of the limits of integration as long as $2/L_e < k_{min} < 2/D$ and $2/\eta > k_{max} > 2/D_{min,e}$. There are two problems with this approach. First, $D_{min,e}$, which is the minimum eddy size, is defined arbitrarily. Second, Eastwood et al.[16] showed that if we take the lower limit as $k_{min} = 2/L_e$, the breakup frequency decreases with drop size. Figure 2.2) shows this decreasing trend with $k_{min} = 2000$ (with $L_e = max.\ drop\ size = 1\ mm$). This actually contradicts the model assumption that eddies with size larger than the particle only contribute to the transport and straining, but not the breakup of the particle.

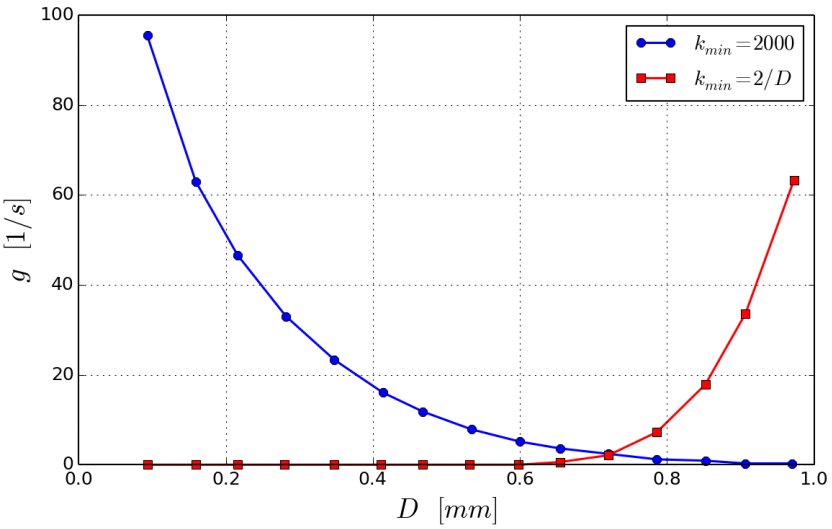

Figure 2.2: Breakup frequency of Tsouris & Tavlarides' model [66] with different lower integration limits. $\sigma = 0.072\ N/m$, $\rho = 1000\ kg/m^3$, $\epsilon = 1\ m^2/s^3$.

Luo & Svendsen [36] criticized the previous models because they require two or more parameters that need to be determined experimentally. Similar to Tsouris & Tavlarides [66], this model assumes that only eddies with size equal to or smaller than the particle diameter induce oscillation on the particle surface. Also, in parallel to Prince & Blanch [53], the breakup frequency is calculated by multiplying the particle-eddy collision efficiency and collision frequency. Another assumption is that the particle oscillation frequency is larger than the eddies arrival frequency, meaning that particle breakage is caused by only one eddy

with sufficient turbulent kinetic energy. The collision frequency is defined as follows:

$$\dot{\omega}_{De}(D) = \frac{\pi}{4}(D + D_e)^2 \overline{u_t} \frac{dn_e}{dD_e} \tag{2.16}$$

where the turbulent velocity, u_t has been defined earlier, in Equation (2.13) and dn_e/dD_e is defined in Equation (2.17).

This is modeled slightly different than in Prince & Blanch. In Equation (2.12), we saw that the collision frequency used in [53] is directly related to the concentration of eddies. In contrast, the collision frequency from Luo & Svendsen [36] is related to the derivative of the concentration of the eddies.

$$\frac{dn_e}{dD_e} = \frac{0.822(1 - \epsilon_D)}{D_e^4} \tag{2.17}$$

where ϵ_D is the particle phase volume fraction.

Luo & Svendsen [36] used the same definition of collision efficiency as Coulaloglou & Tavlarides [13] (Equation (2.10)), but the form of E_c, and $\overline{E}$ are defined differently. The surface energy is $E_c = C_f \pi \sigma D^2$ is defined similar to Coulaloglou & Tavlarides model [13], but the coefficient, $C_f = f_v^{2/3} + (1 - f_v)^{2/3} - 1$, depends on the volume fraction of the daughter particles, i.e. $f_v = D_1^3/D^3$, where D_1 is the diameter of one of the daughter particles (assuming binary breakup). The mean turbulent kinetic energy is defined as $\overline{E} = 0.17\pi\rho\epsilon^{2/3}D^{11/3}\xi^{11/3}$, in parallel to Coulaloglou & Tavlarides [13], but with the addition of $\xi^{11/3}$, where $\xi = D_e/D$.

Following the same derivation, the breakup frequency in which a particle with diameter of D breaks into two particles with diameters D_1 and $(D^3 - D_1^3)^{1/3)}$ becomes:

$$g(D_1, D) = 0.923(1 - \epsilon_D)\left(\frac{\epsilon}{D^2}\right)^{1/3} \int_{\xi_{min}}^{1} \frac{(1+\xi)^2}{\xi^{11/3}} exp\left(-\frac{12 C_f \sigma}{2.045\rho\epsilon^{2/3}D^{5/3}\xi^{11/3}}\right) d\xi \tag{2.18}$$

In this equation, the lower integration limit is defined as $\xi_{min} = D_{e,min}/D$, where $D_{e,min}$ is the minimum eddy size in the inertial subrange. Similar to some of the earlier models, the

integration limits are chosen based on empirical assumptions: the upper limit indicates that eddies larger than the particle size D do not contribute to the breakup. However, it could be argued that eddies with sizes comparable to the particle can also induce deformation of the particle surface. Eastwood et al. [16] showed that if the upper integration limit is chosen as $\xi_{max} = 2$ instead of $\xi_{max} = 1$, the breakup frequency increases significantly (Figure 2.3).

Since the interest is on the breakup frequency regardless of the size of the daughter particles, we integrate Equation (2.18) over all possible daughter particles and obtain:

$$g(D) = \frac{1}{2} \int_0^1 g(D_1, D) df_v \tag{2.19}$$

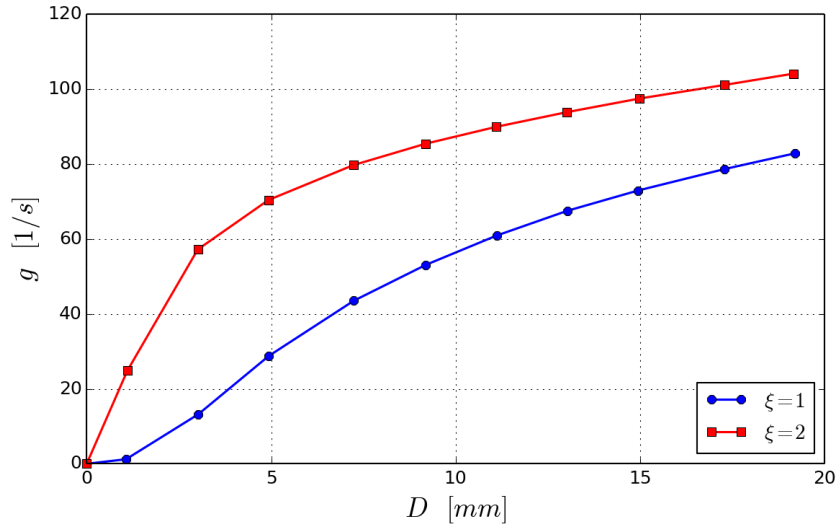

Figure 2.3: Breakup frequency of Luo & Svendsen's model [36] with different upper integration limits. $\sigma = 0.072\ N/m$, $\rho = 1000\ kg/m^3$, $\epsilon = 1\ m^2/s^3$.

Although developed based on the same eddy-particle collision idea, Martínez-Bazán et al.'s model [39] uses a different approach. Instead of the energy argument used by [13, 53, 66, 36], Martínez-Bazán et al. [39] proposed a dynamic point of view to model the breakup frequency. It defines the confinement stress, τ_s, and the average deformation stress, τ_t, as shown in Equation (2.20). It assumes that viscous effects are negligible, so the confinement

stress is only due to surface tension. The deformation stress is due to the velocity fluctuations between two points in the flow separated by a distance D, the diameter of the particle.

$$\tau_s(D) = \frac{6\sigma}{D} \qquad \& \qquad \tau_t(D) = \frac{1}{2}\rho\overline{\Delta u^2}(D) \tag{2.20}$$

where $\overline{\Delta u^2}(D)$ can be calculated using Equation (2.2). Break-up of the particle happens when $\tau_t > \tau_s$, so the critical diameter can be defined by equating τ_t and τ_s in equation 2.20 and solve for D (Equation (2.21)). This implies that a particle with size $D > D_c$ will break as the average deformation stress exceeds the confinement stress.

$$D_c = \left(\frac{12\sigma}{C_8\rho}\right)^{3/5} \epsilon^{-2/5} \tag{2.21}$$

where $C_8 = 8.2$ [7].

Martínez-Bazán et al. [39] then assumed the breakup time of a particle to be $t_b \propto D/u_b$, where $u_b = \sqrt{\overline{\Delta u^2}(D) - 12\sigma/(\rho D)}$ is a characteristic interface deformation velocity. This represents a modified form of the difference between the average deformation stress and the confinement stress. From this, the breakup frequency can be obtained by taking the inverse of the breakup time:

$$g(D) = 1/t_b = C_9\frac{u_b}{D} = C_9\frac{\sqrt{\overline{\Delta u^2}(D) - 12\frac{\sigma}{\rho D}}}{D} \tag{2.22}$$

where $C_9 = 0.25$ is obtained experimentally.

It is important to note that Martínez-Bazán et al.'s [39] model does not require the definition of arbitrary integration limit like some previous models because the kinematic approach does not require breakup efficiency that originated from the particle-eddy collision. This implies that the model assumed breakup will occurs as long as the deformation stress is greater than the confinement stress.

To summarize, the eddy-particle collision idea pioneered by Kolmogorov [31] and Hinze [22], has been developed into functional models over the last four decades. There are two general approaches to apply this idea. The first one is to base the efficiency of the collision

based on the surface energy of the drop and the kinetic energy of the eddies. A more sophisticated version of this approach incorporates the frequency of the collisions, which is based on the concentration of the eddies, the cross-sectional area of the collision and the relative velocity of the eddies and the particles. The second approach uses a dynamic balance, which is based on the inequilibrium between the confinement stress and the deformation stress. Figure 2.4 summarizes these approaches.

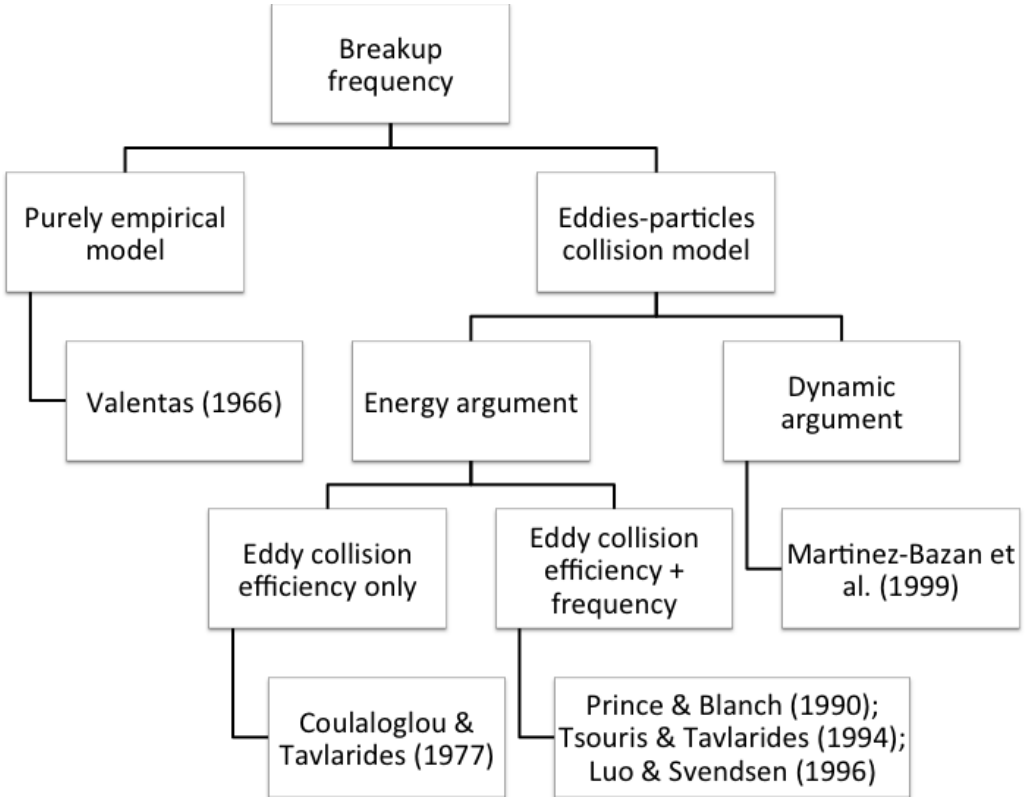

Figure 2.4: A summary of different approaches of modeling the breakup frequency.

2.3 Daughter particle size distribution models

As mentioned in section 2.1, the complete formulation of the population balance model requires not just a term for the breakup frequency, but also modeling of the mean number of daughter particles, $m(D_o)$, and the daughter particle size distribution, $f(D, D_o)$, where

D_o is the mother particle. Most models in the literature assume binary breakup, which means a mother particle will break into two daughter particles. Mathematically, this implies $m(D_o) = 2$.

Early models of the daughter particle size distribution were purely statistical. Valentas et al. [68] proposed two models for the breakup kernel, including the daughter particle size distribution. The first model, shown in equation 2.23, used a delta function. This means binary break-up results in two equal-sized daughter particles. In the second model, Valentas et al.[68] used a normal distribution, shown in equation 2.24. The variance of this distribution (Equation (2.25)) depends on $m(D_o)$, so this model no longer assumed binary breakup. Instead, $m(D_o)$ must be found experimentally. The mean value of the distribution is given by $\overline{D} = D_o/m(D_o)^{1/3}$, so the most probable breakup still is into equal-sized daughters.

$$f(D, D_o) = \delta\left(D - \frac{D_o}{2^{1/3}}\right) \tag{2.23}$$

$$f(D, D_o) = \frac{1}{\sigma\sqrt{2\pi}} exp\left[-\frac{(D-\overline{D})^2}{2\sigma^2}\right] \tag{2.24}$$

$$\sigma = \frac{D_o}{C_{10} m(D_o)^{1/3}} \tag{2.25}$$

where C_{10} is a specified tolerance of the diameter range.

Despite being one of the first studies to provide physical reasoning on the model of breakup frequency, Coulaloglou & Tavlarides [13] relied on a statistical model for their daughter particle size distribution. They used the normal distribution from Valentas et al. [68] but with different parameter values. Since the daughter particle size should never exceeds the mother particle size, the variance was set such that 99.6% (3 standard deviations) of the resulting daughter particles were in the range 0 to $\pi D_o^3/6$ (mother particle volume). Also, by assuming binary breakup, their model became:

$$f(D, D_o) = \frac{2.4}{D_o^3} exp\left[-\frac{4.5(2D^3 - D_o^3)^2}{D_o^6}\right] \tag{2.26}$$

Lee et al. [34] applied a different statistical model for the daughter particle size distribution. They developed a model based on the beta function. The complete model is shown in Equation (2.27).

$$f(V, V_o) = \frac{(V/V_o)^{C_{11}-1}}{V_o}\left[1 - \left(\frac{V}{V_o}\right)\right]^{C_{12}-1} B_e(C_{11}, C_{12}) \tag{2.27}$$

where V is the volume of the daughter particle. V_o is the volume of the mother particle. $B_e = \int_0^1 x^{C_{11}-1}(1-x)^{C_{12}-1}dx$ is the beta function. $C_{11} > 0$ and $C_{12} > 0$ are constant to be determined experimentally. For binary breakup, the ideal values are $C_{11} = C_{12} = 2$. However, Lee et al. [34] also proposed a multi-particle breakup model. They suggested the mean number of daughter particles be given by :

$$m(V_o) = 2 + C_{13}V_o^{C_{14}} \tag{2.28}$$

where C_{13} and C_{14} are empirical constants.

The best fit for their experimental data occurs when $C_{13} = 10$ and $C_{14} = 0.5$. In this case, $C_{11} = 2/(m(V) - 1)$ and $C_{12} = 2$ are the ideal values used in Equation (2.27). Although it is physically more realistic not to assume binary break-up and equal-size daughter particles, models like [34] require four empirical constants. Since these constants could change depending on the type of flow, these models might not be practical in some applications.

Unlike the statistical approach used by previous authors, Nambiar et al. [45] provided a model based on the eddy-particle collision approach. They proposed that the daughter particle size distribution depends on the probability of collision with an eddy that is within the effective size range for break-up (Equation (2.32)). This effective size range is given as $D_{min,e} \leq D_e \leq D$. The upper limit implies that an eddy with size greater than the mother particle does not contribute to breakup. $D_{min,e}$ can be found by finding D_e that satisfy the inequality (2.29) and $D_e \leq D$.

$$\frac{2}{\sqrt{\alpha}} tan^{-1}\left(\frac{1}{2\sqrt{\alpha}}\right) \leq \left(\frac{ReG}{We}\right)\left(\frac{D}{D_I}\right)^{-1/3}\left(\frac{D_e}{D}\right)^{2/3} \tag{2.29}$$

where Re is the Reynolds number, We is the Weber number, α is defined in Equation (2.30) and G corresponds to the surface energy change from the break-up of a mother particle to daughter particles, defined in Equation (2.31). Nambiar et al. study focused on the breakup process in a stirred reactor where the turbulent motion is induced by a rotating impeller, so the length scale of the problem was chosen to be the impeller diameter, D_I.

$$\alpha = \frac{C_{15}(D_e/D)^{2/3}We}{G}\left(\frac{D}{D_I}\right)^{5/3} - \frac{1}{4} \tag{2.30}$$

where C_{15} can be determined by the mean inertial stress of the stirred vessel using $\overline{\tau_T} = C_{15}\rho N^2 D_I^{4/3} D_e^{2/3}$, where N is the speed of the stirrer.

$$G = \frac{\left(\frac{V_o - V}{V_o}\right)^{2/3} + \left(\frac{V}{V_o}\right)}{2^{1/3}} \tag{2.31}$$

With the effective size range defined, the daughter particle size distribution can be found using the following equation:

$$f(V, V_o) = \frac{4sin|\frac{\pi - 2\phi}{3}|h(D_e|D_{min,e} \leq D_e \leq D)}{\pi D_e D sin\phi} \tag{2.32}$$

where $\phi = cos^{-1}\left(1 - \frac{2V}{V'}\right)$, and $h(D_e|D_{min,e} \leq D_e \leq D)$ is the probability of an eddy within the effective size range.

Figure 2.5 shows the daughter particle size distribution, $V_o f(V, V_o)$, from the model in [45]. The probability of a mother particle breaking up into a large and a small daughter particles is higher than the equal-sized breakup. This is the opposite of some of the previous models, such as the normal distribution models, where equal-sized breakup are the most probable. In fact, it takes less energy to produce a large and a small particle than two equal-sized particles, so the model by Nambiar et al.[45] is consistent with an energy minimization criteria. However, there is one drawback to this model, namely, that the probability of equal-sized breakup is zero. Although it takes more energy for equal-sized breakup, it is unphysical to assume that the probability for such break-up event is zero.

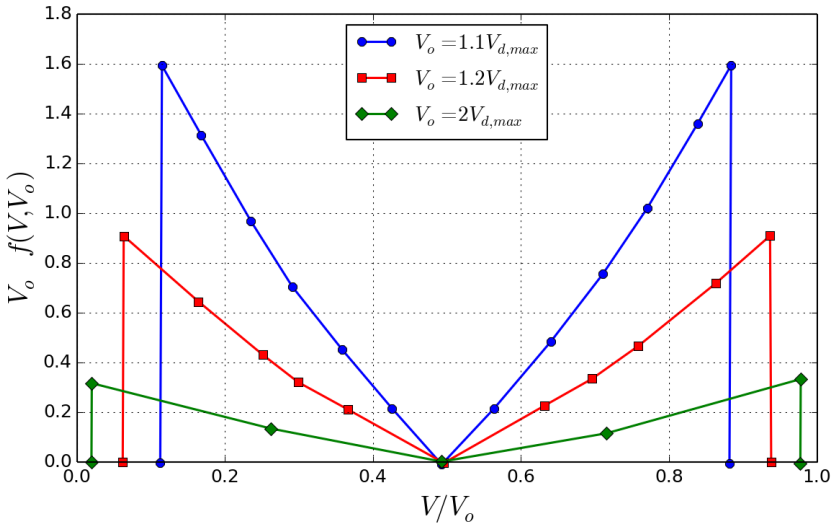

Figure 2.5: A daughter particle size distribution predicted by Nambiar et al.'s model [45].

Tsouris & Tavlarides [66] proposed that the daughter particle size is inversely proportional to the energy required to break a mother particle. And, the energy to break the mother particle is proportional to the excess surface area from the daughter particles. Since the maximum surface area of the daughter particles occurs for equal-sized breakup, the maximum surface energy of the daughter particles is $e_{max} = \pi\sigma D_o^2[2^{1/3} - 1]$, assuming binary breakup. The minimum surface energy occurs when the breakup results in one large and one small particle. In the limiting case, this occurs when the size of one of the daughter particle equal to the size of the mother particle. However, this results in the probability at both ends of the distribution being infinity. So, a minimum diameter, D_{min}, needs to be defined so that $e(D_{min}) = e_{min}$. Once these are defined, the daughter particle size distribution can be written as:

$$f(D_1, D_o) = \frac{e_{min} + [e_{max} - e(D_1)]}{\int_{e_{min}}^{D_o} e_{min} + [e_{max} - e(D_1)]dD_1} \tag{2.33}$$

The resulting size distribution has a U-shaped profile (Figure 2.6). The minimum point represents the probability of the equal-sized breakup ($\frac{1}{2^{1/3}}$). Similar to the model by Nambiar

et al. [45], Tsouris & Tavlarides [66] model also predicted zero probability for equal-sized breakup. As we mentioned earlier, this is an unphysical scenario. Another criticism of this model is that, as the size distribution depends only on the surface energy of the particles, the turbulent kinetic energy, which is the source of the breakup, does not influence the daughter size distribution.

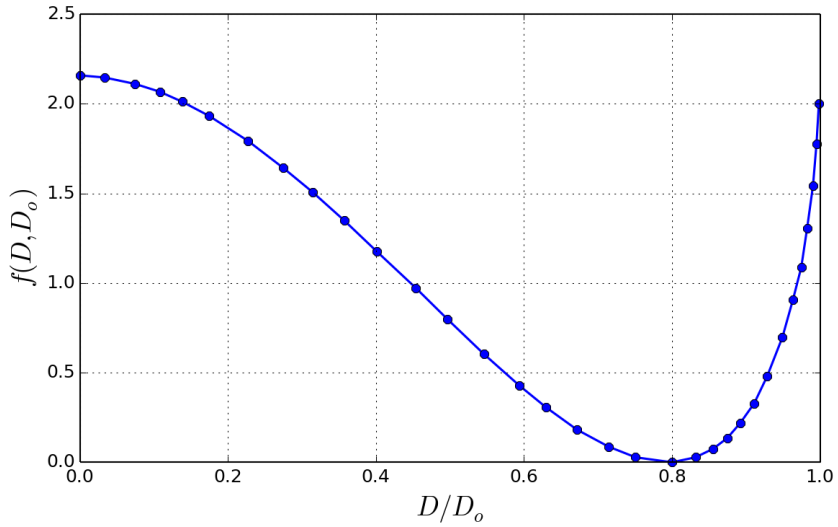

Figure 2.6: A daughter particle size distribution predicted by Tsouris & Tavlarides' model [66].

Luo & Svendsen [36] gives the daughter particle distribution as the result from two breakup frequency models (Equation (2.18) and (2.19)). The first one considers the breakup frequency into different daughter particle sizes by including the distribution of volume into the daughter particles in the analysis. The second one is the global breakup frequency. Thus, the daughter particle size distribution can be obtained from these two equations, assuming binary breakup. The resulting expression is:

$$f(Vf_V, V_o) = \frac{g(Vf_V, V_o)}{Vg(V)} \tag{2.34}$$

where $g(Vf_V, V_o)$ is obtained from Equation (2.18) and $g(V)$ is obtained from Equation

(2.19). Figure 2.7 shows the results from this model. This model predicts the highest probability for break-up into a large and a small particle, and the smallest probability, but distinct from zero, for equally sized particles. This is more realistic than the previously discussed predictions of zero probability for equally-sized particles [45, 66]. Also, the comparison between two different turbulent dissipation rate values shows that as the dissipation rate increases, the probability of getting two similarly-sized daughter particles increases, as there is more energy available in the turbulence to overcome the energy barrier associated with the higher surface energy necessary for breakup into equally-sized drops. However, Figure 2.7 makes painfully obvious, the probability diverges for daughter particles approaching the mother particle size, and thus arbitrary limits have to be placed to keep the distribution probability bounded.

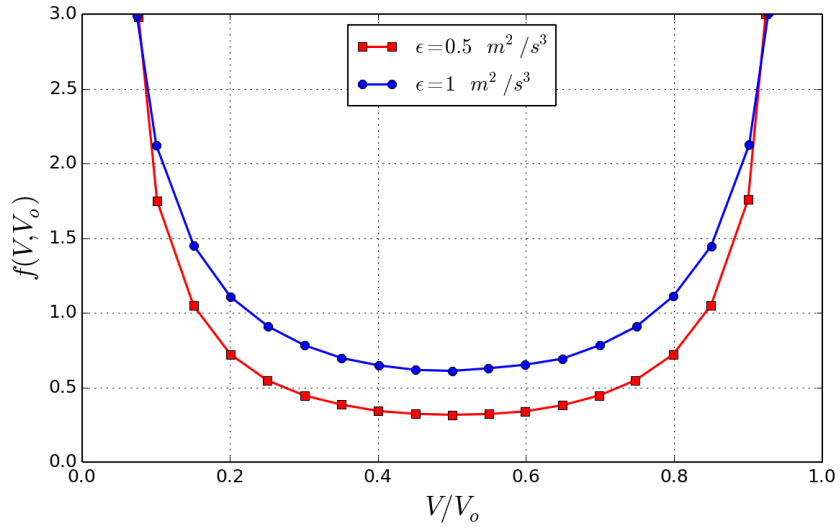

Figure 2.7: A daughter particle size distribution predicted by Luo & Svendsen's model [36]. $\epsilon = 1.0\ m^2/s^3$.

Martínez-Bazán et al. [40] built on the concept of confinement stress, τ_s and deformation stress, τ_t, used in the breakup frequency model, to create their daughter particle distribution. They proposed that the daughter particle size is related to the excess stress provided by

the underlying turbulent eddies. As a result of this concept, D_{min} is defined by solving $\tau_t(D_{min}) = \tau_s(D_o)$. D_{min} represents the minimum diameter at which the deformation stress of an eddy of this size can balance the confinement stress of the mother particle. This implies that the probability of a daughter particle with $D_1 < D_{min}$ is zero.

In Tsouris & Tavlarides [66], the size distribution was based on the excess surface energy of the daughter particles relative to the surface energy needed in the equal-sized breakup case. In parallel, Martínez-Bazán et al. [40] used the excess surface stresses relative to the deformation stresses for predicting the daughter sizes. They proposed that the probability of a mother particle breaking into two daughter particles of size D_1 and D_2 is proportional to the product of the excess surface stresses results from the two daughter particles. The probability can be written as:

$$P(D^*) \propto \left[4.1\rho(\epsilon D_1)^{2/3} - \frac{6\sigma}{D_o}\right]\left[4.1\rho(\epsilon D_2)^{2/3} - \frac{6\sigma}{D_o}\right] \tag{2.35}$$

where $D^* = D_1/D_o$. Since D_1 and D_2 are directly related, it can be simplified to:

$$P(D^*) \propto (4.1\rho(\epsilon D_1)^{2/3})^2[D^{*2/3} - \Lambda^{5/3}][(1 - D^{*3})^{2/9} - \Lambda^{5/3}] \tag{2.36}$$

where $\Lambda = D_c/D_o$ and D_c is the critical diameter, which is obtained by equating the two stresses in Equation (2.20) and solving for D.

The definitions of D_c and D_{min} are very similar as they are both derived from Equation (2.20). Physically, D_c represents the critical diameter for a mother particle to break, whereas D_{min} represents the minimum eddy size that can contribute to the breakup of a mother particle. The daughter particle size distribution can be written as:

$$f(D^*) = \frac{[D^{*2/3} - \Lambda^{5/3}][(1 - D^{*3})^{2/9} - \Lambda^{5/3}]}{\int_{D^*_{min}}^{D^*_{max}}[D^{*2/3} - \Lambda^{5/3}][(1 - D^{*3})^{2/9} - \Lambda^{5/3}]} dD^* \tag{2.37}$$

Figure 2.8 shows the prediction of the daughter particle size distribution using the model by Martínez-Bazán et al. [40]. The peak of the distribution is predicted for equal-sized breakup, which goes against energy-based models, where the probability is minimum (or

even zero) for equal-sized breakup. A comparison of three different turbulent dissipation rate values, ranging from 10 to 1000 m^2/s^3 in Figure 2.8, shows that as the dissipation rate increases, the size distribution gets wider and more uniform. This is consistent with the increase in energy contained in the small turbulent scales resulting in higher probability of breakup into smaller particles.

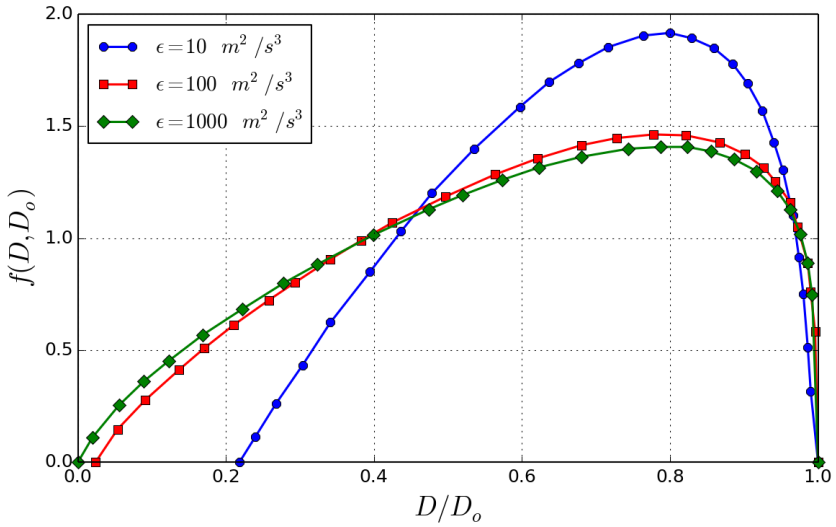

Figure 2.8: A daughter particle size distribution predicted by Martínez-Bazán's model [40].

In summary, the modeling of the daughter particle size distribution is mainly aligned with two distinct approaches: statistical or phenomenological (eddy-particle collisions) models. A number of statistical models have been proposed, some based on binary breakup and some not. Lee et al. [34] developed models for both cases and concluded that the multi-particle break-up model better represented their data. However, all phenomenological models assume binary break-up. There is a wide variety of daughter particle size distributions predicted, regardless of the approach. Specifically, there is no consensus as to whether the equal size break-up should be the most probable or the least probable case. Thus, experimental results on daughter particle size are needed to validate this aspect of the modeling. Figure 2.9 shows a chart with all the approaches to the modeling of daughter particle size distribution

reviewed in this section.

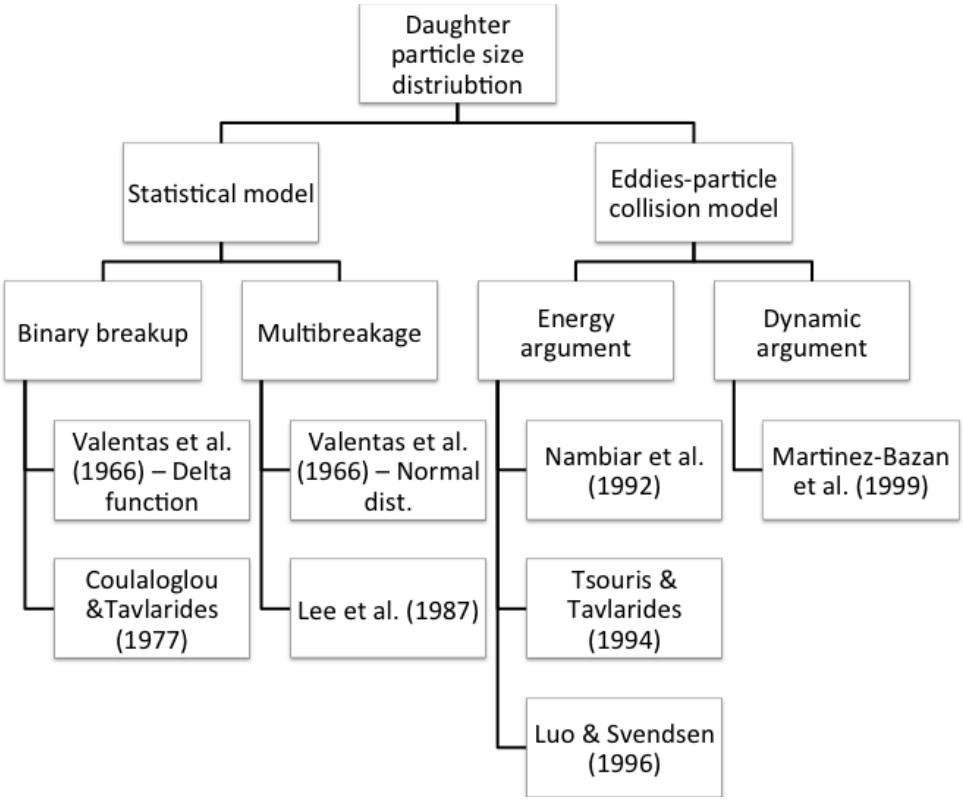

Figure 2.9: A summary of different approaches of modeling the daughter particle size distribution.

Chapter 3

EXPERIMENTAL SETUP FOR THE STUDY OF PARTICLE BREAKUP IN A TURBULENT JET

3.1 Experimental facility

The break-up experiments were conducted in a high Reynolds number turbulent round jet. The submerged water jet issued in an octagonal acrylic tank designed and built to house this experiment. The overall dimensions of the tank are 1.8 m tall and 1.2 m wide. The volume of the interior of the tank is about 600 gallon. The size of the tank was designed to minimize the confinement effect on the flow from the jet. The hexagonal shape of the tank was chosen so that the side walls form different angles (30°, 45°, 60° and 90°) with each other in order to accommodate different optical setups in Phase Doppler Particle Analysis measurements. For Particle Image Velocimetry measurements, the line of sight of the camera is perpendicular to the laser plane, so a pair of perpendicular walls are used for illumination and imaging.

Four holes are located at the bottom of the tank for filling and draining purposes. A donut shape mounting piece is also located at the bottom of the tank for the mounting of the jet nozzle. An access door was placed on one of the side walls, one feet from the bottom, for easy access to the nozzle and droplet-injection needle arrangements.

At the top of each side wall, a slot was cut to allow the injected liquid to flow out of the tank and into overflow boxes that are mounted on each slot. The liquid from these overflow boxes flows down by gravity through a network of ducts that connect all the overflow system to the drain. The overflow system maintains a constant hydrostatic pressure during the experiments, even when the amount of liquid injected by the high Reynolds number jet into the tank is large. This constant boundary condition further minimizes the confinement effect. A drawing of the tank design is shown in Figure 3.1.

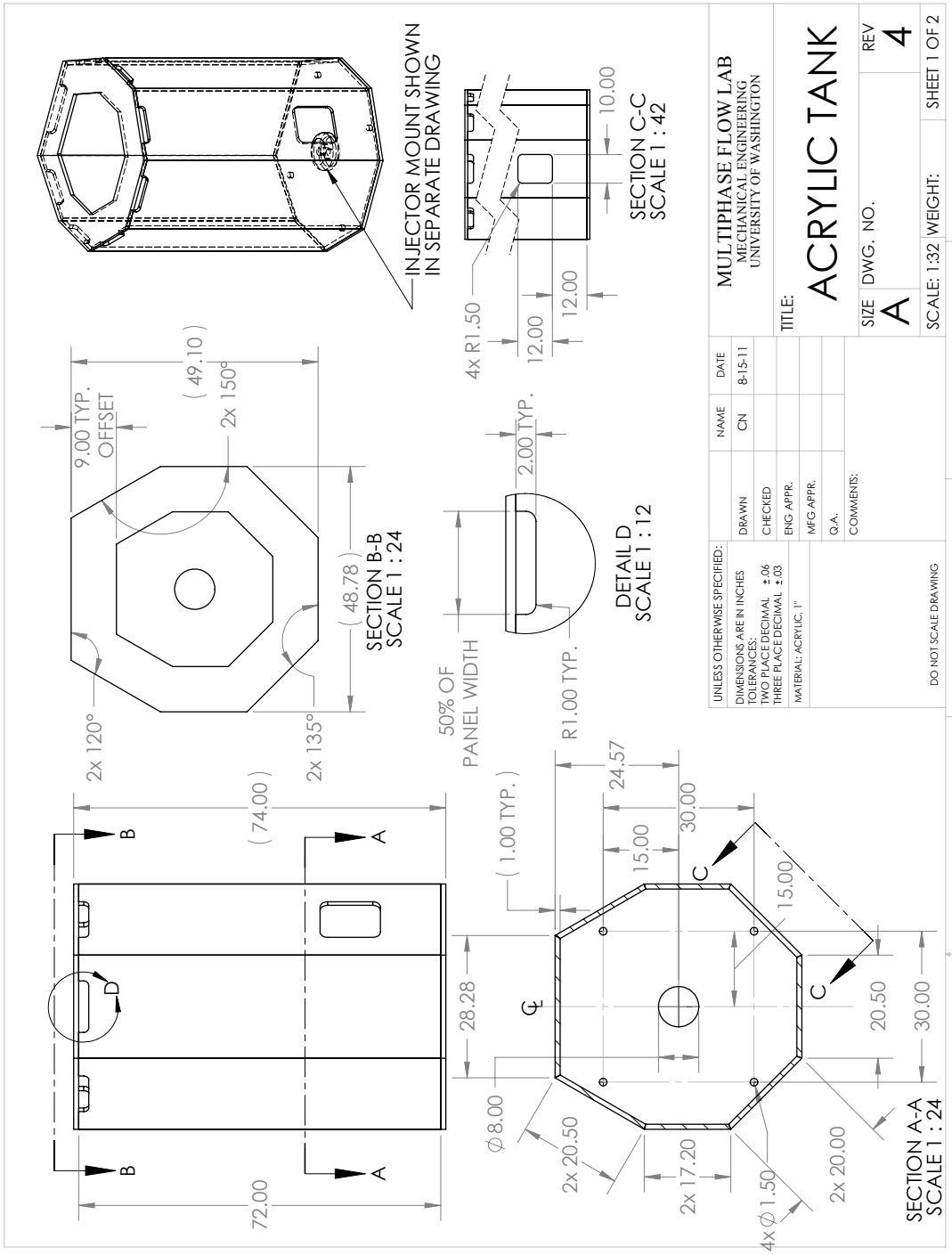

Figure 3.1: A drawing of the octagonal acrylic tank.

The tank is mounted on a steel table that is custom-designed with cutouts to fit the filling/draining holes and the mount for the nozzle. The table provides 0.7 m of ground clearance to accommodate the necessary ducts and components for the jet and droplet injection underneath the tank. In addition, adjustable feet were built-in to the table to ensure the table can be leveled on any surface.

3.1.1 Turbulent jet

The submerged jet is injected into the full tank, filled with the same liquid (fresh water) from the building supply. Two 30 μm filters are installed in series, upstream of the filling/draining holes to filter out any particle larger than 30 μm. These large particles can affect the flow field and the PIV measurements since, depending on flow conditions, they may not be good flow tracers. Particles smaller than 30 μm do not alter the baseline flow and are used as natural flow seeding for the PIV measurements.

The liquid in the high Reynolds number turbulent jet is injected using a pressurized bladder tank with a capacity of 0.03 m^3 (30 L). A diaphragm separates the liquid and compressed air in the bladder tank. The injection liquid is put in the liquid compartment in the bladder tank (the bottom) by gravity, while the tank is at atmospheric pressure. After the injection liquid has been placed in the bladder tank, the outlet valves are closed and the compressed air (top) compartment is pressurized up to 6.8 bar (85 psia) absolute pressure. This pressure allows the flow rate to reach the values needed for the high Reynolds number jet (up to 250,000) and stays constant for the limited extend of the experiments (typically around 30-60 s). Liquid injection flow rate is controlled using a combination of a ball valve, a needle valve, and a volumetric flowmeter. The flowmeter is a turbine type flowmeter that is factory-calibrated up to 0.63 L/s (10 gallon/min) with an accuracy of $\pm 1\%$ of the reading.

The nozzle diameter was varied to provide a range of accessible Reynolds numbers in the experiment. As the diameter of the nozzle increases the Reynolds decreases because the velocity decreases faster than the diameter increases, thus reducing the product in the numerator of the Re (the kinematic viscosity in the denominator is obviously kept constant).

For a constant flow rate, the velocity decreases with the square of the diameter inverse. For a constant pressure head from the bladder tank, the flow rate can increase slightly with the nozzle diameter, but this only reduces the dependency of the velocity with the inverse of the diameter to an exponent lower than 2, but higher than 1. Thus, we designed and built nozzles with diameter of 1, 3, 4, 7 and 10 mm to create a wide range of Re while keeping large spatial scales in the flow for the largest diameters. An optimum trade off between high Re and large spatial scales that can be fully resolved with the PIV and shadowgraphy imaging was found to be at 4 mm nozzle diameter. The interior profile of the nozzle follows a third order polynomial (Equation (3.1)) in order to create a top-hat velocity profile at the exit [24]. A drawing of the nozzle is shown in Figure 3.2.

$$r = \frac{d_i}{2} - \frac{3}{2}(d_i - d_e)\left(\frac{z}{L}\right)^2 + (d_i - d_j)\left(\frac{z}{L}\right)^3 \tag{3.1}$$

where r is the local radius of the interior surface, d_i is the initial diameter of the nozzle, d_j is the exit diameter of the nozzle, and L is the length from the entrance to the exit of the nozzle.

3.1.2 Disperse phase injection

Air, canola oil and silicon oil were chosen to study the influence of disperse phase properties, such as viscosity and surface tension, on the process of turbulent particle breakup. All of the disperse phase fluids are immiscible in water, thus solubility is not a factor in this experiments and this process does not affect the measured particle size.

The disperse phase is injected via a syringe pump (NE-1000, New Era Pump Systems Inc. NY) at a known, constant rate into the jet to study the breakup process. It is a displacement pump with an electronic flow rate control, which has an accuracy of $\pm$ 1% of the range. The pump is programmed to maintain a desired injection flow rate by pushing the piston of the syringe at the linear speed required, determined from the syringe inner diameter. Injected liquid is pushed out of the syringe through flexible tubing and a check valve. The dispersed

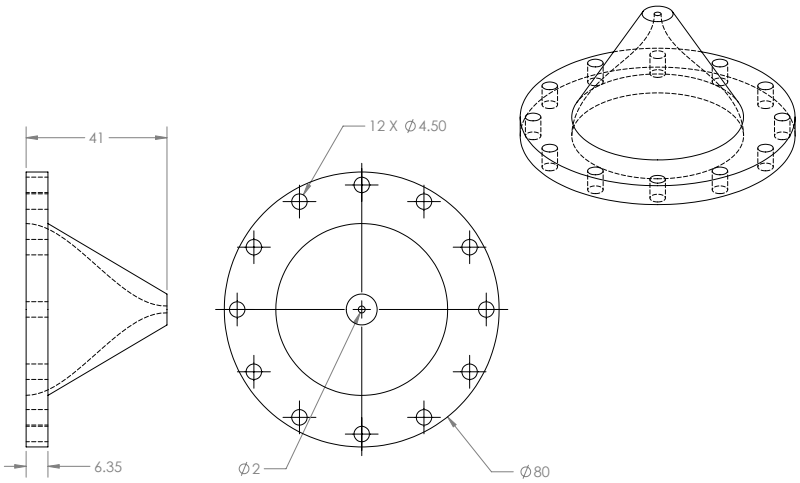

Figure 3.2: A drawing of the nozzle showing the third order polynomial interior surface.

phase fluid (air bubbles or oil drops) is ultimately introduced into the submerged jet through a small diameter needle. The needle was mounted inside the tank with a custom-made needle mount. Three different needle sizes were used in order to control the initial particle size. Since the needle size is usually described in gauge, Table 3.1 summarizes the outer and inner diameters of the needles used in the experiments described in this thesis.

The needle mount was designed for several functions: First, the mount can be fixed relative to the center axis of the jet, setting the orientation of the needle so that it is always pointing at the center axis. This is done through a circular base of the mount that has an inner diameter equal to the diameter of the nozzle and can be braced coaxially with it. Second, an aluminum structure, made up of t-slot segments, is attached to the circular base for support. The t-slot structure allows for easy adjustment in the vertical and radial placement of the injection needle.

Gauge size	**OD [mm]**	**ID [mm]**
16	1.65	1.19
20	0.91	0.60
22	0.72	0.41

Table 3.1: A summary of the needle sizes used in this experiment and their equivalent outer and inner diameter.

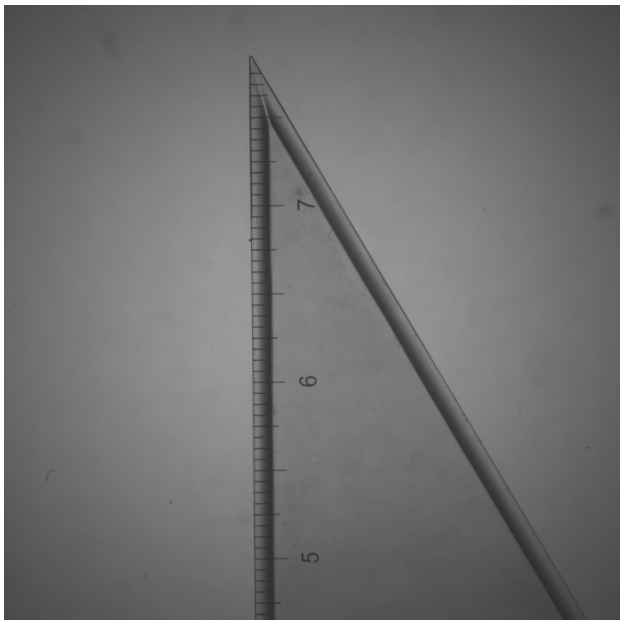

Figure 3.3: An example of the calibration target in the imaging field of view.

A measurement scale was attached to the mount, as shown in Figure 3.3, to provide a calibration target in the field of view of the camera. This scale arrangement also allowed for the easy determination of the relative position for multiple imaging locations, vertically along the streamwise axis of the jet. A schematic of the needle mount with the needle and the scale attached on it is shown in Figure 3.4

The injection needle was always mounted horizontally, oriented perpendicular to the

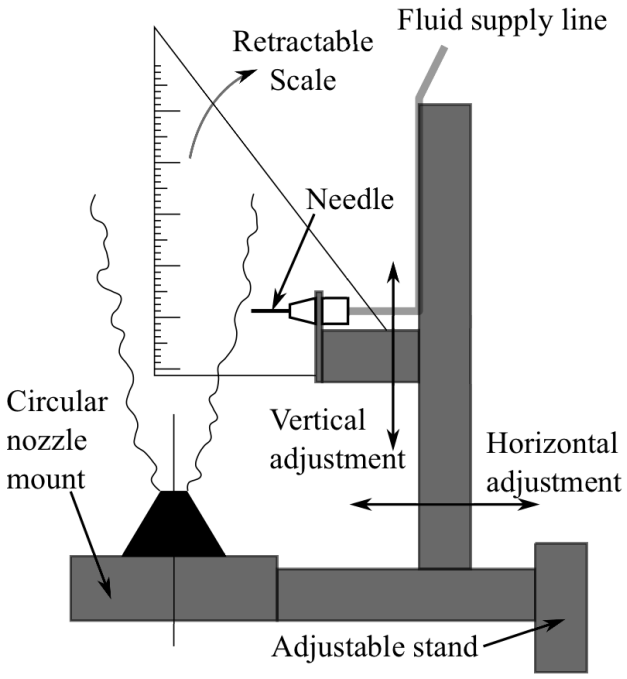

Figure 3.4: A schematic of the needle mount with the needle and spatial calibration target attached to it.

jet axis. Depending on the experiment, the needle was positioned at different locations downstream of the jet nozzle, between $z/d_j = 15$ to $z/d_j = 25$. Thus, the particles were introduced into the jet in the region of fully-developed turbulence. The needle outlet was placed at $2r_{1/2}$ from the centerline of the jet, where $r_{1/2}$ is the half width of the jet, that is in the outer region away from the centerline of the jet. The particles, thus introduced near the edge of the jet, are not suddenly exposed to the high velocity core of the jet, but rather have the opportunity to accelerate from the lower velocity region, sensing the mean shear and the inertial-scale turbulent fluctuations while they attain the local velocity of the jet as they are entrained towards the jet centerline. The half width is calculated from the PIV velocity measurements, using Equation (3.2) from Pope [52].

$$r_{1/2} = S(z - z_o) \tag{3.2}$$

where $S = 0.094$ is the spreading rate, z_o is the virtual origin of the jet.

3.1.3 Confinement effects

Hussein et al. [25] studied the influence of the presence of the walls at a finite distance and found that they can cause reverse flow that reduces the momentum of the jet, breaking the universality of a free-shear round jet. To study the effect of the reverse flow, they performed a first order momentum balance, developing an expression of the momentum ratio (Equation (3.3)).

$$\frac{M}{M_o} = \left[1 + \frac{16}{\pi B_m^2}\left(\frac{z}{d_j}\right)^2 \frac{A_o}{A_R}\right]^{-1} \tag{3.3}$$

where $B_m = 6.5$, $A_o = \pi d_j^2/4$ is the area of the nozzle, and $A_R = 1.3$ m^2 is the approximate cross-sectional area of the tank. The momentum ratio represents the effect of confinement. We can further simplify this expression, by simply substituting the expression of A_o in the equation, and use it to evaluate the influence of confinement on the measurements in this experimental setup.

$$\frac{M}{M_o} = \left[1 + \frac{4}{A_R}\left(\frac{z}{B_m}\right)^2\right]^{-1} \tag{3.4}$$

When M/M_o approaches unity, the effect of confinement is negligible. By setting an acceptable value of M/M_o, we determine the downstream distance z over which we can assume that confinement is negligible and the baseline turbulent jet in the experiments described in this thesis behaves as a canonical free-shear jet. For $M/M_o = 0.95$ and $M/M_o = 0.99$, the downstream distances for which the confinement effects can be considered to not influence the measurements are $z = 0.85$ m and $z = 0.37$ m, respectively. These represent slightly less than half or one quarter of the height of the tank (1.8 m), but more importantly, it goes downstream between $z/d_j = 100$ and $z/d_j = 850$ for the different tolerances and jet nozzle diameters (1 or 4 mm).

3.2 Imaging techniques

3.2.1 PIV setup

In order to characterize the turbulent jet that serves as the baseline flow in the turbulent breakup experiment, we used Particle Image Velocimetry (PIV) to measure the instantaneous jet velocity. We further computed the statistics of the turbulent velocity fluctuations in the jet by spatially and temporally averaging different moments of the velocity field.

PIV is an optical measurement technique that computes the displacement field of the flow by statistically correlating the light scattered from tracer particles seeded in the flow as it is captured in consecutive images. Velocity is calculated by simply dividing the displacements by the time between the two image snapshots (which is taken to be short enough to compute the velocity in the limit of zero delta t). In the experiments reported in this thesis, the seeding particles were illuminated in a thin plane created by expanding a laser beam via an spherical and a cylindrical lens. The measurement plane was placed so that it cuts diametrically across the centerline of the jet, in order to provide a two dimensional velocity field (axial and radial components of the jet), as shown in Figure 3.5. Only the seeded particles that pass within the laser sheet were illuminated, ensuring only the velocity field inside the imaging plane was measured. Since the jet is axisymmetric, the two-dimensional velocity field obtained from PIV fully characterizes the mean velocity field in the jet as well as the most important components of the Reynolds stress tensor ($\sqrt{\overline{u'^2}},\ \sqrt{\overline{v'^2}},\ \sqrt{\overline{u'v'}}$).

The PIV measurement setup consists of a specialized CCD camera (MegaPlus ES4020, Princeton Instruments, Trenton, NJ), a high-power pulsed Nd:YAG laser (Solo XT200, New Wave Inc, Portland, OR) and a synchronizer (BN 4050, Berkeley Nucleonics, Berkeley, CA.) that triggers the two camera exposures and two laser pulses to coordinate the right timing in the acquisition of the image pair. For PIV to accurately reproduce the velocity field of the fluid imaged, the laser pulses must illuminate the tracer particles in the flow over very short periods of time, in order to freeze their motion. At the same time, the time between images must be large enough to produce some measurable displacement of the tracer particles,

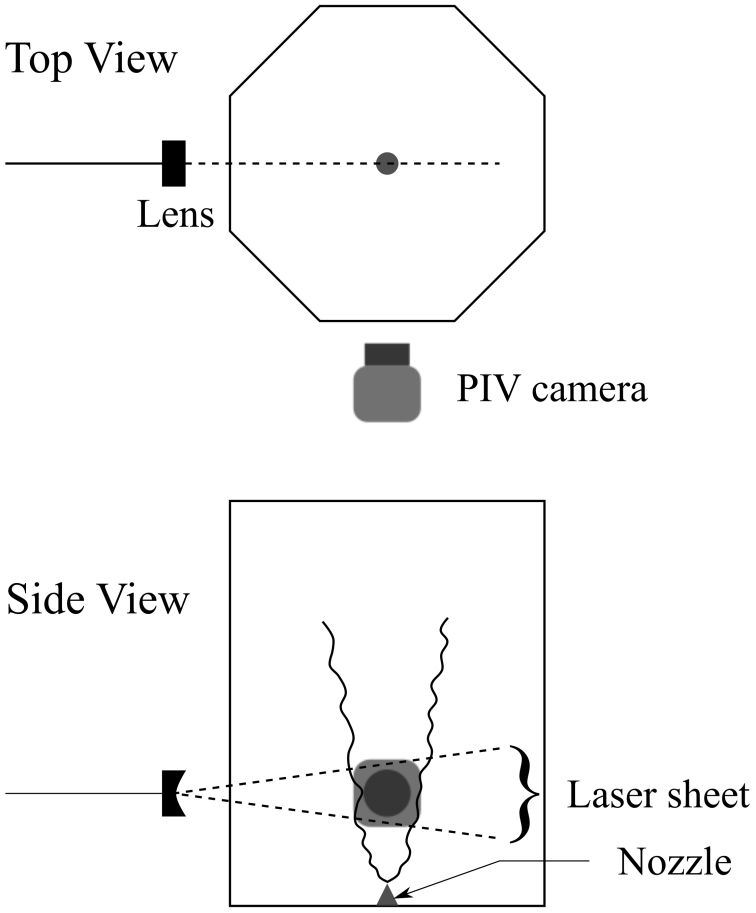

Figure 3.5: Schematic of the PIV setup for the cross-section of the turbulent jet.

compared to the spatial resolution of the camera setup, but small enough that the tracer particle images can be correlated with minimum noise. These places strict requirements on the performance of the different elements that conform the PIV system, particularly for a high Reynolds number flow. The image pairs are captured with 500 ms interframe time. The laser pulses, with a wavelength of 532 nm, deliver 200 mJ of energy within 5 to 10 ns pulse duration. The synchronization between the pulsed laser and the camera was done via the delay generator triggering the two laser cavities and Q-switches at a user-defined time delay and the two camera exposures right after the firing of each laser pulse. The details of the

image acquisition, transfer to the frame grabber, recording in computer memory, commonly used in PIV, is described by Adrian and Westerweel [1].

The vertical laser plane used to illuminate the cross-section along the centerline of the jet, is created by shaping the beams from the pulsed laser with a series of lenses. Figure 3.6 shows the optical setup. The laser beam first goes through a spherical lens, to open the beam into a cone. A convex cylindrical lens focused the laser cone in the horizontal direction. The focal point was placed at the centerline of the jet, creating a thin laser sheet in the vicinity of the nozzle. The laser then passed through a concave cylindrical lens to further expand the laser in the vertical direction, forming a plane that covers the entire field of view of the camera with a Gaussian intensity profile.

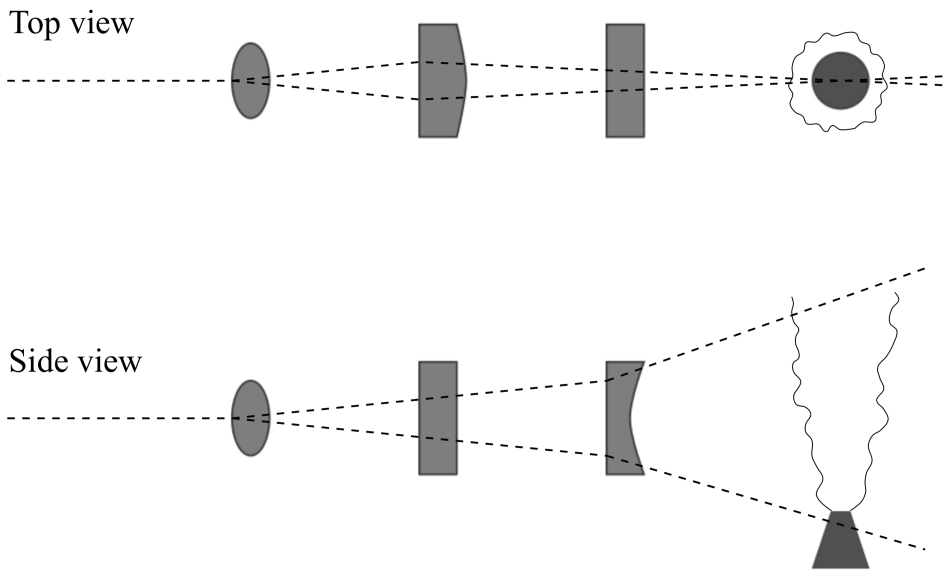

Figure 3.6: Lense arrangement used to create the laser plane for illumination of the PIV images.

The seeding particles flowing with the jet along the laser plane are illuminated and scatter light into the camera. Thus, the 2D-2C PIV measurements in this thesis are always representative of the axial and radial velocity components in a thin slice of fluid that extends

downstream of the nozzle and includes the jet's centerline. Axisymmetry is assumed to interpret the velocity measurements in an average sense and compute fluxes.

Lycopodium spores were used as seeding particles for PIV. These 30 μm average-diameter particles, roughly spherical and with a relative density of 1.05, were premixed in water to avoid forming air micro bubbles, and injected into the bladder tank with the jet fluid. The concentration of lycopodium particle in the jet is very dilute, about 30 ppm, so it has negligible effect on the jet properties. Lycopodium particles were chosen as seeding particles for their light scattering characteristics, as well as for their size and density that allow them to passively follow the flow (see Appendix D for more details).

3.2.2 PIV image processing

Images of the particle-seeded flow were preprocessed before applying the PIV algorithm to them. Since two different laser beams illuminate each image in the PIV pair, there is usually a slight difference in brightness between the two images, as noted by [1] and [54]. Typically, consistent brightness between the images can be achieved by normalizing the brightness of the images. This technique also enhances the contrast between the particle scattering and the background, improving the performance of the PIV correlation seeking algorithm [1]. An example of an image pair before and after image pre-processing is shown in Figure 3.7.

Two different PIV algorithms were used to analyze the images. These two PIV correlation software packages were assessed to ensure their results were consistent and independent of the specifics of the processing chosen. The first algorithm is MatPIV, a Matlab-based script developed by Kristian Sveen at the University of Cambridge [64]. The second algorithm used is GPIV, an open source code developed by Gerber van der Graaf [20] at Delft University. Both algorithms gave consistent results, independently of the specific settings used in the correlation search. Thus, only results from MatPIV are shown in the remaining of this thesis.

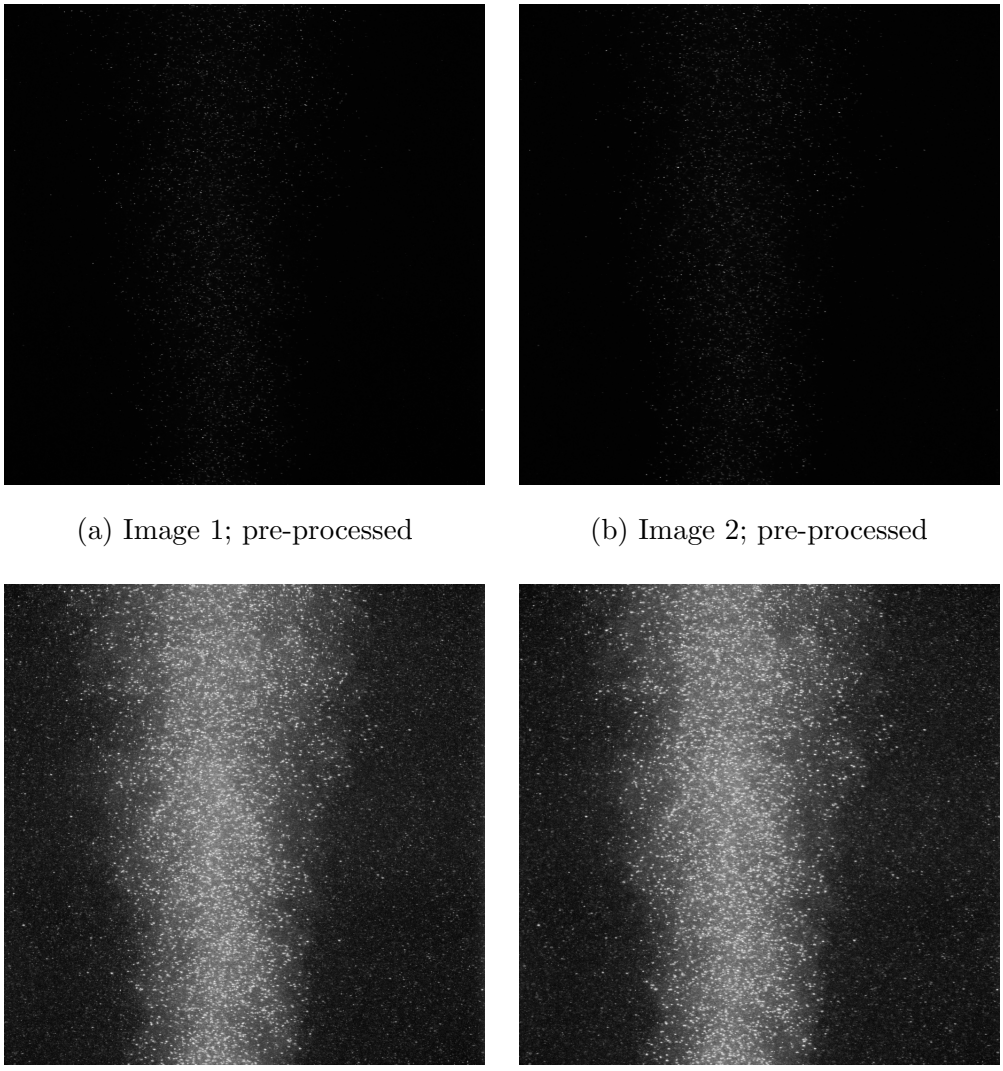

(a) Image 1; pre-processed

(b) Image 2; pre-processed

(c) Image 1; post-processed

(d) Image 2; post-processed

Figure 3.7: Image pairs of an lycopodium particle seeded jet ($Re = 25000$) before (top) and after (bottom) contrast normalization. Time delay between images is 20 μs.

3.2.3 Shadowgraphy setup

Backlighted shadowgraphy was used to image the particles during the breakup process. This technique images the cross section of the particles by recording the light transmitted through

the transparent carrier flow. Light is scattered by the disperse phase fluid (air or oil) due to their different index of refraction with respect to the continuous phase fluid. Thus, a shadow is casted by the subject particles on the camera sensor. The high contrast between the carrier flow and the particles, in particular the well-defined edge along the particle perimeter, makes these images optimum to detect the location and cross-sectional area of the particles through simple post-processing techniques. The camera was placed on one side of the tank looking across the tank directly into the collimated light source. The LED light was directed straight into the camera, with the axis of the light perpendicular to the camera sensor. This arrangement back-illuminated the flow over a 10 cm x 10 cm area, much larger than the camera field of view. The shadowgraphy setup is shown in Figure 3.8.

The duration of a typical particle breakup event in the turbulent jet is of the order of 1-10 microseconds. We utilized a high-speed camera (Phantom V12, Vision Research, Wayne, NJ) to capture the dynamics of the breakup process. Similar to the PIV setup, the exposure time of the camera is small to freeze the motion of the particles, so adequate lighting was needed. In this case, a high intensity LED array light (Constellation 120, IDT vision Ltd., Tallahassee, FL) was chosen for its uniform output (20,000 lumen) across a relatively large area (10 cm x 10 cm). Unlike incandescent lights where the output intensity depends on the input current, which fluctuates at 60 Hz, this LED light provides constant output intensity. This light is designed for high-speed imaging and it is collimated to maximize the light intensity and uniformity across the illuminated area.

The breakup of particles was imaged with two different optical setups. First, the time-averaged size distribution of the particles was captured at a lower frame rate (60 fps) over very long times, much larger than the integral time scale of the turbulence and the shedding frequency of the jet, to ensure time-independent statistics. The second setup was used to study individual breakup events. The behavior of the particles during the breakup was observed and analyzed with image post processing that reconstructed the particle trajectories and the change of projected area as the particles deformed and broke into smaller daughter particles. Experiments were conducted at a very high frame rate (5000 fps) to collect the

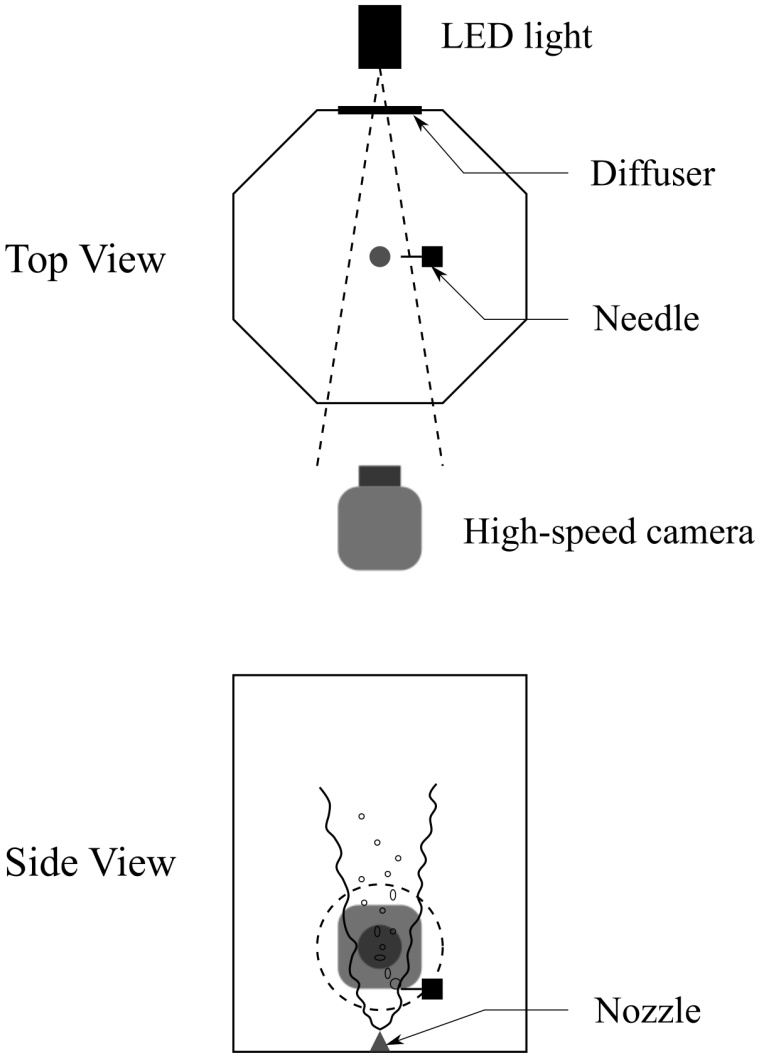

Figure 3.8: Schematic of the high-speed imaging setup for the particle breakup experiment.

time-resolved motion of the particles and the deformation/breakup due to the local turbulent motion of the carrier fluid.

Using a combination of camera lens and distance from the image plane, the appropriate field of view for different experiments was selected. For the size distribution experiments (60 fps), two to three vertical locations were used for the camera to image the flow sequentially downstream of the nozzle. The field of view was either 88 mm x 88 mm or 78 mm x 49 mm

in these experiments. The width of the field of view was chosen so that the imaging area covers the entire width of the jet (defined as 4 $r_{1/2}$) at its maximum spread on the $z/d_j = 55$ downstream station for the 4 mm nozzle. Multiple fields of view were stacked along the axial direction to provide coverage for 20 d_j downstream of the nozzle, at each imaging station.

For the experiments that captured the individual breakup events (5000 fps), the field of view did not have to cover the entire width of the jet or capture all particles. Instead, it was crucial to capture the entire sequence of particle locations and deformed shapes so as to reconstruct individual breakup events. This led to the use of a 49 mm x 78 mm field of view in order to maximize the coverage in the axial direction as particles could travel a long distance during a breakup event.

3.2.4 Shadowgraphy image post-processing

In order to obtain useful data from the images, they were processed using ImageJ, an open-source image processing software developed by the National Institutes of Health. The goal of the processing was to remove all the unnecessary artifacts from the original images. An example of these artifacts would be the Gaussian light intensity distribution from the background. Before conducting each experiment, a background image was taken with the same image settings as in the experiment. This background image was subtracted from every image captured in each experiment. Although this step removes all the artifacts, the particles on the subtracted image have different gray scale due to the original background brightness not being uniform. To improve the recognition by the post-processing software of the particles with different gray intensities, a technique called binary contrast enhancement, also known as thresholding, was used. Thresholding creates a new image by taking the pre-defined range of gray intensities and converting it to black, while every pixel that has the gray scale outside of this range is converted to white. This results in a binary image with clearly defined particles (any pixel with value 0 is inside particle while any pixel with a value of 254, or 4095 in 12 bit images, is outside of the particles). Figure 3.9 shows the original and the post-processed images at each step of the process.

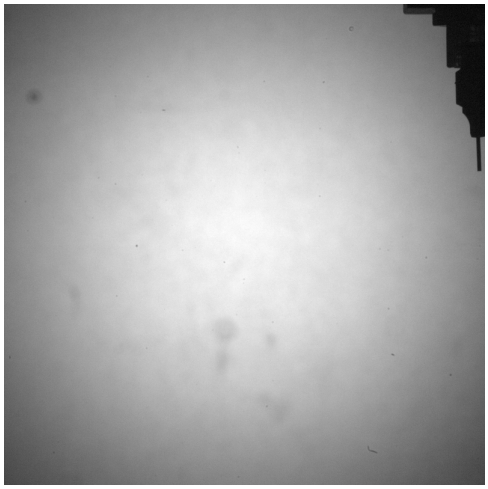

(a) An image of the background

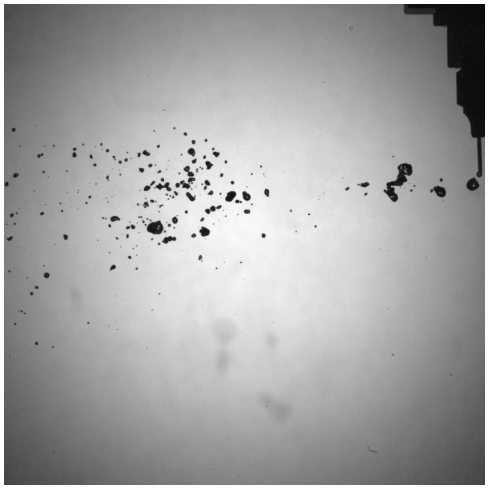

(b) An image of an instance in an experiment

(c) A resulting image from background subtraction

(d) An image after thresholding

Figure 3.9: Illustration of different steps in the image processing sequence.

3.2.5 Converting shadowgraphy images into quantitative data

For the particle size experiments (60 fps), the images were first discretized into multiple interrogation zones, as shown in Figure 3.10. The downstream extent of each zone is 8 mm, which is at least 50% larger than the initial bubble/drop injected from the needle. Each zone overlaps 50% of the area of the previous zone. Since particles falling on the edge of the zone are not counted, the overlapping mechanism allows particles on the edge of one zone to be taken into consideration in the neighboring zone. The width of each zone was taken to be the full width of the image. As mentioned earlier, the width of the image covers four times the jet half width at $z/d_j = 55$.

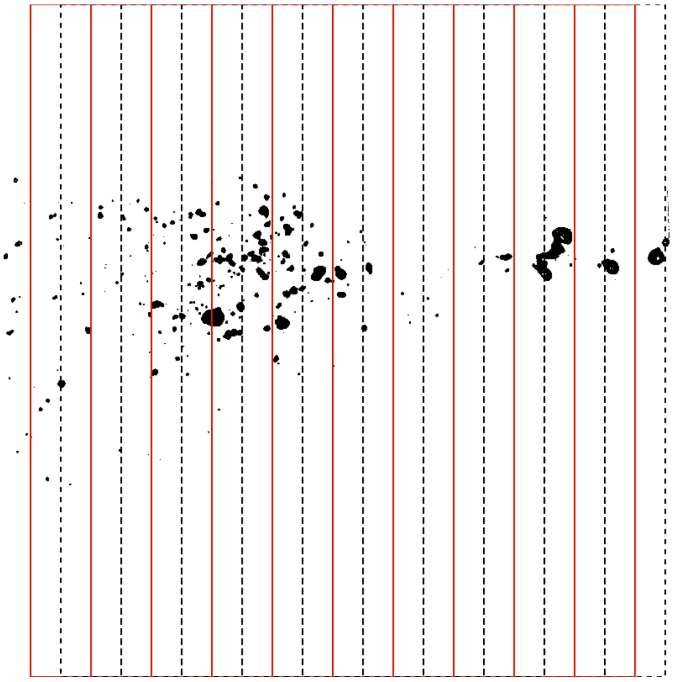

Figure 3.10: Illustration of the overlapping interrogation zones applied on an binary image.

After the discretization process, each zone was analyzed by an edge detection algorithm. This algorithm scanned each zone and found all the edges of particles. Particles that has open edges, such as the one that fall on the zone boundaries, were discarded. If an closed

edge is enclosed within another closed edge (i.e. holes), the hole was filled and they were considered as a single particle. This usually happens when light travel through a particle, so the scattering is weaker in the interior of the particle than on the edges, leaving a "hole" in the shadow that should be ignored in the identification of the particle and in the measurement of the particle projected area.

In each interrogation zone, the algorithm counted the number of qualified particles and recorded information on each particle. This information includes: the projected area of the particle, the circularity of the particle, the perimeter of the particle, and the coordinates of the centroid. In addition, a "fit-ellipse" function was applied to each particle. As the name suggests, this function computes the best fitted ellipse to the particle and report the ellipse major and minor axis lengths. These properties associated with each particle were used in the breakup event analysis that is discussed in Chapter 8. The analysis of the breakup event images (taken at a fast sample rate of 5000 fps) followed the same image post-processing procedure, with the exception that there was no region discretization of the field of view, as the tracking of particles was conducted along the entire downstream extend of the images. The breakup detection and particle tracking algorithm, discussed in Chapter 5, was applied to the image sequences to extract the breakup paths and the associated particle shape and size changes.

Chapter 4

VALIDATION OF JET PROPERTIES

The single-phase turbulent round jet has been studied extensively. So, the first set of experiments are to reproduce the jet and validate it with the existing experimental results and theories. According to Pope [52], the self-similar region of the jet occurs at $z/d_j > 30$, so our experiment took images of the jet up to $z/d_j = 50$. However, this cannot be done with one imaging setup as the field of view can not be too large in order to have a reasonable resolution on the jet. Therefore, experiment is done in multiple locations with various sizes of the field of view (Figure 4.1). Results from different locations are scaled and translated accordingly in order to stitch them together. In addition, since the flow rate is recorded using the NIST-calibrated flowmeter, the initial jet velocity is known.

The random nature of turbulent flow means that the velocity at a particular point and a particular time cannot be described exactly as it contains a fluctuating component of the velocity. In general, the velocity can be written as a mean velocity plus a velocity fluctuation, as shown in Equation 4.1.

$$\mathbf{U} \equiv \overline{\mathbf{U}} + \mathbf{u} \tag{4.1}$$

where $\mathbf{U}$ is the velocity vector, $\overline{\mathbf{U}}$ is the mean flow velocity vector, and $\mathbf{u}$ is the velocity fluctuation vector.

To obtain the measured mean velocity and the velocity fluctuation, many realizations of the flow is required. PIV measurements of each image pair provides a realization of the flow. In these experiments, about 1800 images are taken at each location, so each experiment provides about 900 realizations of the flow. The mean velocity of the flow is calculated by averaging the velocity field over all realizations. The velocity fluctuation is obtained by

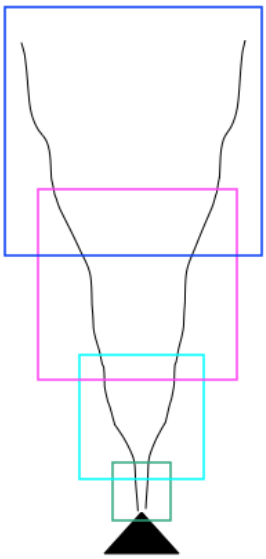

Figure 4.1: An illustration of imaging multiple locations of the jet with different sizes of field of view.

subtracting the mean velocity field from the velocity field of each realization. To ensure that each realization is statistically independent to others, the time between each image pair is taken long enough (about 33 to 67 ms) that the particles appears on one image pair have completely gone out of the frame of the next image pair. Note that the time between each image pair is different than the time delay between two images of a pair, which is about $\mathcal{O}(10^{-4})$ s.

4.1 Mean velocity

After stitching the PIV results of multiple imaging windows, the two dimensional mean velocity field is obtained. The axial velocity field (Figure 4.2a) provides a good qualitative visualization of the velocity decay and the spreading angle of a typical turbulent round jet. The radial velocity field (Figure 4.2b) shows the velocity of the surrounding fluid points towards the jet, which confirms that the surrounding fluid is being entrained into the jet.

On the other hand, the jet fluid is going to the outward direction, which suggests that mixing occurs between the jet and the surrounding fluid as expected in a turbulent round jet.

The centerline velocity of a turbulent round jet decay with $1/z$. The mathematical expression for this decay is shown in Equation (4.2). A comparison between our experimental results and this model is shown in Figure 4.3. Like the velocity field plots, the discontinuity points on this figure are the "stitching" points between different frame of view. Our experimental data collapsed to the model at about $z/d_j > 20$, indicating that the jet becomes fully developed in this range.

$$\frac{U_o}{U_j} = \frac{B}{(z - z_o)/d} \tag{4.2}$$

where U_o is the centerline velocity, U_j is the jet velocity at the exit, $B = 5.8$ [52] is an empirical constant, and z_o is the virtual origin for which $z_o/d_j = 4$.

Figure 4.4 shows of the velocity profile normalized by the centerline velocity. The results from the three axial distance ($z/d_j = 25$, 35 and 45) collapse in to one curve, which indicates self-similarity. Also, our results shows good agreement with experimental data from Hussein et al. [25] and Wygnanski & Fiedler [71].

Schlichting [52] developed the expression (Equation (4.3)) of the self-similar velocity profile using the boundary-layer momentum equation. The model is also plotted in Figure 4.4. Our experimental results are in good agreement with the model near the center region ($r/(z - z_o) < 0.1$). Outside this region, there is a slight disagreement between the two. The reason for this disagreement is due to the assumption of constant turbulent viscosity in the model. The model assumes $\hat{\nu_T} \approx 0.028$, which is a good assumption for the near center region, but beyond that, the turbulent viscosity decrease rapidly (see Figure 4.5). Thus, it results in inaccurate velocity near the edge of the jet.

$$h(r_n) = \frac{1}{(1 + (\sqrt{2} - 1)\hat{\nu_T} r_n^2/S^2)^2} \tag{4.3}$$

where $r_n = r/(z - z_o)$, S is the spreading rate, $\hat{\nu_T}$ is the normalized turbulent viscosity.

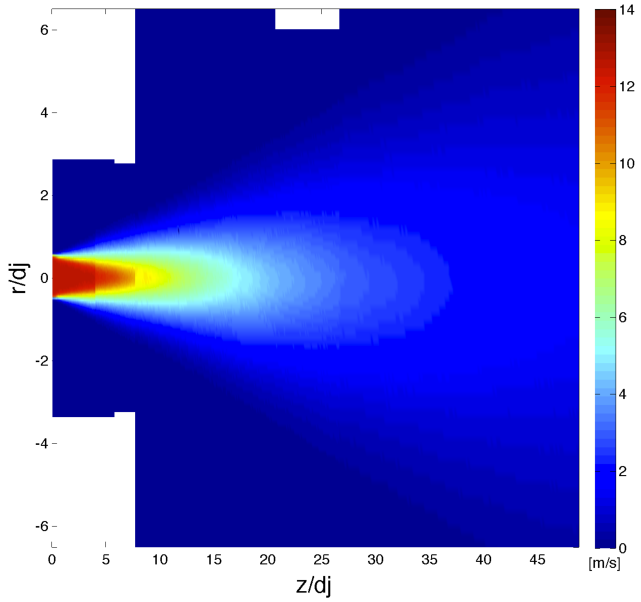

(a) Axial velocity

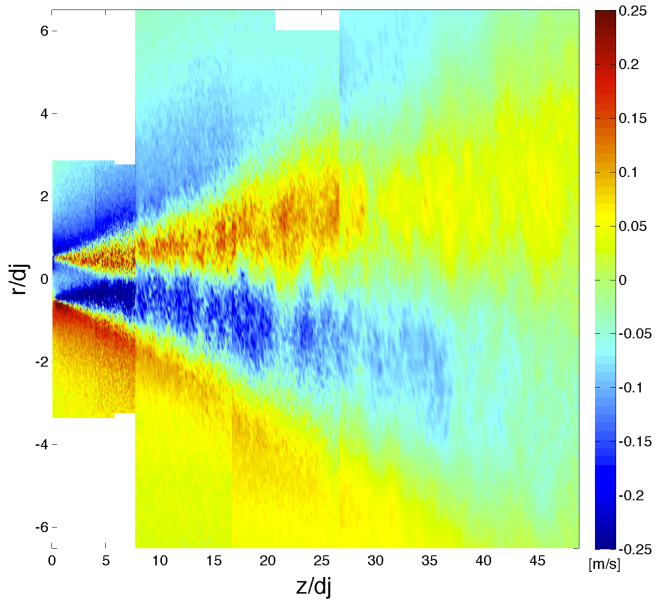

(b) Radial velocity

Figure 4.2: Mean velocity field obtained by stitching multiple PIV results of different imaging windows. $Q_j = 2.5$ GPM and $d_j = 4$ mm.

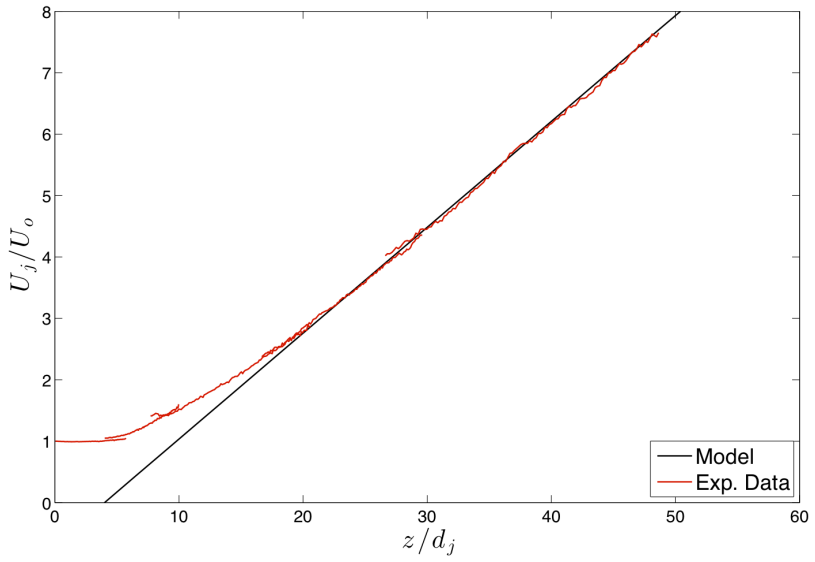

Figure 4.3: A comparison of the normalized centerline velocity decay between our experimental results and the prediction from theory.

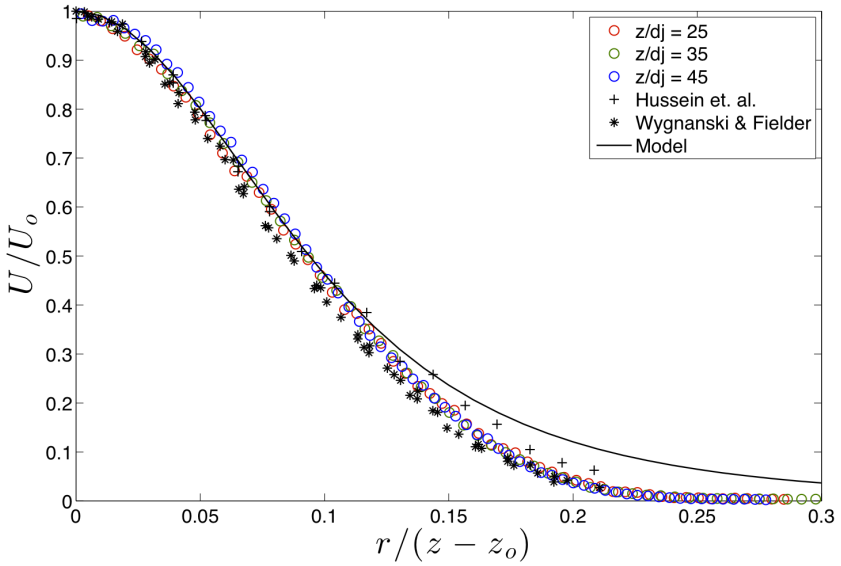

Figure 4.4: A comparison of the normalized velocity profile between our experimental results, previous results in the literature and the prediction from theory.

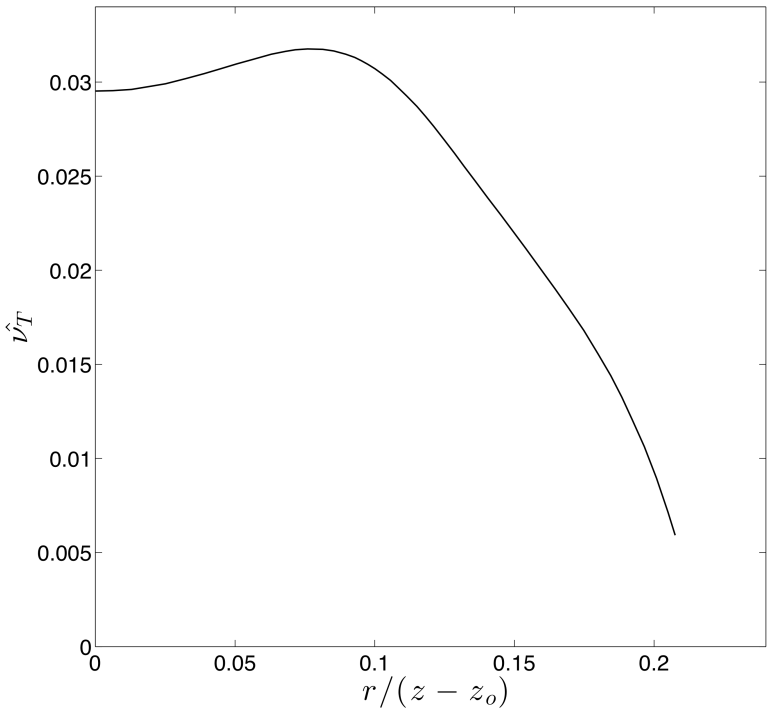

Figure 4.5: Normalized turbulent viscosity of a self-similar jet. [52]

4.2 Reynolds stresses

The Reynolds stresses are defined as the mean of the velocity fluctuation square. With the axial and radial direction of the velocity fluctuation (u and v, respectively) obtained from the PIV measurements, three Reynolds stresses, $\overline{u^2}$, $\overline{v^2}$ and $\overline{uv}$, were calculated. Figure 4.6, 4.7 and 4.8 shows the comparison between our experimental data and the curve fit of the laser-Doppler anemometry (LDA) data from Hussein et al. [25]. Like the velocity profiles, the normalized Reynolds stresses at three different axial distances collapse onto each other well, displaying the self-similar behavior. In general, our data display the same trend as Hussein's data [25]. However, there are some discrepancies near the center region for the $\overline{u^2}$ plots. The results from the higher axial distance have a better agreement with Hussein's data [25], this suggests that the secondary statistics may not be fully developed at the axial distance we tested. Since Hussein's results [25] were obtained at $z/d_j = 100$, we expect those discrepancies will be minimized if the measurements were taken at those locations.

For the purpose of the validation, our measurements, both for first and second order statistics, exhibit good agreements with previous results and models. This ensures that our experimental facility is capable to produce a turbulent round jet and our measurement technique is reliable.

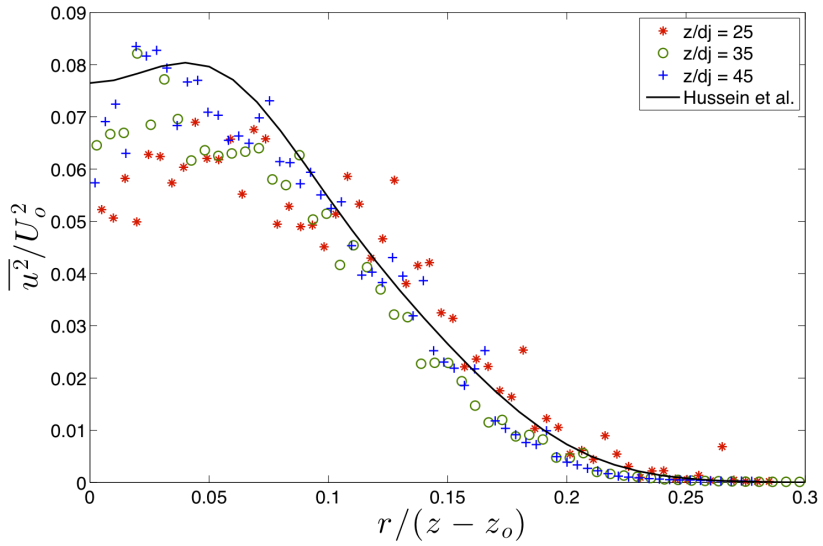

Figure 4.6: A comparison of the $\overline{u^2}$ between our experimental results and results in the literature.

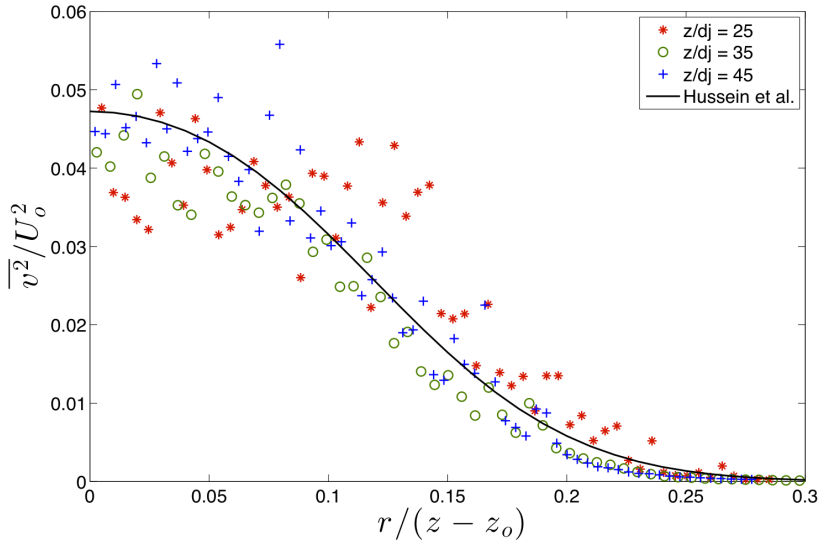

Figure 4.7: A comparison of the $\overline{v^2}$ between our experimental results and results in the literature.

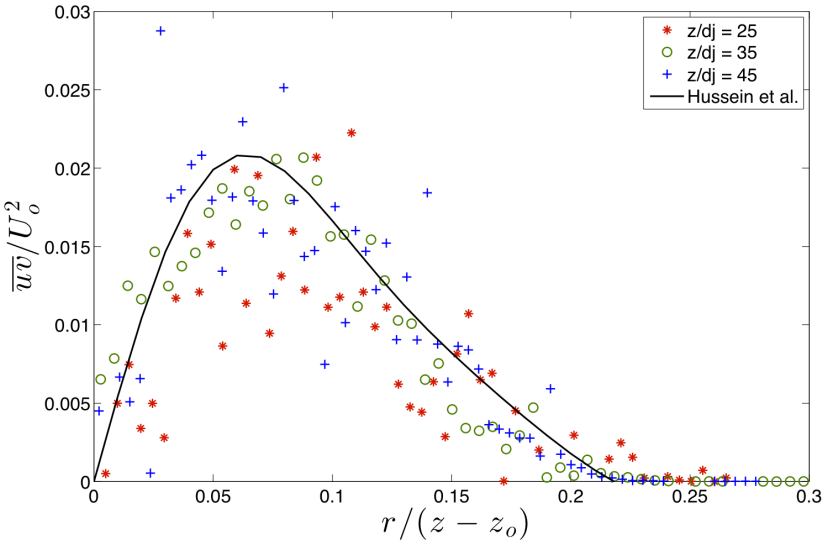

Figure 4.8: A comparison of the $\overline{uv}$ between our experimental results and results in the literature.

4.3 Turbulent dissipation rate

As we discussed in Chapter 2, many existing size distribution models for turbulent breakup assume only eddies with comparable size as the particles can contributes to the breakup. Since the particles are within the inertial subrange, this implies that eddies that are responsible for breakup has the size within the inertial subrange. According to the Kolmogorov theory, the kinetic energy of the eddies of these sizes depends only on two parameters: the kinematic viscosity and the turbulent dissipation rate. Thus, it is important to know the dissipation rate as a function of location of the jet.

To calculate the turbulent dissipation rate using the turbulence kinetic energy equation requires experimental data from all three dimensions. However, Hussein et al. [25] provided an axisymmetric estimate (Equation (4.4)) that can be applied to our two dimensional PIV data. A model of the centerline dissipation rate used by Eastwood et al. [16] is used to validate our experimental results, its expression can be found in Equation (4.5).

$$\epsilon_{axi} = \nu \left[\frac{5}{3} \overline{\left(\frac{\partial u}{\partial z} \right)^2} + 2 \overline{\left(\frac{\partial u}{\partial r} \right)^2} + 2 \overline{\left(\frac{\partial v}{\partial z} \right)^2} + \frac{8}{3} \overline{\left(\frac{\partial v}{\partial r} \right)^2} \right] \tag{4.4}$$

$$\epsilon = \frac{36 U_j^3}{d_j} \left(\frac{z}{d_j} - \frac{z_o}{d_j} \right)^{-4} \tag{4.5}$$

Figure 4.9 compares the centerline turbulent dissipation rate of our experimental results and the model. Although they both have a exponentially decaying trend, there is a clear disagreement between the two. To quantify the difference, the dissipation rate is normalized by $U_o^3/r_{1/2}$. Since we know that the dissipation rate is self-similar ([48, 49]), the normalized centerline dissipation rate is constant, which allows us to compare the experimental and theoretical values regardless of the axial location. From Figure 4.10, we observed that the mean value of the normalized centerline dissipation rate from the experimental data is about an order of magnitude lower than the theoretical value.

The difference between the experimental and theoretical values is caused by the limitation of the measurement techniques. Unlike other results, such as Reynolds stresses, obtaining

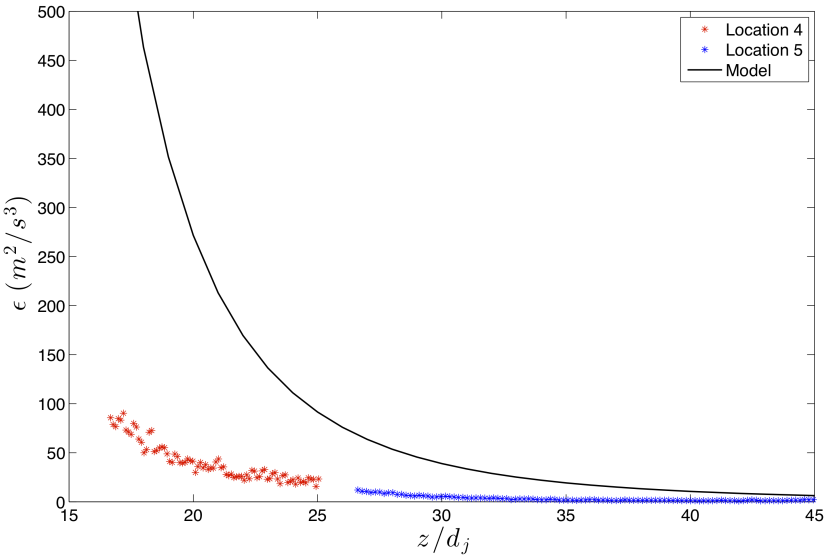

Figure 4.9: A comparison of the centerline turbulent dissipation rate between experiment and model.

dissipation rate from the experimental data requires first order derivatives. Thus, the result is sensitive to the discretization because turbulence is a multi-scale phenomenon. If the discretization is too large, the smaller scale motion is not captured. It implies that energy contained in the smaller scale motion is filtered out if $\triangle z$ and $\triangle r$ (since $\triangle z = \triangle r$, we will refer both as $\triangle z$ from now on) is larger than the smaller scale motion in the flow. $\triangle z$ depends on the final PIV interrogation window size. Since the PIV algorithm relies on pattern matching, the interrogation window size needs to cover enough space to form a pattern of particles within the window, so it limits how small $\triangle z$ can be. In this experiment, $\triangle z$ is limited to $\sim \mathcal{O}(10^{-4})$ m. The smallest scale in a turbulent motion is the Kolmogorov scale, it is defined as:

$$\eta = \left(\frac{\nu^3}{\epsilon}\right)^{1/4} \tag{4.6}$$

In the range where the breakup experiment takes place ($z/d_j > 15$), η is between $\sim$

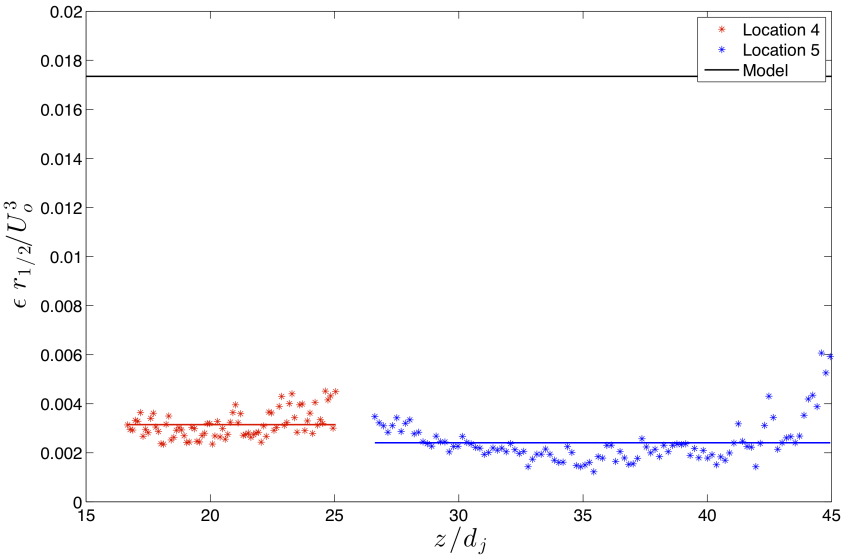

Figure 4.10: A comparison of the normalized centerline turbulent dissipation rate between experiment and model. The red and blue lines represent the mean values of the experimental results for each location.

$\mathcal{O}(10^{-6})$ m and $\sim \mathcal{O}(10^{-5})$ m. So, $\triangle z$ is about one to two orders of magnitude larger than the smallest turbulent motion. Therefore, a portion of the energy contained within $\triangle z > l > \eta$ is not captured in our our results, which explains the discrepancy of the dissipation rate plot. Because experimental data show a relatively good agreement for the first (mean velocity) and second order statistics (Reynolds stresses), it is reasonable to believe that the jet produced from our facility has the same turbulent dissipation rate as the model and previously published data. With this assumption, the dissipation rate values used in the following chapters are calculated using Equations (4.4) and (4.5).

Chapter 5

TRACKING ALGORITHM FOR BREAKUP EVENTS

5.1 Background

As mentioned in Chapter 2, the population balance equation provides the complete description of the particle size distribution from a breakup process. This equation requires multiple closure functions, such as the breakup frequency, number of daugther particles and the daughter particle size distribution. Over the years, many models has been developed for these functions, but only a few of them considered the effect of the dispersed phase viscosity. With the popularity of the high-speed imaging techniques in the past decade, we have observed that the viscous particles behave differently during the breakup process [16], [4] and [19]. Thus, it is crucial to develop models that takes into account of the viscous effect.

By taking advantage of the high-speed imaging of the breakup sequences, we can capture the short-lived (on the order of millisecond) breakup sequences. This allows us to identify some important properties, such as the breakup time, the fraction of drops that break and the shape and size along the breakup path. In order to take advantage of these high-speed imaging sequences that contain many breakup events, we need an algorithm that can detect the breakup events, follow the particles and collect information (location, size, shape, etc) along the breakup paths.

The general approach of Lagrangian particle tracking is to minimize the particle displacement between two frames, as shown in Equation (5.1). Some more sophisticated schemes include the minimization of acceleration and the change in acceleration using three or more frames [47]. In order to identify the breakup event, Rodríguez-Rodríguez et al. [61] developed a particle Tracking and Breakup Detection Algorithm (TBDA). This algorithm uses not only the location of the particle, but also the projected area of the particle as inputs

from the images.

$$\phi_{ij} = ||\mathbf{x}_j - \mathbf{x}_i|| \tag{5.1}$$

where the index i represents the particle from a given frame n and index $j = 1, ..., J$ is a candidate from the next frame $n + 1$.

They defined a pseudo-distance function (see Equation (5.2)) that takes into account the change in projected area. The matching particle (index j) is found by minimizing the pseudo-distance function, Δ_{ij} for all potential particles j.

$$\Delta_{ij}^2 = ||\mathbf{x}_j - \mathbf{x}_i||^2 + K_A \left(\frac{A_j - A_i}{A_i} \right)^2 \tag{5.2}$$

where K_A is a constant of the order one.

The above minimization allows tracking of particles as they travel through space, but it does not identify when the breakup events occur. To account for this, TBDA applied the above minimization backward, meaning it searches for a match in frame n that corresponds to a particle in frame $n + 1$. When multiple particles in frame $n + 1$ find the same match in frame n, it indicates a breakup had occurs and these particles in frame $n + 1$ are the daughter particles from the breakup. In addition, when breakup is detected, a factor based on the conservation of volume is calculated (Equation (5.3)). Ideally, when both the mother and the daughter particles are spherical, VCP becomes zero. Realistically, the particles are not spherical, so Rodríguez-Rodríguez et al. [61] found that the VCP ranges from -0.6 to 0. By setting the upper and the lower limit of VCP, many spurious breakup event can be eliminated.

$$VCP = \frac{\sum_{j=1}^{m} A_j^{3/2}}{A_i^{3/2}} - 1 \tag{5.3}$$

where m is the number of daughter particles corresponds to the breakup of particle i.

TBDA uses the combination of the forward and backward application of the pseudo-distance function to identify the breakup. However, the pseudo-distance function relies on

the change in projected area in one of the terms and the change in projected area between a mother and its daughter particles can be significant. This means that the value of the pseudo-distance function for a matching mother-daughter set might not be minimum among all potential matches. In the other words, the use of pseudo-distance function is good for tracking, but not for breakup detection.

Although the the pseudo-distance function provides some uniqueness of the search by including the change-in-area term, it might not be sufficient to distinguish a true or false match. For example, in a high particle density area, it is very likely that particles with similar projected area locate next to each other. Adding to the fact that the projected area of a particle could change slightly due to the change in orientation and/or deformation, the change-in-area term might be similar for all the potential matches. Thus, the pseudo-distance function becomes the displacement function (Equation (5.1)) used in the basic particle tracking algorithm.

Because of these aforementioned weaknesses, it appears that the current state of the particle tracking algorithm is not adequate for the tracking of the breakup of the viscous particles. In the following section, we will present a new particle tracking algorithm specifically designed for the breakup of viscous particles based on some ideas discussed in this section.

5.2 Ligament identification and back-tracking algorithm

In this section, we introduce a new particle breakup tracking algorithm called the Ligament Identification and Back-Tracking (LIBT) algorithm. The underlying idea of the LIBT algorithm originated from the observation of the unique breakup behaviors of the viscous particles through the high-speed images. Thus, we will begin with a demonstration of a typical breakup sequence.

Let us preface that in this section, the description of the sequence shown in Figure 5.1 focuses on the unique behaviors that will be used in the new algorithm to improve tracking and breakup identification. The description of the actual mechanism of the breakup is shown

in Chapter 8.

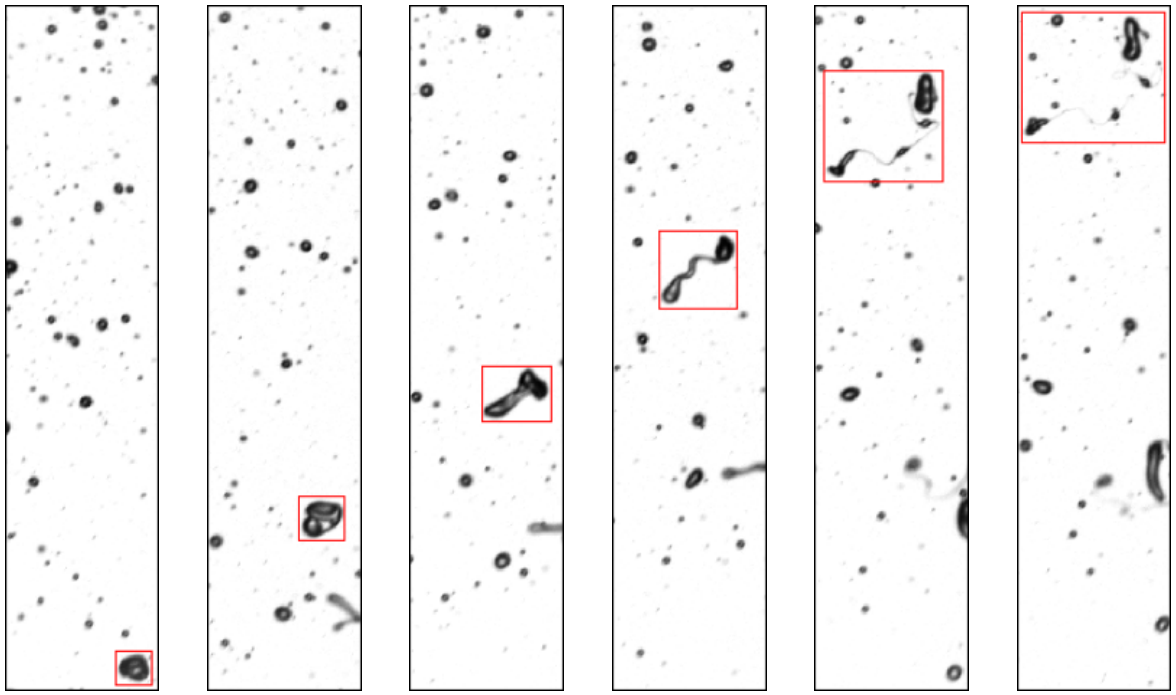

(a) $t = 0$ (b) $t = 2.8$ ms (c) $t = 4.6$ ms (d) $t = 6.2$ ms (e) $t = 8.4$ ms (f) $t = 9.2$ ms

Figure 5.1: A visualization of a typical breakup sequence of viscous particle. $Re = 80000$ and $Q_p = 20$ mL/min. Needle positioned at $z/d_j = 20$. 100 cSt silicone oil.

One of the most obvious observation from this sequence is that viscous particles deform significantly during the breakup process. Specifically, the particle started to stretched into long ligament from $t = 7.0$ ms. As the elongation process continued, the ligament got bent by the surrounding turbulent flow and formed unique curves along the string ($t = 6.2$ ms). In addition, the particle could change orientation during the deformation process. The combination of these processes significantly changed the shape of the particle in the breakup path. This behavior is different than the breakup of inviscid particles that TBDA [61] were designed to track. So far, no breakup detection algorithm that we know of takes advantage of the unique shape of the viscous particles.

A thinning process is observed once the ligament was stretched over a certain length. This resulted in the development of thin strings along the ligament ($t = 8.4$ ms). When the breakup of the mother ligament occurred, the ligament disintegrated at these thin strings and formed multiple daughter particles. Shortly after the breakup, these strings recoiled quickly back towards the daughter particles. Thus, the shape of the daughters resembled more to particles than ligaments.

This unique breakup process resulted in daughter particles that had distinct size and shape compared to their mother ligament ($t = 9.2$ ms). The implication of this observation is this: *breakup occurs right after a highly elongated ligament is identified and this ligament does not belong to any tracking path in a future time.* This simplifies the breakup detection process compared to the previous algorithm. It is also the main reason why LIBT is designed to track particles backward in time.

The LIBT algorithm begins by looping through the images backward in time. For each images, the sub-routines described in the following sections are executed consecutively.

5.2.1 Ligament identification

A clear definition of a ligament is needed in order to identify them. Since ligaments are unique in shape, we could utilize shape related properties in order to distinguish between a ligament and a spherical or slightly deformed particle. One of these properties is the circularity (Equation (5.4)). Its value ranges from 0 to 1, where 1 represents a perfect circle.

$$CC = 4\pi \frac{A}{P^2} \tag{5.4}$$

where A is the projected area and P is the perimeter of the particle.

In addition, a basic ligament is shown in Figure 5.2 to illustrate the limiting case of what is considered as a ligament. The circularity of this basic ligament is calculated by assuming string thickness, b, is negligible and the string length, l, equals to the radius of the fluid lumps (i.e. $l = 0.5D$). With these assumptions, the circularity of the basic ligament becomes

$\pi^2/(2(\pi+0.5)^2) \approx 0.372$. These value are used as the threshold for ligament identification. Any particles with a lesser circularity value is considered as a ligament. Note that the value of circularity may not be accurate for small particles because square pixels with size on the order of the particle size cannot approximate the curvature of such particle well. Therefore, smaller particles (< 20 pixel) are filtered out from the ligament identification process.

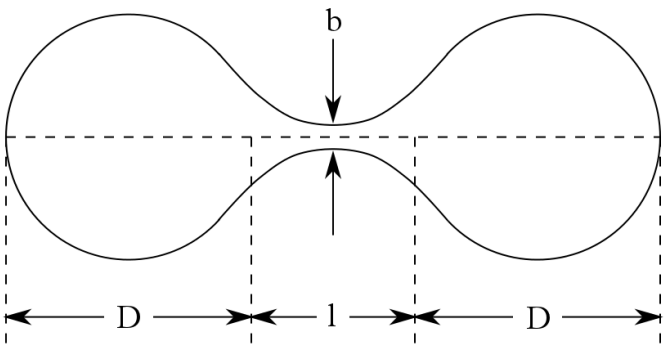

Figure 5.2: An illustration of a basic ligament.

Once all the ligaments are identified in each image, LIBT loops through each ligament and check if it belongs to any future breakup path. If it does not, it is identified as an original ligament. For the reason mentioned before, the algorithm considered a disintegration of the particle occurs in the frame after which an original ligament is identified.

5.2.2 Shape matching function

Each original ligament represents a breakup event. So, LIBT finds the breakup path of each original ligament by finding a match in each successive frame backward in time. Given a particle i in frame n of a breakup path, the potential match in frame $n-1$ (backward in time) should be within a close proximity of the $\mathbf{x}_i^n$. Thus, instead of searching for a match through out the entire frame, it searches within an interrogation area. The interrogation area is taken as the bounding box area of particle i plus a tolerance in each direction. The bounding box area is a rectangular area where each side touches the vertex of the particles

in the horizontal and vertical directions. This interrogation area also shifted based on the displacement of the particle calculated from the last image pair. For the calculation of the first pair, the displacement is set to be zero. An illustration of the interrogation area is shown in Figure 5.3.

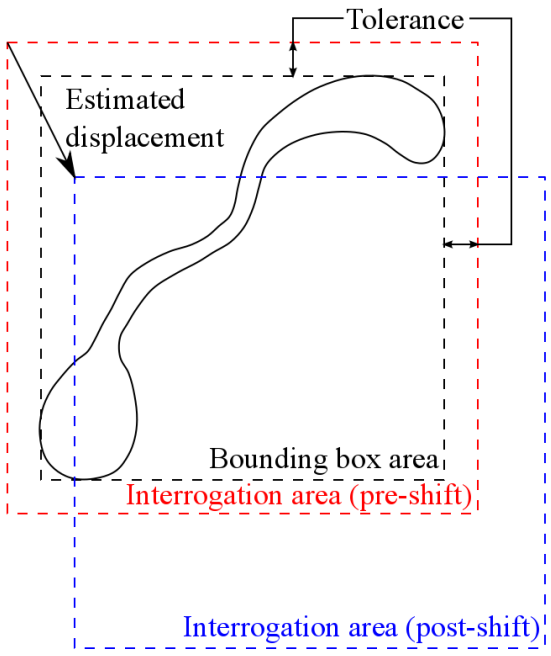

Figure 5.3: Interrogation area for searching potential match.

A shape matching function is applied to all particles ($j = 1...J$) within the interrogation area in frame $n-1$. This function (Equation (5.5)) takes the change in shape and size of the particles into consideration and output a value ranges between 0 to 1. A low value from a particle (j) in the interrogation area means its size and shape are very similar to the target particle (i). Particles with the value below a threshold of 0.5 are identified as the potential matches. These matches are passed to the next sub-routine: displacement minimization.

$$SMF = \frac{\left(\frac{CC_j - CC_i}{CC_i}\right) + \left(\frac{A_j - A_i}{A_i}\right) + \left(\frac{BBA_j - BBA_i}{BBA_i}\right)}{3} \tag{5.5}$$

where CC is the circularity and BBA is the bounding box area.

The change of circularity and the change of projected area terms in the shape matching function take the shape and the size of the particle into consideration, respectively. The change of bounding box area term is added to improve the robustness of the tracking in high density area, especially when particles overlap each other. An illustration of this situation is shown in Figure 5.4. The circularity and projected area of the ligament change significantly before and during the overlapping occurs. Long ligaments are prone to have particle overlapping because there is a higher chance for particles to cross over the long string. However, the bounding box area remains the same in most of these situations. So, the addition of the bounding box area term reduces the chance of tracking ends abruptly due to particle overlapping.

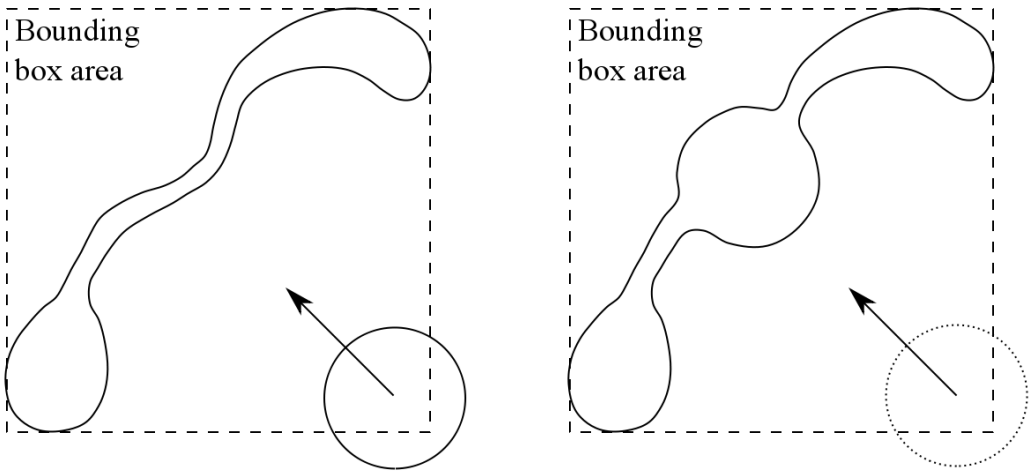

Figure 5.4: Illustration of how particle overlapping affect the ligament's size, shape and bounding box area.

5.2.3 Displacement minimization

A minimization process is applied to all the potential matches to find the best match. Equation (5.1) minimizes the displacement of the particles between frames, but this assumes the particle movement is negligible, which is not the case in turbulent flow. So, the minimization is based on the estimated velocity measured from the previous image pair. The minimization function is shown in Equation (5.6).

$$\phi_{ij} = ||(\mathbf{x}_j^{n-1} - \mathbf{x}_i^n) - \mathbf{u}_i^n \Delta t|| \tag{5.6}$$

where

$$\mathbf{u}_i^n = \frac{\mathbf{x}_i^n - \mathbf{x}_i^{n+1}}{\Delta t} \tag{5.7}$$

The shape matching function and the displacement minimization could be combined into one step, but the advantage of separating the two processes is as follows. At the beginning of the breakup path (tracking from the original ligament), the estimated velocity is not available. However, at this point the target particle is highly deformed, so it's unlikely to have a particle that is similar in shape and size in the interrogation area. In this situation, only one potential match could be found by the shape matching function. As a result, estimated velocity is not required as the minimization process is not needed. On the other end of the breakup path, the particle has a higher circularity value, meaning its shape is similar to the surrounding undeformed particle. So, many potential matches could be found, but since the estimate velocity is available, LIBT can still accurately track the particle without needing the uniqueness of the particle shape. Taking advantage of different information available in different stages of the breakup path is another benefit that the back-tracking method provides over the forward-tracking method.

5.2.4 Exit condition

In the forward-tracking method, the tracking ends when breakup occurs. In the back-tracking method, an exit condition is needed to determine when the tracking ends. A particle could travel along the flow undeformed until it collides with some eddies energetic enough to cause deformation, and ultimately, breakup. Since the focus of the study is on the breakup event, the period of time before a particle is deformed is not in our interest. Therefore, the tracking ends when the circularity of a particle begins to reach above certain threshold. This circularity threshold is different than the one used for ligament identification. A basic particle illustrated in Figure 5.5 is used to define the circularity threshold. For $l = 0.5D$, the circularity of this basic particle becomes $\pi(\pi + 2)/(\pi + 1)^2 \approx 0.942$. A breakup path that ends by satisfying the exit condition is called a completed path.

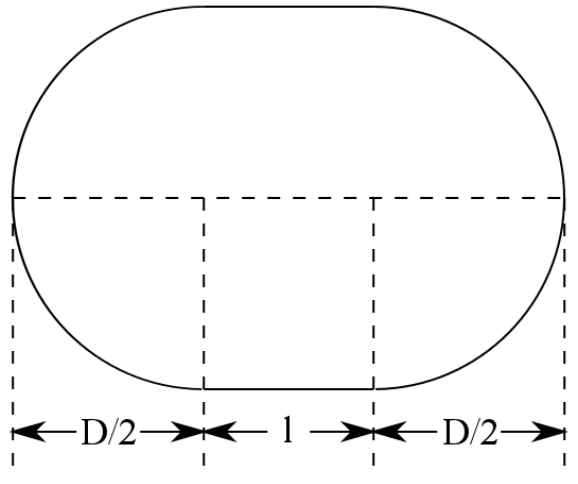

Figure 5.5: An illustration of a basic particle.

Not all breakup paths started from a spherical particle. Many begins as a highly deformed particle or a ligament that is a originated from another breakup. For example, in the breakup event of a long ligament, breakup could occur at a certain part of the ligament while the other part continues to deform/stretch. This is captured in Figure 5.6 where the mother

particle is highlighted by the red box and the daughter ligaments are highlighted by the blue and green boxes. LIBT begins the tracking when the first breakup occurs, so the breakup of the daughter ligaments are considered as a separate breakup path. In these secondary breakup paths, the exit condition mentioned above would not be matched. However, since these daughter ligaments have very different shape and size than their mother, the results from the shape matching function would be below the threshold, so the tracking ends where the primary breakup occurs. A breakup path that ends without satisfying the exit condition is identified as an incomplete path.

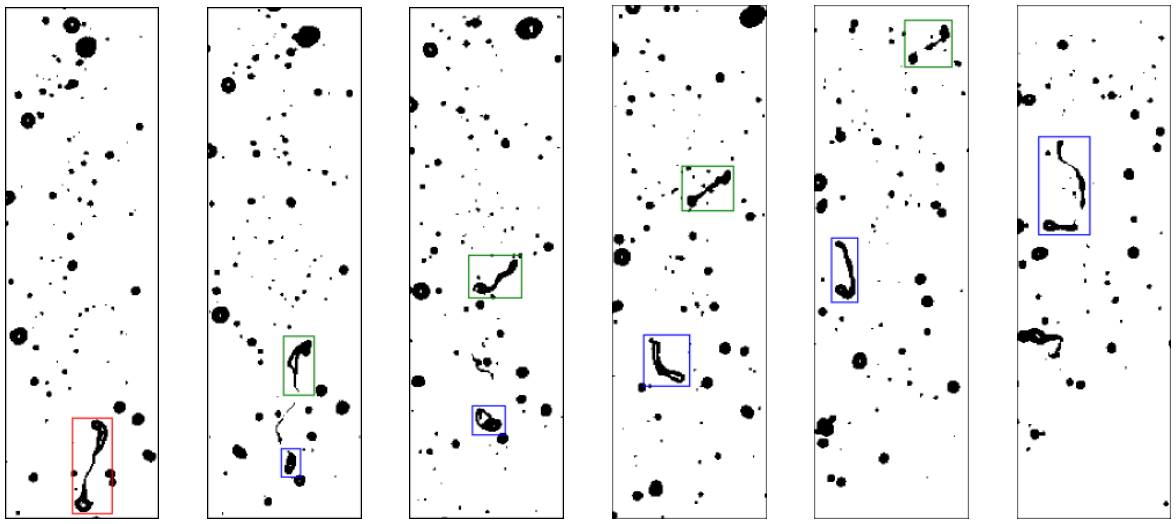

(a) $t = 0$ (b) $t = 1.2$ ms (c) $t = 2.4$ ms (d) $t = 3.8$ ms (e) $t = 6.2$ ms (f) $t = 8.4$ ms

Figure 5.6: A visualization of the formation of daughter ligaments and their breakup. $Re = 60000$ and $Q_b = 20$ mL/min. Needle position at $z/d_j = 20$. Canola oil.

5.3 Demonstration of LIBT

Figure 5.7 shows the breakup path (green) obtained from LIBT overlaid on the images of the breakup sequence. The dashed line and the solid line of the breakup path (green) represents two separate stages of breakup, which will be discussed in Chapter 8. This particular

breakup sequence is chosen as it presents multiple situations that are particular difficult for particle tracking. First, the path began in a region with high particle density, so there were surrounding particles with similar size and shape. Sometimes, these surrounding particles overlapped with the target particle, which altered its size and shape temporarily. Second, the target particle changed direction between $t = 4.4$ to 7.2 ms and it slowed down significantly during this period. Third, during the stretching stage (between $t = 7.2$ to 10.8 ms), the particle significantly altered its orientation by completing a full rotation. In this sequence the target particle underwent a significant change in size, shape, orientation, direction and velocity of the target particle, while being located in a particle-dense region. Nonetheless, LIBT were able to provide an accurate tracking path. Furthermore, it correctly identified when the breakup occurred as we see the disintegration of the ligament at the end of the path ($t = 10.8$ ms).

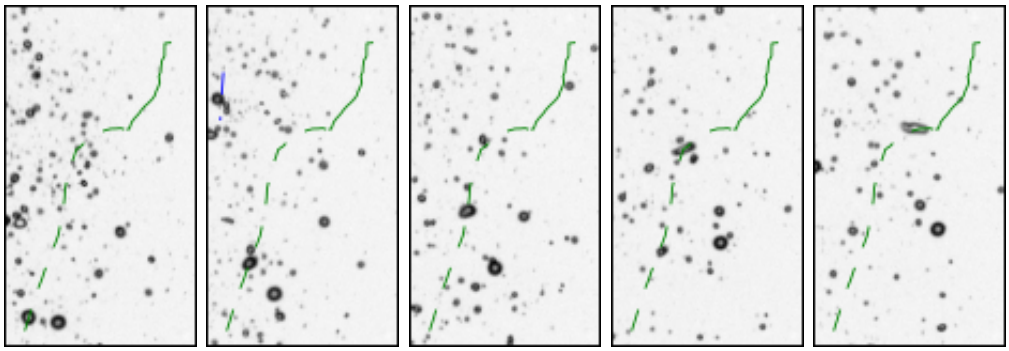

(a) $t = 0$ (b) $t = 1.4$ ms (c) $t = 2.8$ ms (d) $t = 4.4$ ms (e) $t = 5.4$ ms

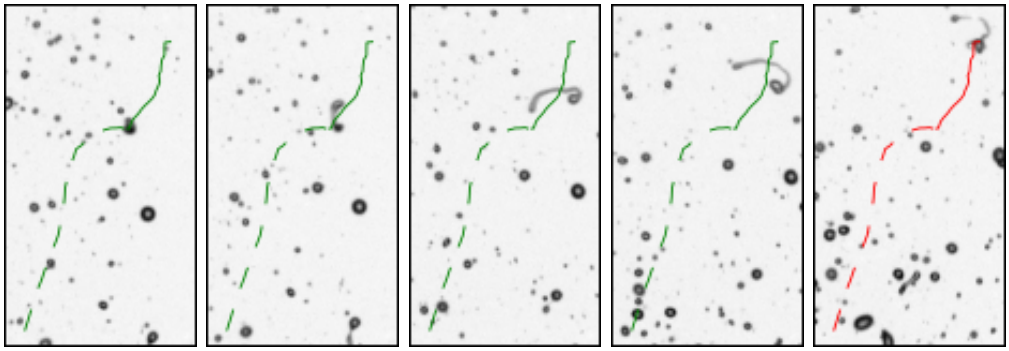

(f) $t = 6.6$ (g) $t = 7.2$ ms (h) $t = 8.4$ ms (i) $t = 9.4$ ms (j) $t = 10.8$ ms

Figure 5.7: A demonstration of a breakup path overlaid on the breakup sequence. $Re = 80000$ and $Q_p = 20$ mL/min. Needle positioned at $z/d_j = 20$. Canola oil.

5.4 Daughter particles identification

The LIBT algorithm tracks particles in the pre-breakup period (from begining of the deformation to the instant when breakup occurs). However, we are also interested in the post-breakup period, especially the formation of daughter particles, so a daughter particles identification algorithm is needed in addition to LIBT. In this section, we will present a daughter particle identification algorithm.

Our daughter particles identification algorithm is a sub-routine that runs along with LIBT. Once an completed path is identified by LIBT, the daughter particles identification algorithm begins the search for the daughter particles. As mentioned in Section 5.2, when an ligament is identified in LIBT and that it does not belong to any future track, it is assumed to be at the point just before the breakup occurs. So, the search of the daughter particles begins at the frame where the mother ligament is identified. Naturally, the search has to be done forward in time unlike in the LIBT algorithm.

There are a few difficulties in daughter particle identification. First, because a daughter particle has a very different size, shape and position (the centroid of an long mother ligament could be far away from a daughter that formed from the end of the ligament) than its mother particle, any attempt to identify the daughter particles through a direct tracking method between the mother and daughter particle is impractical. Second, the disintegration process does not always happen instantly. In the case of the breakup of long ligaments, multiple week points will develop along the string. These weak points could break in a different time. Generally, all weak points break within a short amount of time. However, the slight difference in the time of breakup means that the tracking of the daughters should last for more than one frame after the first disintegration of the ligament.

5.4.1 Primary daughter particles identification

The first task in this algorithm is to identify the daughter particles following the first disintegration of a ligament. This process takes place between the frame where the original

ligament is identified (pre-breakup, frame n) and the first frame after that (post-breakup frame $n+1$). The daughter particles identified in this process is called the primary daughter particles.

Since we cannot directly track between the mother and the daughter particles, an indirect tracking method is needed. The idea of this method is to search for a match in frame n for the particles ($j = 1...J$) in frame $n+1$. If a match is found in frame n for particle j and the match is not the mother particle, particle j is not a daughter particle as it belongs to another particle path. Particles j that does not have a match in frame n are considered daughter particles.

Since this identification method relies on the surrounding particles, it is more efficient to employ interrogation areas to minimize the number of searches. The interrogation areas are defined in a similar fashion as in the ones used in LIBT, thus it can be illustrated using Figure 5.3. Since the daughters are in close proximity of the mother particle, the interrogation area in frame $n+1$ uses the bounding box of the mother particle plus a tolerance in each direction. It is also shifted from the bounding box in frame n using the predicted displacement calculated from the tracking of the mother ligament. The interrogation of frame n uses the bounding box of the mother particle plus double the tolerance used in frame $n+1$. The reason of having a larger interrogation in frame n is because the surrounding particles j might have a different velocity than the mother particles, so a larger interrogation area is needed to ensure the potential match is not out of the interrogation area in frame n.

The tracking of particles j uses the same shape matching function and displacement minimization sub-routines described in Section 5.2. Given there are particles in frame n that satisfy the SMF, the displacement minimization sub-routines will always produce a match. However, we know that a match is not necessary because a daughter particle should not have a match. So, a displacement threshold is imposed to filter out spurious match that has unusual displacement.

5.4.2 Secondary daughter particles identification

As we mentioned before, the primary daughter particles are not necessary spherical particles. A highly deformed daughter ligament could potentially lead to secondary breakup and form smaller daughter particles. The goal of this algorithm is to identify all daughter particles originated from the mother particles. However, if secondary breakup exists, the corresponding primary daughter particle is not considered to avoid double counting. This means only daughter particles that do not lead to subsequence breakup are considered. From now on, we called these the true daughter particles. To identify all true daughter particles, the following procedures are applied to each primary daughter particle.

Step 1: Examine if the daughter is spherical

A spherical daughter is considered to be a true daughter particle. This is a valid assumption because daughter particles are typically small and they are located in the region with low flow intensity, so unless they are highly deformed, the surrounding flow do not have enough energy to cause breakup. If the circularity of the daughter particle is greater than 0.942, which is the exit condition used in LIBT, the daughter particle is consider a true daughter particle. If this condition is not satisfied, proceed to Step 2.

Step 2: Determine if the daughter belongs to any secondary breakup path

A secondary breakup event occurs after the primary breakup, so when the daughter particle identification algorithm is activated, all future breakup paths are already identified by LIBT as it tracks backward in time. Thus, to determine if secondary breakup exists for a particular daughter, we only need to search if it belongs to any future breakup path. If a daughter particle belongs to a secondary breakup path, we need to identify the daughter particles from the secondary breakup (Step 3). If a secondary breakup path is not found, it does not mean there is no secondary breakup event. In many cases, there is a gap between the beginning of the secondary breakup path and the formation of daughter particles from the primary breakup path. Therefore, we need to tracks the daughter particle forward in time (Step 4) until either a secondary path is found or the particle reverts back to spherical.

Step 3: Identify secondary daughter particles

A secondary breakup path behaves the same as a primary breakup path. Thus, the secondary daughter particles identification process uses the same routine discussed in Section 5.4.1. All secondary daughters are sent back to Step 1 until all true daughters are found.

Step 4: Forward tracking

A tracking process is activated for the daughter particle in frame n. It utilizes the same tracking sub-routines in LIBT, including the use of interrogation area, shape matching function and displacement minimization. The tracking process is applied forward in time between frame n and $n+1$. If a match is found, the particle in frame $n+1$ is sent back to Step 1. Otherwise, the daughter particle in frame n is considered to be a true daughter particle.

5.5 Demonstration of daughter particle identification algorithm

Figure 5.8 shows the identified daughter particles overlaid on the images of the breakup sequence. The cross symbol represents true daughter particle and the circle symbol represents daughter particles that will lead to subsequence breakup. The primary breakup occurred at $t = 0.6$ ms at a weak point, this produced two daughter ligaments (the left and center circles). On the image, we see a string attached between the identified two daughters. However, this is a very thin string, which means the contrast between the string and the background is low. Thus, the string was not recognized by the image processing algorithm, instead, it recognized two separate ligaments. Ultimately, this does not affect the result as the thin strings always break and the resulting number of daughters is the same.

The primary daughter identified on the right (cross symbol) was not a daughter particle from this breakup, but it was identified because it touched the mother ligament just before the breakup ($t = 0.4$ ms) and separated in the subsequence frame. A secondary breakup path (the blue path) was found for the primary daughter on the left immediately. The primary daughter in the center broke into two daughter at $t = 1.4$ ms. We can see these two daughters were ligaments, so the circle symbols are appropriate. The blue path on the right

indicates a breakup path was found for the secondary daughter on the right. At $t = 2.4$ ms, one of the secondary daughters broke into two true daughter particles. Another secondary breakup occurred at $t = 3.0$ ms, this produced two daughters but four were identified by the algorithm. This is because the ligament was surrounded by multiple particles, some of which overlapped with the ligament just before it broke. Finally, the secondary daughter on the left broke into two true daughter particles at $t = 4.0$ ms.

This sequence shows that the daughter identification algorithm is capable of identifying both primary and secondary daughter particles. However, false identifications were observed. In this case, out of all the 13 daughters (9 true daughters) identified, 3 were false identifications. These false identifications all occurred in region with high particle density. With particles moving across the ligament during the breakup process, it significantly increases the chance of false identification. Therefore, unlike LIBT which performs well in particle-dense region, the daughter particle identification algorithm is recommended to be used in region with low particle density.

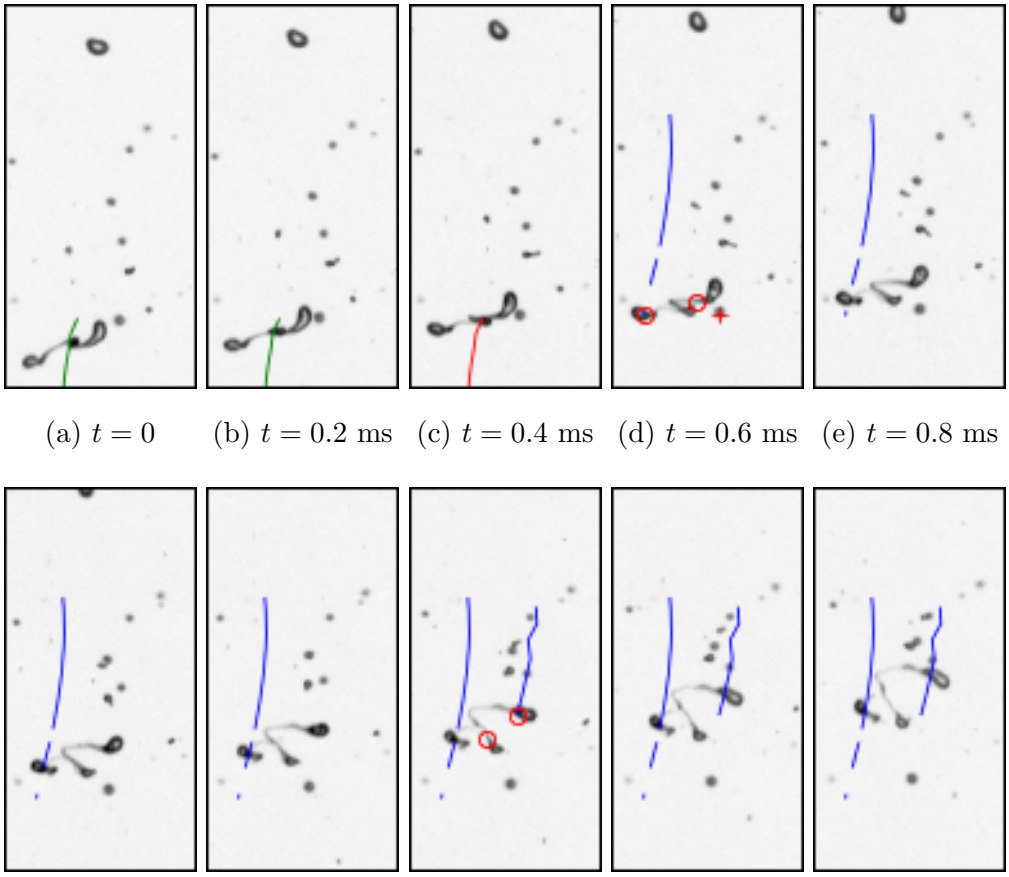

(a) $t = 0$ (b) $t = 0.2$ ms (c) $t = 0.4$ ms (d) $t = 0.6$ ms (e) $t = 0.8$ ms

(f) $t = 1.0$ ms (g) $t = 1.2$ ms (h) $t = 1.4$ ms (i) $t = 1.6$ ms (j) $t = 1.8$ ms

Figure 5.8: A demonstration of the daughter particle identification algorithm. $Re = 80000$ and $Q_p = 20$ mL/min. Needle positioned at $z/d_j = 20$. Canola oil.

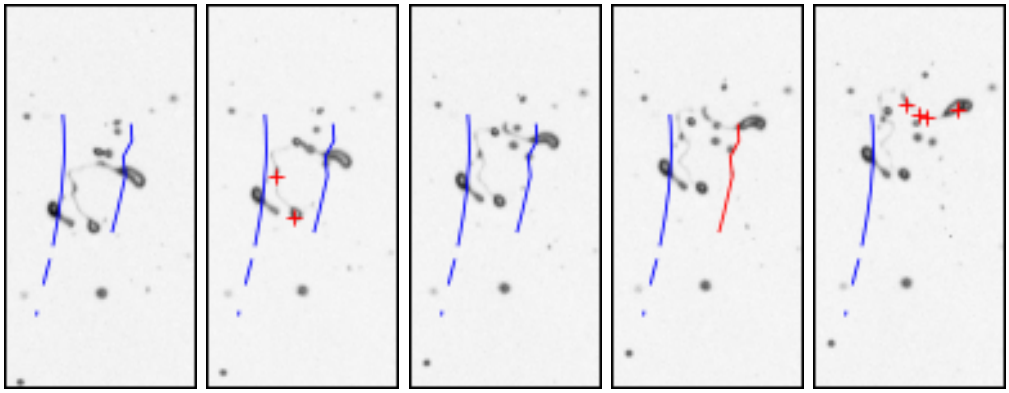

(k) $t = 2.0$ ms (l) $t = 2.4$ ms (m) $t = 2.6$ ms (n) $t = 2.8$ ms (o) $t = 3.0$ ms

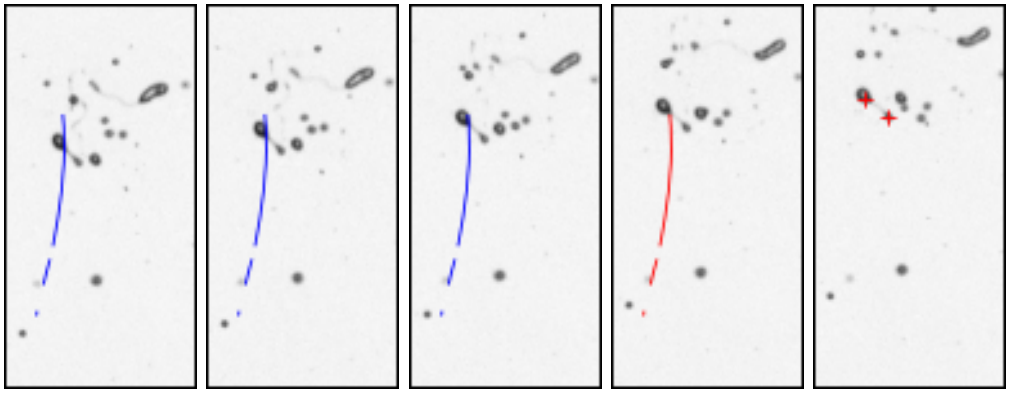

(p) $t = 3.2$ ms (q) $t = 3.4$ ms (r) $t = 3.6$ ms (s) $t = 3.8$ ms (t) $t = 4.0$ ms

Figure 5.8 (Continued): A demonstration of the daughter particle identification algorithm. $Re = 80000$ and $Q_p = 20$ mL/min. Needle positioned at $z/d_j = 20$. Canola oil.

Chapter 6

BREAKUP OF INVISCID PARTICLES

Various factors contribute to the dynamics of particle breakup, such as the velocity of the jet, the turbulent motions, the initial size of the particles and the fluid properties. In this chapter, we studied how each individual factor affect the breakup process, but to simplify our analysis, the dispersed phase was limited to air bubbles so that the viscous effect was not considered in this chapter.

6.1 Bubble flux

To begin our investigation, we first look at evolution of the number of bubbles in Figure 6.1. N_b' is the number of bubbles per image. The Reynolds number for this experiment was about 60000 and the air flow rate, $Q_b = 20$ mL/min. The three curves represents data taken with three different camera locations. There is a drop off in the number of bubbles at the beginning and the end of each camera location. Recall from Chapter 3 that the light intensity at the edge of the image is lower due to the Gaussian distribution of the light intensity. Even after applying the image processing techniques described in previous chapter, the contrast between the background the bubbles near the edge of the frame is inherently lower. This affects the amount of smaller particles being recognized at the edge of each camera location. Nonetheless, it is clear that there is a steady increase in the number of bubbles over distance, which indicate breakup occurs. However, using the number of bubbles in each zone as an indication of the breakup is not representative. This is because bubbles are traveling at a different velocity in different zones. In zones where the jet velocity is slow, the resident time of a given particle is longer, so the high bubbles count represents not just the breakup events, but also the increase of bubbles due to longer resident time. A more appropriate

measurement is the bubble flux at each location. The bubble flux is defined as $N_b' U_o / L_z$, where U_o is the mean centerline velocity and L_z is the axial length of the interrogation zone.

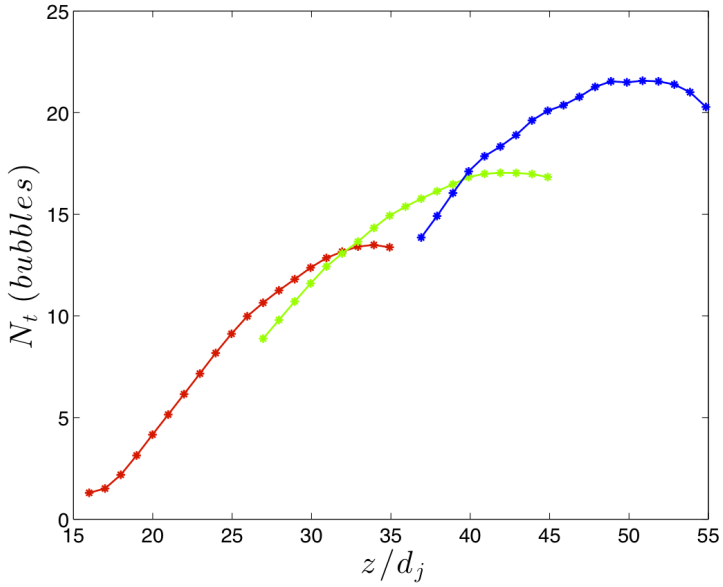

Figure 6.1: The number of bubbles per image over axial distance. $Re = 60000$ and $Q_b = 20$ mL/min.

Figure 6.2 shows the flux of the bubbles passing through each zone. Again, the drop off in the bubble flux indicates the edge of the image. Instead of the monotonic increase shown in Figure 6.1, the bubble flux increases initially and reaches a steady value. Assuming the coalescence of bubbles does not occurs, this indicates breakup is completed about 15 d_j from the air injection location. Similar trend is observed in other experiments, for example, Figure 6.3 shows the bubbles flux for three different Reynolds numbers. Since higher Reynolds number jet contains higher turbulent kinetic energy, the breakup occurs more frequently and smaller size bubbles have higher probability to break into even smaller bubbles, resulting in a higher bubble flux.

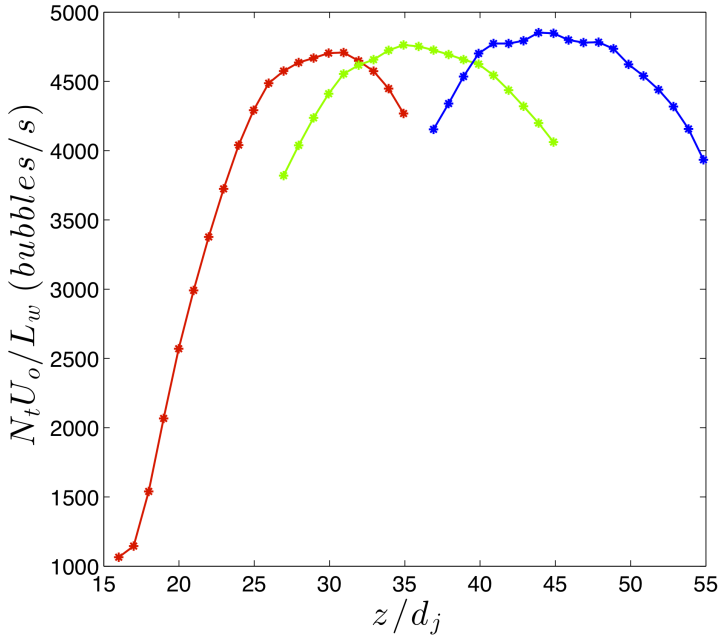

Figure 6.2: Bubble flux over axial distance. $Re = 60000$ and $Q_b = 20$ mL/min.

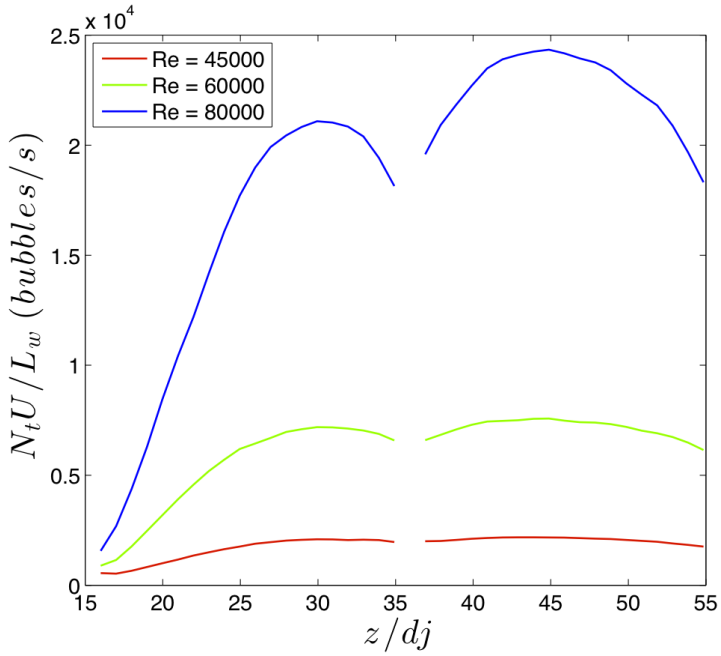

Figure 6.3: Bubble flux over axial distance. $Q_b = 42$ mL/min.

6.2 Bubble size and size distribution

Characterization of the particle size distribution is usually represented by the probability density function (PDF). To obtained the PDF from experimental data, the number of particles, N_i, that fall within $D_i - \triangle D/2$ and $D_i + \triangle D/2$ is recorded for each zone. $\triangle D$ is chosen to be 0.1 mm to allow sufficient number of particles fall within each size range while maintaining good resolution. The total number of particles is defined as $N_T = \sum N_i$ and the PDF is given in Equation (6.1).

$$PDF(D_i) = \frac{1}{\triangle D}\frac{N_i}{N_T} \tag{6.1}$$

In a distribution where the larger particles have significantly less quantity than the smaller particles, the larger particles are "hidden" in the PDF. However, these particles could carry a significant portion of the total volume, so the volume probability density function (VPDF) provide a better visualization for this kind of distribution. VPDF is basically a PDF weighted by the volume of the particles. It is given in Equation (6.2).

$$VPDF(D) = \frac{D^3 PDF(D)}{\int_{D_{min}}^{D_{max}} D^3 PDF(D) dD} \tag{6.2}$$

Another way to characterize the particle size is to use Sauter mean diameter, D_{32}. D_{32} is a single statistical value used to represents a distribution of particles. It is defined as $D_{32} = \sum N_i D_i^3 / \sum N_i D_i^2$. In following sections, we will employ these statistical tools, namely PDF, VPDF, CVPDF (cumulative VPDF) and D_{32}, to study the effect of different parameters on the bubble size.

6.3 Evolution of the size distribution of air bubbles

The evolution of the bubbles size distribution over axial distance for three different Reynolds numbers are shown in Figure 6.4, 6.5 and 6.6. The first measurement point for each experiment was taken at $z/d_j = 19$, which was 4 d_j downstream of the injection needle position. Prior to this point, the bubbles came out of the needle as a big lump of fluid that have been

stretched and deformed by the initial shear from the jet, so it was difficult to accurately obtained the bubble size.

The initial size distribution of these experiments is broad. As observed from the CVPDF plots, over 50% of the volume weighted particles are over 2 mm in diameter at the initial measurement location for all three experiments. Bubbles large enough to fall within the inertial subrange were deformed by the underlying turbulence. Some of these bubbles broke into smaller bubbles. Thus, we see that the peak of the VPDF moving from the larger bubble size to the smaller bubble size. As the bubbles moved downstream, the energy contained in the underlying turbulence decreased and the amount of bubbles large enough to be affected by the turbulent motion decreased, so the breakup events occurred less frequently. Eventually it reached a point where all the bubbles were too small to be broken up by the turbulence motion and no further breakup occurred. At this point, the size distribution is said to have reach the frozen state. This is evident in the overlapping of VPDF and CVPDF at the last few axial distances.

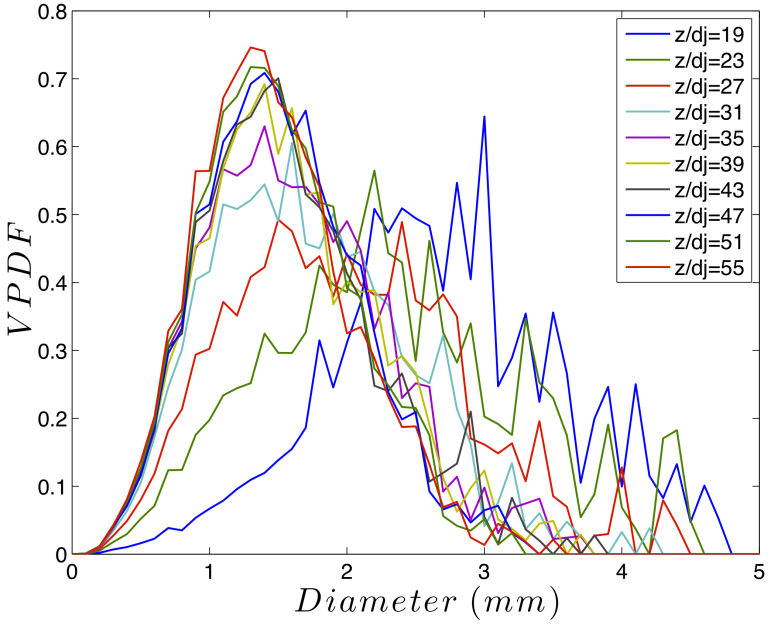

(a) VPDF

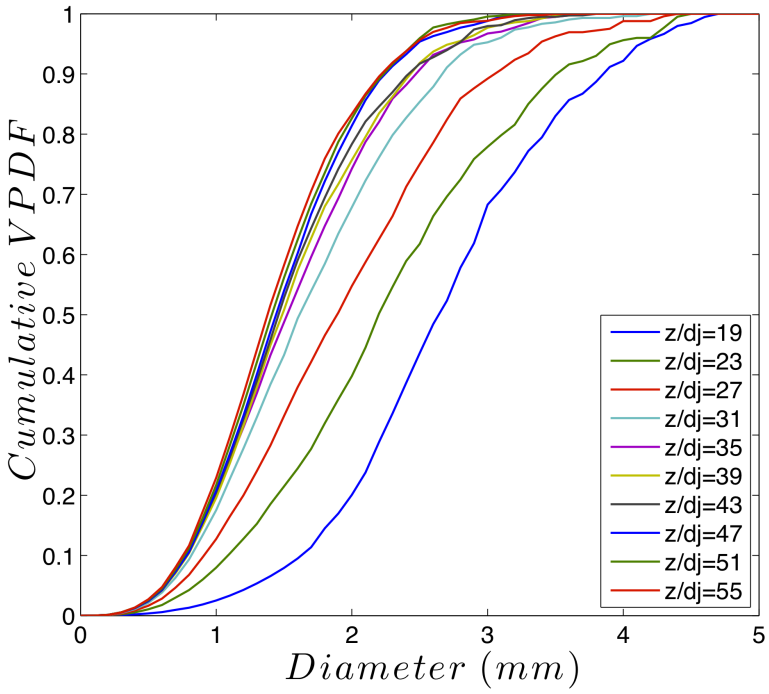

(b) CVPDF

Figure 6.4: The evolution of the size distribution (VPDF and CVPDF). $Re = 45000$ and $Q_b = 42$ mL/min.

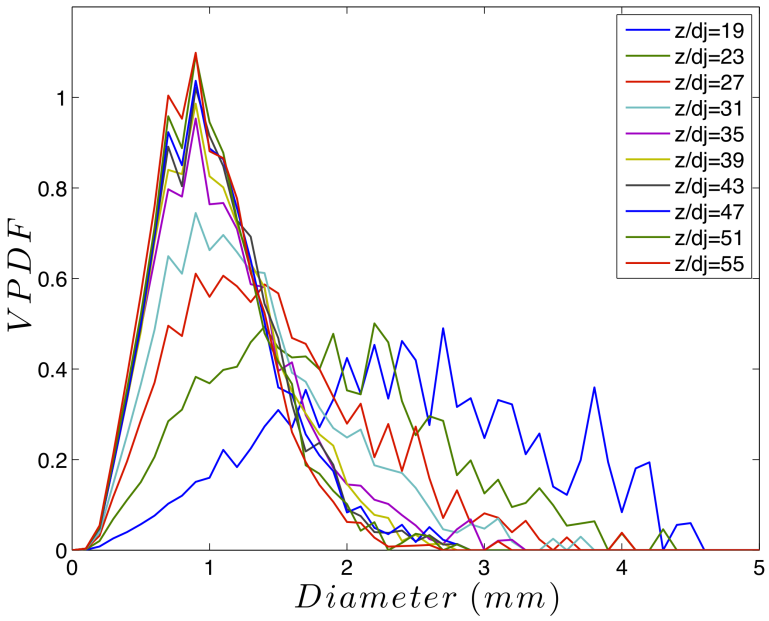

(a) VPDF

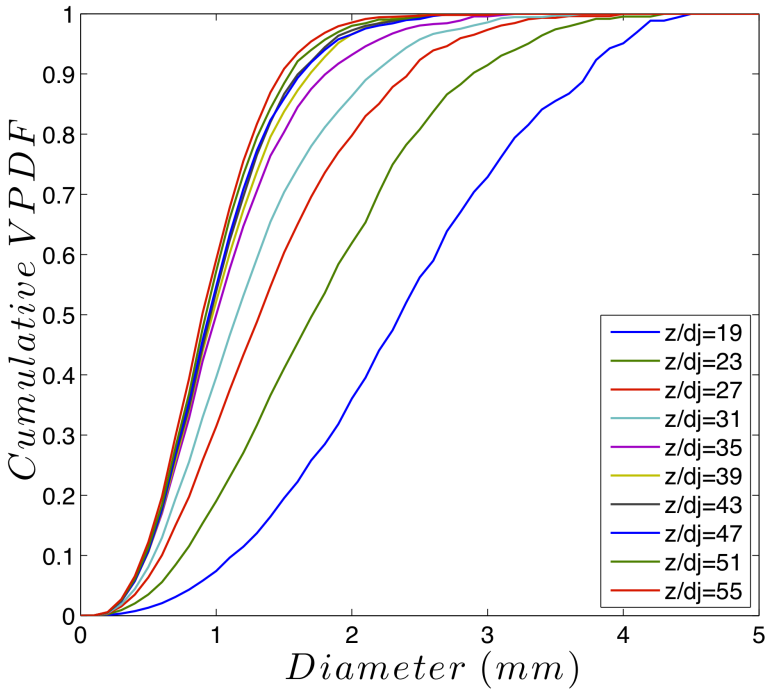

(b) CVPDF

Figure 6.5: The evolution of the size distribution (VPDF and CVPDF). $Re = 60000$ and $Q_b = 42$ mL/min.

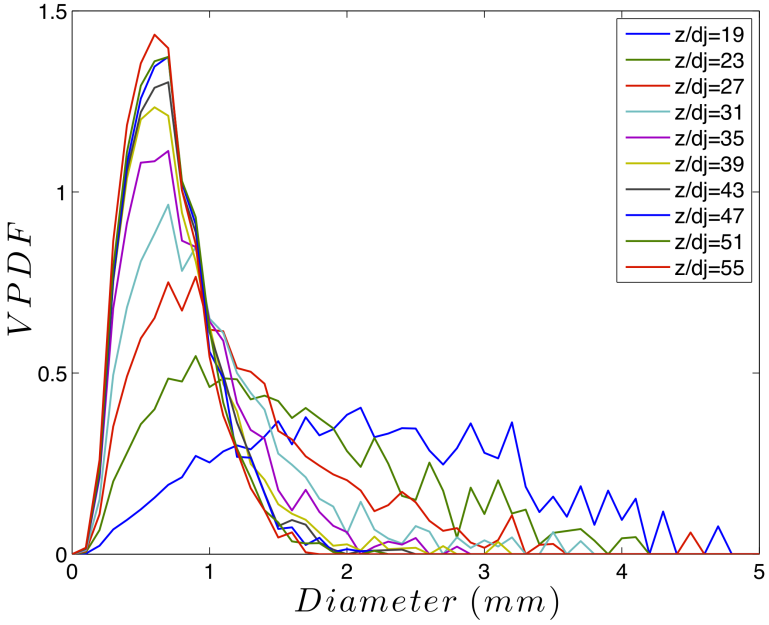

(a) VPDF

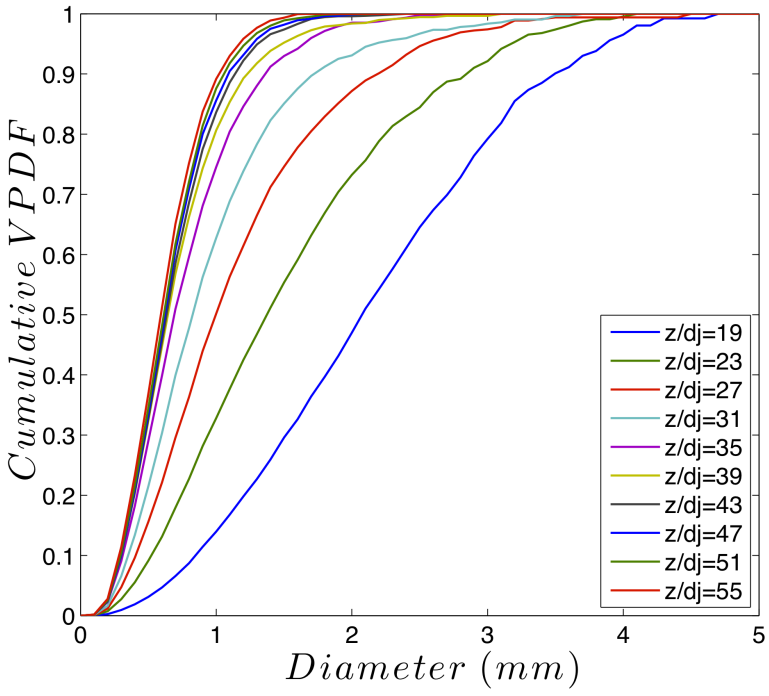

(b) CVPDF

Figure 6.6: The evolution of the size distribution (VPDF and CVPDF). $Re = 80000$ and $Q_b = 42$ mL/min.

6.4 Effect of Reynolds number and turbulent dissipation rate

Figure 6.7 compares the CVPDF for the three different Reynolds numbers. Initially, the size distribution of the three cases are relatively similar. Since the bubbles are created using the same needle ($d_b = 0.41$ mm) and the same bubble flow rate ($Q_b = 42$ mL/min), the initial difference between the three cases is mainly due to the shear since the bubbles have not accelerated to match the speed of the jet. The gap widens as the bubbles being convected downstream because bubbles in the higher Reynolds number jet experience more energetic turbulent motion. Once the size distributions reach the frozen state, there is a significant difference between the three cases.

The frozen state PDFs of the three Reynolds numbers are shown in Figure 6.8. In the logarithmic scale, the tail of the PDFs is almost linear. The prominent effect of the Reynolds number appears to be on the slope of the tails. The higher the Reynolds number the steeper the slope. If we normalize the diameter by the D_{32} and calculate the PDF based on the normalized diameter, the three PDFs collapse together, as shown in Figure 6.9. This self-similar behavior suggests that the Sauter mean diameter is the only parameter needed to describe the bubble size in the frozen state.

To further understand the effect of Reynolds number on the frozen state, Figure 6.10 shows the D_{32} at the frozen state versus the jet Reynolds number for a collection of experiments. These experiments include variations in d_j, Q_j, Q_b and the needle position. Although our previous analysis shows that the higher the Reynolds number, the smaller the bubbles size, there is no clear trend shown here. Unlike in Figure 6.7 where all variables were held constant except for Q_j, the change in needle position significantly changes the turbulence kinetic energy the bubbles experience even for the same Reynolds number. Therefore, the size of the bubbles in the frozen state should depend on a parameters that changes with the needle position instead of the Reynolds number. Since we assumed that the length scale of the turbulence responsible for the breakup is in the inertial subrange, the Kolmogorov hypothesis stated that the energy from these turbulence motion depends only on the turbu-

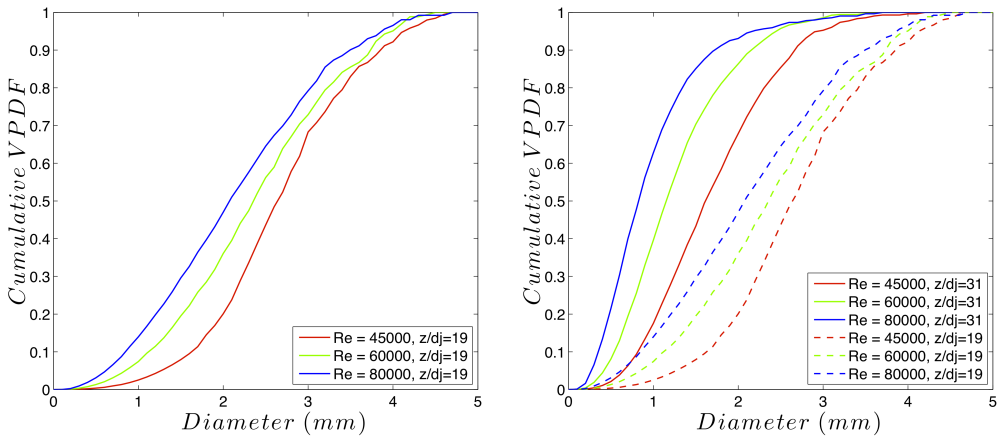

(a) $z/d_j = 19$

(b) $z/d_j = 31$

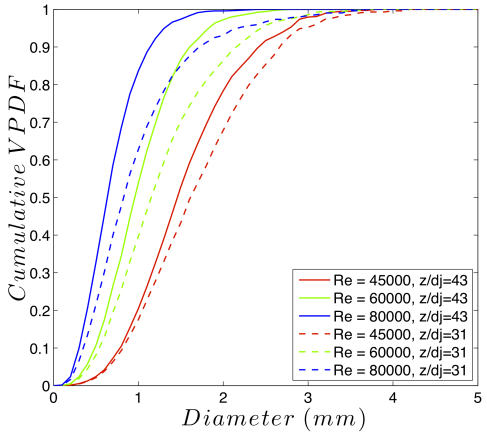

(c) $z/d_j = 43$

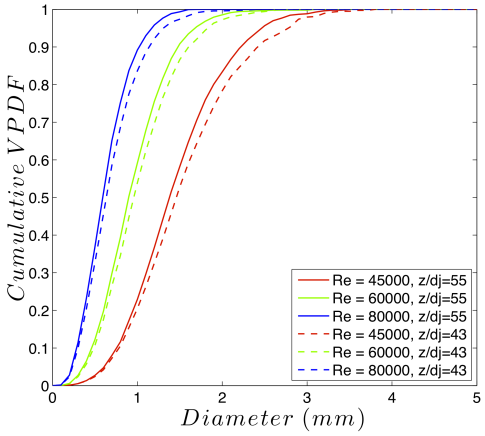

(d) $z/d_j = 55$

Figure 6.7: A comparison of the CVPDF between $Re = 45000$, $Re = 60000$, and $Re = 80000$. $Q_b = 42$ mL/min. Dashed lines represents the size distribution from the last measurement location.

lent dissipation rate. So, the bubbles size should depends on the turbulent dissipation rate. Figure 6.11 shows the D_{32} at the frozen state vs the centerline dissipation rate at the needle position. In this case, there appears to be an exponential decaying trend. This strengthens our believe that the Kolmogorov hypothesis applies in the turbulent breakup in our experi-

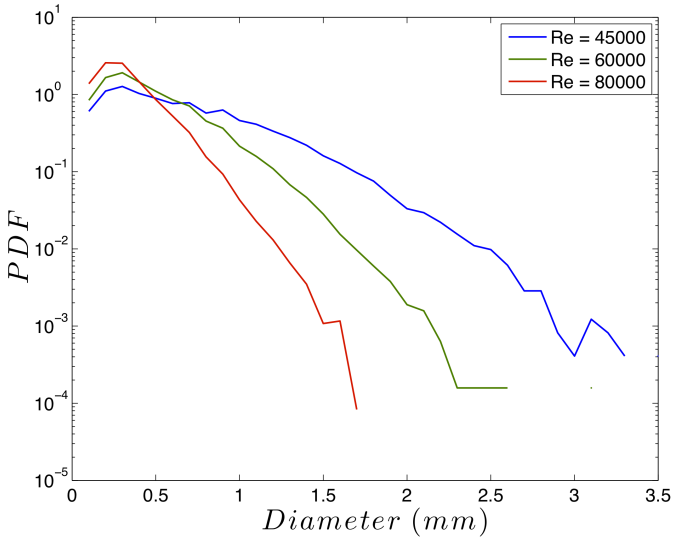

Figure 6.8: A comparison of the frozen state PDF between $Re = 45000$, $Re = 60000$, and $Re = 80000$. $Q_b = 42$ mL/min.

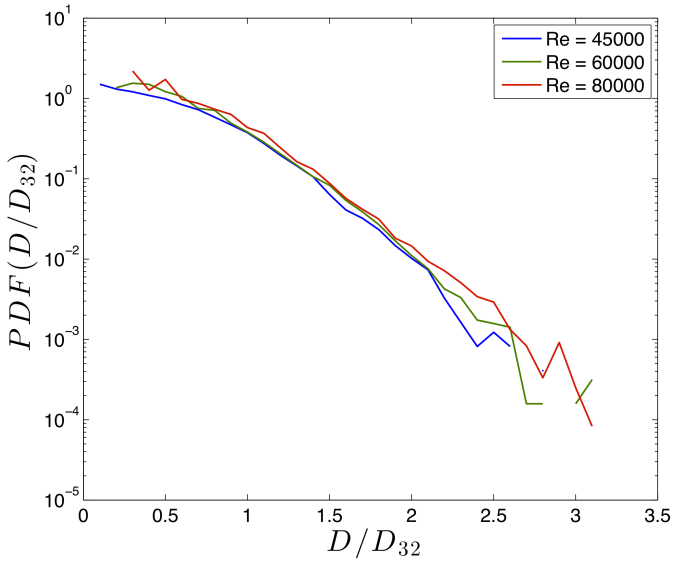

Figure 6.9: A comparison of the frozen state PDF (nomalized by D_{32}) between $Re = 45000$, $Re = 60000$, and $Re = 80000$. $Q_b = 42$ mL/min.

ments, which in turn strengthens our assumption that the turbulent scale responsible for the breakup is in the inertial subrange.

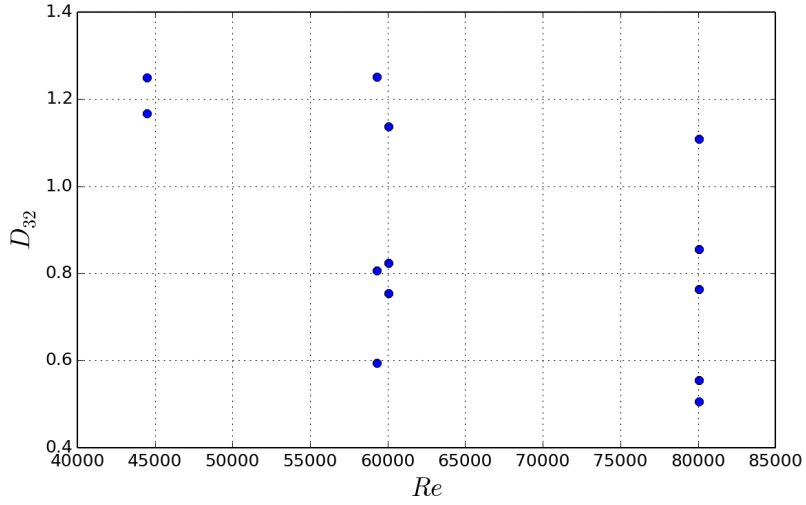

Figure 6.10: Sauter mean diameter vs Reynolds number for different experiments.

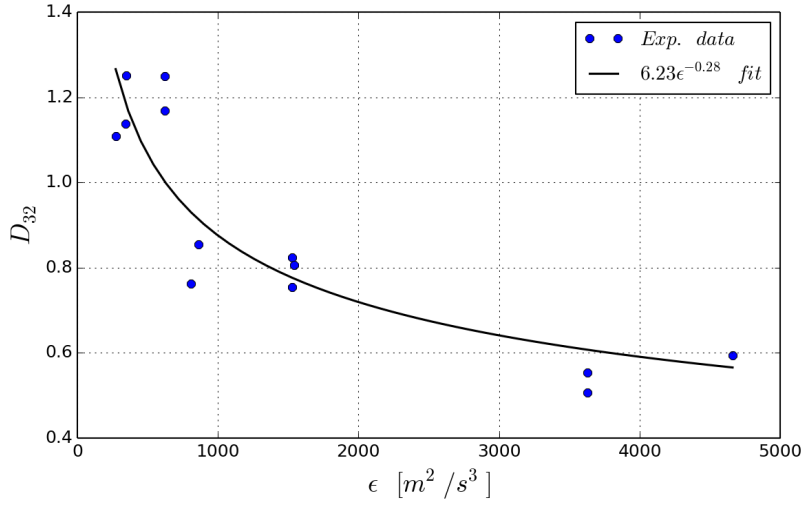

Figure 6.11: Sauter mean diameter vs initial turbulent dissipation rate for different experiments.

6.5 Effect of air void fraction

Two experiments (identified as test A and test B) were performed with different d_j, Q_j, and needle position. The combination of these parameters were made such that the centerline velocity, U_o, and the turbulent dissipation rate at the needle position were effectively the same. In addition, the evolution of the centerline velocity and dissipation rate were also effectively the same from the needle position so that bubbles experienced the same turbulent kinetic energy with the same resident time. A summary of the experimental parameters are shown in Table 6.1. Because the bubbles from the two experiments were exposed to basically the same flow condition, we expect the size distribution to be virtually identical. Since the needle position were placed at different z/d_j, we could not compare the size distribution of the two experiments at the same z/d_j. Instead, we compare the size distribution of the two experiments in the zone with the same dissipation rate (which is also the same axial distance relative to the needle position). This comparison is shown in Figure 6.12.

Interestingly, the size distribution between the two experiments never collapsed as we expected. One could contributes the difference to experimental error or the fact that the dissipation rate was not the exactly the same for the two experiments, although the difference in initial dissipation rate was less than 3%. However, notice that the initial size distributions ($\epsilon \approx 210$) of the two experiments were relatively similar compare to the downstream counterparts. This indicates other factors might have an effect on the size distribution.

One thing that have not been taken into consideration between test A and B was the air void fraction. The void fraction is defined as the bubble flow rate divided by the jet flow rate (i.e. Q_b/Q_j). Although the bubble flow rate was kept the same between test A and B, the jet flow rate changed. Thus, the void fraction between the two experiments is different. In this case, the void fraction of test B is about 35% larger than test A. To verify that the air void fraction plays a role in changing the size distribution, we performed another experiment (identify as test C) with the same parameters as test B, but we adjusted Q_b in order to match the void fraction in test A. Figure 6.13 shows the comparison between test A and C.

Test	d_j (mm)	Q_j (GPM)	Q_b (ml/min)	z/d_j	U_o (m/s)	ϵ (m^2/s^3)
A	4	2.7	42	20	4.91	342
B	3	2	42	25	4.93	351
C	3	2	31.1	25	4.93	351

Table 6.1: Experimental parameters of test A and B. z/d_j, U_o and *epsilon* values are taken at needle position.

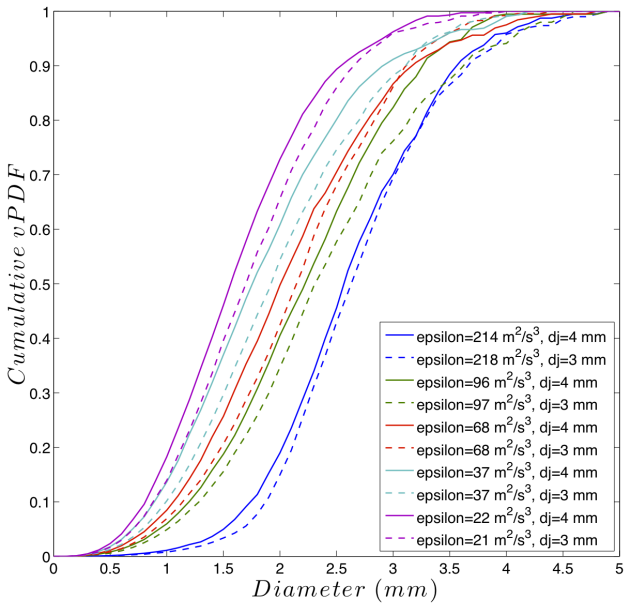

Figure 6.12: A comparison of the size distribution between test A and B over five different turbulent dissipation rate.

The size distribution between test A and C are in better agreement than between test A and B, confirming the believe that the void fraction plays a role in the size distribution.

One possible explanation of how the void fraction affect the size distribution is that it

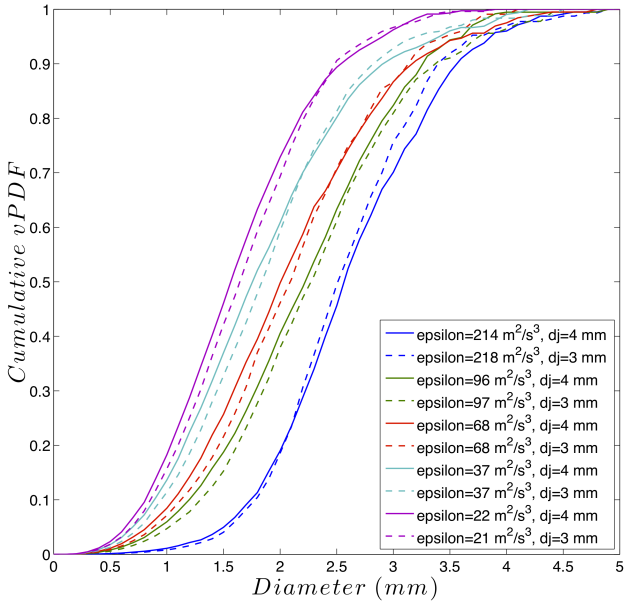

Figure 6.13: A comparison of the size distribution between test A and C over five different turbulent dissipation rate.

inhibits the underlying turbulence. To test this theory, one would need to measure the turbulence dissipation rate of the jet while having bubbles injected inside. Unfortunately, this is outside of the capability of the available measurement techniques we possessed. Nonetheless, we found that the effect of void fraction is small compare to the effect of the dissipation rate for the range of void fraction tested in our experiment.

6.6 Effect of initial size distribution

In order to produce a different initial size distribution, different sizes of the injection needle were used. Figure 6.14 shows the initial size distribution and the frozen state size distribution for two needles (d_b = 1.19 mm and d_b = 0.41 mm). Not surprisingly, the larger needle produced more larger size bubbles and less smaller size bubbles. As the bubbles traveling downstream, the size distributions for the two experiments slowly become indistinguishable.

This suggests that the initial size distribution does not affect the final size distribution providing the following two conditions are met. First, there should be sufficient time for the size distribution to reach the frozen state. Second, the initial particle size should be large enough to be broken up by the underlying turbulent kinetic energy. The implication of this result is significant for many industrial applications, where the underlying turbulence is controllable, but the initial particle size distribution is not practical to be measured.

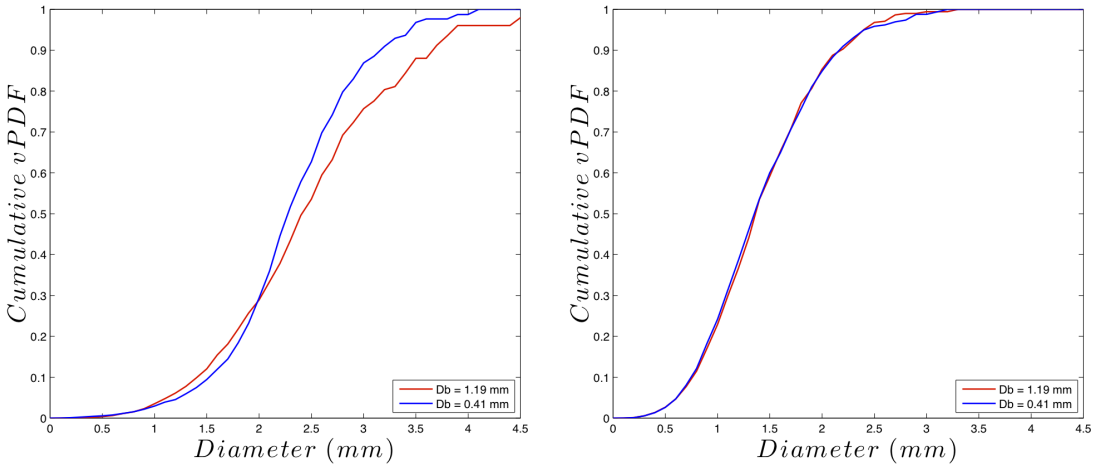

(a) $z/d_j = 19$ (b) $z/d_j = 47$

Figure 6.14: A comparison of the CVPDF between different nozzle diameters. $Re = 45000$ and $Q_b = 10$ mL/min.

6.7 Comparison to an existing model

As mentioned in Chapter 2, the current state of modeling of turbulent breakup evolves around the population balance model, shown in Equation (2.4). Three simplifications were made for the our problem. First, since we are interested in the steady-state process, the time dependent term on the left side of the equation is zero (i.e. $\partial p/\partial t = 0$). Second, the void fraction is always less than 0.6% for all experiments and particles tend to disperse

radially inside the jet, so particle coalescence is unlikely to happen. So, the coalescence rate is considered to be negligible (i.e. $\dot{Q}_c = 0$). Finally, we assume that the breakup process to be one-dimensional. With these simplifications and substituting Equation (2.5) in to Equation (2.4), the population balance equation becomes:

$$\frac{\partial(U(D)n(D))}{\partial z} = \int_D^\infty m(D_o)f(D, D_o)g(D_o)n(D_o)dD_o - g(D)n(D) \tag{6.3}$$

where $U(D)$ is the mean velocity of the particle of size D, $n(D)$ is the probable number of particle of size D, $m(D_o)$ is the mean number of daughter particle results from the breakup of a mother particle, D_o, f is the daughter particle size distribution, and g is the breakup frequency.

In order to solve Equation (6.3), models for the daughter particle size distribution and the breakup frequency is required. We have summarized a few notable models in Chapter 2. For the comparison to our experiment, we will utilized Martínez-Bazán et al. model [39, 40] because they have successfully demonstrated their model performed well for the breakup in turbulent jet, while other models are developed for other applications such as stirred vessel. Their model of breakup frequency and the daughter particle size distribution are given in Equation (2.22) and (2.37), respectively. Martínez-Bazán et al. [40] also assumed binary breakup, so $m(D_o) = 2$. The mean velocity of the particles, $U(D)$, is taken as the mean velocity of the jet at each zone. Integrating Equation (6.3) requires the initial condition of n, which is taken experimentally from the first zone where the particles are traveling at the same velocity as the flow so that the initial shear effect is negligible.

Comparison of the CVPDF between the model and the experimental data are shown in Figure 6.15, 6.16 and 6.17. The size distribution at $z/d_j = 31$ of each case is used as the initial condition for the model. The agreement of the size distribution at the intermediate axial distance is not great, but the model predicts the frozen state size distribution well. Since the completion of the breakup is determined by the critical diameter, D_c (Equation (2.21)), it implies that the modeling of D_c using the balance of stresses accurately represents the range of drop size that could be broken up by the available turbulent motion.

Figure 6.18 shows the comparison of D_{32} between the model and the experimental data for the three Reynolds numbers. The general trend of the evolution of D_{32} is captured by the model, but it slightly over-predicted the the Sauter mean diameter for $Re = 60000$ and $Re = 80000$.

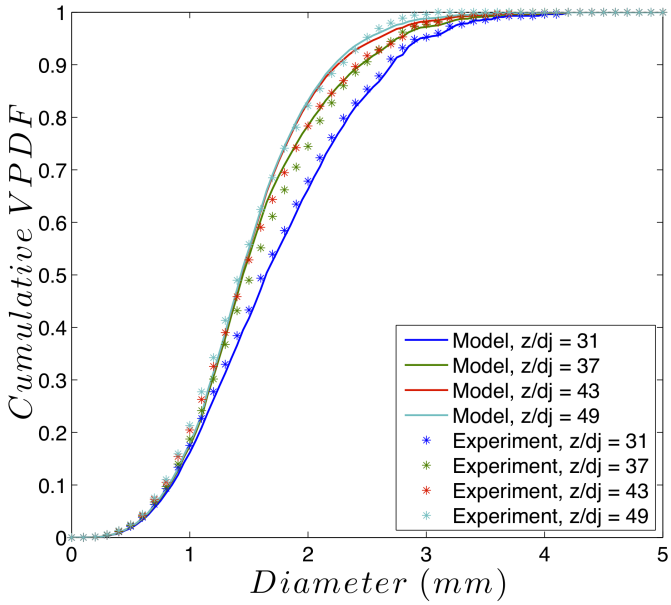

Figure 6.15: A comparison of the CVPDF between the model and the experimental data. $Re = 45000$ and $Q_b = 42$ mL/min.

Two aspects of the model are suspected to contribute to the difference between the model and the experimental data. First, Martínez-Bazán et al. [39] assumes binary breakup, meaning that each breakup event results in two daughter particles (i.e. $m(D_o) = 2$). However, binary breakup may not be the dominant case. In fact, Lee et al. [34] showed that their multibreakage model have a better prediction to their experimental data than their binary breakup model. Second, the daughter particle size distribution from Martínez-Bazán et al. model [40] has the highest probability for equal-sized breakup. This is in contrary to some other models, such as the one from Tsouris and Tavlarides [66], where equal-sized breakup has the lowest probability. Since the surface area of two equal-sized daughter particles is

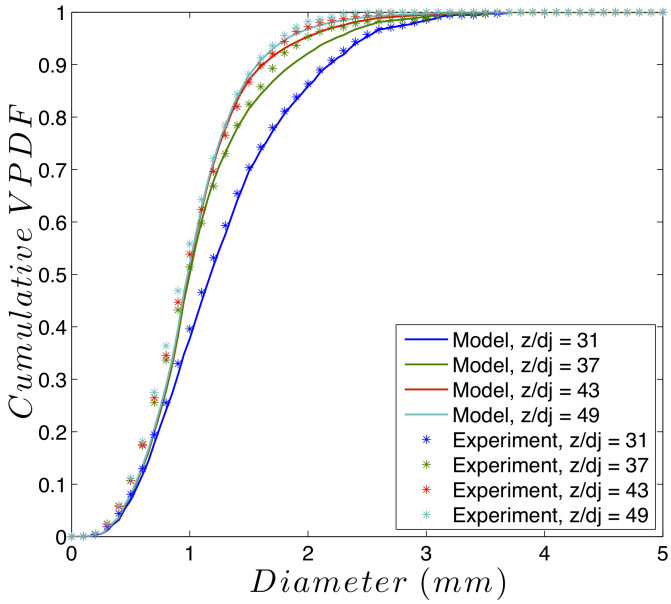

Figure 6.16: A comparison of the CVPDF between the model and the experimental data. $Re = 60000$ and $Q_b = 42$ mL/min.

maximum for the given volume, it is unlikely equal-sized breakup has the highest probability since surface tension effect tends to minimize the surface area.

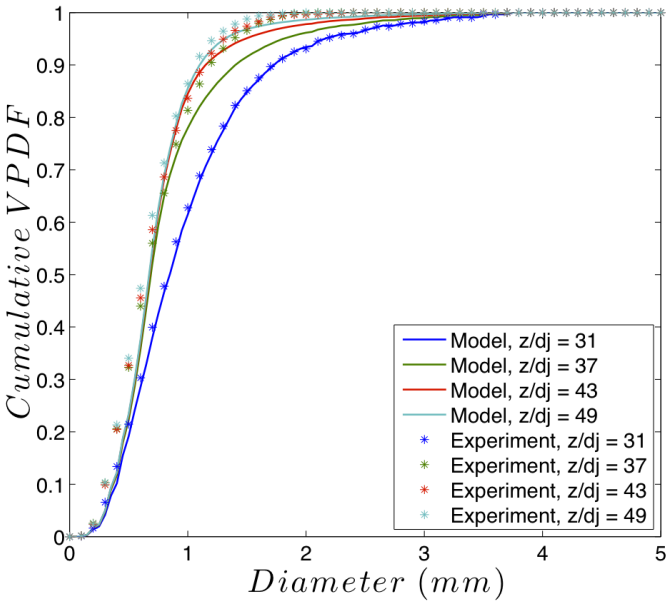

Figure 6.17: A comparison of the CVPDF between the model and the experimental data. $Re = 80000$ and $Q_b = 42$ mL/min.

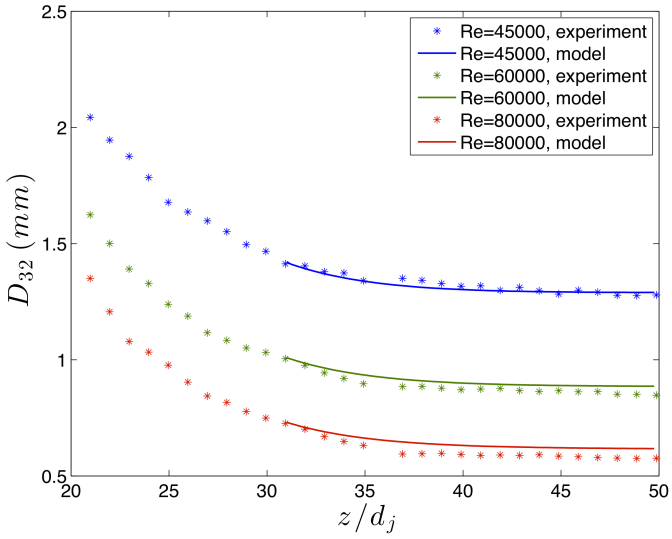

Figure 6.18: A comparison of the D_{32} between the model and the experimental data for three Reynolds numbers. $Q_b = 42$ mL/min.

6.8 Visualization of bubble breakup

Knowing whether breakup resulting in multiple daughter particles occurs and whether equal-sized breakup has the highest probability not only affect the accuracy of the model, but it is also crucial to our understanding of turbulent breakup. Therefore, we will explore the validity of these two scenarios using high-speed visualization of breakup events.

Figure 6.19 shows a sequence of the breakup of multiple bubbles. This sequence was recorded at 5000 fps. Three original mother bubbles were the targets of this sequence, they were labeled as A, B and C. The bubbles were convected downstream from the bottom of the frame to the top of the frame. The bottom of the frame was located at about $z/d_j = 37$ and the top of the frame was located at about $z/d_j = 44$. At the beginning of the sequence, $t = 0$, all three labeled mother bubbles were not spherical in shape, they were deformed by the underlying turbulence. At $t = 2.6$ ms, the deformation of bubble A reached a critical stage, a pinch off action was observed and it broke into two daughter bubbles A1 and A2 at $t = 3.0$ ms. Note that these two daughter bubbles has significant difference in size. At $t = 4.4$ ms, bubble C has broken up into two similar sized bubbles C1 and C2. At the same time, bubble B was about to be pinched off. 0.2 ms later, it formed two daughter bubbles, B1 and B2, with significantly different size. Bubble A1 still had the majority of its mother bubble volume, so it was large enough to be affected by the underlying turbulence. At $t = 7.2$ ms, a ligament has been stretched from bubble A1, which resulted in three daughter bubbles (A11, A12 and A13) about 0.2 ms later. All three of the daughter were different in size. As bubble A11 being convected further downstream, it was again deformed ($t = 8.6$ ms) and broken up into three daughter bubbles (A111, A112 and A113) with different sizes.

In this sequence, we observed five breakup events from three original mother bubbles resulting in eleven total daughter bubbles. Out of these breakup events, three were binary breakup and the other two resulted in multiple daughter bubbles. All the breakup events resulted in one big bubble with one or two smaller bubbles, with the exception of the breakup of bubble C, which results in two similar size bubbles. This is consistent with the idea that

surface tension tends to minimize the surface area of the daughter bubbles, which results in daughter bubbles with significantly different sizes. Although the visualization of this breakup sequence does not carry any statistical significant, based on our observation these breakup events are typical in the range of experiments we have conducted. Thus, we believed that Martínez-Bazán et al. assumption of binary breakup [39] and that the equal-sized daughter particles have highest probability [40] may not be appropriate for our experiments.

Although the visualization revealed some of the assumptions that do not accurately represent the physical mechanism, it exhibited the fundamental behavior that the model is based on. For example, deformation was not only seen on the target bubbles in Figure 6.19, but also on bubbles with similar size. These deformed bubbles have wave-like structure developed on the surface with the wavelength on the order of the bubble size. This indicates these bubbles were affected by the turbulent eddies of similar scale. For the smaller bubbles, they maintained a fairly spherical size. The turbulent eddies that were energetic enough to deform the larger bubbles did not affect these smaller bubbles. This strengthen the fundamental idea that only eddies with size similar to the bubble could contribute to breakup. Since it appears that the smaller bubbles were not affect by the eddies similar to their size, it implies that those eddies are not energetic enough to overcome the surface tension. Thus, this supports the idea that there exists a critical diameter for which bubbles smaller than it cannot be broken up by the underlying turbulence.

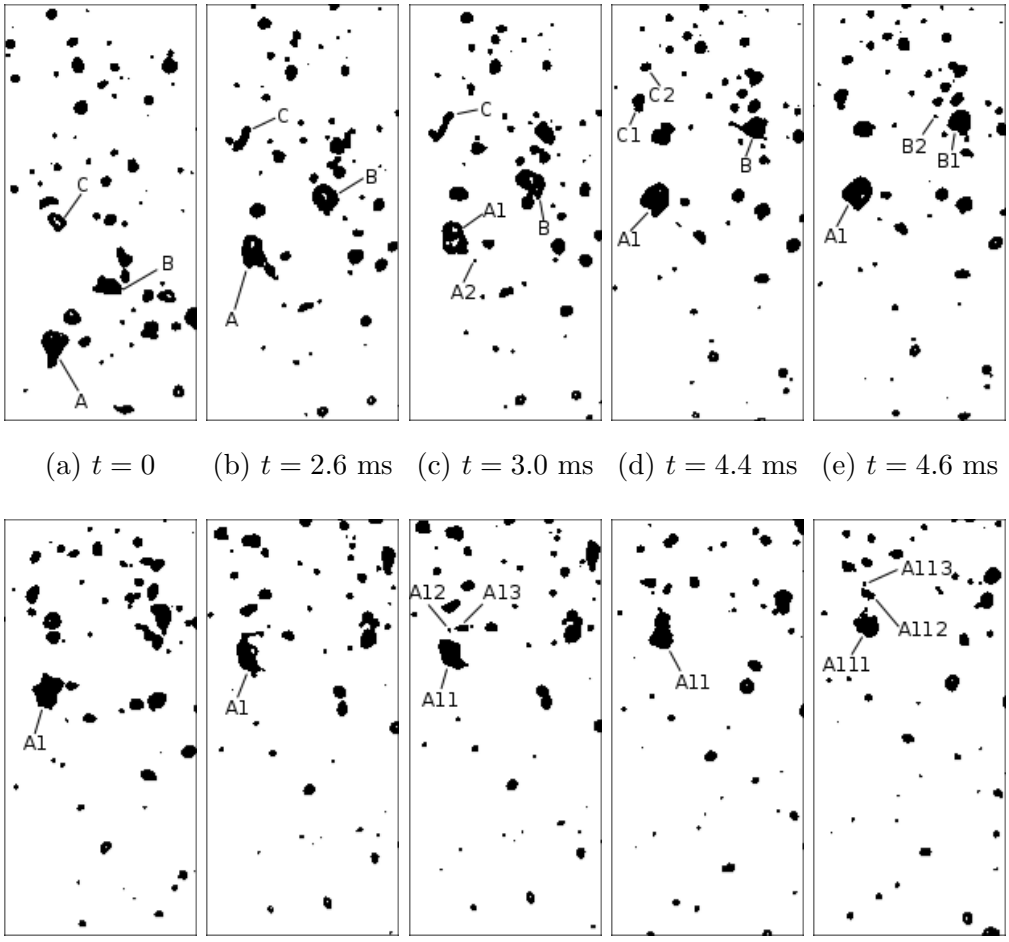

(a) $t = 0$ (b) $t = 2.6$ ms (c) $t = 3.0$ ms (d) $t = 4.4$ ms (e) $t = 4.6$ ms

(f) $t = 5.2$ ms (g) $t = 7.2$ ms (h) $t = 7.4$ ms (i) $t = 8.6$ ms (j) $t = 9.4$ ms

Figure 6.19: A visualization of a sequence of bubble breakups. $Re = 60000$ and $Q_b = 42$ mL/min. Needle positioned at $z/d_j = 15$.

Chapter 7

BREAKUP OF VISCOUS PARTICLES: PARTICLE SIZE ANALYSIS

The studies of the breakup of air bubbles allowed us to learn how different physical parameters affect the breakup mechanism. In this chapter, we will explore the effect of different dispersed phase fluid properties. Specifically, we will investigate the particle size results from the breakup of different viscous oils and oils with surfactant.

All experiments with the viscous dispersed phase fluids (discussed in this chapter and the next) were performed with the particle injection needle positioned at $z/d_j = 20$. The field of view is a combination of two imaging positions capturing a range from $z/d_j = 28$ to 48. This lower end of the field of view was chosen to allow sufficient distance for the particles to be entrained toward the centerline and ensure particles are sufficiently dispersed to minimize particle overlapping. Also, all breakup events were completed by the time they reach the upper end of the field of view. As mentioned in Chapter 3, the image sequences used for the size distribution analysis were caputured at 60 fps to ensure independent statistics between frames for each zone.

7.1 Dispersed phase fluid properties

The dispersed phase density and viscosity, along with the interfacial tension between the jet fluid and the dispersed phase fluids are the important properties in this multiphase flow problem. Four different base fluids were selected in this study. These fluids were selected to cover viscosity ranging from 10 cSt to 200 cSt. The base fluids were mixed with the Triton X-100 surfactant to alter the interfacial tension between the dispersed phase and the jet fluids. Three different concentrations of Triton X-100 were chosen: 0, 100 and 1000 ppm.

A total of 10 dispersed phase fluids were used in the experiments. A summary of all the dispersed phase fluid properties is shown in Table 7.1.

The density and viscosity of the laboratory grade silicone oils used in this study were given by the manufacturer (Sigma-Aldrich, measured at 25 °C). The density of the canola oil were measured by a pycnometer. The viscosity of canola oil was measured using a rotary viscometer (NDJ-5S). The interfacial tension values between the dispersed phase fluid and water were measured using the pendant drop method. In this method, a liquid drop is injected into another liquid medium. The heavier liquid was chosen to be the drop to avoid any buoyancy effect that could alter the shape of the drop. An image of the drop was taken once the drop was injected in the liquid medium and formed a pendant drop shape (i.e. just before it detached from the needle). The interfacial tension between the two liquids was determined by fitting the curvature of the drop to the Young-Laplace equation [21].

	Fluid	Set	ρ_p $[kg/m^3]$	μ_p $[kg/(m\ s)]$	σ $[10^{-3}N/m]$
0 ppm X-100	Canola oil	1A	916	0.0488	23.81
	10 cSt silicone oil	1B	930	0.0093	25.29
	100 cSt silicone oil	1C	1060	0.106	26.80
	200 cSt silicone oil	1D	1050	0.21	34.13
100 ppm X-100	Canola oil	2A	916	0.0488	15.23
	10 cSt silicone oil	2B	930	0.0093	17.23
	100 cSt silicone oil	2C	1060	0.106	18.53
1000 ppm X-100	Canola oil	3A	916	0.0488	6.65
	10 cSt silicone oil	3B	930	0.0093	8.80
	100 cSt silicone oil	3C	1060	0.106	9.15

Table 7.1: Properties of the dispersed phase fluids. All properties were measured at $25°C$.

7.2 Dimensionless quantity

With a wide array of fluid properties, dimensionless quantities are the ideal tools to compare the relative importance of different properties between experimental sets. Dimensional analysis reveals five dimensionless numbers that are important to the particle breakup problem. They are density ratio, viscosity ratio, the jet Reynolds number, the Weber number, and the Ohnesorge number.

$$Re = \frac{\rho_j U_j d_j}{\mu_j} \tag{7.1}$$

$$We_t = \frac{2\rho_j(\epsilon d_p)^{2/3} d_p}{\sigma} \tag{7.2}$$

$$Oh_p = \frac{\mu_p}{(\rho_p \sigma d_p)^{1/2}} \tag{7.3}$$

The Reynolds number is defined using the jet liquid properties and the jet exit velocity. It is the only dimensionless number needed to described the jet regardless whether the dispersed phase is present. Each dispersed phase fluid was tested in three different jets with Reynolds number of 45000, 60000 and 80000. The combination of different jets and fluid properties resulted in a total of 30 experiments. Both the Weber number and the Ohnesorge number take the dispersed phase fluid into consideration. The characteristic velocity in the Weber number was taken as the mean turbulent velocity fluctuation, $2(\epsilon d_p)^{1/3}$, because it is the main driving force of turbulent breakup. $d_p = 1.19\ mm$ is the inner diameter of the 16 gauge needle used throughout all oil based dispersed phase experiment. It was chosen as the length scale in the Weber and Ohnesorge numbers to represent the initial particle size. The turbulent dissipation, ϵ, was taken as the centerline turbulent dissipation at the needle exit. The Ohnesorge number is defined using the dispersed phase viscosity and density as it provides the relative importance between the internal viscous effect and the surface tension effect. Table 7.2 shows the dimensionless numbers for each experimental set.

Set	μ_p/μ_j	ρ_p/ρ_j	Oh_p	We_t ($Re = 45000$)	We_t ($Re = 60000$)	We_t ($Re = 80000$)
1A	54.2	0.919	0.303	30.0	54.7	97.3
1B	10.3	0.933	0.056	28.3	51.5	91.6
1C	117.8	1.063	0.577	26.7	48.6	86.4
1D	233.3	1.053	1.017	20.9	38.2	67.9
2A	54.2	0.919	0.379	46.9	85.6	152.0
2B	10.3	0.933	0.067	41.5	75.6	134.4
2C	117.8	1.063	0.693	38.6	70.3	125.0
3A	54.2	0.919	0.573	107.5	195.9	348.3
3B	10.3	0.933	0.094	81.2	148.1	263.2
3C	117.8	1.063	0.987	78.2	142.5	253.3

Table 7.2: Dimensionlesss numbers for each experimental set.

7.3 Particle flux

The particle flux is defined as $N_p' U_o / L_w$, where N_p' is the number of particle per frame, U_o is the mean centerline velocity and L_w is the axial length of the interrogation zone. Figure 7.1 shows the evolution of the particle flux over axial distance for the four different base fluids. There is a drop off in the particle flux at both ends of the field of view on both the lower and the higher imaging locations. As we explained in Chapter 6, this is because of the lower light intensity at the edge of the image, which caused some smaller particles not being recognized due to low contrast. Comparing between different experimental sets, the higher dispersed phase fluid viscosity results in the lower particle flux. This is the initial evidence of the effect of viscosity on the breakup process.

In additional to the number of all the particles in the flow, it is also interesting to look into the number of ligaments (highly deformed particles) in the flow. In this case, we are going to identify all particles that has the circularity smaller than $\pi^2/(2(\pi+0.5)^2) \approx 0.372$ as

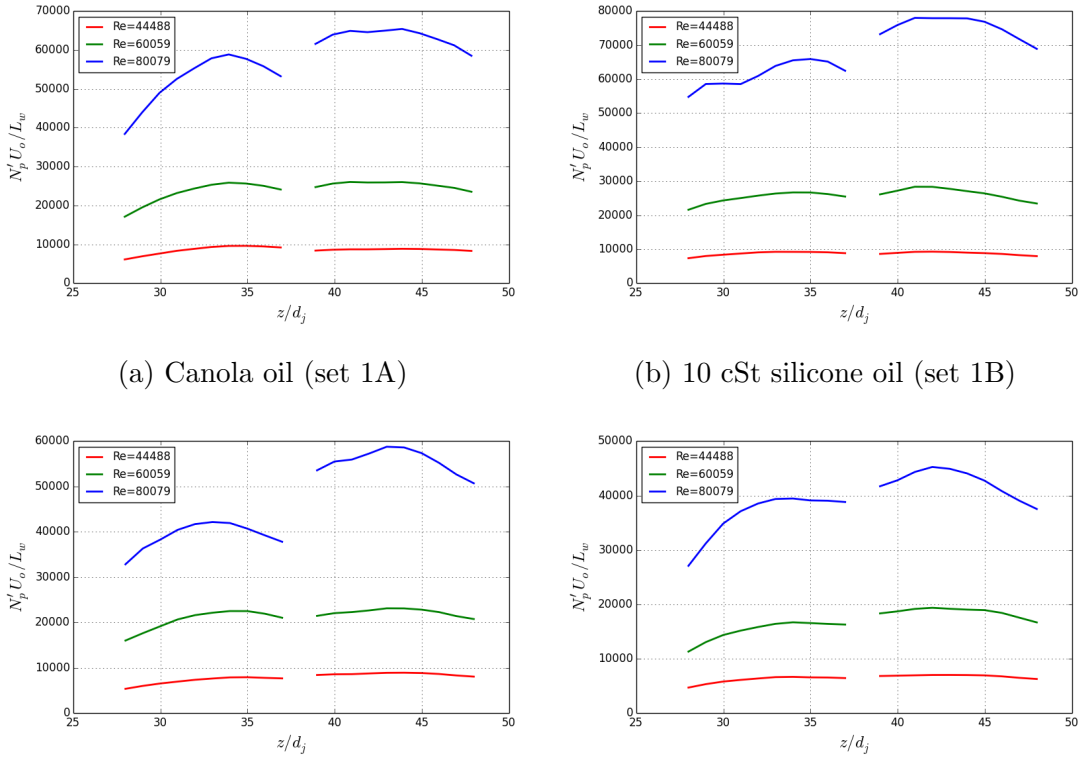

(a) Canola oil (set 1A)

(b) 10 cSt silicone oil (set 1B)

(c) 100 cSt silicone oil (set 1C)

(d) 200 cSt silicone oil (set 1D)

Figure 7.1: Particle flux over axial distance.

ligament. This is the same definition used to identify potential breakup path in the tracking algorithm (see Section 5.2.1). The ligament flux is obtained in the same way as the particle flux, i.e. $N_p' U_o / L_w$, where N_p' is now the number of ligament per image.

Figure 7.2 shows the evolution of the ligament flux over axial distance for the four base fluids. Aside the experimental set 1B, all experimental sets display a monotonic decaying trend. This means that as the ligaments got convected downstream, they disintegrated and formed smaller spherical particles. The low ligament flux at the end of the field of view suggests that the breakup was mostly completed, because highly deformed particle/ligament is a necessary stage for a breakup events.

The index of refraction of the 10 cSt silicone oil is very close to the index of refraction of

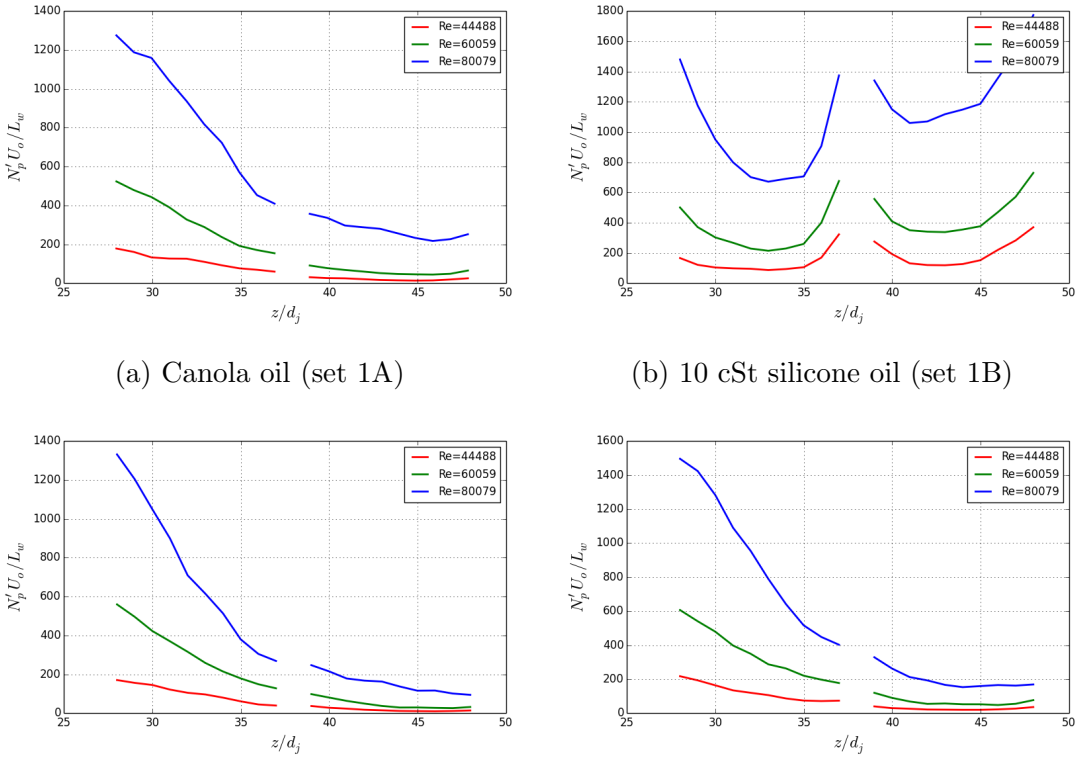

(a) Canola oil (set 1A)

(b) 10 cSt silicone oil (set 1B)

(c) 100 cSt silicone oil (set 1C)

(d) 200 cSt silicone oil (set 1D)

Figure 7.2: Ligament flux over axial distance.

water (1.403 vs 1.33), so light passes through the particle more easily than other sets. From the imaging stand point, this means that instead of capturing a dark shadow of the particle, there is a bright spot within the particle. Similar effect was observed in other dispersed phase fluids, but because of their higher index of refraction, the bright spot is often small compared to the shadow region. Thus, these bright spots were filled by the image processing algorithm during the thresholding process. If a particle is located at the edge of the image, the angle between the light source and the particle caused the bright spot to shift to the side of the particle. Combining this effect with the large bright spots found in of the 10 cSt silicone oil particles, it could result in some crescent shaped particles on the edge of the field of view (See Figure E.2 in Appendix E). The bright spots of these crescent shaped particles

cannot be filled with the image processing algorithm because there is no edge around it, so these particles would have a low circularity even though they are spherical. As a result, there is an artificial increase in ligament flux near both ends of the two fields of view for the experimental set 1B.

7.4 Evolution of the particle size of viscous dispersed phase fluid

Figures 7.3, 7.4 and 7.5 show the comparison of the evolution of the size distribution over axial distance between three Reynolds numbers. For this comparison, the base fluid was chosen to be canola oil (set 1A). The initial size distribution is broad with 80% of dispersed phase volume consists of particle diameter within 2.3, 2.0 and 1.7 mm (known as D_{v80}) for Re = 45000, 60000 and 80000, respectively. As the axial distance increases, the size distributions shift aggressively towards smaller size for z/d_j below 36. However, the change in size distributions slow down significantly afterward. Eventually, they become almost indistinguishable at high axial distances, which are known as the frozen state size distribution. At the frozen state, D_{v80} = 1.3, 0.8 and 0.6 mm for the three Reynolds number cases.

The evolution of the size distribution over axial distance of the other three base fluids (sets 1B, 1C and 1D) are shown in Figures 7.6, 7.7, 7.8. Only the medium Reynolds number case is shown for each of the base fluid. The general trend of the evolution of the size distribution is the same for all base fluids. The major difference is the particle size. For the frozen state size distribution, D_{v80} is approximately 0.8, 0.7, 1.1 and 1.3 mm for sets 1A, 1B, 1C and 1D, respectively. The increase of the particle size is consistent with the increase of the dispersed phase viscosity.

Using the characteristic diameter, D_{32}, to represent the entire size distribution at each axial distance allows us to have a direct comparison of multiple experimental sets. Figure 7.9 shows the comparison of the evolution of D_{32} over axial distance for the four base fluids. By holding Ohnesorge number constant (same symbol plots), D_{32} decreases with the increase of Weber number. On the other hand, if we keep the Weber number near constant (same color plots), D_{32} increases with the increase of Ohnesorge number. These trends show how

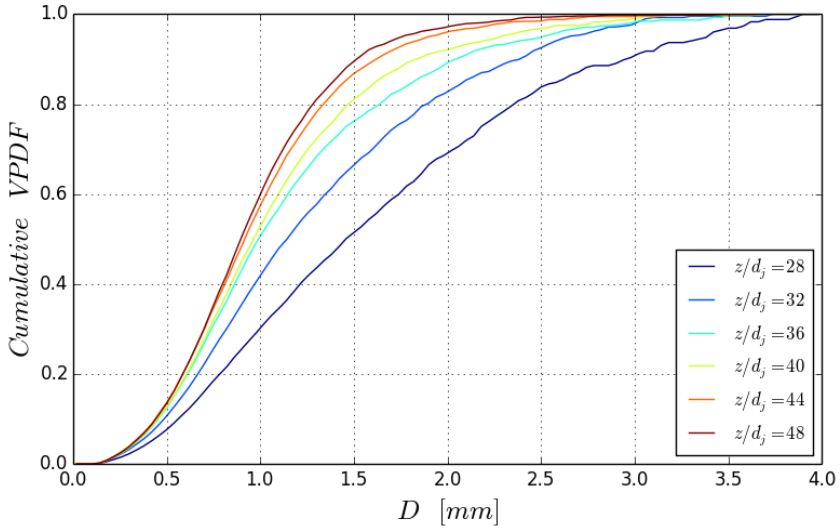

Figure 7.3: The evolution of the size distribution (CVPDF) of set 1A (canola oil). Re = 45000.

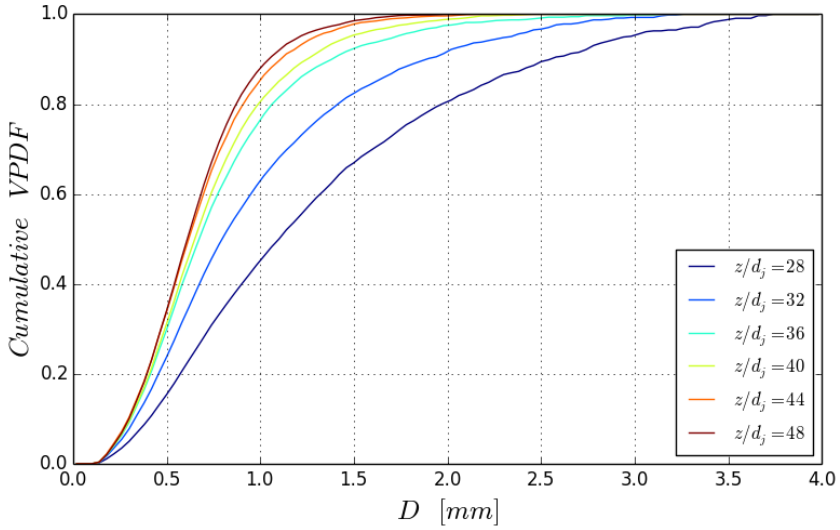

Figure 7.4: The evolution of the size distribution (CVPDF) of set 1A (canola oil). Re = 60000.

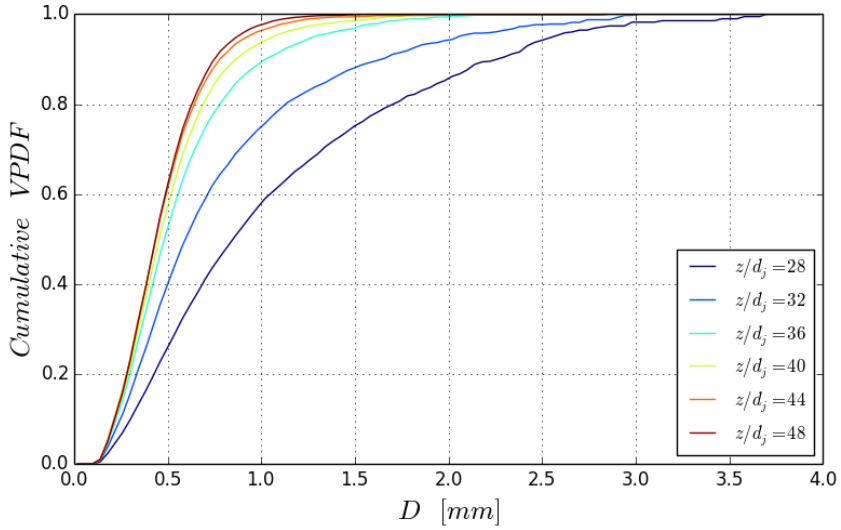

Figure 7.5: The evolution of the size distribution (CVPDF) of set 1A (canola oil). Re = 80000.

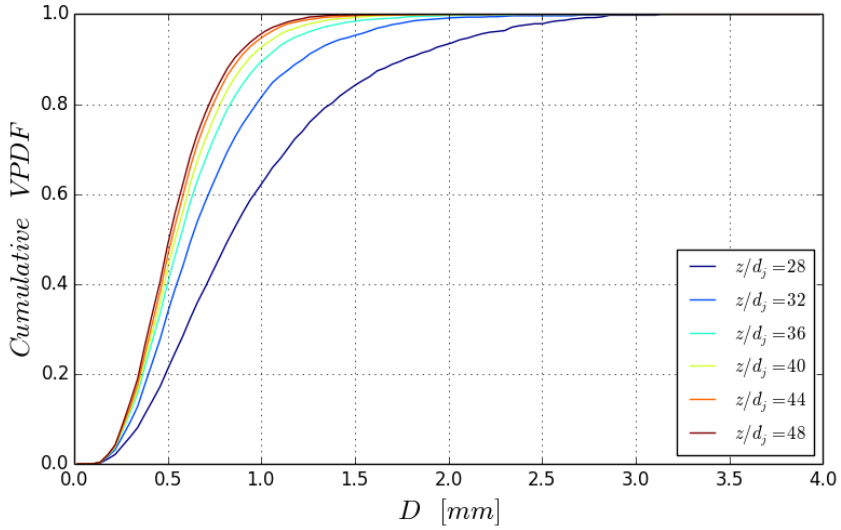

Figure 7.6: The evolution of the size distribution (CVPDF) of set 1B (10 cSt silicone oil). Re = 60000.

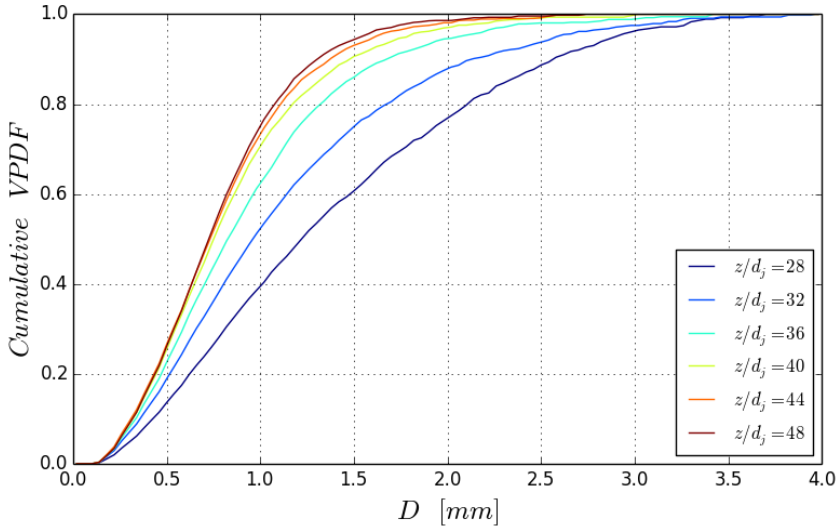

Figure 7.7: The evolution of the size distribution (CVPDF) of set 1C (100 cSt silicone oil). $Re = 60000$.

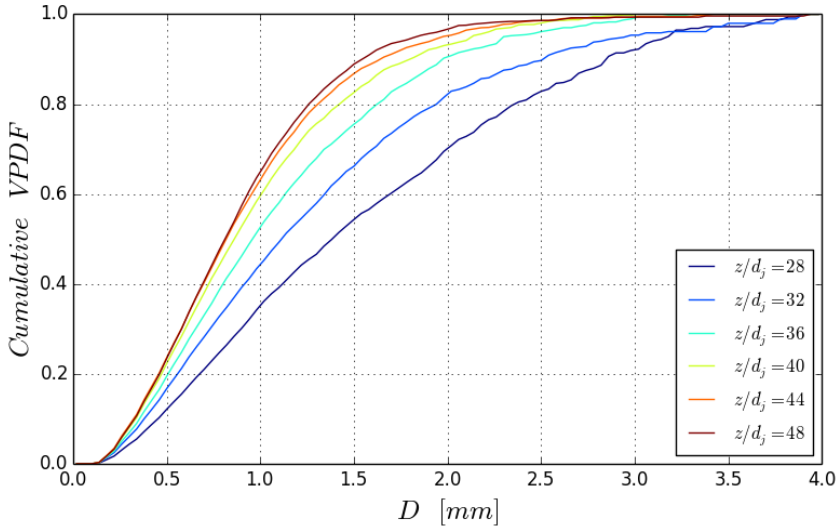

Figure 7.8: The evolution of the size distribution (CVPDF) of set 1D (200 cSt silicone oil). $Re = 60000$.

the disruptive and confinement effects influence the breakup process. Weber number shows the importance of the turbulent velocity fluctuation over the surface tension effect, so a high Weber number indicates a stronger disruptive effect, which leads to more breakup events. Ohnesorge number shows the relative importance of the two confinement effects: viscous damping and surface tension. Because the surface tensions of the four base fluids are similar, the Ohnesorge number becomes the indication of the viscous effect. The viscosity of the dispersed phase damped the internal fluid motion, so more energy is required to deform a particle. Thus, it reduces the number of breakup events for high viscosity fluid, which results in larger particle size.

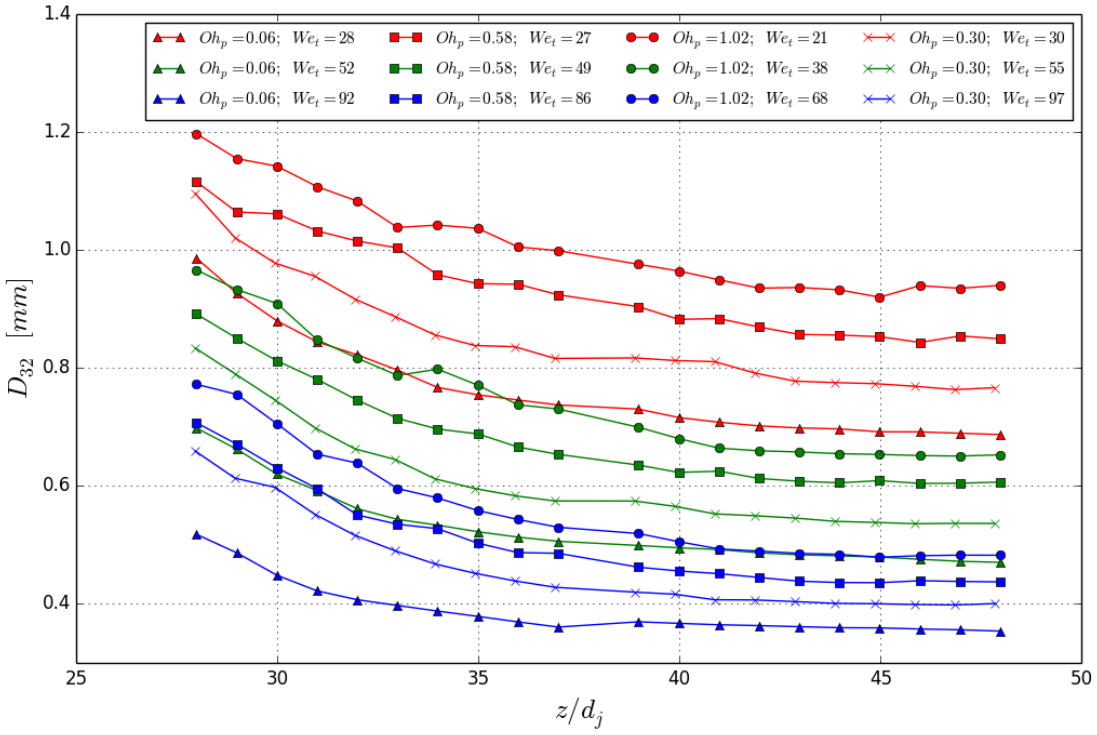

Figure 7.9: Comparison of the evolution of D_{32} for sets 1A, 1B, 1C and 1D. Re = 45000 (red), Re = 60000 (green) and Re = 80000 (blue).

7.5 Comparison to an existing model

We compared the experimental size distributions with the predictions from the population balance equation using the breakup frequency and daughter particle size distribution models derived by Martínez-Bazán et al. [39, 40]. The application of the model was described in Section 6.7. The initial condition of the size distribution, $n(D_o)$, was taken at $z/d_j = 32$. Figure 7.10 shows the comparisons between the experimental results and the model predictions for the four base dispersed phase fluids. In these comparisons, only the medium Reynolds number case ($Re = 60000$) is shown for each base fluids.

We have seen from Chapter 6 that the predictions from the model agreed well with the experimental data of the breakup of inviscid particles, especially for the frozen state size distribution. This is not the case for the breakup of oil drops as the predictions do not agree well with the experimental data. However, the differences between the predictions and the data are narrower for the lower viscosity cases. Specifically, the prediction for the 10 cSt silicone oil size distribution is relatively good compared to the other base fluids. Recall that Martínez-Bazán's model assumes that the dispersed phase viscosity is negligible. This hinted that the lower viscosity cases are approaching the regime of inviscid breakup. In the high viscosity cases, the model predicts more finer particles and less larger particles. The discrepancy indicates that the viscous effect and/or some additional mechanisms have to be incorporated in the model.

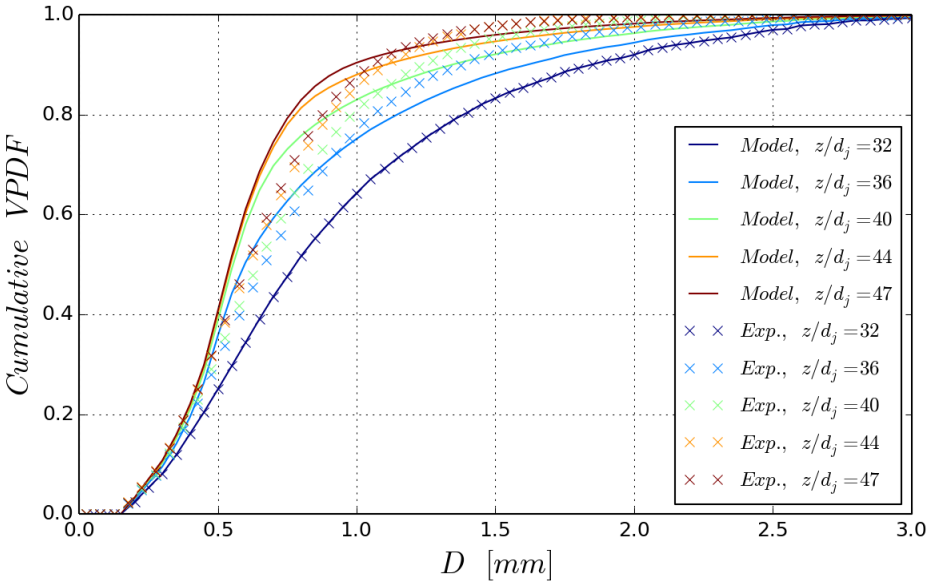

(a) Canola oil (set 1A)

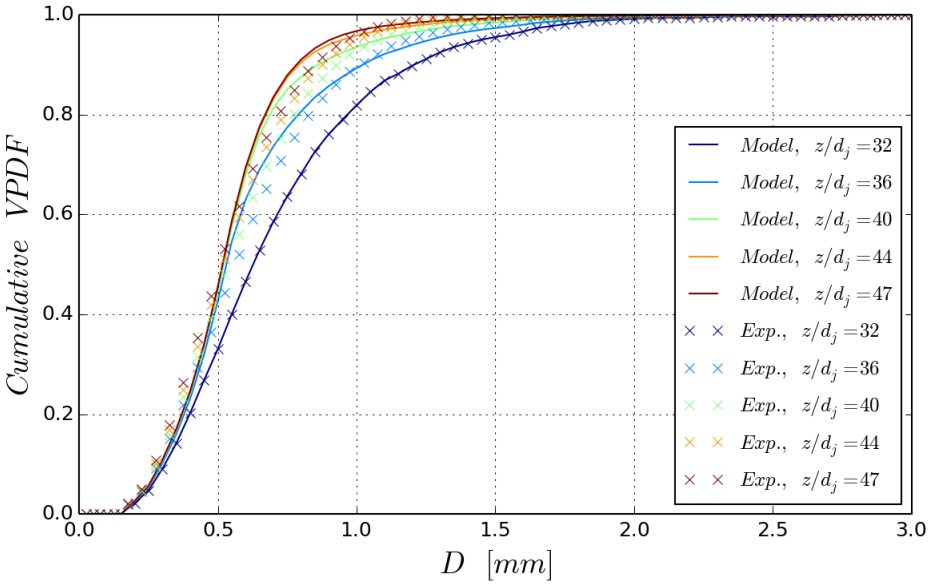

(b) 10 cSt silicone oil (set 1B)

Figure 7.10: A comparison of the CVPDF between the model and the experimental data for sets 1A, 1B, 1C and 1D. $Re = 60000$.

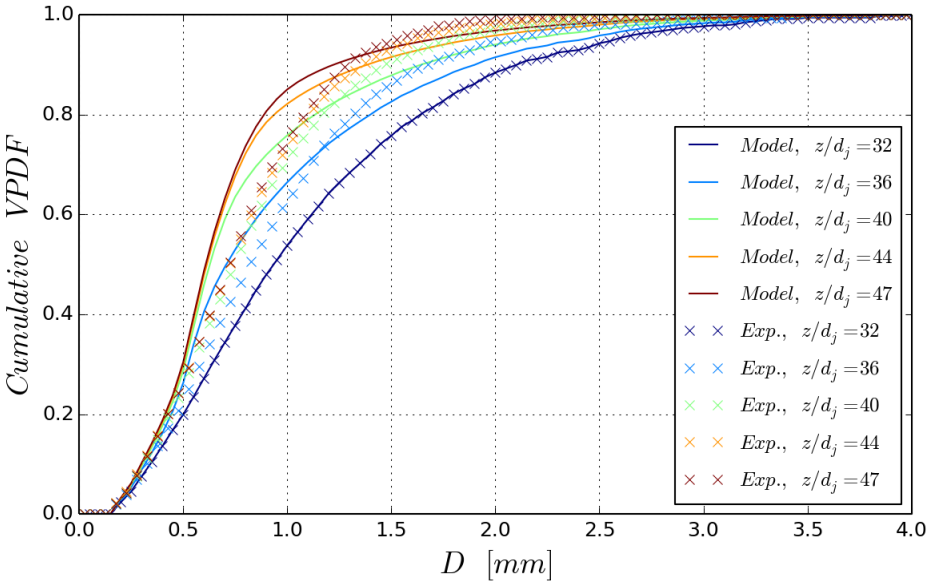

(c) 100 cSt silicone oil (set 1C)

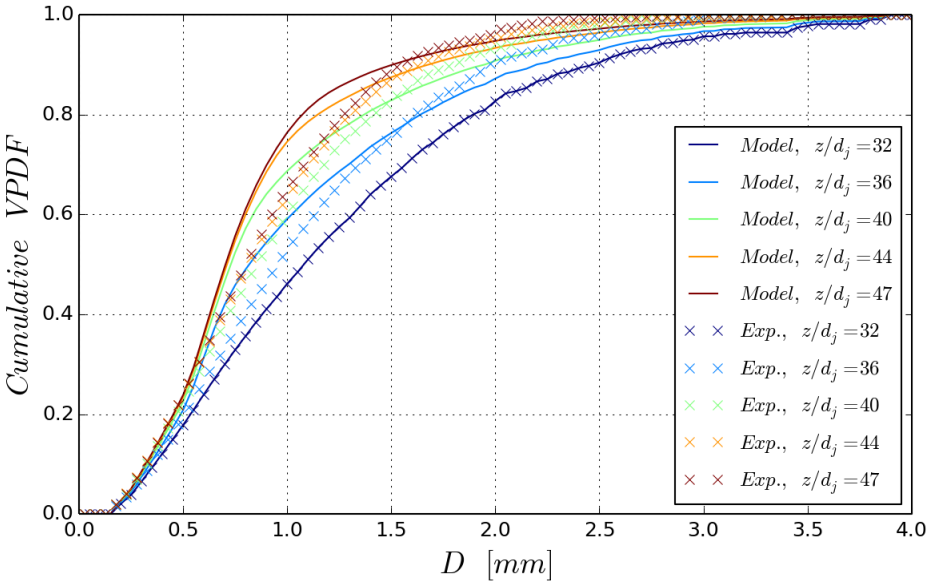

(d) 200 cSt silicone oil (set 1D)

Figure 7.10 (Continued): A comparison of the CVPDF between the model and the experimental data for sets 1A, 1B, 1C and 1D. $Re = 60000$.

7.6 Frozen state particle size of viscous dispersed phase fluid

The comparison of the frozen state CVPDFs for the four base fluids is shown in Figure 7.11, 7.12 and 7.13. Again, the difference in Oh_p of the four sets is mostly due to the difference in viscosity. So, these figures show that the higher the dispersed phase viscosity is, the broader the size distribution will be.

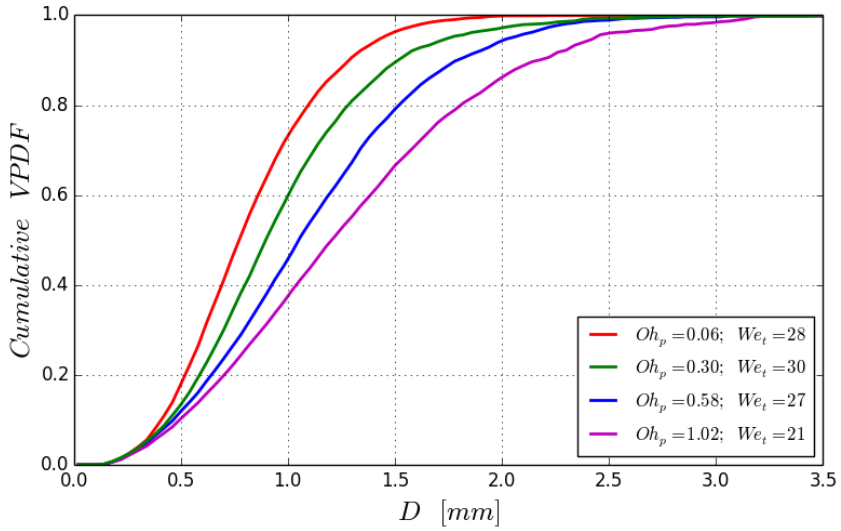

Figure 7.11: A comparison of the frozen state CVPDF for sets 1A, 1B, 1C and 1D. Re = 45000.

In the early studies of the particle breakup in liquid-liquid stirred tank systems [42, 41], the average equilibrium particle size were predicted using a semi-empirical Weber number scaling model. In this model, the particle size is proportional to the Weber number to the power of $-3/5$ (Equation (7.4)). Since the breakup process in these stirred tank system follows the Kolmogorov-Hinze theory [10], this model could potentially be applied in our turbulent jet experiment.

$$\frac{D_{32}}{L} \propto We^{-3/5} \tag{7.4}$$

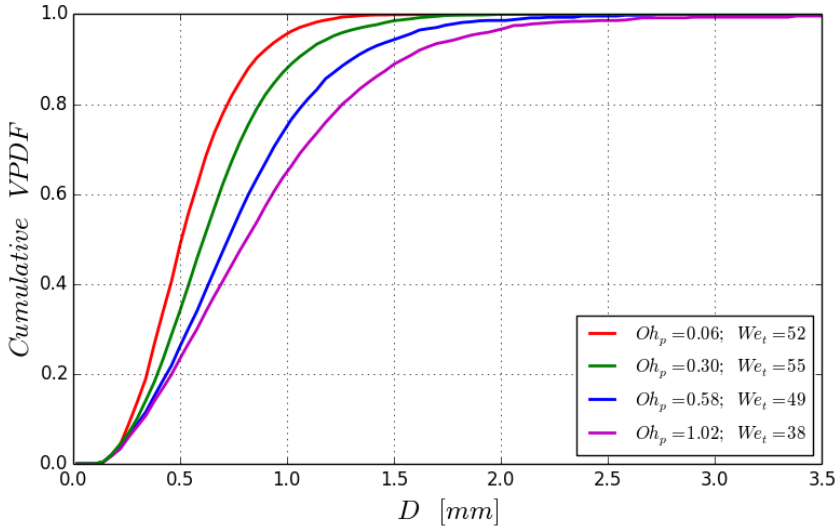

Figure 7.12: A comparison of the frozen state CVPDF for sets 1A, 1B, 1C and 1D. Re = 60000.

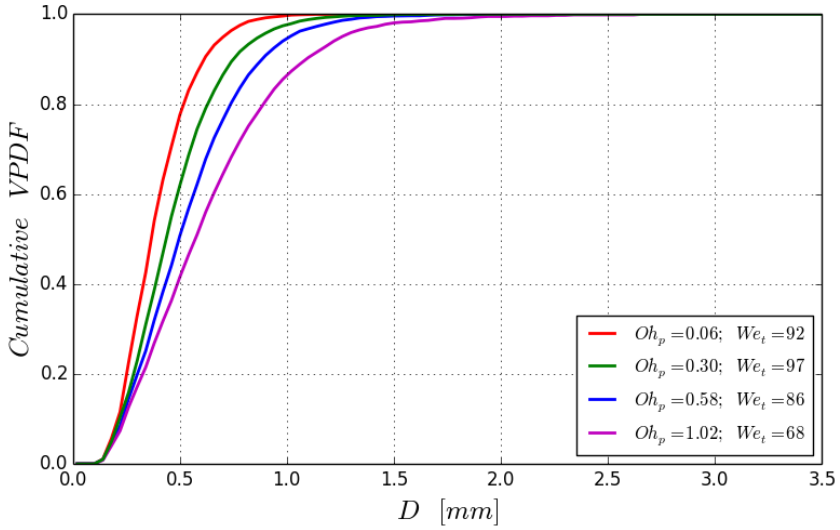

Figure 7.13: A comparison of the frozen state CVPDF for sets 1A, 1B, 1C and 1D. Re = 80000.

where L is a characteristic length scale in the problem.

Figure 7.14 shows the relationship of the normalized frozen state D_{32} and $We_t^{-3/5}$. The data collapsed together for experimental sets 1A to 1D, which display a wide range of viscosity. This is surprising because We_t does not consider the effect of viscous stress. It represents the ratio between the external turbulent stress and the surface restoring pressure. The linear trend suggests that the Weber number scaling model is valid and that the frozen state particle size depends mostly on the surface tension. The exceptions are the three data points in red, which are slightly shifted below other experiments. These data points represent data from 10 cSt silicone oil (set 1B). Notice that Oh_p for set 1B is an order of magnitude less than the other three sets. In comparison, the second lowest Oh_p (set 1A) is only about 1/3 of the highest Oh_p (set 1D). Since Oh_p is the ratio of viscous and surface tension effects, the difference between set 1B and others indicates that the relative importance of the two effects could be crucial in predicting the particle size. This implies that the Weber number scaling model does not fully capture the physics of the breakup process.

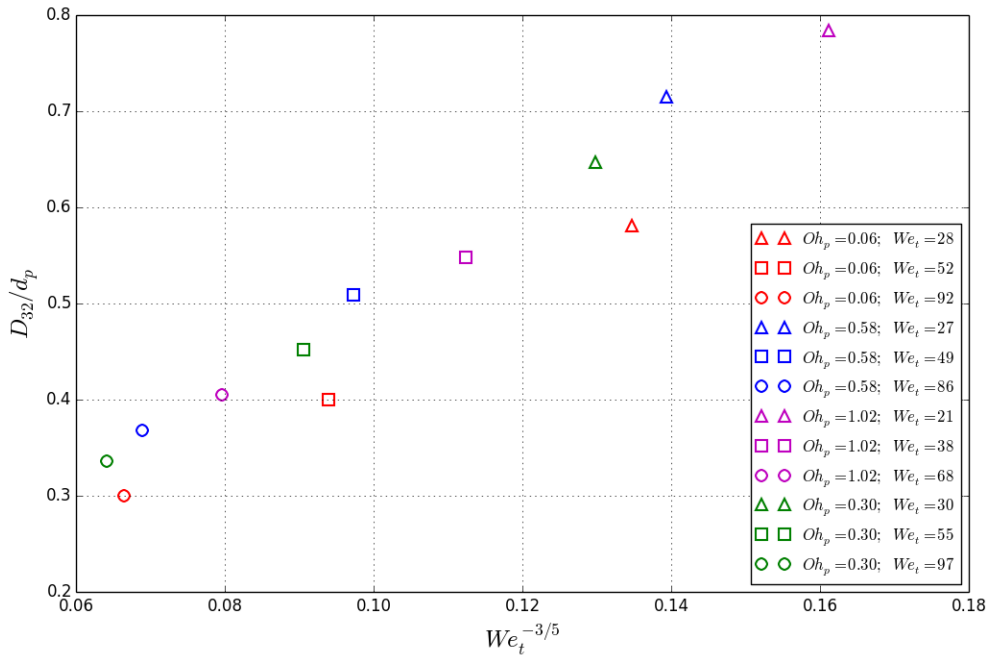

Figure 7.14: Weber number scaling of the frozen state D_{32} for sets 1A, 1B, 1C and 1D.

7.7 Effect of surfactant on particle size

So far, we have been studying the effect of viscosity through sets 1A to 1D. These four base fluids were intentionally chosen to have very different viscosity yet relatively similar surface tension with water. In this section, we explore the effect of surface tension by adding different concentrations of Triton X-100 to the base fluids (sets 2s and 3s).

The effect of surfactant on the particle size is shown in Figures 7.15 and 7.16. There are two ways to increase the Weber number. The first way is to increase the turbulent intensity (through the increase of turbulent dissipation term). Another way to increase the Weber number is to reduce the surface tension. If we focus on the frozen state size distribution for the canola oil case. Between the solid red line and the solid blue line, the Weber number increases by a factor of about 3 through the increase in turbulent intensity.

There is also an approximate 3 times increase in the Weber number from the solid red line (no surfactant) to the dotted red line (1000 ppm Triton X-100). However, the solid blue line represents a much smaller size distribution than the dotted red line. This is because by reducing the surface tension, the Ohnesorge number increases due to the increase of the relative importance between the viscous to surface tension effect. Thus, with roughly the same amount of increase in Weber number, the higher Ohnesorge number case results in larger particle size.

Another observation is the reduction of the effectiveness of surfactant in the higher Reynolds number cases. For example, the gap between the solid blue line and the dotted blue line (blue group) is smaller than the gap between the solid red line and the dotted red line (red group). Interestingly, both the red group and the blue group have an increase in Weber number and Ohnesorge number by the roughly the same factor. The only difference is that the Weber number in the blue group is higher. This indicates that the reduction in particle size due to the effect of surfactant is approaching an asymptotic behavior at higher Weber number. Finally, we observed that the effect of surfactant is further reduced in the 100 cSt silicone oil experiments because the Ohnesorge number is higher in these experiments.

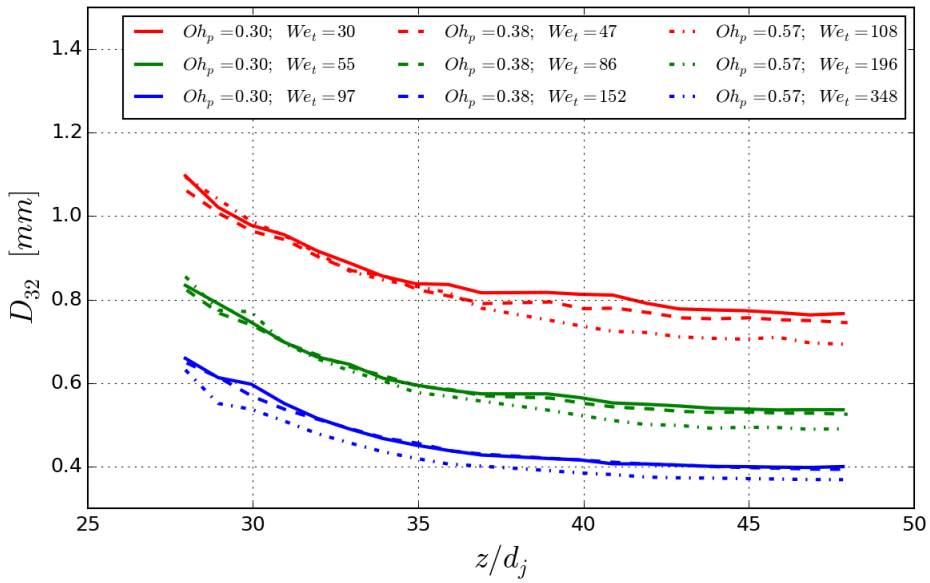

(a) Evolution of D_{32}

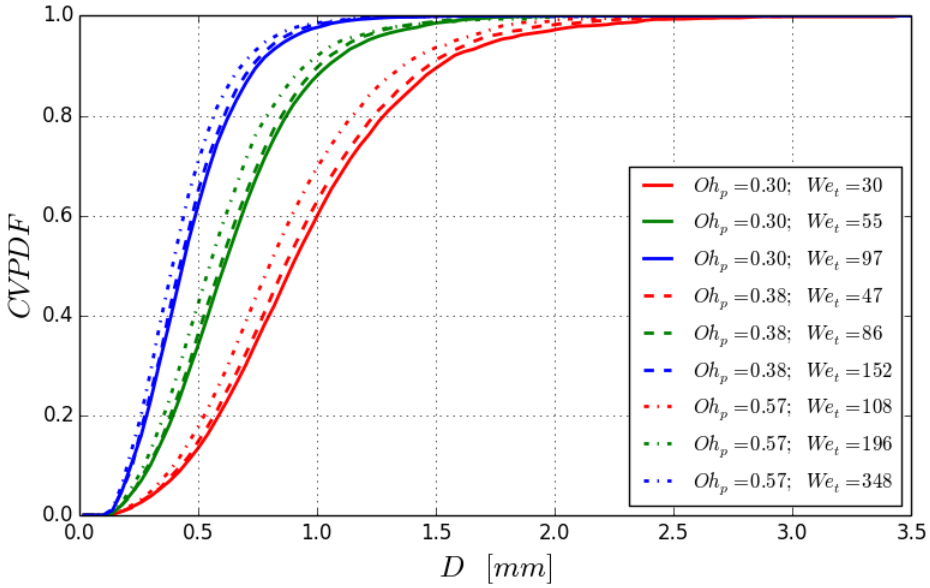

(b) Frozen state CVPDF

Figure 7.15: A comparison of the particle size with different concentration of Triton X-100 in canola oil. Set 1A (solid line), set 2A (dashed line) and set 3A (dotted line). $Re = 45000$ (red), $Re = 60000$ (green) and $Re = 80000$ (blue).

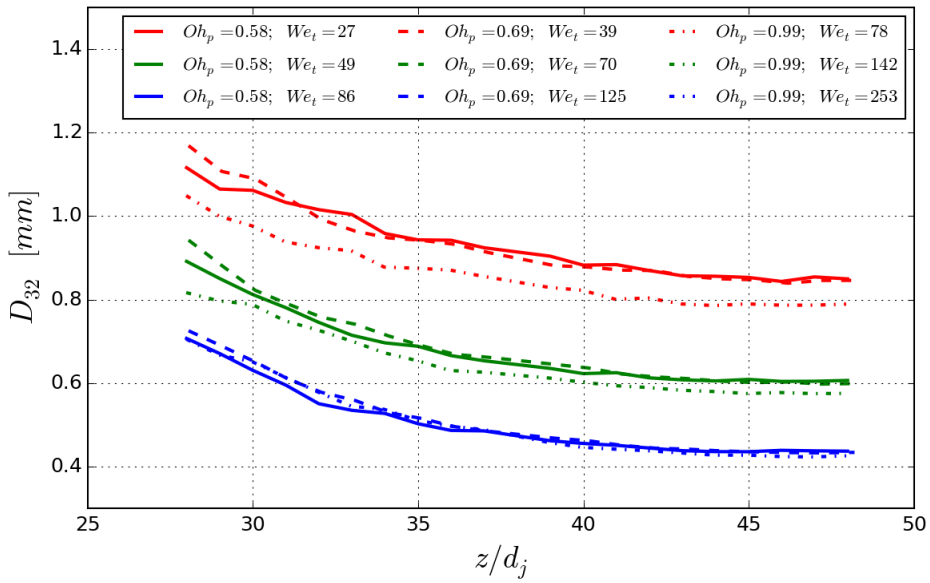

(a) Evolution of D_{32}

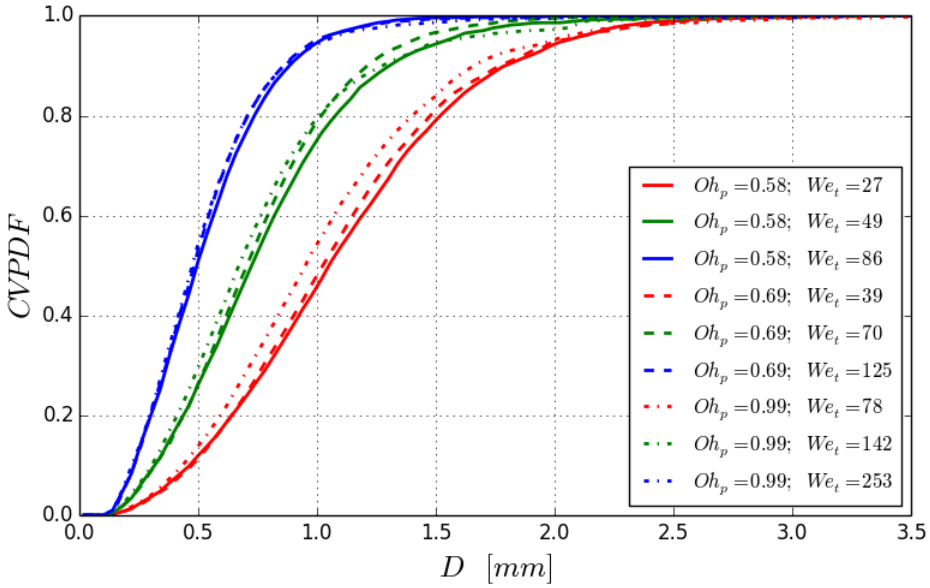

(b) Frozen state CVPDF

Figure 7.16: A comparison of the particle size with different concentration of Triton X-100 in 100 cSt silicone oil. Set 1C (solid line), set 2C (dashed line) and set 3C (dotted line). $Re = 45000$ (red), $Re = 60000$ (green) and $Re = 80000$ (blue).

We applied the Weber number scaling model to the experimental sets with and without the added surfactant (Figure 7.17). At the first glance, there is no obvious trend with the inclusion of the surfactant experiments. The open symbols are the data set for the four base fluids, which are already shown in Figure 7.14. In the discussion from last section, we were surprised by the results because the base fluids differs mostly by viscosity and We_t does not consider such effect. Based on the limited data in our last analysis, we concluded that the Weber number scaling model is valid, with the exception of the 10 cSt silicone data (red open symbols). If we assume that the Weber number scaling model is valid for the open symbol (0 ppm X-100) linear trend, then the half filled symbol trend (100 ppm X-100) and solid symbol (1000 ppm X-100) should collapse on the open symbol trend because the only change is the reduction of surface tension, which is captured in We_t. However, this is not the case, so the linear trend we see for each surfactant concentration group (open, half filled and solid symbols) is not due to Weber number scaling.

On the other hand, by grouping the data by the same color (same base fluid) and the same symbol shape (same jet Reynolds number), we observed a different kind of linear trend (with a much shallower slope). Each of these groups has the same viscosity and flow field, the only difference is the surface tension (by changing the surfactant concentration). In each of these groups (with the exception of the red symbols, which we will explain later), not only does D_{32} increase with the decrease of We_t, but the slopes of these lines are also similar for different groups. Thus, the Weber number scaling is valid for each of the individual group, but it is obviously not a complete model as these lines (which have different viscosity and jet Reynolds number) do not collapse together. This calls for a new scaling model that includes both the viscous and surface tension effects.

Shifting our focus on the red symbols, we see a counter-intuitive trend: the set with no surfactant (open symbol) has a smaller particle size than the sets with surfactant. As mentioned before, the 10 cSt silicone oil has an index of refraction very close to water. Thus, a significant amount of light pass through the particle to form a big bright spot on the particle. For smaller particles, this could mean too much light passes through the particle

such that it cannot be captured by the camera. Sets 2B (red, half filled symbol) and 3B (red, solid symbol) should have the most smaller particles as they have the lowest viscosity and surface tension. Thus, our camera could have missed these smaller particles, resulting in larger D_{32} than the set 1B.

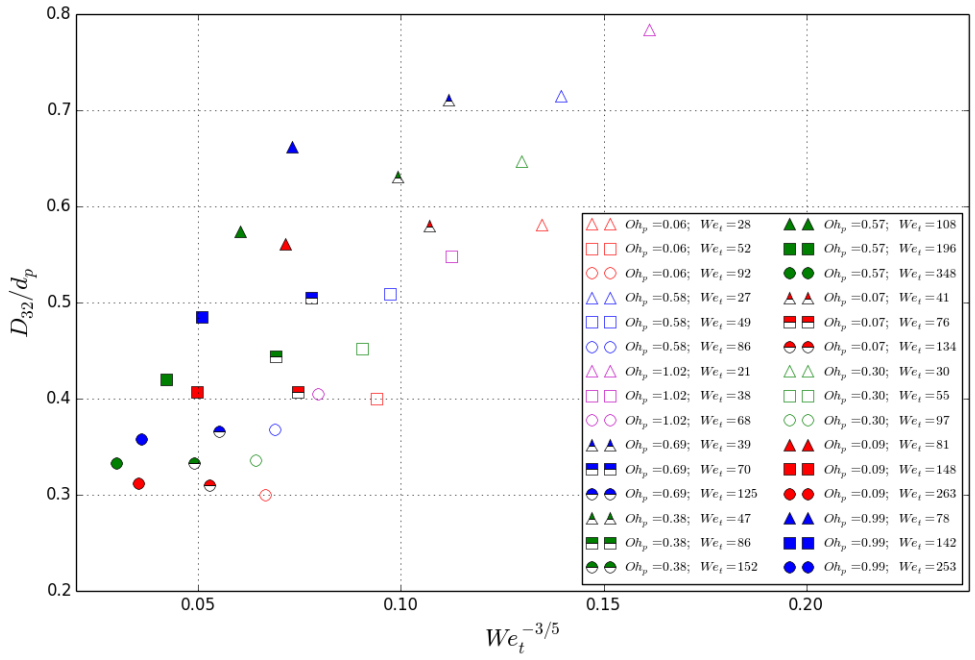

Figure 7.17: Weber number scaling of the frozen state D_{32}. 0 ppm (open symbol), 100 ppm (half filled symbol) and 1000 ppm (solid symbol)

7.8 Frozen state particle size prediction model

To understand the breakup mechanism of viscous particles, we begin with a dynamic approach using force balance. For a particle to break, the disruptive effect must overcome the confinement effect. Based on the Kolmogorov-Hinze theory, the disruptive effect is caused by the velocity fluctuation of the turbulent motion in the inertial subrange. Traditionally, only the surface restoration force is considered as the confinement effect. The viscous resistant of

the internal fluid flow is assumed to be negligible. However, in the case of viscous dispersed phase fluid, this resistant could be on the order of the surface restoration effect. Thus, the confinement effect should include both the surface restoration force and the internal viscous stress. Although both effects are considered the confinement effect, their roles in the breakup process are very different.

Because a sphere has the least surface area for a given volume, surface tension resists any deviation of the the particle shape in order to maintain the lowest surface energy. Internal viscous stress depends on the rate of the deformation. Typically, this means when there is an external force applying on the particle. So, the faster the deformation, the higher the internal shear stress, which slows down the deformation process. The effect of the internal viscous stress is movement dependent and the effect of the surface restoration pressure is size and shape dependent. In other words, if there is no external force applying on the particle, the internal viscous stress does not exist, but the effect of surface tension is always present to maintain the particle shape.

Assuming the particle size has the length scale in the inertial subrange, the disruptive stress can be modeled using the average turbulent velocity fluctuation based on the Komogorov-Hinze theory (Equation (7.5)).

$$\tau_t = \frac{1}{2}\rho_j \overline{\Delta u^2} \tag{7.5}$$

The square of the velocity fluctuation is a function of the turbulent dissipation rate and a length scale. It is obtained by integrating the energy spectrum over the size range less than the particle diameter because the eddies larger than the particle can only steer it. Only eddies with size equal or less than the particle could deform it. The result of the integration is expressed in Equation (7.6).

$$\overline{\Delta u^2} = C(\epsilon D)^{2/3} \tag{7.6}$$

Combining the two equations above, and using $C = 2$ [22], the turbulent stress can be

written as:

$$\tau_t = \rho_j(\epsilon D)^{2/3} \tag{7.7}$$

The internal viscous stress can be expressed as $\mu_p U_i/D$. The characteristic internal flow velocity, U_i, is caused by the external stress on the particle, so it can be written as $U_i \sim \sqrt{\tau_e/\rho_p}$ [22]. In this case, the external stress is τ_t. Combining these formulations, the internal viscous stress can be expressed in Equation 7.8. The other confinement effect, the surface restoration pressure, is given in Equation (7.9).

$$\tau_i \sim \mu_p \left(\frac{\rho_j}{\rho_p}\right)^{1/2} \epsilon^{1/3} D^{-2/3} \tag{7.8}$$

$$\tau_s \sim \frac{\sigma}{D} \tag{7.9}$$

The turbulent disruptive stress, the internal viscous stress and the surface restoration pressure are the only stresses acting on the particle. A balance of these stresses (Equation (7.10)) can be used to determine the critical diameter, which is the maximum stable diameter. The values given by Equation (7.8) and (7.9) are not exact, but they represent the order of magnitude for each effect. Nonetheless, we assume the addition of the two represents the confinement stresses for the following analysis.

$$\tau_t = \tau_i + \tau_s \tag{7.10}$$

The equation above can be rearranged to obtain Equation (7.11). This is an implicit equation of the critical diameter, D_c, that cannot be solved directly. Similar expression has been obtained by Calabrese et al. [10] using the energy balance approach.

$$D_c = \left(\frac{\mu_p D_c^{1/3}}{(\rho_j \rho_p)^{1/2} \epsilon^{1/3}} + \frac{\sigma}{\rho_j \epsilon^{2/3}}\right)^{3/5} \tag{7.11}$$

For inviscid dispersed phase fluid, the first term on the right side of the equation is small compared to the second term. This simplifies into an explicit equation of D_c. Dividing d_p on both sides of the equation, we obtain:

$$\frac{D_c}{d_p} = \left(\frac{\rho_j (\epsilon d_p)^{2/3} d_p}{\sigma} \right)^{-3/5} = We_t^{-3/5} \tag{7.12}$$

Assuming that the characteristic diameter of the particles, such as D_{32}, is proportional to the critical diameter (i.e. $D_{32} \propto D_c$), we see that the normalized D_{32} is proportional to the Weber number to the $-3/5$ power (Equation (7.12)). This is the same expression as in Equation (7.4).

On the other hand, if the viscous effect dominates the surface tension effect, the second term on the right hand side is negligible. Thus, Equation (7.11) reduces to Equation (7.13). The right hand side of the equation is in the form of a Reynolds number. However, this is different than the jet Reynolds number as the characteristics velocity is taken as the turbulent velocity fluctuation and the dispersed phase fluid properties are present. Figure 7.18 shows the relationship of the D_c (viscous effect dominated case) and the frozen state D_{32}.

$$\frac{D_{32}}{d_p} \propto \left(\frac{(\rho_j \rho_p)^{1/2} (\epsilon d_p)^{1/3} d_p}{\mu_p} \right)^{-3/4} \tag{7.13}$$

As we can see from Figures 7.17 and 7.18, isolating either the internal viscous effect and the surface restoring effect is not effective. Thus, it is necessary to solve Equation (7.11) for D_c using a numerical method. Figure 7.19 shows the relationship between D_c and D_{32}. Experiments with different jet Reynolds number are grouped by different color. Each group consists of all ten experimental sets. The ten experimental sets have a range of Ohnesorge number spans over two orders of magnitude (from 0.056 to 1.017). Even with a wide range of the relative importance of the surface tension and internal viscous effects, all ten sets collapse together for each Reynolds number group. Moreover, the three groups display a linear trend with similar slope.

Since we know the three groups are Reynolds number dependent, it is logical to scale

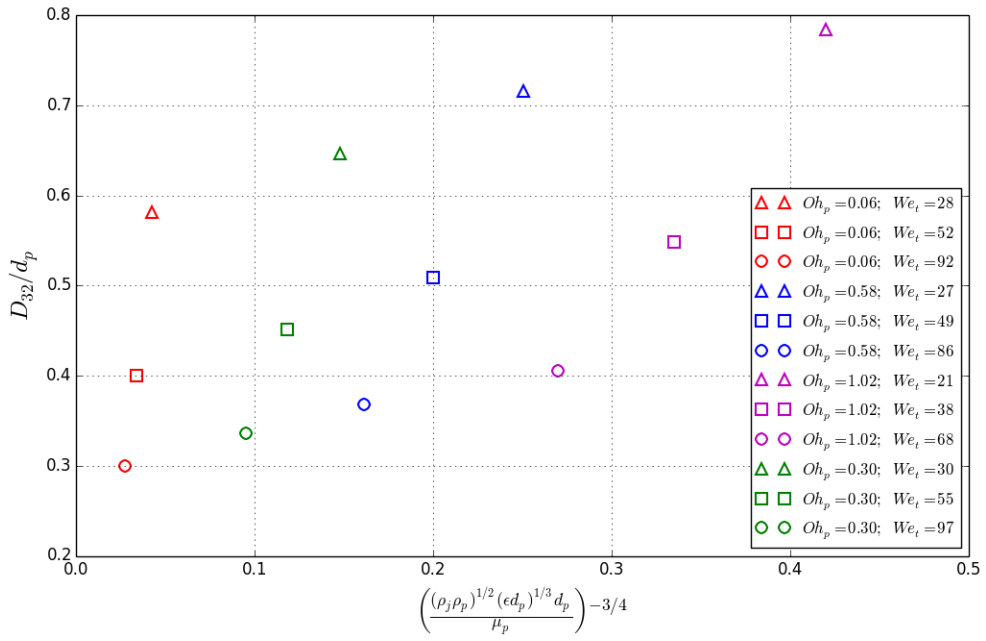

Figure 7.18: D_c (viscous effect dominated case) scaling of the frozen state D_{32} for sets 1A, 1B, 1C and 1D.

the critical diameter with the Reynolds number. We found that all data collapse together (Figure 7.20) with the addition of the Re^{-2} scaling (Equation (7.14)). There is a linear trend for lower value of $(D_c/d_p)Re^{-2}$ (< 2). The increase of D_{32} gradually slows down at high value of $(D_c/d_p)Re^{-2}$.

The formulation of D_c includes the disruptive turbulent stress, which is the source of the breakup process. The Reynolds number represents the inertial force of the jet as the jet viscosity is the same for all experiments. Thus, the addition of the Reynolds number scaling appears to be redundant. Recall that the disruptive turbulent stress is formulated based on the pressure fluctuation of eddies with the similar size as the particle, so it only captures the Kolmogorov-Hinze mechanism. The jet Reynolds number is defined using the jet exit velocity and the nozzle diameter. They represent the large scale motion contained in the jet.

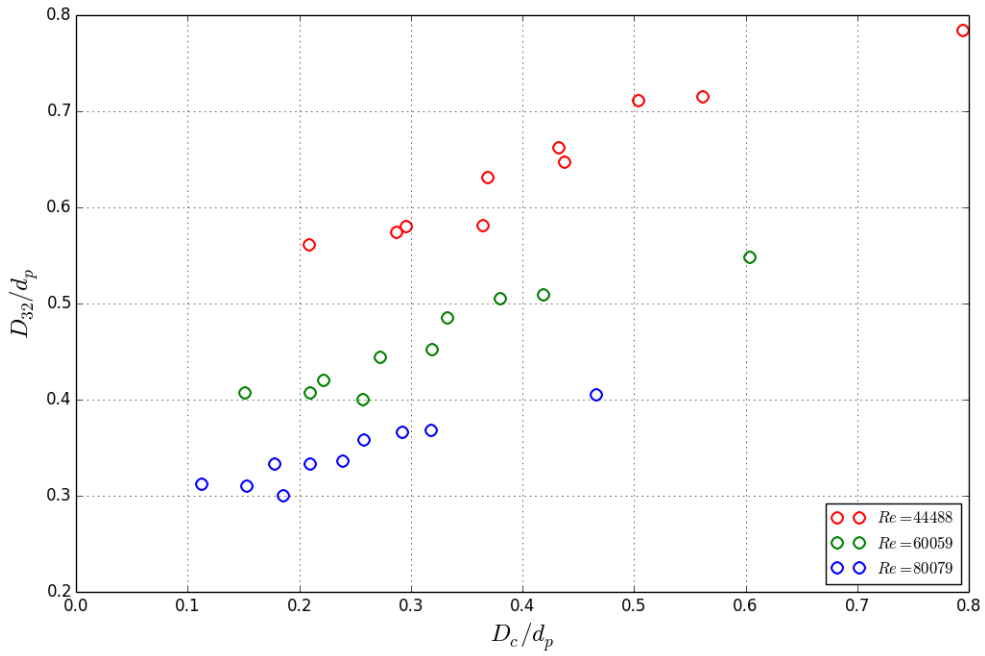

Figure 7.19: Prediction of the frozen state D_{32} using D_c for all 10 experimental sets.

The Kolmogorov-Hinze theory suggests that eddies larger than the particle size transport the particle but do not contribute to breakup. However, we observed viscous particles were stretched to multiple times its original size, the stretching mechanism cannot be caused by the eddies in the inertial subrange, so they must be caused by large scale motion in the jet. Therefore, the Kolmogorov-Hinze mechanism do not completely describe the breakup process. The jet Reynolds number scaling accounts for the integral scale motion that is responsible for the stretching of the ligament, which ultimately affect the resulting size of the breakup.

$$\frac{D_{32}}{d_p} \propto \frac{D_c}{d_p} Re^{-2} \tag{7.14}$$

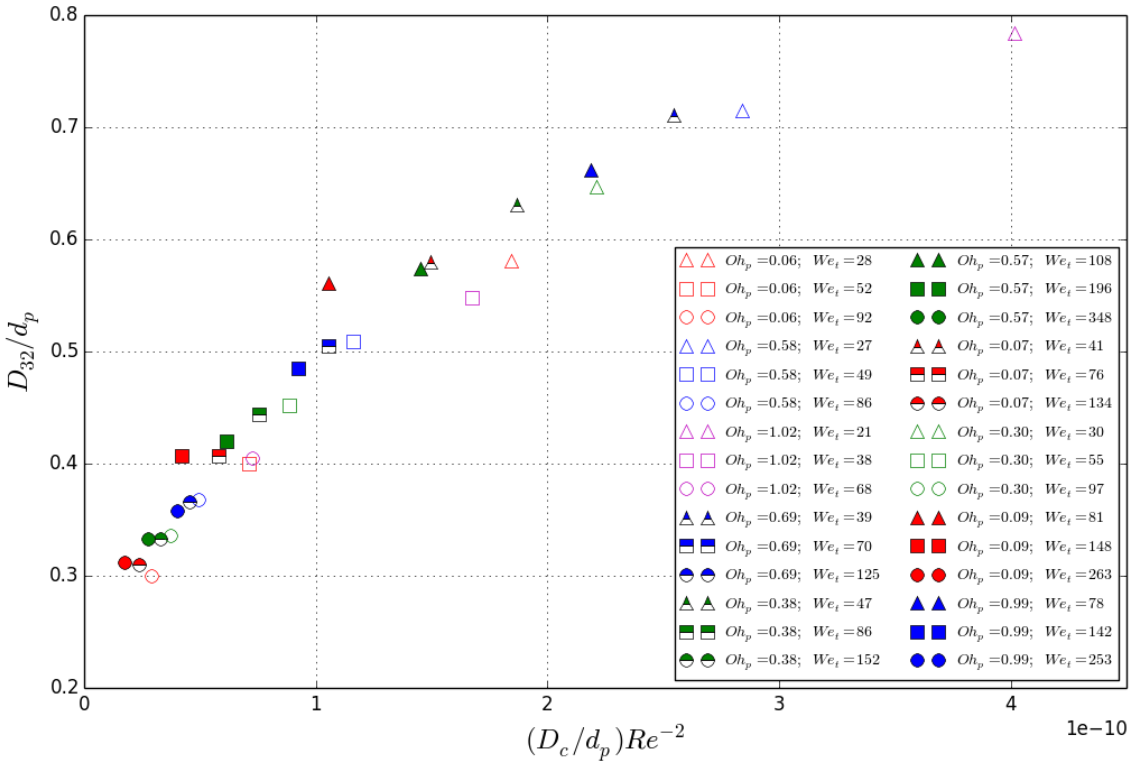

Figure 7.20: Prediction of the frozen state D_{32} using D_c with Reynolds number scaling for all 10 experimental sets.

Chapter 8

BREAKUP OF VISCOUS PARTICLES: BREAKUP EVENT ANALYSIS

Chapter 7 utilized a statistical analysis to study the particle sizes as a result of the breakup. The main focus was on the frozen state size distribution where the breakup events have been completed. In this chapter, we focus on the mechanism of the breakup. As shown by previous works discussed in Chapter 2, the breakup mechanism of particles in turbulent flow can be attributed to the Kolmogorov-Hinze theory. We have confirmed this in Chapter 6, by showing the prediction agrees with our experimental data for inviscid particle breakup. However, prediction from a previous model (Section 7.5) and qualitative observation (Section 8.1) suggested that additional mechanism are involved in the breakup of viscous particles.

Because of the different breakup mechanism, the closure functions, such as breakup frequency, used in the population balance equation have to be re-developed accordingly. To construct these functions, information of a particle at different stages of a breakup event is needed. For example, to estimate the time for a breakup event to occur, we need to track a particle from its undeformed state to the point of the breakup. In Chapter 7, the size distributions were obtained through time averaging using only static information (e.g. "snap shot" of particle size and shape). This is because the evolution of the size distribution from many breakup events is a steady state process. This explains why the images used in the size distribution analysis were recorded at a lower frame rate (60 fps). However, the breakup of an individual particle is a transient process. To analyze the mechanism of these breakup events, dynamic information of individual particles, such as the progression of the particle shape along its breakup path, is required. Therefore, high frame rate image sequences (5000 fps) were used to capture the entire sequence of the breakup events. The breakup paths were

identified using a new particle tracking algorithm specifically designed to track the unique nature of the viscous particles. The details of the algorithm is discussed in Chapter 5. Along the breakup path, important quantities of the particle and the surrounding flow are recorded. These quantities allowed us to perform a more in depth analysis on the individual breakup event.

The image sequence we captured for each experiment contains many breakup paths, so we analyzed all of them statistically. Each recorded breakup event is unique as they each have a unique combination of particle size, shape and surrounding flow condition, so individual breakup event cannot be reproduced. However, the statistical quantities of each experiment do not change between experiments. In essense, we are combining analysis of individual breakup events and statistical analysis of all events. Hence, the analysis shown in this chapter can be considered as a semi-deterministic approach.

8.1 Visualization of viscous particle breakup

To understand the breakup mechanism, we present a typical breakup sequence of viscous particles (Figure 8.1). In this case, it is the breakup of a canola oil drop in a turbulent jet with $Re = 60000$. The bottom of the frame was located at about $z/d_j = 31$ and the top of the frame was located at about $z/d_j = 40$.

The sequence began at $t = 0$ with a spherical particle with a diameter of about 1.1 mm. As the particle got convected downstream, the particle went through a couple cycles of deformation. Up until $t = 5.8$ ms, the degree of deformation on the particle was small, so the particle retained mostly spherical shape. At $t = 7$ ms, the deformation quickly transformed into a stretching process, which formed a long ligament. This elongation process is not observed in the breakup of air bubbles. As the stretching reached a certain point ($t = 9.8$ ms), thinning of the ligament occurred. Typically, the thinning occurs in the middle of the ligament, which forms a thin string. At the same time, significant amount of fluid accumulates at both ends of the string. The thinning process did not occur evenly along the ligament. As the ligament got stretched to a longer length, thinning occured faster in some locations along the ligament. This created multiple fluid accumulation points where small fluid lumps developed ($t = 13.0$ ms). At $t = 13.8$ ms, the strings connecting these fluid lumps became too thin and broke. This produced two large particles on both ends and multiple smaller particles along the string.

From this sequence, we notice distinct behaviors occurring at different period of time during the breakup process. Specifically, the entire breakup event can be divided into three stages. The first stage is the deformation stage. Particles in the deformation stage behave similarly to the breakup of inviscid particle. The "dents" developed on the surface of the particle had a similar length scale as the particle size. This suggests that the deformation in this stage is caused by the collision of turbulent eddies described in the Kolmogorov-Hinze theory.

The second stage is the stretching/thinning stage. At the end of the stretching stage, the

ligament has been stretched to over 5 mm. This is about five times of the initial diameter. Besides the obvious difference in the shape of the particles, another behavior that stands out is that the size and number of daughters are dictated during the stretching stage. As we mentioned before, alternating thin strings and fluid lumps structure was developed on the stretched ligament. These fluid lumps that would eventually become daughter particles. In the example shown here, five daughter particles were formed, but in some cases, more than ten daughters were observed from a single breakup event. In the case of the invsicid particle breakup, a small portion of the mother particle is pinched off to form one large (similar in size as the mother) and one small daughter particles. Because of the pinch-off process, most breakup events are binary (at most three daughter particles were formed from our observation). With the differences in the pre-breakup shape and the daughter formation process, the stretching stage is what differentiates between the breakup of inviscid and viscous particles.

The third stage is the disintegration of ligament. This occurs when the thin strings connecting the fluid lumps disintegrate and recoil back to the daughter particles. This process happens very quickly (less than 1 ms). In addition, all the thin strings developed on the ligaments break almost simultaneously (within a fraction of a ms). Thus, the duration of this stage is significantly less than the deformation and the stretching stage, so only the deformation time and the stretching/thinning time are considered in the analysis of the breakup time.

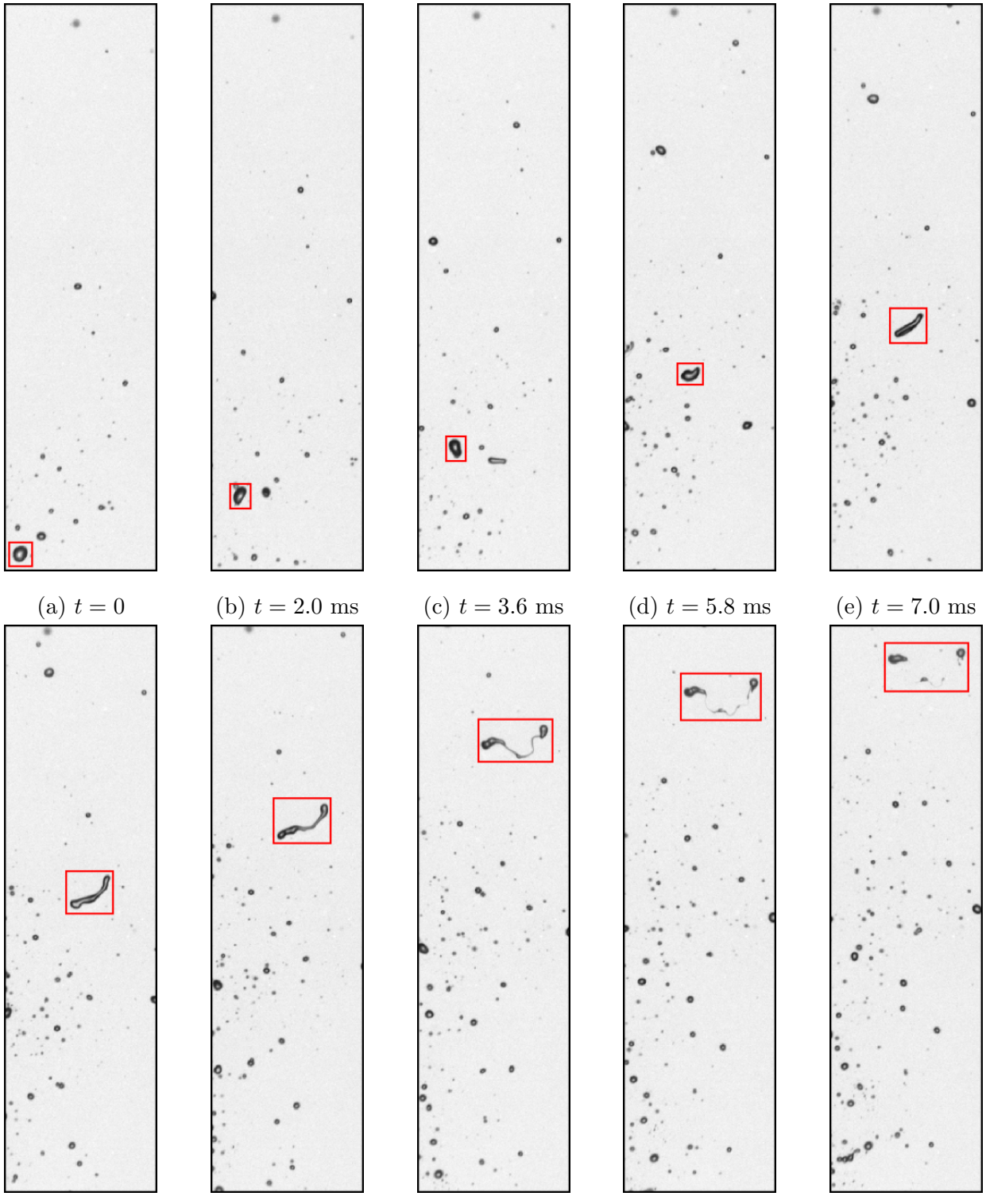

(a) $t = 0$ (b) $t = 2.0$ ms (c) $t = 3.6$ ms (d) $t = 5.8$ ms (e) $t = 7.0$ ms

(f) $t = 8.2$ ms (g) $t = 9.8$ ms (h) $t = 11.8$ ms (i) $t = 13.0$ ms (j) $t = 13.8$ ms

Figure 8.1: A visualization of a typical breakup sequence of viscous particle. $Re = 60000$ and $Q_p = 20$ mL/min. Needle positioned at $z/d_j = 20$. Canola oil.

8.2 Deformation to Stretching transition

From the qualitative observation of the high-speed image sequences (Section 8.1), we hypothesized that the breakup event can be divided into three stages: the deformation, stretching/thinning and disintegration. The duration of the disintegration stage appears to be significantly less than the other two stages. Assuming the disintegration time is negligible, the breakup time can be divided into deformation time and the stretching/thinning time. Thus, it is important to be able to identify the transition between the deformation and stretching stage (D-S transition).

The main distinction between the two stages is the degree of deformation of the particle. Specifically, particles get stretched multiple times of its original size. So, it appears that the change in the length and the thickness of the particle are good quantitative measures to determine the D-S transition. Using the combination of the equivalent rectangle method and the fit ellipse method (described in Appendix F), the equivalent length and the thickness of the particle can be determined.

To describe the shape of the ligament, one obvious choice would be the aspect ratio. However, it is an unbounded quantity, so it is difficult to visualize in a plot when the aspect ratio changes significantly during the breakup event. Another typical measure a stretched ligament is the deformation factor [55]. It is defined as follows:

$$DF = \frac{l_e - b_e}{l_e + b_e} \tag{8.1}$$

where l_e is the equivalent ligament length and b_e is the equivalent ligament thickness.

Since both the aspect ratio (AR) and the deformation factor are function of l_e and b_e. The deformation factor can be viewed as a bounded version of the aspect ratio. In fact, AR can be written as a function of DF as follows:

$$AR = \frac{l_e}{b_e} = \frac{1 + DF}{1 - DF} \tag{8.2}$$

Figure 8.2 shows two examples of the deformation factor along the breakup path. In gen-

eral, the path began with low value of DF . Its value fluctuated in the first portion of the path, but it typically remained low. This indicates the shape of the particle was constantly changing, but not significantly. This is consistent with our qualitative established deformation stage. After that, a rapid monotonic increase of DF was observed. This corresponds to the stretching stage we observed in the high speed image sequences. In some cases, fluctution of DF occured during the stretching stage. Since most ligaments have a three dimensional geometry, the change in their orientation could significantly alter the shape captured by the camera, thus causing the fluctuation in DF.

In the deformation stage, the fluctating behavior of DF means that a particle was undergoing a few cycles of deformation. In terms of the mechanism of the deformation, it indicates that a partcle experienced multiple series of eddy collisions, but these eddy collisions did not have enough strength to cause further deformation except the last series. The last series of eddy collisions pushed the particle to the stretching stage. The rapid monotonic increase in DF implies that the stretching mechanism is caused by a single eddy. Because the particle was stretched to multiple times its original size (in the integral length scale), this eddy must correspond to the large scale motion in the flow.

The key to find the D-S transition is to identify the point where DF changes from a fluctuating behavior to a rapidly increasing trend. Unfortunately, finding this transition from the data is difficult as they are noisy. Therefore, a Gaussian filter was applied to the DF path. The filtered path is shown in Figure 8.2 as the solid line. By smoothing out the DF paths while retaining the general trend, it removes the rapid fluctuations that were not beneficial to our analysis.

To determine the D-S transition, we use the following procedures. First, we identified the time with the maximum DF. In almost all cases, this is located at the end or near the end of the breakup path. From this time, we searched backward in time until we found a local minimum. Then, we calculated the difference between the maximum DF and the local minimum DF. If this difference is larger than 50% of the total DF range (absoule maximum - absolute minimum) of the path, this local minimum is considered to be the temporary D-S

transition. If the condition of the 50% of the total DF range is not satisfied, the search continues to the next local minimum and this process repeated until the temporary D-S transition was found.

The search did not end when temporary D-S transition is found. This is because in many cases, ligaments change their orientation during the stretching, so some fluctuation in DF could happens during this time. Thus, the search continued to find the next local minimum backward in time. Once that is found, the difference between the DF of the temporary D-S transition and the DF of the new local minimum was calculated. If this difference is greater than 50% of the difference between the maximum DF and the local minimum DF (this was used to determine temporary D-S transition), the new local minimum was considered to be the new temporary D-S transition. This process continued until the all local minimums were examined. The last temporary D-S transition was considered to be the actual D-S transition. For DF paths that have a monotonic increase, the D-S transition is set at the beginning of the plot as we assume the deformation stage does not exist for these particles. Figure 8.3 shows some of the DF paths for two different experiments. The D-S transition obtained from the method mentioned above is overlaid on each path.

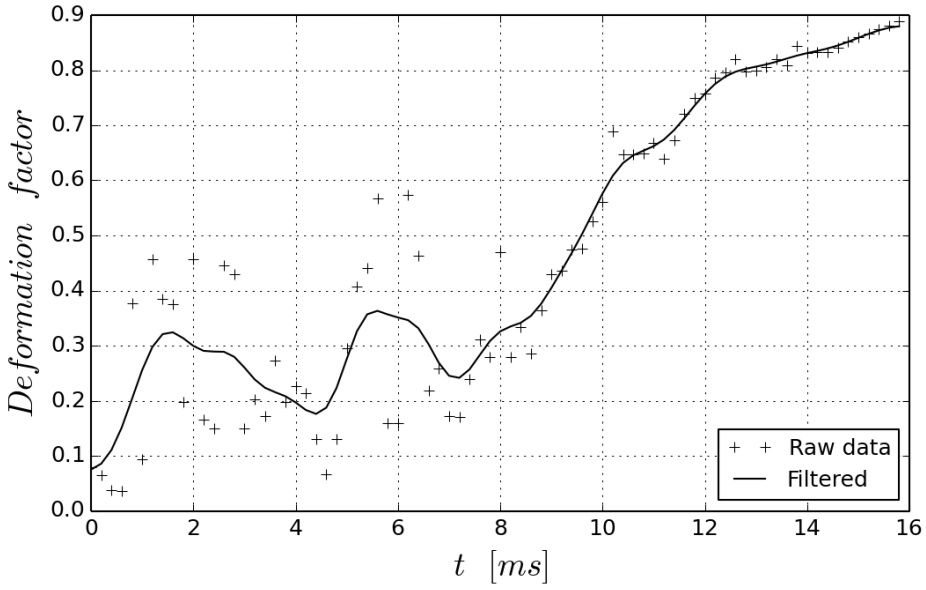

(a) Example 1

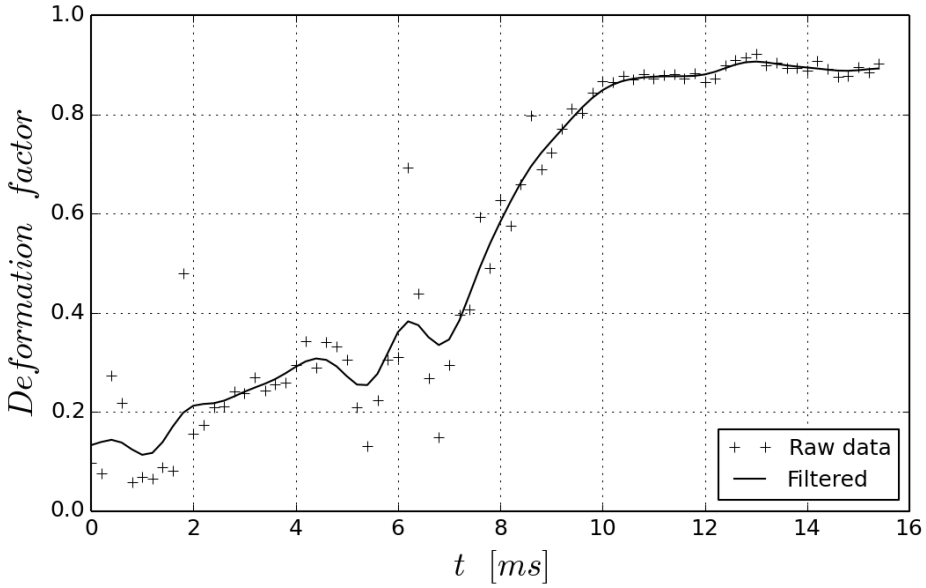

(b) Example 2

Figure 8.2: Evolution of the deformation factor along the breakup path for two separate breakup events.

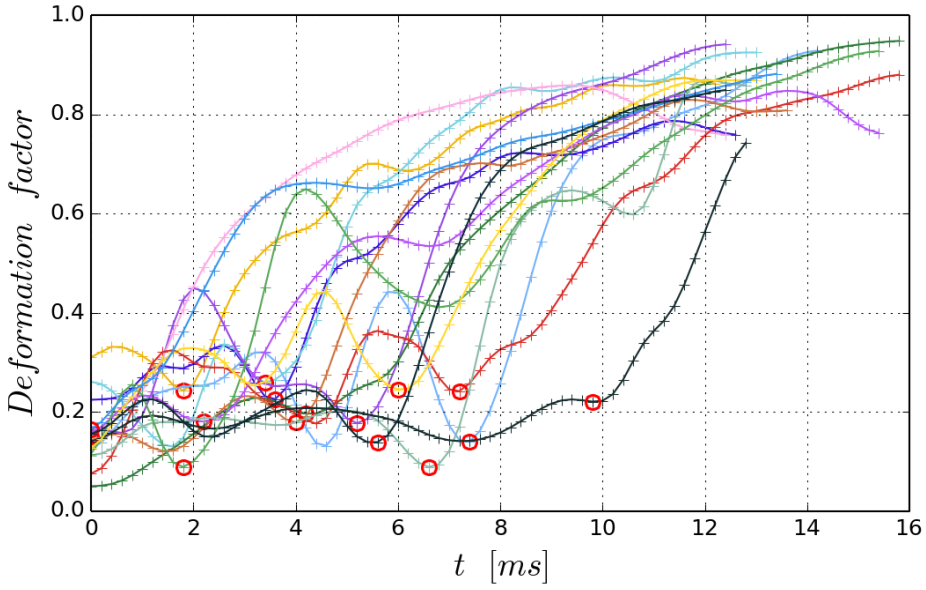

(a) $Re = 60000$

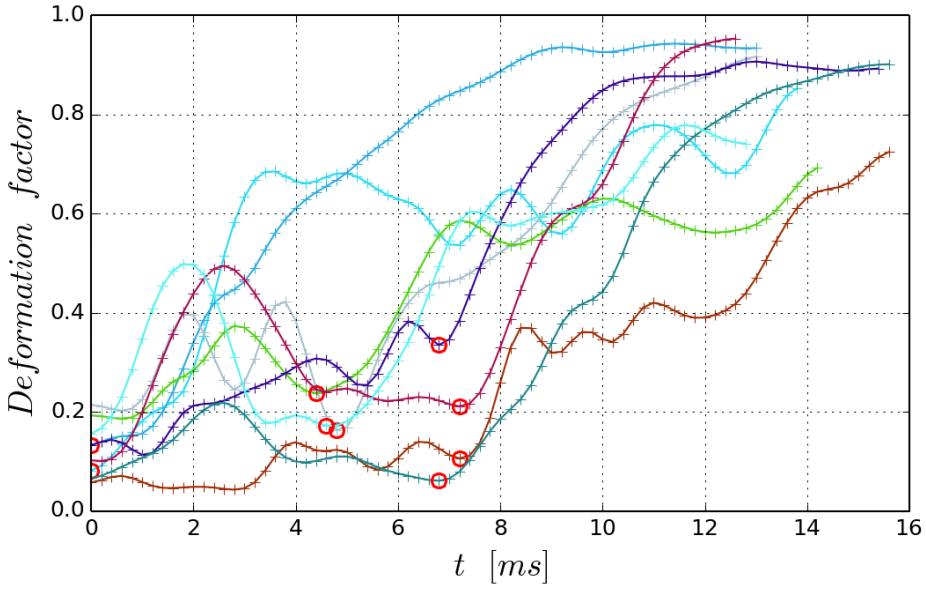

(b) $Re = 80000$

Figure 8.3: Evolution of the deformation factor along the breakup path for multiple breakup events. D-S transition of each path is shown as a red circle.

8.3 Breakup time

As mentioned in Section 8.1, the duration for a breakup event can be separated into three different stages. Assuming the duration of the disintegration stage is negligible, the breakup time can be divided into the deformation time and stretching/thinning time (Equation (8.3)). With the D-S transition identified in Section 8.2, we can study the duration of the two stages separately.

$$T_b = T_d + T_s \tag{8.3}$$

where T_b is the breakup time, T_d is the deformation time, and T_s is the stretching/thinning time.

8.3.1 Stretching/thinning time

The stretching/thinning process is unique for the breakup of viscous particles. This process is complicated as we observed different behaviours occurring simuntaneously in the high-speed image sequences. This suggests that multiple mechanisms are involved in this process.

One of the obvious mechanisms is the stretching of the particle. Because the particle is stretched to multiple times of its original size, the length scale of the ligament is beyond the inertial subrange. Therefore, the Kolmogorov-Hinze theory would not apply to the stretching mechanism. Instead, the stretching should be caused by the integral scale motion. In studies [8] [55] [65] where particle stretching was observed in laminar flows, the driving force is the local strain rate. For a turbulent jet, the strain rate in the integral length scale can be approximated by $\frac{dU}{dr}$ [52].

Although the stretching is due to the integral scale shear motion, Rallison [55] found that for $\mu_p/\mu_j > 4$, simple shear flow cannot break a particle no matter how large the capillary number is. Capillary number (Equation (8.4)) is a ratio of the external flow forces to surface tension. If the capillary number exceeds the critical value, the particle would break under the external flow. Figure 8.4 shows that the critical capillary number approach to infinity

at high viscosity ratio for shear flow. Similar results were obtained by Bentley & Leal [8] for similar flow types. However, these studies were peformed under laminar flows. In a turbulent jet, however, the shear effect represents only the integral scale motion. Smaller scale turbulent motions are also present in the jet. This suggests that the stretching of the particle is due to shear, but the disintegration is due to motions in a different length scale.

$$Ca = \frac{\mu_j G L}{\sigma} \tag{8.4}$$

where Ca is the capillary number, G is the local strain rate of the surrounding flow, and L is the length scale of the particle.

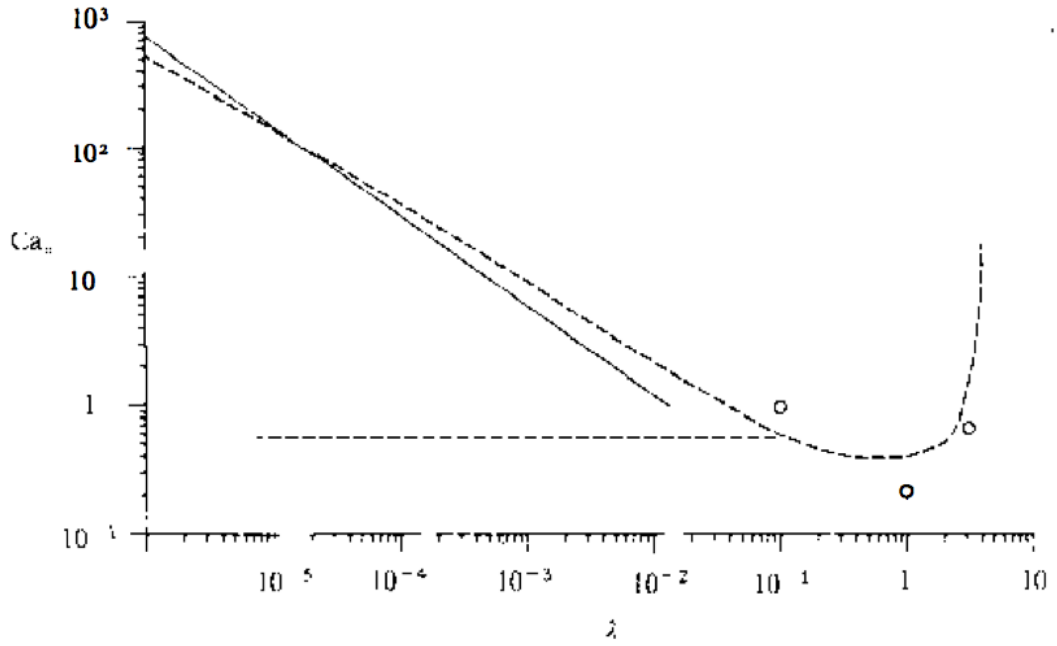

Figure 8.4: Critical capillary number vs viscosity ratio for simple shear flow [55].

During the stretching stage, a particle can be stretched into a long ligament by the integral scale motion in the flow. At the same time, the ligament is constantly bombarded by eddies in different scales. Although the length of the ligament can reach the integral length scale, the thickness always stays within the inertial subrange (providing the original particle size is

in the inertial subrange). Thus, the thin portion of the ligament can be affected by the eddies in the inertial subrange. This implies that the thinning and, ultimately, the disintegration of the ligament could be due to the history of these eddy collisions.

As discussed in Chapter 2, Martínez-Bazán et al. [39] assumed that the breakup time of a particle to be proportional to the particle size and inversely proportional to a characteristic velocity. We apply a similar idea to model the thinning of the ligament due to the collisions of inertial scale eddies. We posulate that the duration of this process is proportional to the change in the ligament thickness over the characteristic internal thinning velocity:

$$\Delta T = \frac{\Delta b_e}{U_i} \tag{8.5}$$

The characteristic internal thinning velocity can be written as $U_i \sim \sqrt{\tau_e/\rho_p}$ [22]. The external stress, τ_e, is caused by the turbulent velocity fluctuation with a length scale similar to the thickness of the ligament, so it is defined as:

$$\tau_e = \rho_j(\epsilon b_e)^{2/3} \tag{8.6}$$

Substituting these back into Equation (8.5) and integrating both sides of the equation over the stretching stage, we obtain:

$$T_{\epsilon,thin} = \frac{3}{2}\left(\frac{\rho_p}{\rho_j}\right)^{1/2} \epsilon^{-1/3}(b_{e,DS}^{2/3} - b_{e,BU}^{2/3}) \tag{8.7}$$

where $T_{\epsilon,thin}$ is the thinning time due to eddy collisions on the thickness of the ligament, $b_{e,DS}$ is the ligament thickness at the D-S transition, and $b_{e,BU}$ is the ligament thickness just before breakup.

Figure 8.5 shows the relations between our model, $T_{\epsilon,thin}$, and the measured stretching/thinning time, T_s. For each breakup path, the turbulent dissipation is taken as the mean turbulent dissipation over the duration of the stretching/thinning stage because the thinning depends on the history of continuous collisions of turbulent eddies. Each figure

shows all three Reynolds number cases of each dispersed phase fluid. T_s and $T_{\epsilon,thin}$ appear to have a positive correlation, but this trend has a large variation.

There are several reasons for the variation. First, T_s is obtained from the number of frames between the D-S transition and the pre-breakup point. The calculated D-S transition is based on the distinct behavior of the two stages. In particular, the stretching stage is assumed to be a monotonic increases, so the D-S transition was placed where fluctuation in the deformation factor occurs. However, the deformation and/or stretching of a particle is not the only cause for the fluctuating behavior in deformation factor. The rotation of the ligament or the overlapping of surrounding particles can also create fluctuation in the deformation factor along the path. These factors mask the actual D-S transition, as a result, they contribute to the variation in the T_s.

Another reason is that we do not know the true radial location of the particle. During the experiment, our camera focused on the center-plane of the jet, with a depth of view larger than two times the half-width of the jet. This was done to ensure all particles, including the ones that dispersed radially outward, were in focus. On the image, we can identify the horizontal distance of the particle relative to the centerline of the jet, but we cannot determine the depth of the particle relative to the focal plane. For example, a particle appears at the centerline on the image could locate at a distance from the focal plane, which results in a non-zero true radial distance from the centerline. The implication is that we do not know the exact flow intensity around the particle. However, since we have the true axial location (independent to th distance from centerplane) of the particles from the image, we can estimate the intensity of the flow field based on its axial location. This means that we are assuming particles at the same axial distance experience the same flow field, so it contributes to the variation we see in Figure 8.5.

Figure 8.6 combines the data from the four base fluids into one plot. Even with a wide range of dispersed phase viscosity between the four base fluids, the data fall on a similar trend. Recall from Equation (8.7) that our model does not include the effect of viscosity. This is interesting because this suggests that the stretching/thinning time is independent (or

weakly dependent) of viscosity.

Given that our model is based on eddies colliding with the thin portion of the ligament, the damping effect from the dispersed phase viscosity is minimized due to the amount of liquid across the thickness of the ligament is small. In addition, although the thinning process is caused by eddy collisions, the nature of the collisions on the particle in the deformation stage is different. In the deformation stage, eddies colide on the particle from all directions causing uneven deformation on the particle. So, the internal flow field is not organized and it keeps changing based on the history of collisions. Thus, the internal viscous effect is important as the internal flow field accelerates in different directions during the deformation. In comparison, the internal flow field of the thin portion of the ligament behaves differently. Because the ligament is stretching in a dominant direction, all eddy collisions only result in thinning of the ligament. This means that the acceleration of the internal flow field due to the change in the deformation direction is minimized, thus, the internal viscous effect is not as significant in the thinning process.

The thinning time model was derived to provide an estimate of the measure stretching time, so it is not expected to have a one-to-one relationship with T_s. However, from the linear fit that we applied to the data, we found that the slope of the fit is about 2, so a predictive model should me 2 times of our thinning time model. Note that the intercept at the y-axis for the linear fit is set to be zero because if the measured stretching/thinning time is zero, the thinning process does not exist.

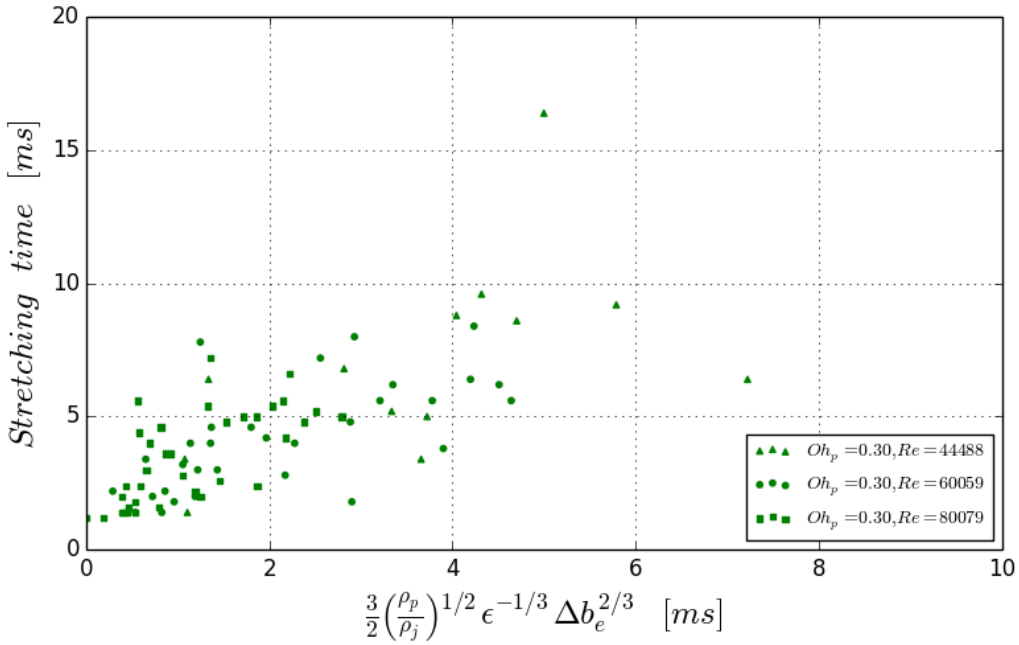

(a) Canola oil

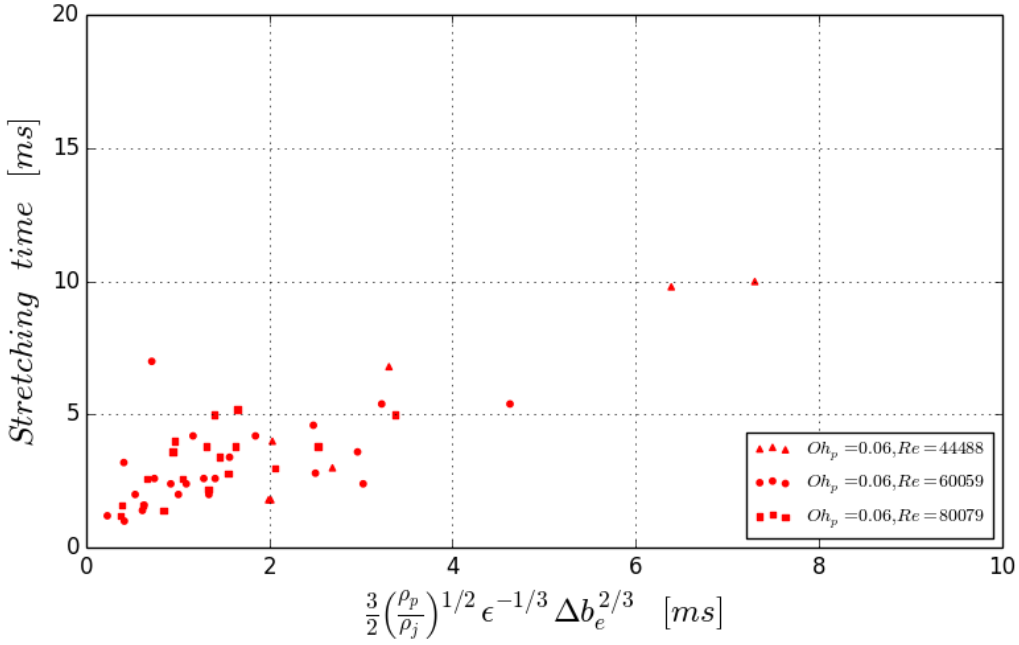

(b) 10 cSt silicone oil

Figure 8.5: Measured stretching/thinning time vs modeled thinning time based on eddies collision.

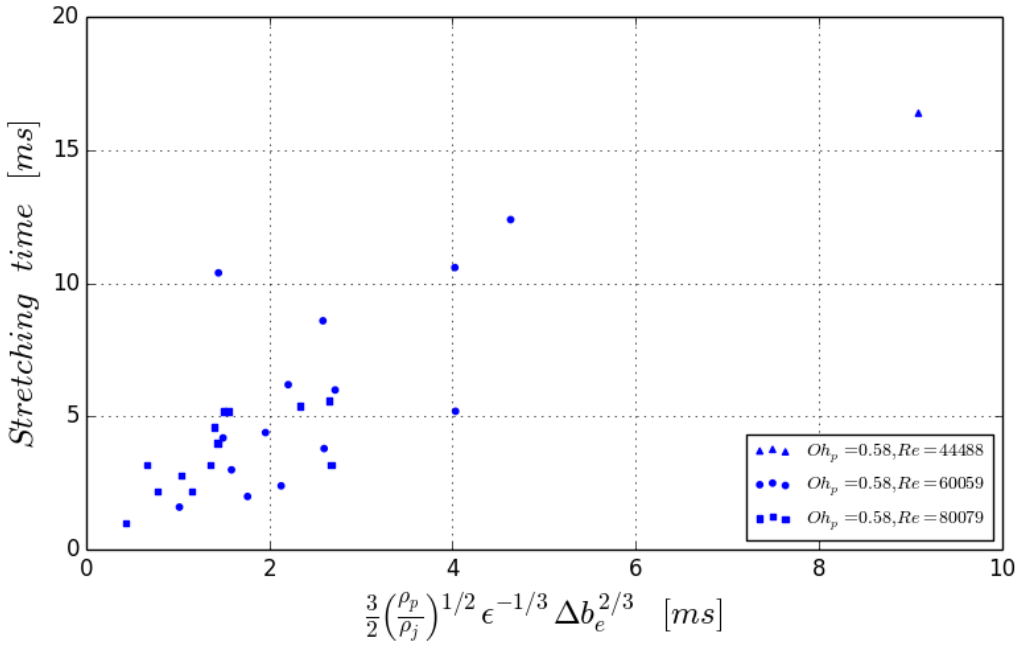

(c) 100 cSt silicone oil

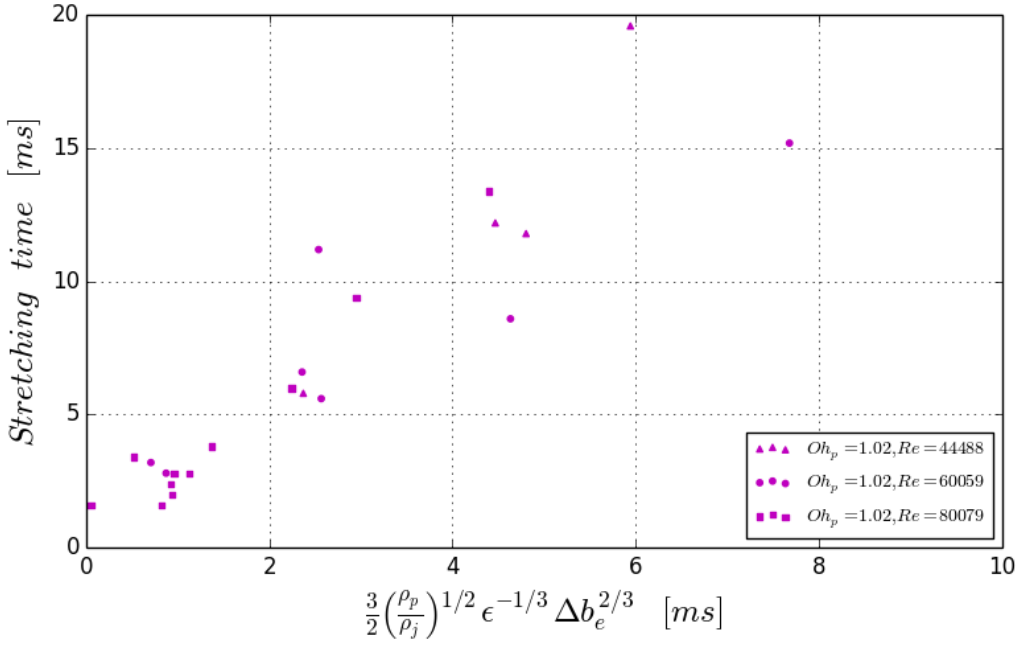

(d) 200 cSt silicone oil

Figure 8.5 (Continued): Measured stretching/thinning time vs modeled thinning time based on eddies collision.

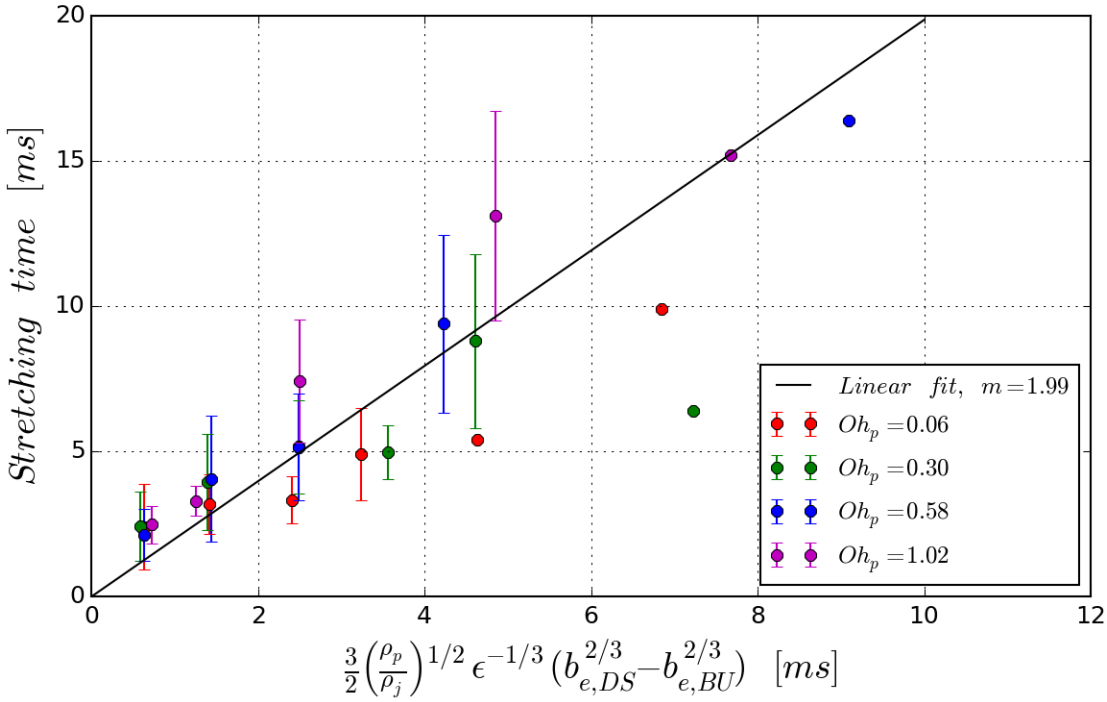

Figure 8.6: Measured stretching/thinning time vs modeled thinning time based on eddies collision with linear fit.

So far, we assumed that T_s scales with the thinning time due to the inertial subrange eddy collision (referred this as the eddy collision mechanism in this section). As discussed before, the stretching mechanism due to the integral scale motion (referred as the shear mechanism) occurs concurrently, so the time scale due to this mechanism could be important in predicting the stretching/thinning time. To evaluate which mechanism dictates the time scale of the stretching/thinning stage, we can compare the thinning speed from both mechanisms.

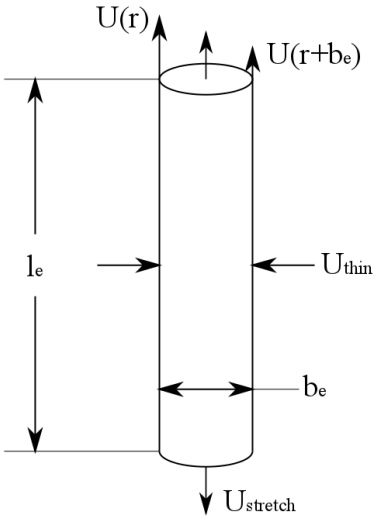

Figure 8.7: Illustration of the stretching and thinning of a cylindrical shape ligament.

The shear mechanism is primarily responsible to the stretching of the particle, but thinning is also a consequence because of the volume conservation of the particle. Assuming the ligament has the shape of a cylinder (Figure 8.7), the volume can be written as $V = (\pi/4)b_e^2 l_e$. Since the volume is conserved during the stretching stage, $dV/dt = 0$. Knowing that both b_e and l_e are function of time, we can apply the product rule. This results in the following relationship between the stretching and thinning velocity.

$$\frac{db_e}{dt} = \frac{-b_e}{2l_e}\frac{dl_e}{dt} \tag{8.8}$$

where $\frac{db_e}{dt}$ and $\frac{dl_e}{dt}$ are the thinning velocity ($U_{G,thin}$) and stretching velocity ($U_{G,stretch}$), re-

spectively.

Since we assume the stretching mechanism is caused by the integral scale motions in the jet, the stretching velocity can be approximated by using the local strain rate:

$$U_{G,stretch} = b_e \frac{dU}{dr} \tag{8.9}$$

Substituting this back to Equation (8.8), we obtain:

$$|U_{G,thin}| = \frac{b_e^2}{2l_e} \frac{dU}{dr} \tag{8.10}$$

This is the instantaneous thinning velocity, so averaging along the stretching stage is required to obtain the mean thinning velocity, $|\overline{U}_{G,thin}|$. For the eddy collision mechanism, the mean thinning velocity can be obtained by dividing the difference of the ligament thickness by the $T_{\epsilon,thin}$:

$$|\overline{U}_{\epsilon,thin}| = \frac{b_{e,DS} - b_{e,BU}}{T_{\epsilon,thin}} \tag{8.11}$$

The duration of the stretching/thinning stage depends on how fast the ligament gets thin enough to reach disintegration. Figure 8.8 shows that $\overline{U}_{\epsilon,thin}$ is about an order of magnitute faster than $\overline{U}_{G,thin}$. Although both mechanisms occur concurrently, the large difference in thinning velocity suggests that the time scale of the stretching/thinning stage depends mostly on the eddy collision mechanism. In other words, $T_{\epsilon,thin}$ is the correct time scale for the stretching/thinning stage.

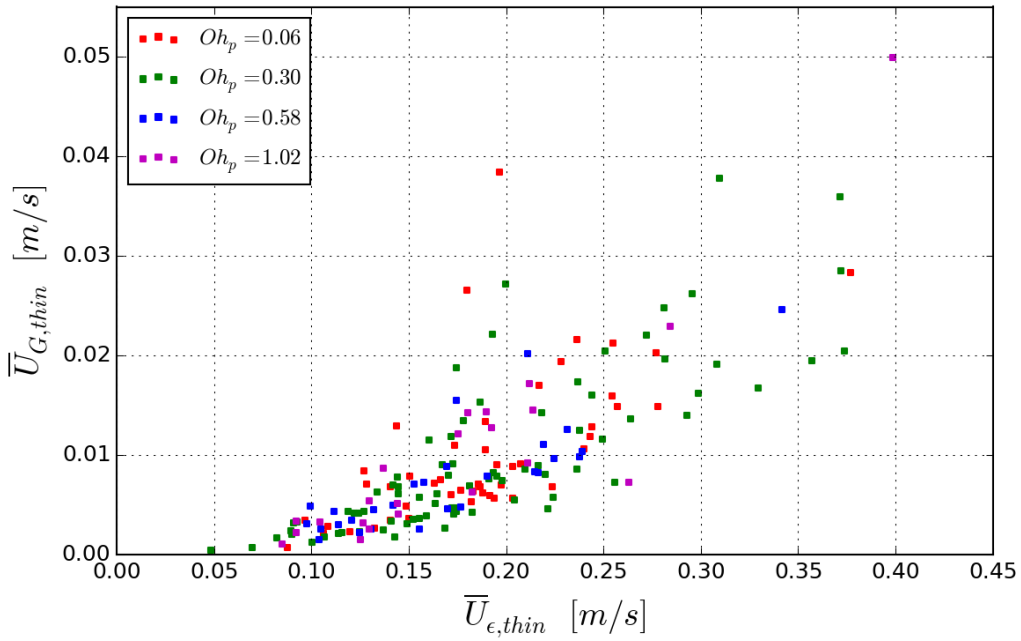

Figure 8.8: Comparison of the thinning velocity between the shear and eddy collision mechanisms.

8.3.2 Deformation time

As mentioned before, the deformation stage is caused by the Kolmogorov-Hinze mechanism as the particle size is within the inertial subrange. Therefore, it is reasonable to apply the same model for $T_{\epsilon,thin}$ shown in Equation (8.7). The ligament thickness term has to be modified for the deformation stage, as shown in Equation (8.12).

$$T_{\epsilon,deform} = \frac{3}{2}\left(\frac{\rho_p}{\rho_j}\right)^{1/2} \epsilon^{-1/3}(D_o^{2/3} - b_{e,DS}^{2/3}) \tag{8.12}$$

Figure 8.9 shows the relation between $T_{\epsilon,deform}$ and the measured deformation time, T_d. The correlation between our model and the measured deformation time is poor, implying our model is not correct for the deformation stage.

Our model assumes all eddy collisions on the particle is effective in the deformation process (i.e. to deform a particle with original particle size, D_o, to the thickness at D-S transition, $b_{e,DS}^{2/3}$). This assumption works well for the stretching/thinning stage because the thinning process is monotonic, which means the process depends on the entire history of the eddy collision. However, in the deformation stage, the deformation factor of a particle fluctuates (see Figure 8.3). This means the particle went through a few cycles of deformation. In the other words, the particle is deformed by a series of eddy collisions, but most of these collisions are not strong enough to cause the transition to the stretching stage. For the transition to occur, the particle has to be sufficiently deformed so that the integral scale motion in the flow can take over with the stretching mechanism. This means that there are two outcomes from the deformation stage. First, if none of the eddy collisions is strong enough to cause the transition to the stretching stage, breakup do not occur. This phenomenon has been observed for many particles, an example of this is shown in Figure 8.10. The second outcome is when the last series of eddy collisions has enough energy to cause the transition to the stretching stage. Because only the last series of eddy collisions is responsible for the transisition, the duration in the deformation stage does not depends on the entire history of collisions. This is why our deformation time model, $T_{\epsilon,thin}$, fails to

predict T_d. In addition, $T_{\epsilon,thin}$ is significantly shorter than T_d because the model ignored all the failed eddy collisions attempts.

Because of the stohastic nature of the process, the number of eddy collisions needed for a particle to transition to the stretching stage is unknown for each breakup event. As a result, the exact duration of the deformation stage cannot be determined as it depends on the number of eddy collision series.

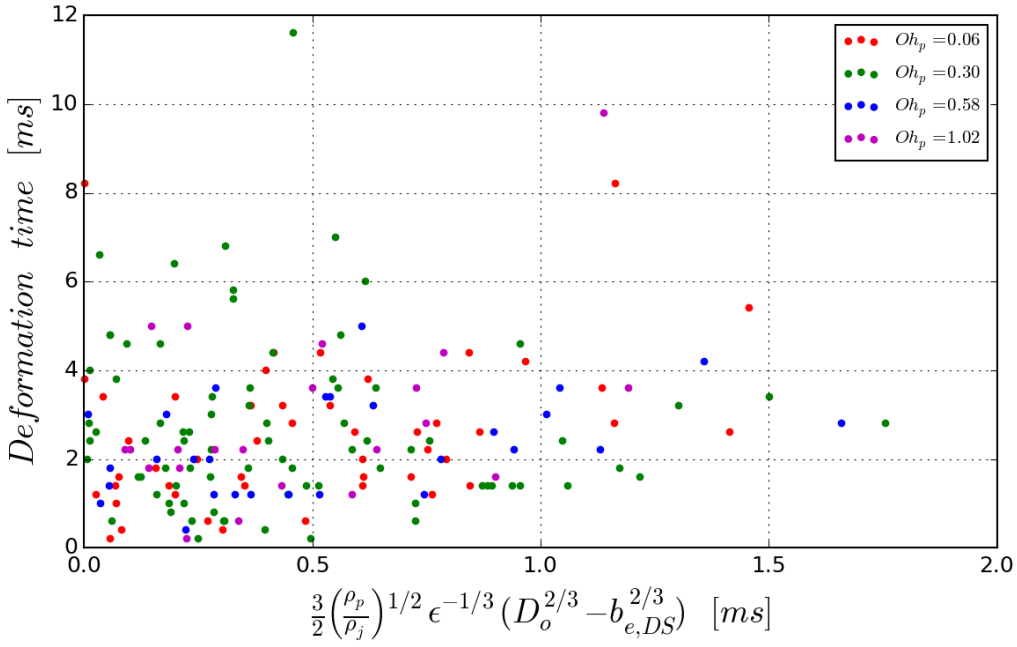

Figure 8.9: Measured deformation time vs modeled deformation time.

8.4 Breakup probability

From the formulation of Martínez-Bazán et al. [39] model, the breakup frequency is proportional to the inverse of the breakup time of a particle. This model assumes that as long as the the disruptive stress exceeds the confinement stress, implying the particle size is greater than the critical diameter, breakup of the particle will occur. However, our qualitative observation from the high-speed image sequences indicates this might not be the case.

From the discussion in Section 8.3.2, we learned that even for eddies that are capable of deforming the particles, they might not be effective in causing the transition to the stretching stage. This behavior is observed in the high-speed image sequence. For example, in Figure 8.10, the particle underwent a few cycles of deformation for more than 10 ms, but it eventually reverted back to a spherical particle at $t = 14$ ms (the particle remained spherical afterward, but the rest of the sequence is not shown here). In addition, the turbulent disspation rate during this period ranges from 160 to 58 m^2/s^3. This results in a critical diameter (see Chapter 7.8) ranges between 0.42 to 0.58 mm, which is smaller than the initial particle size of 0.92 mm. Hence, this shows that even if the particle size exceeds the critical diameter, a breakup event is not guaranteed.

From our qualitative observation, an elongated ligament never reverts back to a spherical particles as the surface restoring pressure is insufficient to cause this reverse process. As a result, the stretching stage is irreversible, which means all particles entering the stretching stage would eventually disintegrate. Therefore, the probability of whether a particle breaks is determined during the deformation stage. A particle is constantly impacted by turbulent eddies, some of these eddies could deform the particle. In some cases, these eddies do not cause sufficient deformation for the integral scale motion to to take over the stretching process. In other cases, the eddy collisions cause enough deformation for the particle to enter the stretching stage. Of course, when a particle is exposed in a high turbulent dissipation region, the amount of eddies with high kinetic energy is greater, so the probability of a particle entering the stretching stage, or simply the breakup probability, would also be higher.

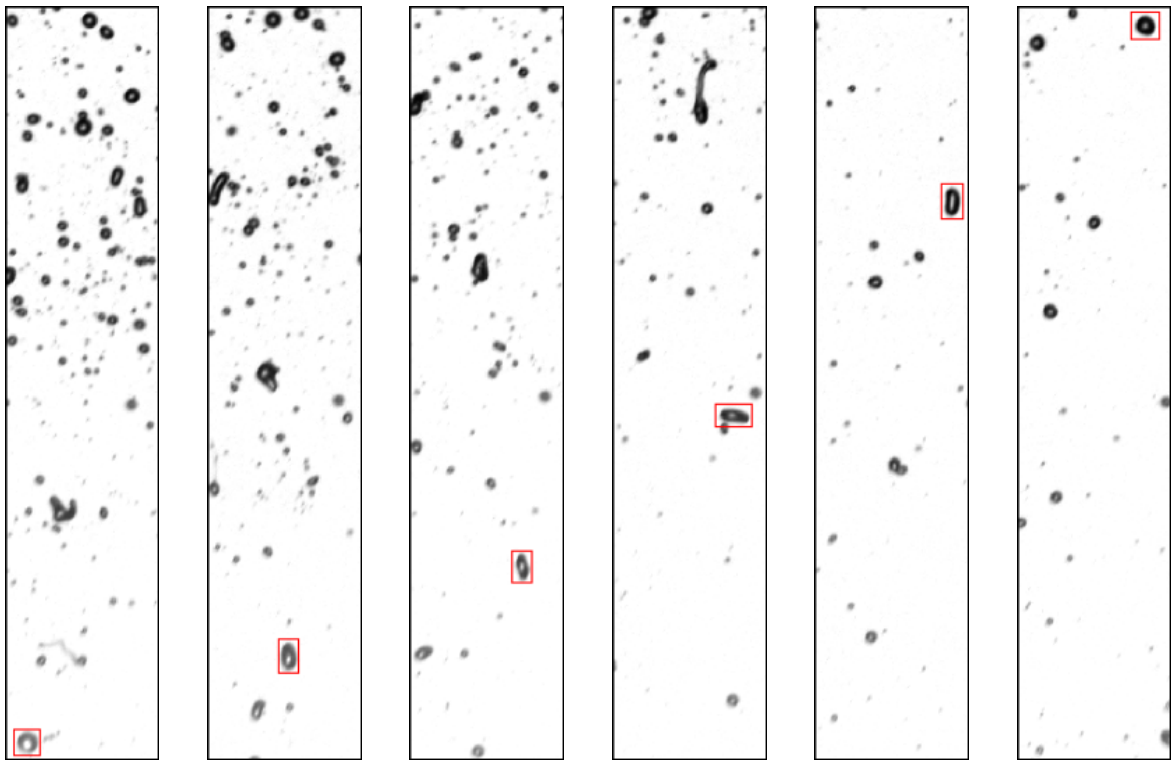

(a) $t = 0$ (b) $t = 2.2$ ms (c) $t = 4.0$ ms (d) $t = 6.8$ ms (e) $t = 11.0$ ms (f) $t = 14.0$ ms

Figure 8.10: An image sequence showing a deformed drop reverted back to spherical shape. $Re = 80000$ and $Q_p = 20$ mL/min. Needle positioned at $z/d_j = 20$. 100 cSt silicone oil.

As discussed in Chapter 2, Coulaloglou and Tavlarides [13] and a number of other researchers [53, 66, 36] used different variations of the breakup probability in their models. Coulaloglou and Tavlarides [13] defined the breakup probability as the fraction of drop breaking. To apply this in terms of our experiment, it is the number of completed breakup paths (breakup path starting from a spherical particle), N_b, divided by the number of available spherial particles, N_p. N_b was obtained from the LIBT algorithm. However, it cannot provide N_p since LIBT only tracked particles that disintegrated. The following section describes a methodology to obtain N_p.

The reason why only completed paths are considered in the breakup probability analysis

is because many incompleted paths are a result of the daughter ligamemts going through the secondary breakup. These ligaments are typically highly deformed and so they begin directly in the stretching stage. As we discussed before, the stretching process is irreversible, so the breakup probability of many incompleted paths is 100%. Therefore, it is appropriate to consider only breakup events that begin with a spherical particle.

$$P_b = \frac{N_b}{N_p} \tag{8.13}$$

where P_b is the breakup probability

8.4.1 Number of available particles

The total number of available particles in a given period of recording can be obtained using Equation (8.14). First, we need to determine the number of particle per frame, N_p'. This is done by counting the number of particle in each frame and taking the average over the number of frames sampled. Only particles with a circularity greater than $\pi(\pi+2)/(\pi+1)^2 \approx 0.942$ (see Section 5.2 on the definition of spherical particle) are considered because we are calculating the breakup probability of completed paths only. Thus, the available particles must be spherical. Although the same particles appear on one frame can appear on the next frame if the sampling rate is high, Appendix G shows that the N_p' is independent of the sampling rate. Thus, we can obtain N_p^prime using any frame rate as long as sufficient samples are used.

$$N_p = N_p' N_f \tag{8.14}$$

where N_p is the total number of particle in a given period of recording, N_p' is the number of particles per frame, and N_f is the number of frames.

The total number of particle in a given period of recording, N_p, however, depends on the sampling rate through N_f. A particle can remain in the field of view for $\mathcal{O}(10)$ to $\mathcal{O}(100)$ of frames. If N_f is too small, we could over-estimate N_p. Similarly, if N_f is too large, we could

under-estimate N_p.

The appropriate value of N_f depends on the average time it takes for a particle to go across the length of the field of view. Assuming the particles travel with the jet velocity, the particle residence time can be calculated using the mean centerline velocity of the jet (Equation (8.15)) . N_f can be obtained by dividing the total time of the recording divided by the particle residence time, as shown in Equation (8.16).

$$T_p = \frac{L_f}{\bar{U_c}} \tag{8.15}$$

where T_p is the mean particle residence time, L_f is the length of the field of view, and $\bar{U_c}$ is the mean centerline velocity within the field of view.

$$N_f = T_r/T_p = T_r \left(\frac{\bar{U_c}}{L_f} \right) \tag{8.16}$$

where T_r is the total time of recording

8.4.2 Influence of different factors on breakup probability

For a particle to deform beyond a critical point to reach the stretching stage, the surrounding flow must have enough intensity to overcome any confinement effect. Figure 8.11 shows that the higher the jet Reynolds number is, the higher the breakup probability will be. Another factor that affects the breakup is the particle viscosity. As a particle transforms its shape, the internal fluid has to move accordingly. Thus, the deformation has to overcome the stress generated from the movement of particle fluid. Since the viscosity of some of the fluids used in our experiment is quite high, the internal stress could significantly slow down the deformation process enough that a particle never get to the stretching stage, which ultimately affects the breakup probability. Evidently, we observed the decrease of breakup probability as the particle viscosity increases in Figure 8.12.

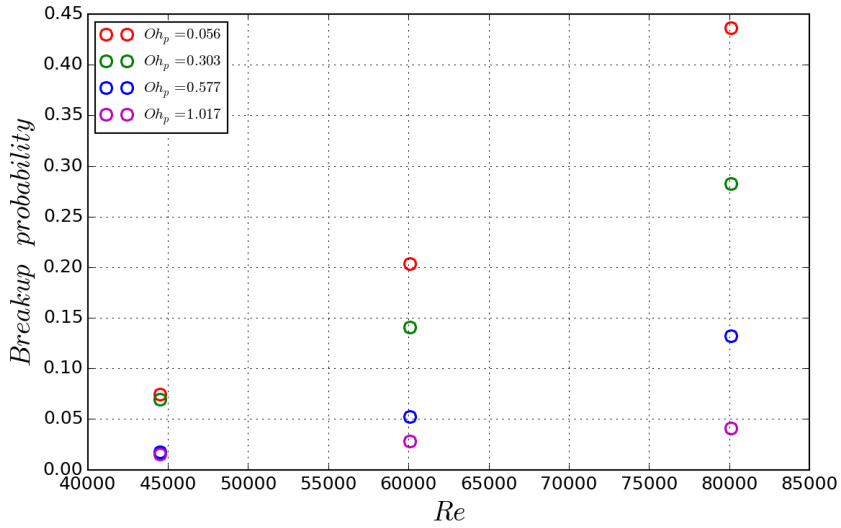

Figure 8.11: Breakup probability vs jet Reynolds numbers for different viscosity ratio.

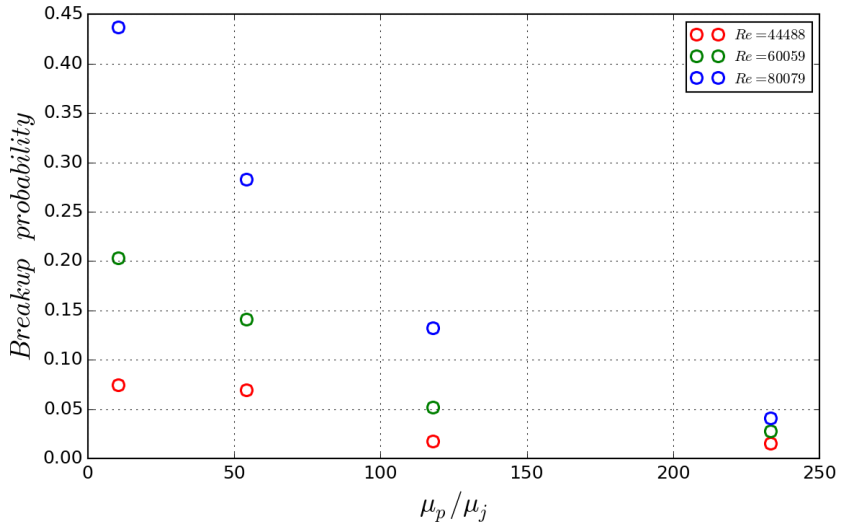

Figure 8.12: Breakup probability vs viscosity ratio for different jet Reynolds numbers.

8.4.3 Breakup probability modeling

The experimental data suggest that both the disruptive effect and the confinement effect play a role in the breakup probability, so we begin by assuming the breakup probability is a

function of the stress ratio, SR, which is the ratio between the confinement and disruptive stresses.

As mentioned before, the breakup probability is determined in the deformation stage. Since the particles have a relatively low deformation factor (see Figure 8.3) prior to entering the stretching stage. The length scale of these particles is within the range where the Kolmogorov-Hinze theory is valid. Therefore, the disruptive stress is a result of the average velocity fluctuation over the distance similar to the particle size.

The confinement stresses are the internal viscous stress and the surface restoring pressure. All three stresses have been formulated in Section 7.8. In the formulation of the frozen state particle size model, we assumed that two confinement stresses have the same weighting. The experimental data supported this assumption as we saw data collapsed into a single curve. Therefore, we are using the same assumption for the formulation of the stress ratio (Equation (8.17)).

$$R_s = \frac{\tau_i + \tau_s}{\tau_t} = \frac{\mu_p \left(\rho_j/\rho_p\right)^{1/2} \left(\epsilon D\right)^{1/3} + \sigma}{\rho_j \epsilon^{2/3} D^{5/3}} \tag{8.17}$$

The relationship between the breakup probability and the stress ratio is shown in Figure 8.13. The experimental data collapse to a single curve and display an exponential decaying trend. This indicates that when the stress ratio is low, the disruptive stress is much higher than the confinement stresses, so there is more excess of energy, resulting in a higher breakup probability.

In the region where $R_s > 1$, the confinement stresses exceeded the disruptive stress. This means that a particle should be able to maintain its shape against the disruptive effect, resulting in zero probability for breakup. However, this is not the case as each data point does not represent the breakup of a single particle. Instead, each data point represents an experiment over a field of view from $z/d_j = 27$ to $z/d_j = 41$. The stress ratio was calculated using the mean centerline turbulent dissipation rate and the mean available spherical particle diameter in the field of view. Because R_s was calculated globally, some particles would experience higher disruptive stress than confinement stresses locally. Thus, it is possible for

breakup to occur in some region of the field of view, resulting in non-zero breakup probability for the $R_s > 1$ cases.

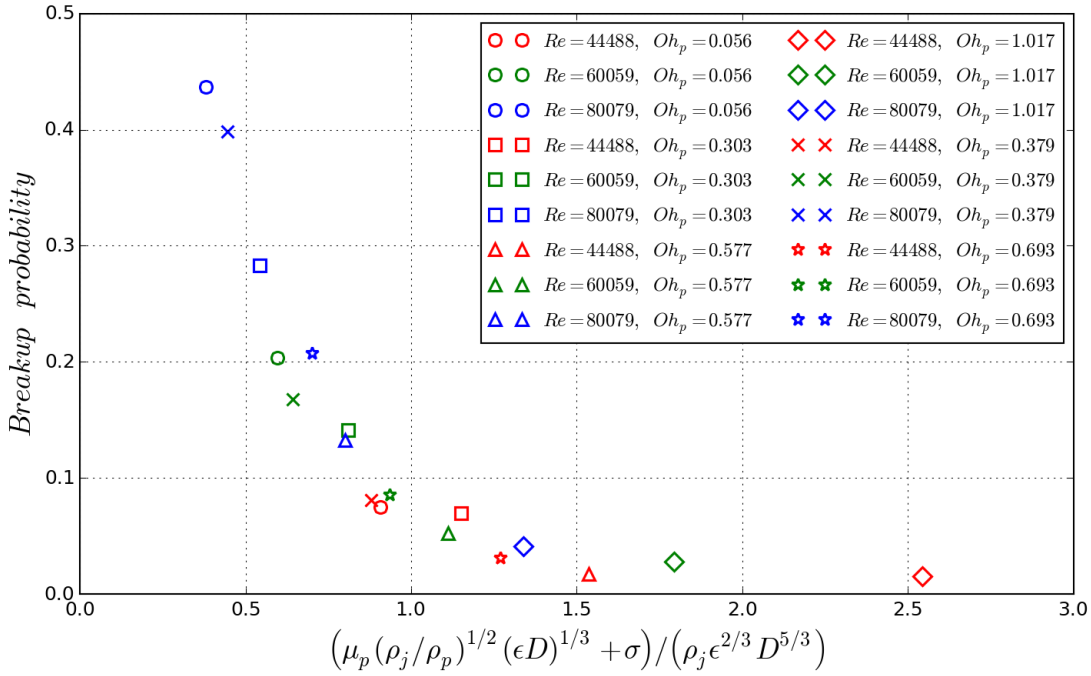

Figure 8.13: Breakup probability vs stress ratio.

Because the data exhibit an exponential decay trend, we performed a curve fitting using the following form:

$$P_b = ae^{-bR_s} \tag{8.18}$$

Because the data exhibit an exponential decay trend, we performed a curve fitting using the form shown in Equation (8.18). The fitting constants were found to be $a = 1.382$ and $b = 2.969$. The exponential fit is plotted over the experimental data in Figure 8.14. The curve fits very well with the data, indicating that Equation (8.18) is the correct function relating the breakup probability and the stress ratio.

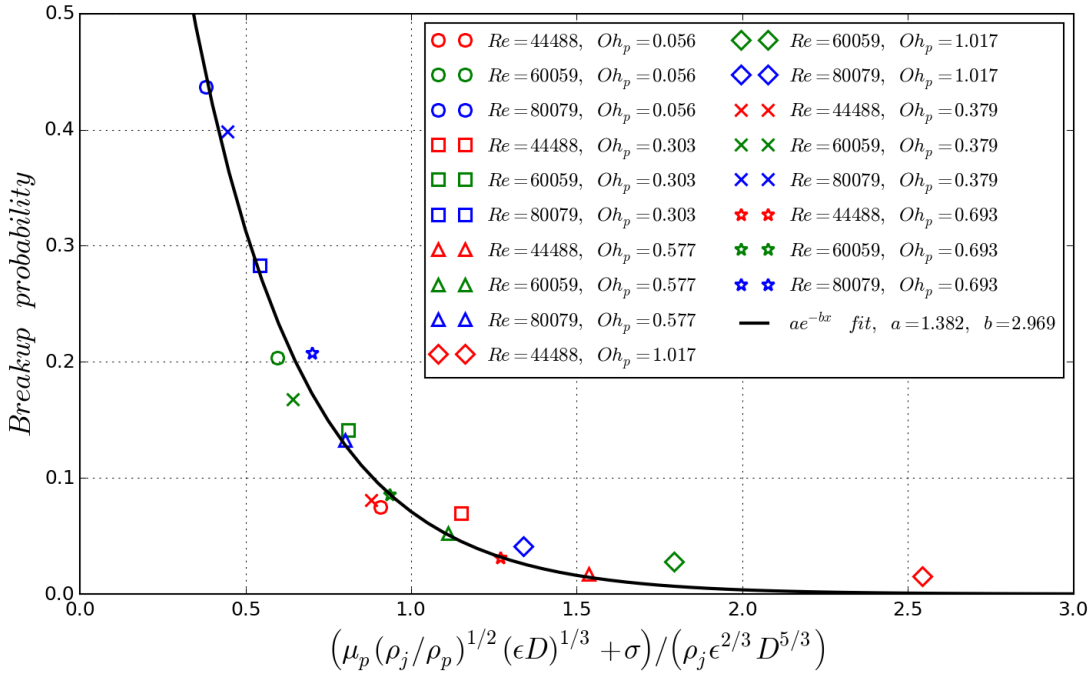

Figure 8.14: Breakup probability vs stress ratio. Exponential fit.

8.5 Breakup frequency

The breakup frequency is one of the closure functions used in the population balance equation. Following the basic formulation from Coulaloglou and Tavlarides [13], we define the breakup frequency as the breakup probability divided by the breakup time (Equation (8.19)). So far, we have proposed models for the breakup probability and the stretching/thinning time. However, the models may not be applied directly to predict the breakup frequency. In this section, we will discuss the needed adjustments in order to apply these models in practical applications.

$$g = \frac{P_b}{T_b} \tag{8.19}$$

8.5.1 Simplified breakup and stretching/thinning time model

The underlying assumption of the stretching/thinning time model is that it is based on the history of eddy collisions on the particle. This is reflected in the model (Equation (8.7)) through the need of the ligament thickness at both the D-S transition and the pre-breakup point. However, the ligament shape at the pre-breakup point is often unavailable in practical applications. Figure 8.15 shows that there is a linear correlation between the thickness at the D-S transition and $b_{e,DS}^{2/3} - b_{e,BU}^{2/3}$. By using the linear fit parameters, we can eliminate the need of $b_{e,BU}$ in the model. The simplified model is shown in Equation (8.20).

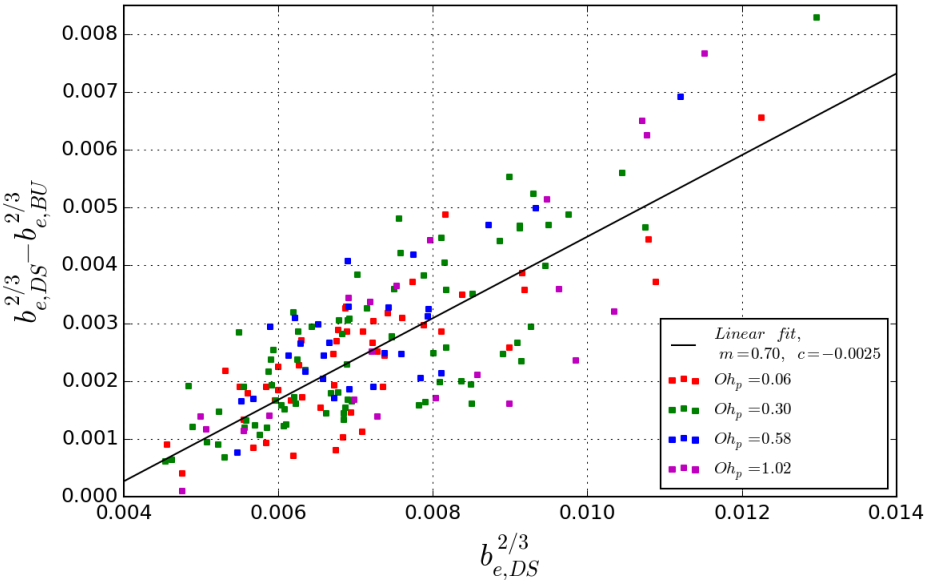

Figure 8.15: Relationship between $b_{e,DS}^{2/3}$ and $b_{e,DS}^{2/3} - b_{e,BU}^{2/3}$. A linear fit is applied to the data.

$$T_{\epsilon,thin} = \frac{3}{2}\left(\frac{\rho_p}{\rho_j}\right)^{1/2} \epsilon^{-1/3}(m_1 b_{e,DS}^{2/3} + c_1) \tag{8.20}$$

where $m_1 = 0.70$ and $c_1 = -0.0025$ are the linear fit parameters obtained experimentally.

As mentioned in Section 8.3.2, the deformation stage consists of multiple series of eddy collisions on the particle. The stohastic nature of the collisions means the deformation time

cannot be precisely predicted. However, the deformation stage could take up a significant amount of the total breakup time. As an estimate, we can apply the same model for the stretching/thinning time on the entire period leading up to the breakup (deformation + stretching/thinning stage). Similar to the simplification made in the thinning time model, we need to eliminate $b_{e,BU}$ for practical purpose. Interestingly, similar linear trend is displayed betweeen $D_o^{2/3} - b_{e,BU}^{2/3}$ and $D_o^{2/3}$. This means the breakup time model can be simplified, as shown in Equation (8.21).

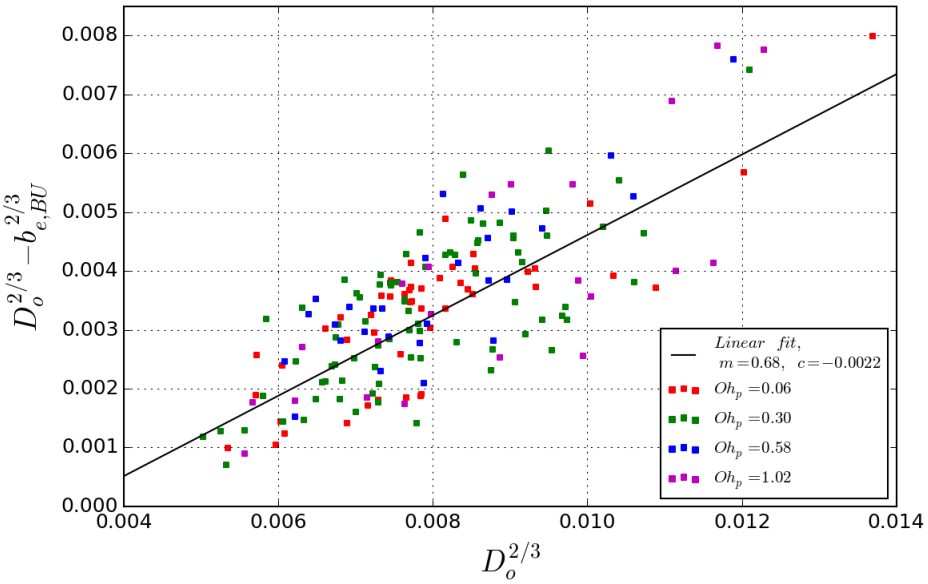

Figure 8.16: Relationship between $D_o^{2/3}$ and $D_o^{2/3} - b_{e,BU}^{2/3}$. A linear fit is applied to the data.

$$T_{\epsilon,breakup} = \frac{3}{2}\left(\frac{\rho_p}{\rho_j}\right)^{1/2} \epsilon^{-1/3}(m_2 D_o^{2/3} + c_2) \tag{8.21}$$

where $m_2 = 0.68$ and $c_2 = -0.0022$ are the linear fit parameters obtained experimentally.

The stretching/thinning time model is not an accurate representation of the entire breakup time, as we saw that the deformation time does not follow this model. The goal of this model, however, is to provide a rough estimate of the magnitude of the entire breakup time through the slope of the linear fit. Figure 8.17 shows the relationship between the simplified model

and the measured breakup time, T_b, along with the slope of the linear fit. The variance of the data is significant as we expected, but the increasing trend is still present, so we will apply the linear fit to these data. The slope of the linear fit is $d_2 = 6.32$. In comparison, the linear fit between the stretching time and the simplified thinning model (Equation (8.20)) is $d_1 = 3.18$. These are the coefficients used to calculate the breakup frequency discussed in the next section.

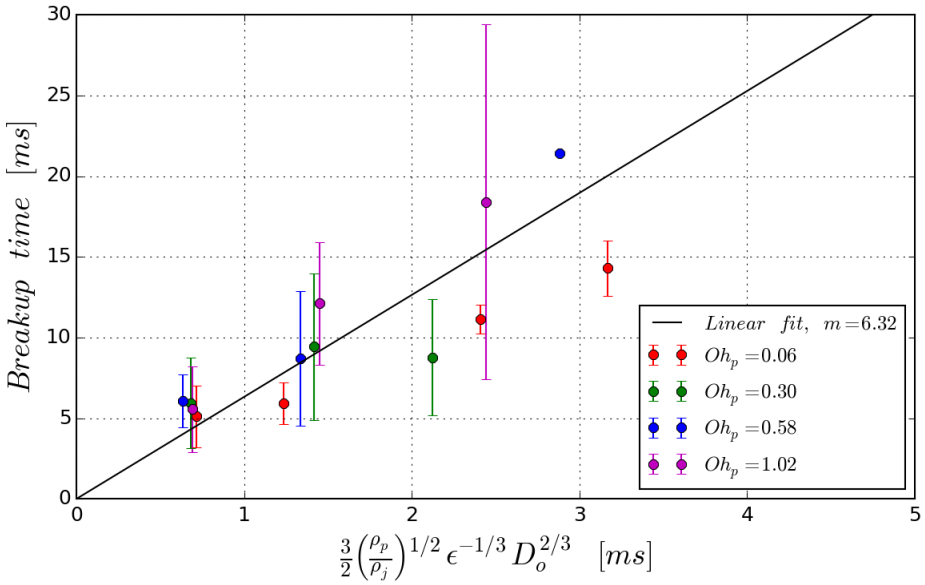

Figure 8.17: Breakup time prediction model using simplified stretching/thinning model. A linear fit is applied to the data.

8.5.2 Simplified breakup frequency model

The simplfied breakup time and stretching/thinning time models (Equation (8.20) and (8.21)) along with the breakup probability model (Equation (8.17) and (8.18)) were developed using the data obtained from the particle tracking algorithm. From the tracking algoirthm, we know whether a particle is going through the deformation stage or the stretching stage. This information is usually unavailable in practical applications. In most cases,

only a "snap shot" (initial condition) of the particle size and shape are known, so whether a given particle is in the deformation stage or the stretching stage cannot be determined using the method described in Section 8.2. However, it is important to know the distinction as the breakup frequency differ drastically between the two stages.

Although it is difficult to obtain the D-S transition based on the static information, it is not entirely impossible. Based on the D-S transition calculation of the four base fluids (Figure 8.18), we found that the deformation factor at the D-S transition are approximately the same for these experiments. The deformation factor has a mean of about 0.25. With the lack of dynamic information, $DF_{thres} = 0.25$ can be used as a threshold value to distingish whether a particle is in the deformation stage or stretching stage.

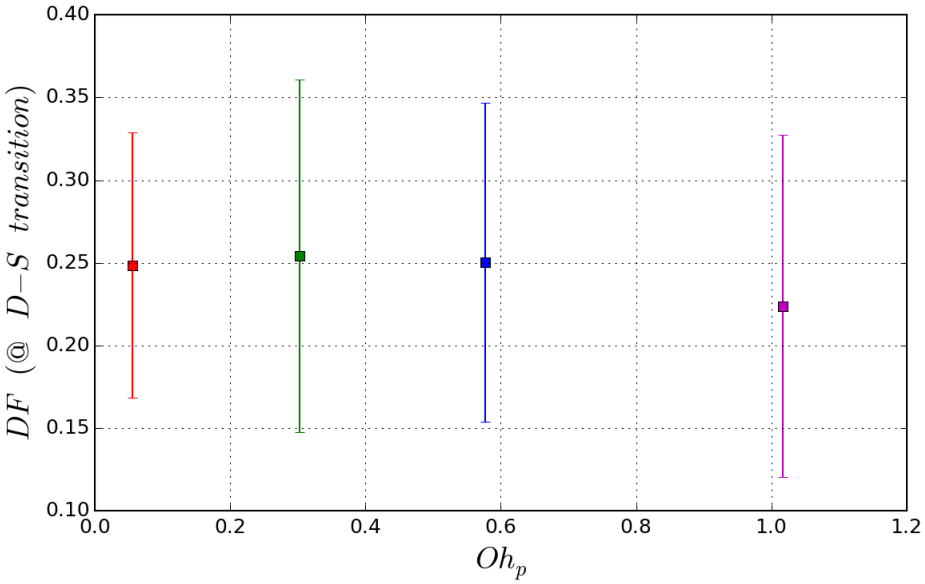

Figure 8.18: Deformation factor at the D-S transition for the 10 cSt, 100 cSt, 200 cSt silicone oils and canola oil.

With the threshold value in place, we can apply the appropriate model for each particle. Recall that when a particle enters the stretching stage, it always leads to breakup. So, if a particle has a deformation factor below DF_{thres}, the breakup probability is 1. Also,

the duration of the breakup event can be estimated by the simplified thinning time model (Equation (8.20)). On the other hand, if a particle has a deformation factor above DF_{thres}, the breakup probability is determined by Equations (8.17) and (8.18), and the duration of the breakup event can be estimated by the simplfied breakup time model (Equation (8.21)). Applying the appropriate models in Equation (8.13), we can summerize the breakup frequency model as follows:

$$g = \begin{cases} \left[\frac{3}{2} d_1 \left(\frac{\rho_p}{\rho_j}\right)^{1/2} \epsilon^{-1/3} (m_1 b_{e,DS}^{2/3} + c_1)\right]^{-1}, & DF \geq DF_{thres} \\ \left[\frac{3}{2} d_2 \left(\frac{\rho_p}{\rho_j}\right)^{1/2} \epsilon^{-1/3} (m_2 D_o^{2/3} + c_2)\right]^{-1} \left(a e^{-bR_s}\right), & DF < DF_{thres} \end{cases} \tag{8.22}$$

The constants a, b, c_1, c_2, d_1, d_2, m_1 and m_2 were obtained experimentally. a and b were obtained in the breakup probability analysis discussed in Section 8.4. m_1 and c_1 are linear fit coefficients relating $b_{e,DS}^{2/3}$ and $b_{e,DS}^{2/3} - b_{e,BU}^{2/3}$. m_2 and c_2 are linear fit coefficients relating $D_o^{2/3}$ and $D_o^{2/3} - b_{e,BU}^{2/3}$. d_1 and d_2 relate the simplified breakup time and stretching/thinning time models with the measured breakup time and stretching/thinning time, respectively.

8.5.3 Measured breakup frequency

To validate the breakup frequency model derived from the previous section, we can compare our model with the measured breakup frequency from experiments. The data used for validation is from the image sequences used in the particle size analysis (Chapter 7). These sequences were recorded at 60 fps, so only a "snap shot" of the particles is available as each particle appears only once in the sequence. This a good example where the complete thinning time model (Equation (8.7)) cannot be applied because of the lack of information. However, the simplified model (Equation (8.22)) is applicable in this situation.

The measured breakup frequency can be calculated from the experimental data through the population balance equation. Assuming particle coalesence is negligible and the process is in steady state, the population balance equation (Equation (2.4)) can be reduced to:

$$\frac{\partial(Un(D))}{\partial z} = \int_D^\infty m(D_o)f(D,D_o)g(D_o)n(D_o)dD_o - g(D)n(D) \tag{8.23}$$

where U is the mean velocity of the particle, n is the number density of particle, and g is the breakup frequency.

The first term on the right hand side of this equation represents the particles (daughter particles) generated from the breakup process. In order to solve for the breakup frequency in this equation, other closure functions in the first term are required. However, we can eliminate this term by limiting the particle size to the largest class size, D_m, available in the flow. Since particle coalesence is negligible, the number of the largest class size cannot be affected by the generation term as the breakup process cannot produce daughter particles larger than their mother. Applying the population balance equation to the largest class size particles, we obtain:

$$\frac{\partial(Un(D_m))}{\partial z} = -g(D_m)n(D_m) \tag{8.24}$$

Because $n(D_m) = N_p'/(AL_z)$, where AL_z is the volume of the interrogation zone, we can replace n with N_p'. Also, assuming the particles travel at the same veloity as the jet, we can replace U with U_o. Rearranging Equation (8.24) to isolate the breakup frequency on one side, we obtain:

$$g = -\frac{1}{N_p'}\frac{\partial(U_oN_p')}{\partial z} \tag{8.25}$$

N_p' is the number of particle per image. By dividing the field of view by interrogation zones, we obtain N_p' and U_o for each zone. This allows us to compute the derivative in the equation.

Using the same definition from Eastwood et al. [16], D_m is defined as the particles with diameter larger than D_{v90}. D_{v90} is defined such that 90% of the total dispersed phase volume in the first interrogation zone consists of particles with smaller diameter. With the largest class size defined, Figures 8.19 and 8.20 show the evolution of $N_p'(D \geq D_{v90})$ and

$N'_p(D \geq D_{v90})U_o$ over axial distance. The number of particles in the largest class size is small as there are less than 1 particle per frame. This indicates the sample size is small for these particles, which explains why the data are noisy. In order to perform the derivative in Equation (8.25), we need to smooth out the data by performing a power fit (shown as dashed lines). Notice that the $Re = 45000$ and $Re = 60000$ data are mostly flat. With small incremental differences of $N'_p(D \geq D_{v90})U_o$ along the axial distances, these data sets may not be reliable in the breakup frequency calculation. Thus, only the $Re = 80000$ data set is used for validation of the breakup frequency for different dispersed phase fluid experiments.

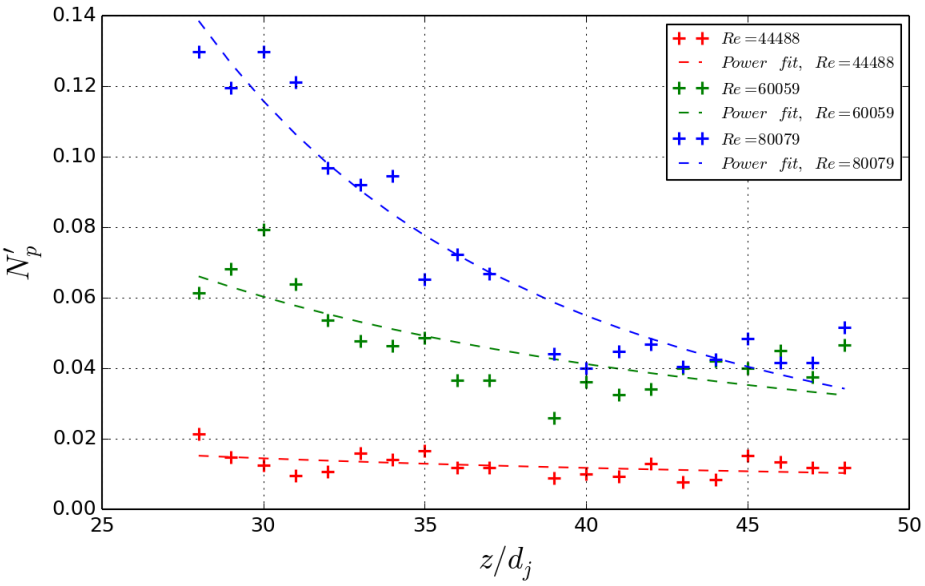

Figure 8.19: Evolution of $N'_p(D \geq D_{v90})$ over axial distances. 100 cSt silicone oil + 1000 ppm Triton X-100.

8.5.4 Validation of the breakup frequency model

Figures 8.21, 8.22 and 8.23 show the comparison between the measured and predicted breakup frequency. The predicted breakup frequency in Figures 8.21a, 8.22a and 8.23a is based on Equation (8.22) with the breakup probability set as 1 for all cases. Essentially, this

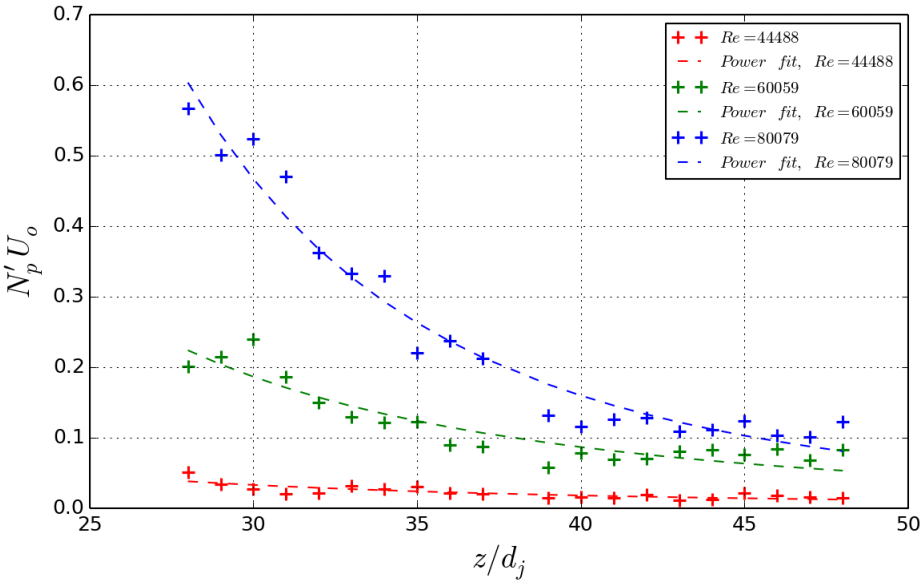

Figure 8.20: Evolution of $N_p'(D \geq D_{v90})U_o$ over axial distances. 100 cSt silicone oil + 1000 ppm Triton X-100.

means the breakup frequency is only calculated by the inverse of breakup time or stretching/thinning time. In Figures 8.21b, 8.22b and 8.23b, the predicted breakup frequency is based on Equation (8.22). The comparison between Figures (a) and (b) shows the effect of the breakup probability.

Without the breakup probability model, the model generally overpredicts the experimental data. This is expected as breakup is assumed to occur for all particles. Thus, there is no surprise that when the breakup probability model is included (Figures 8.21b, 8.22b and 8.23b), the prediction is lower. In fact, the predictions are slightly lower than the measured breakup frequency on all experiments. This can be attributed to several reasons. First, there could be more particles being in the stretching stage than our estimated D-S transition indicates. Breakup in the stretching stage is guaranteed and the breakup time is significantly shorter, so it will have higher breakup frequency. Second, the breakup time model (including deformation time) was derived based on the completed breakup paths, where the paths be-

gins with spherical particles. This means that our model predicts the limiting case of highest deformation time. In reality, when a particle is identified to be in the deformation stage, it could have undergone a significant period in this stage, so our model could overpredict the deformation time, resulting in a lower breakup frequency.

The slope of the predicted breakup frequency generally agrees well with the measured value. This is especially true in higher axial distance. However, at the begining of the field of view of the first camera location (between $z/d_j = 28$ to 32), the prediction has a shallower slope and significantly lower breakup frequency for all experiments. This is likely due to the velocity difference between the particles and the jet, which causes additional shearing effect on the particles that enhances the deformation process. As the particles accelerate to match the speed of the jet further downstream, the breakup process follows the mechanism described by the model. As a result, the predicted slope in this region agrees with the experimental data.

In Figure 8.22, the predictions without the breakup probability model are almost identical for the 10 cSt silicone oil with and without surfactant. Recall that the breakup time or stretching/thinning time model depends on the density ratio, the turbulent dissipation rate and the particle size. This indicates that the two experiments have similar D_{v90} as the density ratio and the turbulent dissipation rate should be the same. The breakup frequency for the case without surfactant decreases with the inclusion of the breakup probability model, while the breakup frequency stays mostly the same for the case with surfactant. The effect of surface tension is included in the breakup probability mode. The lower the surfactant, the higher the breakup probability with other variables being constant. Thus, in the case without surfactant, its surface tension is higher, which results in a lower breakup probability. On the other hand, the 10 cSt silicone oil + 1000 ppm Triton X-100 case has the lowest viscosity and the lowest surface tension among all experiments, so the model indicates the breakup probability is close to 1. This explains why the predictions with and without the breakup probability model are similar.

Note that all fitting parameters were obtained in the tracking analysis using the high-

speed image sequence data described in the earlier sections. No additional fitting parameters were used in predicting the breakup frequency. With many assumptions and simplifications in our breakup freqency model, such as the elimination of ligament thickness difference and the estimation of the D-S transition, the predictions are in good agreement with the measured values. This is a promising result suggesting the breakup frequency model is valid for the breakup of viscous particles and it can be used as the closure function in the population balance equation.

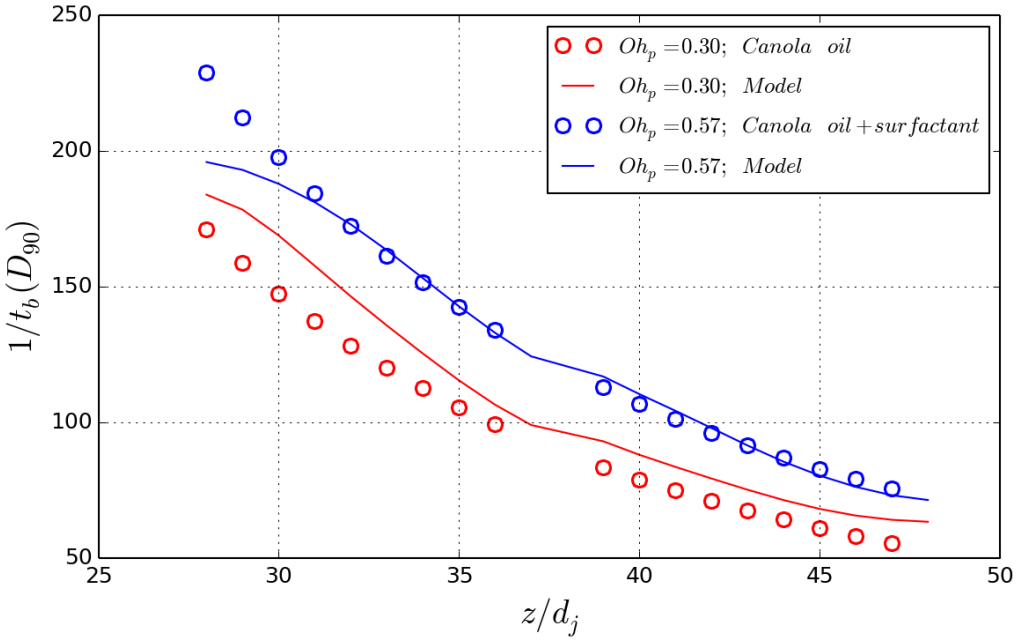

(a) Without breakup probability model

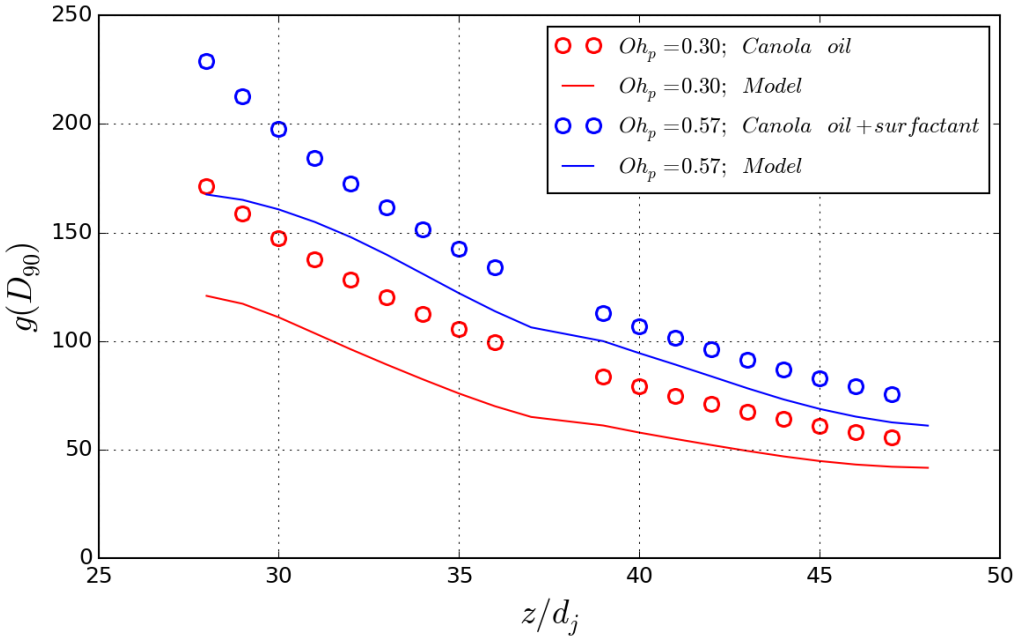

(b) With breakup probability model

Figure 8.21: Comparison between measured and predicted breakup frequency. Canola oil with 0 and 1000 ppm of Triton X-100. $Re = 80000$.

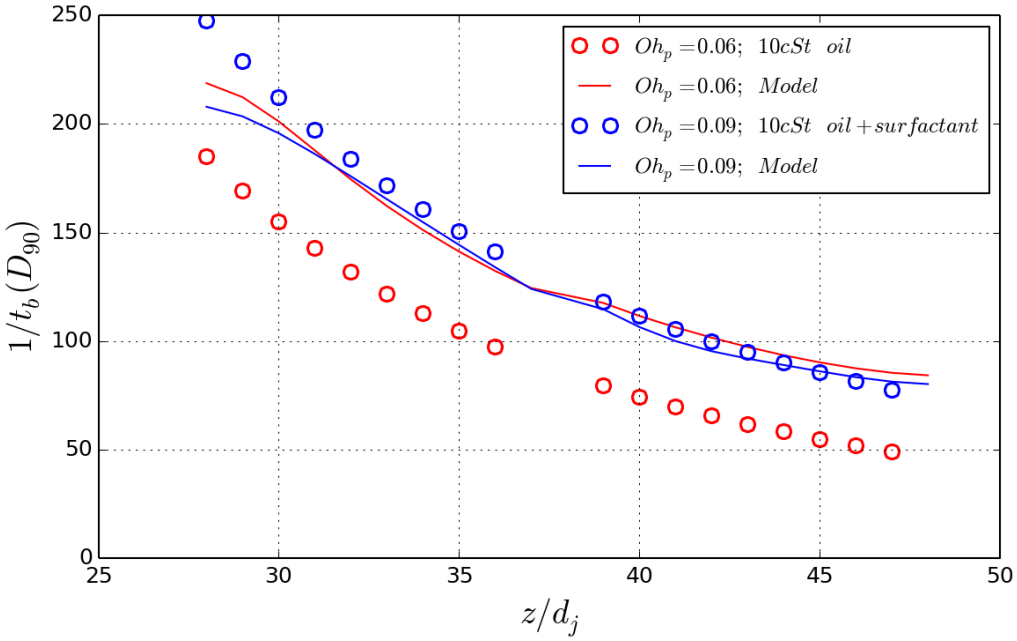

(a) Without breakup probability model

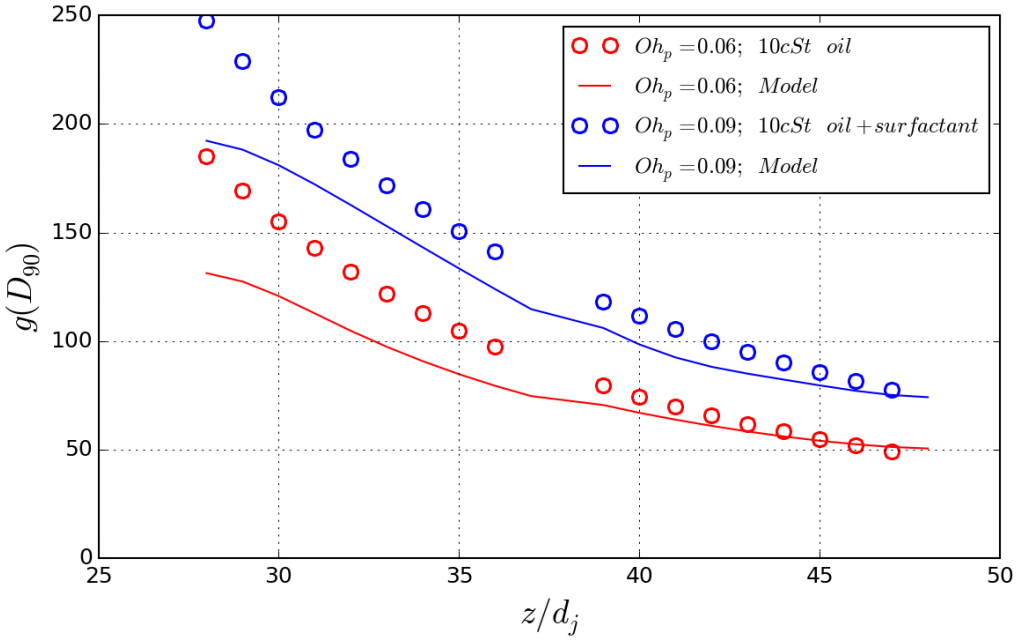

(b) With breakup probability model

Figure 8.22: Comparison between measured and predicted breakup frequency. 10 cSt silicone oil with 0 and 1000 ppm of Triton X-100. $Re = 80000$.

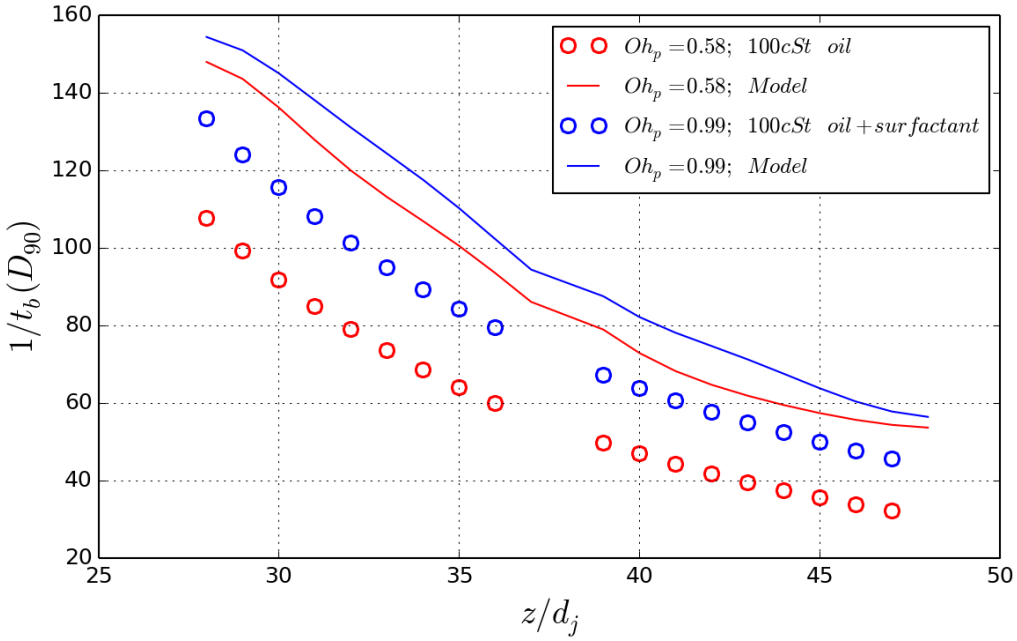

(a) Without breakup probability model

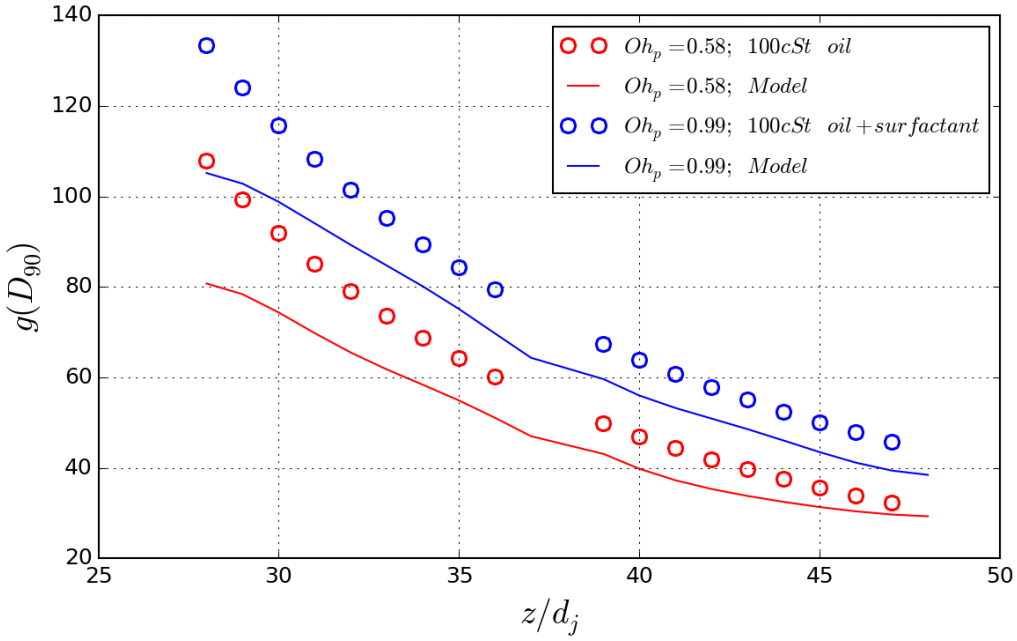

(b) With breakup probability model

Figure 8.23: Comparison between measured and predicted breakup frequency. 100 cSt silicone oil with 0 and 1000 ppm of Triton X-100. $Re = 80000$.

Chapter 9

SUMMARY AND CONCLUSIONS

This thesis focused on the breakup of particles in a turbulent jet. Prevous studies [16, 4, 3, 19] suggested that the breakup of oil drop behaves very differently than air bubbles. So, both dispersed phase fluids were investigated. The breakup of inviscid particles (air bubbles) was discussed in Chapter 6. The breakup of viscous particles (oil drops) was discussed in Chapters 7 and 8. The main objectives of these studies were to determine the size of the particle resulted from the breakup process and to understand the mechanism of the breakup. We addressed these objectives by utilizing different experimental techniques, developing a particle tracking code and modeling the mechanisms of the breakup process.

An experimental facility was designed and built to study the breakup dynamics of fluid particles in a high Reynolds number ($\mathcal{O}(10^5)$) turbulent jet. Particle Image Velocimetry was used to measure different properties of the jet. These properties were validated against published data to ensure a canonical turbulent round jet was achieved in our facility. Dispersed phase fluids, such as air bubbles and oil drops, were injected through an adjustable injection system into the jet inside a submerged tank. Images of the breakup events, in the form of shadowgraphs, were captured using a high-speed camera. Particle size, shape and other related information were extracted from these images using image processing and edge detection algorithms.

9.1 Breakup of inviscid particles

A series of experiments for the breakup of air bubbles with different combinations of the jet Reynolds number, the initial size distribution, air void fraction, and the injection location of the air bubbles were performed. This study focused on how these parameters affect the

resulting particle size from the breakup. The key observations from the experimental results are summarized as follows:

- The frozen state particle size and the turbulent dissipation rate have an exponential decay relationship. This indicates that the Kolmogorov-Hinze theory is valid for the breakup of air bubbles.

- We observed a weak dependence of the bubble void fraction on the size distribution. This could mean that the increase of bubble void fraction could suppress the underlying turbulence, which resulted in a larger bubble size. However, we currently do not possess the necessary data to support this hypothesis.

- No dependency of the initial bubble size distribution on the frozen state size distribution was found.

- The frozen state PDF is self-similar when the bubble diameter is normalized by the Sauter mean diameter. This implies that only one parameter, D_{32}, is requied to describe the entire frozen state size distribution.

One of the widely used particle size prediction models is the population balance equation. Closure functions, such as the breakup frequency and daughter particle size distribution, are required in this equation. As shown in Chapter 2, many researchers developed these closure functions based on the well established Kolmogorov-Hinze theory, which stated that the breakup is caused by the dynamic pressure forces of the turbulent motions that have similar length scale as the particle size.

Martínez-Bazán et al. [39, 40] developed a model based on the Kolmogorov-Hinze theory using a dynamic approach. We compared our experimental results of the breakup of air bubbles with Martínez-Bazán's model. We found that the model predicts the frozen state size distribution well. This confirmed that the breakup of inviscid particles follows the Kolmogorov-Hinze theory.

9.2 Breakup of viscous particles

We compared our experimental results of the breakup of viscous particles with Martínez-Bazán's model [39, 40]. Unlike in the case of inviscid particle breakup, we found that the model over-estimated the number of smaller particles and under-estimated the number of larger particles. This indicated that the Martínez-Bazán's model does not capture the complete mechanics of the viscous particle breakup process. Qualitative observation supports this claim as several unique breakup behaviors, such as the stretching of the particle and multi-breakage along the long string, were not observed in inviscid particle breakup.

In order to address how the dispersed phase fluid properties affect the particle size and the mechanisms of the breakup process, we performed experiments with 10 different dispersed phase fluids and 3 different Reynolds number jets. In these experiments, We_t ranges between 20 to 350 and Oh_p ranges between 0.05 to 1.

9.2.1 Particle size analysis

The aim of this analysis is to study how the fluid properties affect particle size at different location of the jet. The conclusions of this analysis can be summerized as follows:

- The higher the dispersed phase viscosity is, the larger the frozen state particle size will be. This indicates viscosity has a damping effect on the breakup process.

- The added surfactant reduces the frozen state particle size. However, the effect of surfactant approaches to an asymptotic behavior at high Weber number.

- The frozen state particle size does not follow the Weber number scaling model that was previously shown to be valid for inviscid particle in other studies.

- A model was formulated to predict the frozen state particle size, D_{32}, using a stress balance between the turbulent disruptive stress, internal viscous stress, and the surface restoration pressure.

- All data collapsed into a single curve when scaled with the model. This confirms that both viscosity and surface tension resist the breakup process.

- An additional Reynolds number scaling is needed for the model. The Reynolds number represents the mean flow, so this scaling accounts for the large scale motions involved in the breakup process. It is consistent with the observed integral scale stretching mechanism.

9.2.2 Breakup event analysis

This analysis aimed to understand the different mechanisms involved in the breakup process. In the particle size analysis, only "snap shots" of the particles information were needed because the evolution of the size distribution is a steady state process. In contrast, each individual breakup event is a transient process, so high speed image sequences were used to study the breakup events.

From the high speed sequence of the breakup of viscous particles, we observed that the breakup sequence can be divided into three stages. The visual description of each stage can be summarized as follows:

1. Deformation stage: Small deformation occurs on the particle. The degree of the deformation is on the order of the particle size.

2. Stretching/thinning stage: Particle is stretched to multiple times its initial diameter and formed a ligament. A thinning process occurs during this stage that reduces the thickness of the center portion of the ligament into a thin string. As the ligament gets longer, thinning occurs faster in some locations than others, creating an alternating strings and fluid lumps pattern.

3. Disintegration stage: The thin strings are too thin to sustain any continuous stretching/thinning, so they disintegrate and recoil back to the nearby fluid lumps, forming

daughter particles. Note that the disintegration of the strings occurs almost simultaneously. However, if a daughter ligament is formed, the secondary breakup occurs in a later time, essentially forming its own breakup path.

In additional to the quantitative observation of these sequences, we developed a particle tracking algorithm specifically designed to extract information of particles along their breakup paths. The Ligament Identifiation and Back-Tracking (LIBT) algorithm utilizes the unique behaviors of viscous particles in the breakup path to accurately identify the breakup point and track the particles through particle-dense regions.

One of the results obtained from LIBT was the progression of the deformation factor of a particle along the breakup path. It confirmed the qualitative observed deformation and stretching/thinning stages. Data suggest that a particle in the deformation stage experiences a few cycles of deformation (fluctuating DF). This indicates that a particle is collided by multiple series of eddies until one that has enough energy to push the particle to the stretching stage. When a particle reaches the stretching stage, it has a rapid monotonic increase in DF. In this stage, the particle is stretched to multiple times its original length. Because the stretching is one-directional, it suggests that the stretching is caused by interaction with only one large scale (integral scale) eddy. The contrasting behaviors of DF between the two stages allow us to identify the deformation to stretching (D-S) transition.

The breakup time of a particle is divided into the deformation time and stretching/thinning time. Although the stretching mechanism is caused by integral scale motion of the jet, it does not dictate the stretching/thinning time. We found that the thinning of the ligament due to the stretching mechanism (through volume conservation) occurs much slower than the thinning due to the collision of eddies with similar size as the width of the ligament. Thus, the stretching/thinning time is dictated by the history of eddy collision on the ligament. However, the stretching mechanism forces the deformation (stretching) to be one directional so that it enhances the effectiveness of eddy collisions as all collisions contribute only to thinning of the ligament.

Because of the stochastic nature, the duration of the deformation stage cannot be accurately predicted. The fluctuating behavior of DF implies that whether a particle breaks is determined in the deformation stage. In contrast, no stretched ligament has been observed to revert back to a spherical particle. This means that breakup is guaranteed once a particle reaches the stretching/thinning stage.

We found an exponential relationship between the breakup probability and the stress ratio. The stress ratio is the ratio between the confinement stresses and the disruptive stress. The confinement stresses includes the internal viscous stress and the pressure restoration pressure. Because the probability of a breakup event is determined in the deformation stage, where the particles have not been stretched into the integral length scale, the disruptive stress is derived from the Kolmogorov-Hinze mechanism.

One of the closure functions used in the population balance equation is the breakup frequency. The breakup frequency can be obtained by combining the breakup time and breakup probability models. Typical applications provide only static input (no data along tracking paths), so we modified our model to accommodate these situations. We compared our simplified breakup frequency model with the experimentally measured breakup frequency. We found that our model predicts the decaying slope along the axial distance well, especially in higher axial distance. In terms of the magnitude of the breakup frequency, the model slightly under-predicts the experimental data, but the difference is acceptable considering the necessary simplifications made in the model.

9.3 Future work

The stretching/thinning time shows a linear correlation with our model, but the results have a relatively large variance. The main reason is that the exact flow condition (turbulent dissipation rate) around the particle is unknown because the true location of the particle in the 3 dimensional space is unknown. Although the true axial location can be identified in an image, the relative distance of the particle from the focal plane (depth) was not captured in the image. A second camera with a line of view perpendicular to the original camera is needed

to provide 3 dimensional coordinates of the particle. Another benefit of using two cameras is that it can capture the change in orientation of the highly deformed particles/ligaments. With only one line of view, the algorithm cannot distinguish if the change in DF is due to the rotation or the actual deformation of the particle. With two cameras, the spurious change in DF can be eliminated. Because the D-S transition is determined by the progression of the DF, it can be more accurately determined.

The deformation time has not been accurately modeled because it depends on the number of deformation cycles. Whether a series of eddy collisions is strong enough to send the particle to the stretching stage depends on various factors, such as the strength of the eddies and the direction of the collision. However, these factors may be modeled statistically in order to estimate the number of deformation cycles until a particle reaches the stretching stage. This could lead to a more accurate model of the deformation time.

Our data show that the frozen state particle size depends on the surface tension between the two phases, but the effect is not significant. In fact, we observed a reduction of the effectiveness of the surfactant in high Reynolds number case. With the highest concentration of surfactant in our experiments, the surface tension reduced to about 1/3 of the original value. For the surfactant to be effective in reducing the particle size, such as in the oil spill situation, higher concentration of surfactant is needed. Therefore, experiments with higher concentration surfactant is valuable in validating the existing models.

Although we were able to develop a model to predict the frozen state particle size, some applications might require a more detail description of the particle size. The population balance equation provides the complete evolution of the particle size distribution, but solving this equation required models of the closure functions. In addition to the breakup frequency model, the number of daughter particles and the daughter particle size distribution are the other two required closure functions. In many previous studies, binary breakup is assumed. Our high speed image sequences showed that this assumption is invalid for the breakup of viscous particles. In addition, none of the daughter particle size distribution model has been directly verified with experiments. Thus, it is important to measure the daughter particles

size produced from individual breakup events in order to develop accurate models for these closure functions.

In Chapter 5, we proposed a daughter particle identification algorithm. This algorithm works reasonably well in region of low particle density. However, we encountered false identifications in high particle density region. Since the algorithm relies on eliminating surrounding particles that do not belongs to a breakup path, it is not a direct tracking between the mother and daughter particles. In addition, daughter particles typically have a more spherical shape, so it is more difficult to differentiate them with the surrounding particles.

A potential method to improve the accuracy of the daughter particle identification algorithm is to provide tracking of all particles as the input to the algorithm. With a more robust tracking of the surrounding particles (by using more than 1 pair of images), it could reduce false daughter identification. However, the current LIBT algorithm only tracks particles that break. This implies that a complete revamp of the tracking algorithm is necessary.

An alternative would be to perform experiments with a lower particle density. This cannot be achieved easily in a turbulent jet setup. The dispersed phase fluid cannot be introduced into the jet as an individual particle because the velocity difference would immediately break the particle before it accelerates to match the speed of the jet. The particles captured from our experiments are the results of the breakup of continuously injected oil stream. Thus, a different experimental setup with a low mean velocity that allows injection of a single or a few mother particles into the turbulent flow would be ideal for studying the mechanism of daughter particles generation.

Appendix A

AERODYNAMIC BREAKUP: COAXIAL TWIN-FLUID ATOMIZATION WITH PATTERN AIR STREAMS

A.1 Introduction

Atomization of liquid jet is a fundamental problem in multiphase flows with very high industrial relevance. In the pharmaceutical industry, the coating of the tablets is applied by atomizing the coating solution using specially designed atomizers. This tablet-coating process requires very fine droplet size. To achieve fine droplet size in a single-fluid atomizer, it requires a high liquid flow rate. However, the liquid flow rate is limited by the amount of coating solution needed, so it is generally not high enough to achieve the intended droplets size. Because of the lack of balance between liquid flow rate and droplets size for a single-fluid atomizer, the pharmaceutical industry typically uses a coaxial twin-fluid atomizer. In this configuration, the liquid jet is surrounded by an annular high-speed air jet. The high relative velocity between the liquid and air jet is the source of energy for the atomization process.

Pattern air (PA) is used in conjunction with the traditional coaxial twin-fluid atomizer setup in applications where a circular spray pattern is not as desirable as other spray patterns. For example, in the tablet-coating process, a large amount of tablets is placed in a rotating drum which moves the tablets across the spraying zone. Multiple atomizers are mounted inside the drum to create a spraying zone that fills the width of the rotating drum by juxtaposition of the elliptical individual spray areas without overlap [67]. A wider elliptical spray pattern reduces the number of atomizers needed to fill a rectangular strip of the tablet bed surface inside the rotating drum (Figure A.1). In addition, all tablets experience similar residence times in the spraying zone, in an elliptical spray compared to an axisymmetric

spray, resulting in a more consistent coating on the tablets.

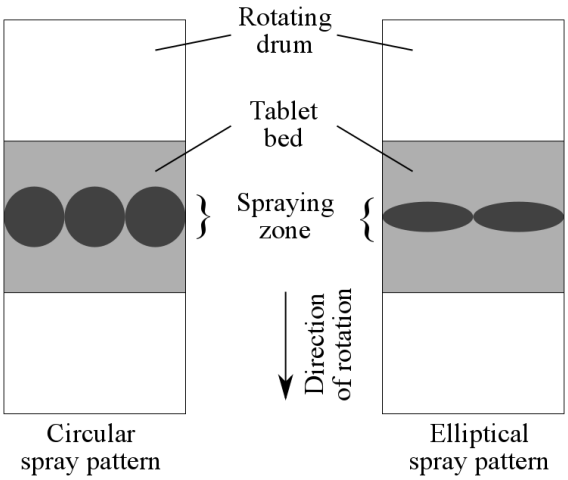

Figure A.1: Comparison between circular and elliptical spray patterns for the tablets coating process. A view from the cross-section of a rotating drum looking down on the tablet bed.

Although this type of patterned-spray atomizer has been studied in applied research related to specific uses in industry for many years, very little is known about the influence of pattern air on the jet breakup mechanism or the impact of pattern air on droplet size segregation and volume fraction inside the spray. Aulton and Twitchell [5] investigated various spray guns with pattern air and provided only quantitative results about the size distribution. Muller and Kleinebudde [44] investigated the influence of pattern air on various spray parameters, such as droplet size, droplet velocity, and spray density. They found that droplets migrate from the spray center to the spray rim with the presence of pattern air. They also found that droplets size decreases in the spray center, but remains unaffected in the spray rim under their test conditions. In the effort to extend the understanding on the effect of pattern air, we focus on studying the droplet size distribution experimentally and developing a model to predict the droplet size of an atomization process with pattern air.

A.2 Experimental setup

A.2.1 Atomizer

The Schlick 970/7-1 S75 atomizer is chosen for this study as a representative example of a coaxial two fluid injector with independent pattern air control. Since our study focuses on the influence of pattern air on spray dynamics, we implemented a system that allowed for flexibility in setting the liquid and coaxial gas streams flow rates in the range relevant to the shear-driven turbulent gas atomization, as well as independent adjustment of the pattern air flow rate from zero to a value equal to the atomizing air flow rate. This typical coaxial twin-fluid atomizer consists of a round liquid nozzle along the axis of symmetry, and an annular gas nozzle, that introduces the atomizing air (AA). In addition, there are two pattern air ports oriented at a 45 degree angle from the centerline and positioned on each side of the centerline symmetrically. These ports are also located slightly behind the liquid nozzle, unlike in the traditional "horn-cap" design. This allows the two 45 degree oriented pattern air streams to impinge on the centerline at only 3.25 mm away from the liquid nozzle, well within the developing region of the shear instability, and thus influencing the break up process. A schematic of the atomizer is shown in Figure A.2 and the dimensions are shown in Table A.1.

Symbol	**Length [mm]**	**Description**
D_l	1	Liquid jet diameter
D_i	1.85	Inner diameter of atomizing air
D_o	2.7	Outer diameter of atomizing air
D_{PA}	1.5	Pattern air port diameter (two total)

Table A.1: Schlick atomizer dimension.

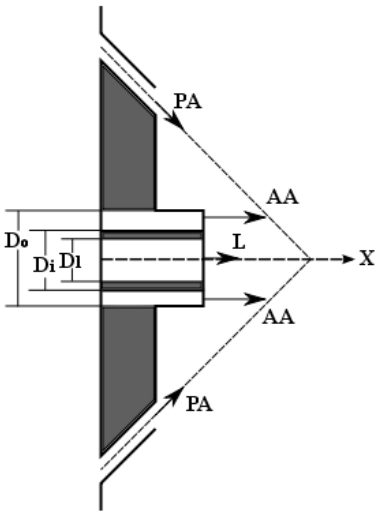

Figure A.2: Cross-sectional view of the Schlick atomizer.

A.2.2 Flow conditions

Experiments are performed injecting water at a constant flow rate of 20 grams/min. This value is chosen to be within the range of the typical operating condition for this atomizer, consistent with negligible momentum in the liquid jet compared to the high speed coaxial gas stream. Three different atomizing air flow rates (28, 42 and 56 liters per minute, LPM) are examined. The highest atomizing air flow rate is chosen so that the resulting velocity is about 10% below the speed of sound to avoid sonic conditions at the nozzle throat. In addition, studies [12] have shown that optimal atomization occurs at values of the mass flux ratio (defined in later section) between 0.1 to 10, with lower values representing finer droplet sizes. In this study, the mass flux ratio ranges between 0.3 to 0.6. Another important dimensionless quantity is the PA/AA ratio. It will be shown that different PA/AA ratio not only changes the shape of the spray, but also the distribution of the droplets. A previous study [43] using the same type of injectors revealed that the maximum value of the PA/AA ratio before the spray takes a dumbbell pattern, a negative development for coating coverage, is about 1. In this study, for each atomizing air flow rate, three PA/AA ratios are investigated

(0, 0.5 and 1) for a total of nine different flow cases.

A.2.3 Measurement and data analysis

Droplets size and velocity measurements are collected by a Phase Doppler Particle Analyzer (TSI Inc., Shoreview, MN), referred to as PDPA. In this system, an argon laser beam is separated into three pairs of color beams: green, blue, and violet. Only the green lasers, with wavelength of 514.5 nm, are used in the experiment. The pairs of laser beams, with the same intensity but a predetermined shift in frequency, are transmitted and focused on a specified location within the spray through the transmitter. The intersection of the two lasers creates a probe volume where all the measurement take place. Droplets passing through this probe volume scatter light in all direction. This scattered light is collected by the receiver oriented at a 70 degree angle with respect to the transmitter. This is done in order to maximize the amount of light scattered by refraction and the sensitivity of the diameter measurements. The scattered light is received by three photodetectors and processed by the Photodetector Modules (PDM) and Flow Size Analyzer (FSA) to obtain raw data, such as the Doppler frequency and phase shift of the scattered light between photodetectors. Using the Doppler theory, the frequency shift is converted to the velocity of the droplet, while Mie scattering theory allows for the phase shift to be converted into droplet sizes. The PDPA system was setup, with a combination of optics and sampling frequency, to measure droplets in the size range from 1.5 to 600 μm and axial velocity up to 90 m/s. Appendix B provides a more in depth description on the physics of these measuring techniques.

A.3 Breakup mechanism of coaxial twin-fluid atomization

The breakup mechanism of the twin-fluid atomization involves a multiphysics process governed by several non-dimensional parameters: (1) the Weber number, $We = \rho_g(U_g - U_l)^2 D_l/\sigma$, represents the ratio between inertial forces that distort the droplets and stabilizing surface tension forces; (2) the Ohnesorge number, $Oh = \mu_l/(\rho_l D_l \sigma)^{1/2}$, represents the ratio between viscous effects and surface tension effects; (3) the dynamic pressure ratio,

$M = \rho_g U_g^2 / \rho_l U_l^2$; and (4) the mass flux ratio, $m = \rho_l U_l A_l / \rho_g U_g A_g$. Note that ρ_g and ρ_l are the density of the gas and liquid; σ is the surface tension; μ_l is the viscosity of the liquid; U_g and U_l are the exit velocities of the gas and liquid; A_g and A_l are the gas and liquid exit cross-sectional areas. These non-dimensional numbers can affect the effectiveness of the atomization [12] or they can completely change the breakup mechanism [50].

In the case of highest interest, with high Weber number ($We > 350$), high dynamic pressure ratio and low mass flux ratio ($m < 1$), the breakup can be described by a two-stage breakup mechanism proposed by Pilch and Erdman [50]. They suggested that the breakup is due to two different instabilities: the Kelvin-Helmholtz and Rayleigh-Taylor instabilities. Varga et al. [69] performed experiments of the twin-fluid atomization using high-speed imaging techniques. They observed the two-stage breakup mechanism from the images as suggested by Pilch and Erdman [50]. In the near nozzle region, waves developed at the liquid jet surface. The wave crests grow into ligaments along the axial direction. This is considered to be the first stage of the breakup mechanism, or the primary instability.

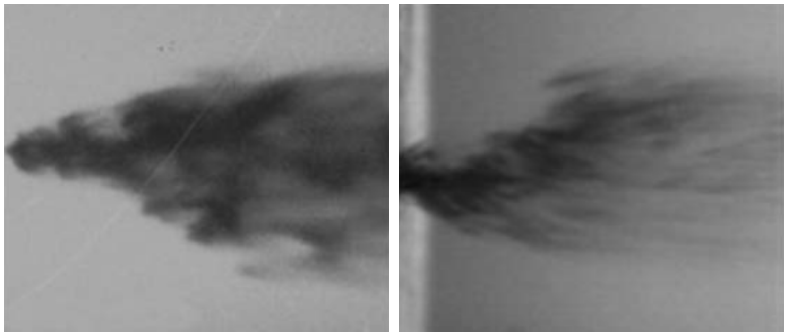

(a) (b)

Figure A.3: A comparison between the breakup of a drop (left) and the breakup of a jet (right) at high Weber number. Varga et al. [69].

Once the ligaments grow long enough, they break into droplets. From the high-speed images, Varga et al. [69] noticed a visual resemblance between the ligament breakup and the

experiments done by Joseph et al. [28], where a liquid drop was exposed to a high-speed gas flow. A comparison of the instantaneous images of the two experiments is shown in Figure A.3. The breakup in both cases started from the wave formation on the liquid (drop or ligament) surface. These waves penetrate the drop or ligaments, eventually breaking up into smaller droplets. The formation of these waves on the ligaments surface is considered to be the second stage of the breakup, or the secondary instability. Because of the resemblance, Varga et al. [69] analyzed the secondary instability and showed quantitatively that its scaling is associated with the Rayleigh-Taylor instability that occurs in the drop breakup experiment.

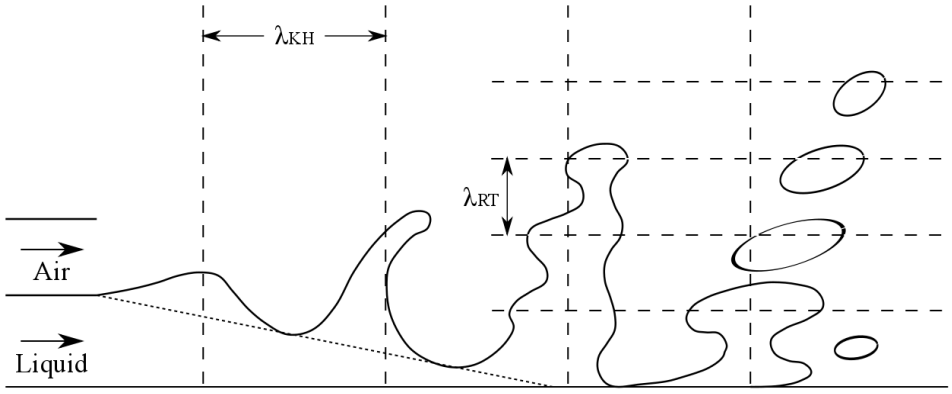

Figure A.4: Illustration of liquid jet breakup due to Kelvin-Helmholtz and Rayleigh-Taylor instabilities. λ_{KH} is the wavelength of the Kelvin-Helmholtz instability. λ_{RT} is the wavelength of Rayleigh-Taylor instability.

A.3.1 Primary instability

The primary instability refers to the shear instability that occurs at the gas/liquid interface upon exit of the nozzle. In the limiting case where $U_g = 0$ (injecting liquid jet in stagnant atmosphere), the Weber number is small. The breakup mechanism is capillary driven because of the circular geometry of the jet. This results into the Plateau-Rayleigh instability. With Plateau-Rayleigh instability, Marmottant and Villermaux [38] found that the undulations

grow along the jet with a wavelength of $4.51D_l$. The resulting droplets also breakup in the size on the order of this wavelength.

As U_g increases, the Weber number increases. At some point, the shear force overcomes the surface tension effects. The primary instability is no longer due to Plateau-Rayleigh instability. Instead, Kelvin-Helmholtz instability becomes the primary instability mechanism. From the classical Kelvin-Helmholtz instability analysis, the growth rate is:

$$n = \frac{k}{\rho_l + \rho_g}\sqrt{\rho_l\rho_g(U_g - U_l)^2 - (\rho_l + \rho_g)\sigma k} \tag{A.1}$$

where n is the growth rate. k is the wave number.

Assuming $\rho_l \gg \rho_g$ and $U_g \gg U_l$, the most amplified wavenumber, k_m, can be found by solving $dn/dk = 0$. k_m becomes:

$$k_m = \frac{2}{3}\frac{\rho_g U_g^2}{\sigma} \tag{A.2}$$

This analysis assumed a velocity discontinuity at the gas-liquid interface. However, since the gas stream and the liquid jet are accelerated separately, with a rigid boundary between them until they exit the nozzle, boundary layers developed for both phases. Thus, upon the exit from the nozzle, a vorticity layer, the region where the velocity profile has an inflection point, developed at the interface. Rayleigh [58] performed stability analysis of the vorticity layer and he showed that the vorticity layer affects the selection of the mode of the instability. Marmottant and Villermaux [38] extended Rayleigh's study to include the density difference between the two phases. They showed that with the assumption that $U_g \gg U_l$, the most amplified wavenumber and the associated growth rate are:

$$k_m \simeq \frac{1}{C_1}\left(\frac{\rho_g}{\rho_l}\right)^{1/2}\frac{1}{\delta_g} \tag{A.3}$$

$$n(k_m) \simeq \frac{\rho_g}{\rho_l}\frac{U_g}{\delta_g} \tag{A.4}$$

where δ_g is the boundary layer thickness of the gas phase.

This implies that the wavelength of the most amplified waves, $\lambda_m = 2\pi/k_m$, is proportional to the the gas boundary thickness. This is consistent with the experiments performed by [38]. Figure A.5 shows that the λ_m to δ_g ratio is mostly constant.

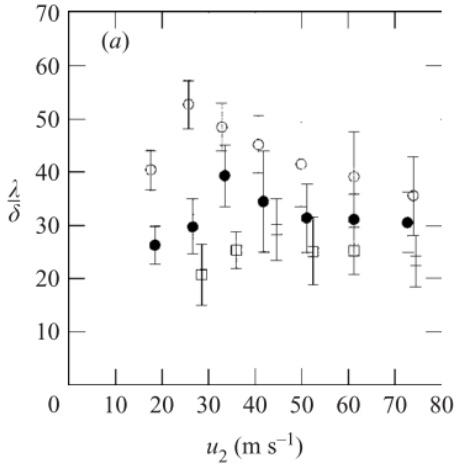

Figure A.5: Ratio of the wavelength of the primary instability to the boundary layer thickness of the gas phase as a function of gas velocity. ∘, U_l = 0.45 m/s; •, 0.94 m/s; □, 2 m/s. Marmottant and Villermaux [38]

A.3.2 Secondary instability

As discussed in the previous section, the breakup due to the secondary instability is believe to have the same mechanism as the breakup of a liquid drop exposed to high-speed gas flow. In essence, the drop breakup problem is equivalent to the classic Rayleigh-Taylor instability problem, where heavier fluid is accelerated onto a lighter fluid. From the high-speed image sequences of obtained by Joseph et al. [27], the drop is first observed to flatten due to the pressure different between the front and the back of the drop. Then, waves form on the surface of the drop which is perpendicular of the flow direction (Figure A.6). Finally, smaller droplets are stripped from the drop. The resemblance between the surface waves on the drop and the waves formed at the interface between the two fluids in the Rayleigh-Taylor

instability problem gives support to the theory that the breakup is due to Rayleigh-Taylor instability. Joseph et al. [27] provided a detailed stability analysis on the drop breakup problem. Using the fully viscous theory and assuming $\rho_l \gg \rho_g$, the dispersion relation is given in Equation (A.5).

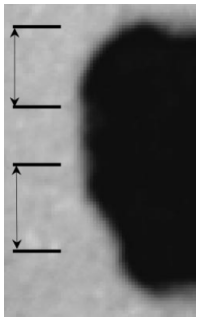

Figure A.6: Rayleigh-Taylor waves observed on the surface of a drop silicone oil drop exposed in high-speed air flow. (Joseph et al. [27]).

$$-\left[1+\frac{1}{n^2}\left(-ak+\frac{\sigma k^3}{\rho_l}\right)\right]+4\frac{k^2}{n}\frac{\alpha_l}{\rho_l}+4\frac{k^3}{n^2}\left(\frac{\alpha_l}{\rho_l}\right)^2(q_l-k)=0 \tag{A.5}$$

where a is the acceleration of the drop, α_l (Equation (A.6)) is the effective shear viscosity of the liquid, and $q_l=\sqrt{k^2+\omega\rho_l/\alpha_l}$.

$$\alpha_l=\mu_l\frac{1+\lambda_2\omega}{1+\lambda_1\omega} \tag{A.6}$$

where λ_1 is the relaxation time, λ_2 is the retardation time.

The critical wavenumber, k_c, can be found from this relationship (Equation (A.7)) by setting $n=0$ and solving for k. Stability is found when $k > k_c$. As a result, if the drop diameter is smaller than the critical wavelength, $\lambda_c = 2\pi/k_c$, the Rayleigh-Taylor instability does not develop on the drop.

$$k_c=\sqrt{\frac{\rho_l a}{\sigma}} \tag{A.7}$$

In addition to the fully viscous theory, Joseph et al. [27] performed the analysis with the viscous potential flow theory. By assuming the perturbation velocity is given by $\mathbf{u} = \nabla\phi$, and again, $\rho_l \gg \rho_g$, the dispersion relation is given in the form of Equation (A.8). They also provided a comparison between the two theories (Equations (A.5) and (A.8)) in Table A.2. The comparison showed that the wavenumber value of the viscous potential theory is within 5.5% of the fully viscous theory except for two cases and the value of the growth rate is within 9% difference.

$$1 = \frac{ka}{n^2} - \frac{k^3\sigma}{n^2\rho_l} - \frac{2k^2\alpha_l}{n\rho_l} \tag{A.8}$$

	Fully viscoelastic			Viscoelastic potential			Percent difference	
λ_2 (s^{-1})	k (m^{-1})	l (mm)	n (s^{-1})	k (m^{-1})	l (mm)	n (s^{-1})	k	n
$\lambda_1/5$	600	10.472	6331.7	800	7.8539	6870.9	33.3	8.5
$\lambda_1/8$	1000	6.2832	7425.1	1000	6.2832	8077.7	0	8.8
$\lambda_1/10$	1000	6.2832	7991.5	1200	5.2359	8684.8	20.0	8.2
$\lambda_1/20$	1800	3.4907	10061.5	1800	3.4907	10945.9	0	8.8
$\lambda_1/100$	4800	1.3090	17000.0	5000	1.2566	18489.8	4.2	8.8
$\lambda_1/1000$	15 000	0.4189	32238.7	15 800	0.3977	34849.6	5.3	8.1
$\lambda_1/10\,000$	22 400	0.2805	43036.2	23 600	0.2662	45074.9	5.4	4.7
0	24 200	0.2596	45697.3	25 000	0.2513	47119.7	3.3	3.1

Table A.2: A comparison between the fully viscous theory and the viscous potential theory. k is the wavenumber, l is the wavelength, n is the growth rate, λ_1 is the relaxation time, and λ_2 is the retardation time. Joseph et al. [27]

The major factor causing the Rayleigh-Taylor instability is the acceleration of the drop. Qualitative observation from experiments reveals that at low enough acceleration (lower gas velocity), liquid is stripped off from the drop. On the other hand, at high enough acceleration (higher gas velocity), the breakup is catastrophic and the resulting droplets are smaller. This suggests that acceleration promotes growth rate (faster breakup) and decreases wavelength (smaller resulting droplets). Using the dispersion relation, Joseph et al. [27] compared the effect of acceleration on the dispersion relation (Figure A.7). The results confirm with

the qualitative observation that acceleration increases the growth rate and decreases the wavelength of the most amplified mode.

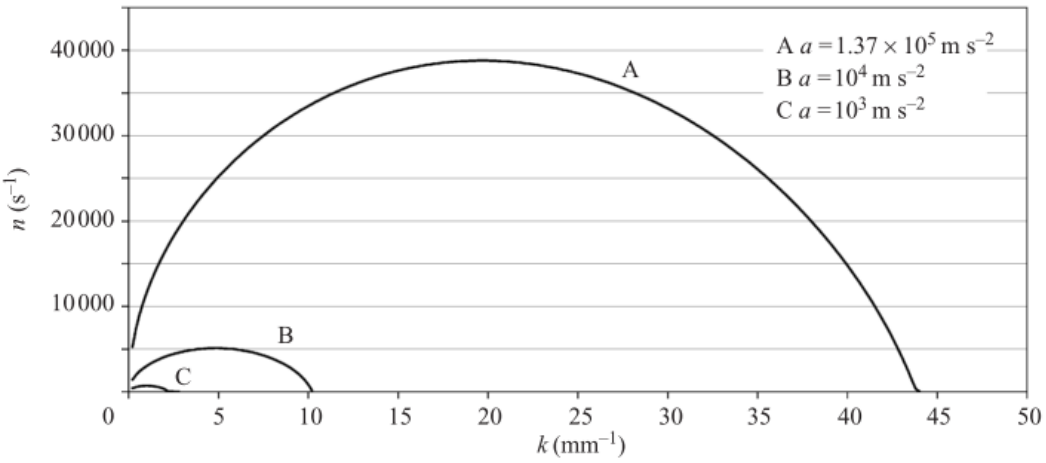

Figure A.7: The effect of acceleration on dispersion relation. (Joseph et al. [27]).

A.4 Prediction model of droplet size

As early in the 19$^{\text{th}}$ century, Rayleigh [57] used surface energy arguments to predict the drop size of a falling liquid jet. Since then, various models has been developed for different kinds of injectors. The prediction of the droplet size in a spray, specifically from a coaxial twin-fluid atomizer, has been studied by many researchers. Models developed by [60, 63, 26, 17, 37] are mostly empirical. Vargas et al. [69] and Aliseda et al. [2] developed models based on the two-stage breakup mechanism. The difference between these two models is that Varga et al. [69] used an inviscid dispersion relation for the Rayleigh-Taylor wavelength, whereas Aliseda et al. [2] used a simplified viscous dispersion relation. Our model is based on these two models with two modifications: (1) accounting for the effect of pattern air on the gas velocity and ligament acceleration and (2) applying the viscous potential theory to calculate the Rayleigh-Taylor wavelength.

The resulting droplet size of a twin-fluid atomization is related to the wavelength of the

two instability mechanisms. As discussed in Section A.3.1, the wavelength of the primary instability is related to the vorticity layer. Converting the most amplified wavenumber from Equation (A.3) to wavelength, we get:

$$\lambda_{KH} = C_1 \delta_g \sqrt{\frac{\rho_l}{\rho_g}} \tag{A.9}$$

where $C_1 \approx 4$ for planar shear layer and $C_1 \approx 1.2$ for coaxial twin-fluid jet configuration (Marmottant and Villermaux, 2004). The vorticity layer thickness is proportional to the gas boundary layer thickness, so it can be written as:

$$\delta_g = \frac{C_2 b_g}{\sqrt{Re_{bg}}} \tag{A.10}$$

where C_2 is a constant that depends on the nozzle design, b_g is the thickness of the gas stream as shown in Figure (A.8), and $Re_{bg} = U_{AA} b_g / \nu_g$. U_{AA} is the velocity of the atomizing air.

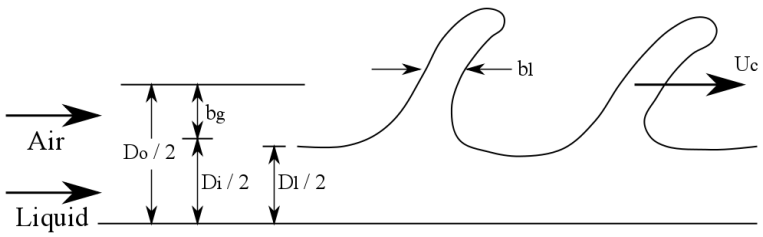

Figure A.8: Illustration of liquid ligaments thickness (b_l), velocity (U_c), and vorticity layer thickness (b_g).

The wavelength of the secondary instability can be found using the dispersion relation derived by Joseph et al. [27]. As shown in Table A.2, the viscous potential theory agrees well with the fully viscous theory. Since the dispersion relation derived from the viscous potential theory is easier to work with, it is chosen in this model. The dispersion relation (Equation A.8) can be written as the growth rate as a function of wavenumber:

$$n = \frac{-k^2\alpha_l}{\rho_l} \pm \sqrt{\frac{k^4\alpha_l^2}{\rho_l^2} - \frac{k^3\sigma}{\rho_l} + ka} \tag{A.11}$$

Since the first term is always negative, the second term has to be positive and greater than the first term for instability to occur. Taking the positive sign on the second term, the most amplified wavenumber can be found by taking the k at maximum n. However, the acceleration, a, is unknown at this point. In [27], a is the acceleration of the drop. In the atomization process, a is the acceleration of the liquid ligament. Using Newton's second law, the acceleration can be found by dividing the net external force by the mass of the ligament. The only external force acting on the liquid ligament is the drag force from the gas, which can be written as:

$$F = \frac{1}{2}C_D\rho_g(U_g - U_c)^2A_e \tag{A.12}$$

where C_D is the drag coefficient. For fragmenting drops, it ranges from 1.5 to 2.9 [69] and $C_D \approx 2$ is typically used. A_e is the projected area.

Varga et al. [69] and Aliseda et al. [2] studied atomization in purely coaxial injectors, without a pattern air nozzle, so the value of U_g used in their model represents the velocity of AA. In our case, the pattern air (PA) plays a role in atomizing the liquid jet, so it needs to be included in our model. Thus, several modifications are made for U_g in the model. First, in addition to the AA velocity, the horizontal velocity components of the PA is included. Second, since the volumetric flow rate of AA and PA are different, the PA term is multiply by the flow rate ratio. Finally, depending on the location where the PA streams impinge with the liquid jet, the contribution of PA to the breakup is different. Therefore, a new parameter C_{PA} is introduced in the model, multiplying the PA term, to take into account the different geometries of the PA ports. Equation (A.13) summarized these modifications of U_g.

$$U_g = U_{AA} + C_{PA}\left(\frac{Q_{PA}}{Q_{AA}}\right)U_{PA}\cos\theta \tag{A.13}$$

where Q_{PA} and Q_{AA} are the volumetric flow rate of PA and AA, respectively, and θ is the angle between the flow direction of PA and the liquid jet. U_c is the convection velocity of the liquid ligament, it is defined as the velocity of the mixing layers of fluids with different density [15]:

$$U_c = \frac{\sqrt{\rho_l}U_l + \sqrt{\rho_g}U_g}{\sqrt{\rho_l} + \sqrt{\rho_g}} \tag{A.14}$$

The volume of a liquid ligament can be approximated by multiplying the projected area with the thickness of the ligament (i.e. $V = A_e b_l$), by dividing Equation (A.12) by the mass of the liquid ligament, $\rho_l V$, the acceleration of the liquid ligament becomes:

$$a \approx \frac{\rho_g (U_g - U_c)^2}{\rho_l b_l} \tag{A.15}$$

Since liquid ligaments are formed as a result of the primary instability, their thicknesses, b_l, are proportional to the wavelength. Varga et al. [69] observed that $\lambda_{KH} \approx 10 b_l$. So, the acceleration can be written as:

$$a \approx \frac{10\rho_g (U_g - U_c)^2}{\rho_l \lambda_{KH}} \tag{A.16}$$

Substituting Equation (A.16) into Equation (A.11), the most amplified wavenumber, k_m, can be found. As a result, the most unstable Rayleigh-Taylor wavelength is $\lambda_{RT} = 2\pi/k_m$. The resulting droplet size is proportional to λ_{RT}. Since a distribution of droplets is presented in a spray, a statistical parameter is used to characterize the droplet size distribution of the spray. Typically, for the study of sprays of interest in combustion and coating, where evaporation characteristics are important, the Sauter mean diameter, D_{32}, is used. The expression of the Sauter mean diameter is:

$$D_{32} = C_3 \lambda_{RT} \tag{A.17}$$

where C_3 is an empirical constant.

The effect of PA is only applied on the acceleration of the liquid ligament, which is the driving force for the Rayleigh-Taylor instability. Since PA does not impinge on the liquid stream at the exit of the nozzle, the primary instability is driven only by AA. Thus, in the derivation of the wavelength of the primary instability, the velocity term in Re_{bg} is U_{AA}, but not the modified gas velocity U_g.

A.5 Results

A.5.1 Prediction of the Rayleigh-Taylor wavelength

As a validation of our model, we compared our prediction of the Rayleigh-Taylor wavelength using the same parameters as some experiments in [69]. Table A.3 provides a summary of this comparison. Two coaxial twin-fluid atomizers are used in [69]. Both injectors have the outside gas diameter of 11.2 mm and the gas inside diameter of 1.3 mm. The only difference is the liquid jet diameter, with one being 0.32 mm and the other one being 1 mm. No pattern air is used, so the coefficient, C_{PA}, is not involved in the calculation.

Instead of the Sauter mean diameter, the Rayleigh-Taylor wavelength is chosen in this comparison because it eliminates the need of C_3 in the calculation. Since C_1 is known for the coaxial twin-fluid jet configuration as mentioned in Section A.4, it leaves C_2 as the only undecided empirical constant. C_2 depends on the nozzle design and the value of 0.6 is used in their model. Applying this value to our model, the predicted R-T wavelength is within 4% of the predicted value from Varga et al. [69] model. Note that their model does not account for viscous effects. So, the comparable results obtained from these two models suggest that for relatively low viscosity liquid, such as water, viscous effects are indeed not important in determining the wavelength of the Rayleigh-Taylor instability. For high viscosity liquids, we expect our model to provide a better prediction.

We	D_l [mm]	U_g [m/s]	U_l [m/s]	Measured λ_{RT} [μm]	Predicted λ_{RT}, Varga [μm]	Predicted λ_{RT} [μm]
38	0.32	100	16.5	200	242	249
50	0.32	100	4.9	185	213	219
78	1	69	1.7	310	331	339
166	1	100	1.7	235	207	212
457	1	165	1.7	95	110	114

Table A.3: Comparison of λ_{RT} between experimental data (Varga et al. [69]) and predictions.

A.5.2 Influence of atomizing air on the atomization process

The Sauter mean diameter of the spray is proportional to the R-T wavelength. As shown in multiple studies through high-speed images of breakup, such as the one in Figure A.9, the resulting droplets either have similar or smaller scale than λ_{RT}. With D_{32} being a representation of these droplets, the proportionality constant, C_3, is expected to be slightly less than unity. Using $C_2 = 0.6$ and adjusting C_3 to fit the data for the case $Q_{AA} = 56$ LPM and $Q_{PA} = 0$, we obtain $C_3 = 0.68$.

Using these values for the model constants, we obtained the droplet size prediction curve with no pattern air, shown in Figure A.10, with a comparison against the experimental data. The experimental D_{32} value represents the entire spray cross-section (The calculation of D_{32} in a spray cross-section using discrete measurement location is shown in Appendix C). This is different from previous studies, where measurements are only taken at the center of the spray. We will show in the next few sections that the droplet size is not uniform across the spray, especially for high PA cases. So, in applications such as spray coating, measurements representing the entire spray cross-section are more valuable. It is important to note that the model predicts droplet size at the completion of the atomization. Typically, the atomization is completed within ten liquid orifice diameters from the nozzle [18]. Our measurements

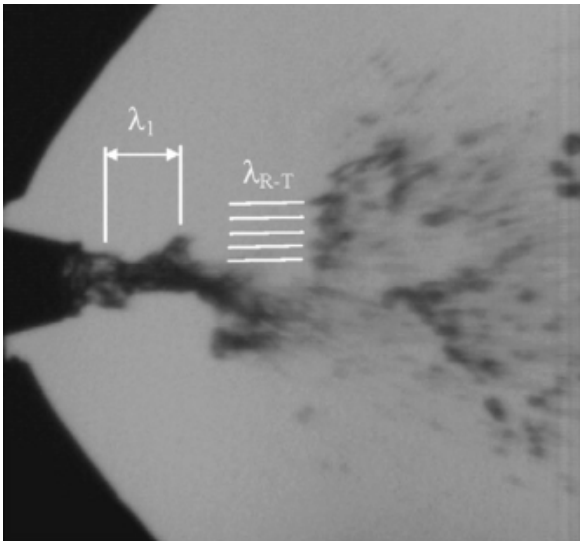

Figure A.9: High-speed image of the breakup process illustrating the scale of λ_{KH} (λ_1 in the image), λ_{RT}, and the resulting droplet size. $We = 153$. Aliseda et al.[2]

are taken at least 16 D_l from the nozzle, so the liquid has been completely atomized at the measurement points.

A.5.3 Influence of pattern air on the atomization process

Previous study [2] suggested that PA does not contribute to the atomization if it impinges on the liquid stream beyond 10 D_l. In our spray gun, however, the PA ports are configured in a way that the two streams impinge on the centerline at about 3.25 D_l downstream from the liquid nozzle, so it is reasonable to believe that PA might contribute to the atomization process.

Figure A.11 shows the experimental data of the nine different flow cases along with our droplet size model. With the increase of PA to AA ratio, a slight decrease in droplet size is observed. This indicates that, in the situations where the PA streams carry significant momentum and impinge on the liquid stream close to the nozzle, the PA flow rate does contribute to the breakup process, but the effect is moderate. In fact, C_{PA} is chosen to be

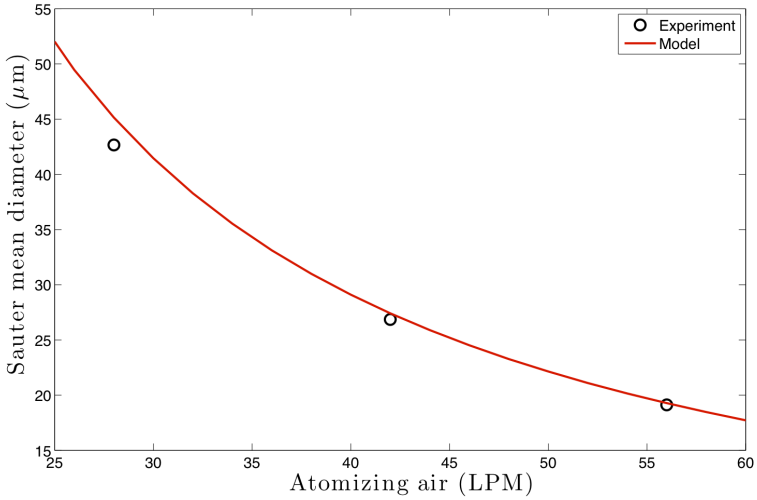

Figure A.10: Comparison between D_{32} prediction and experimental results for cases with no PA.

0.3 for the prediction, meaning that only a small portion of the energy from the pattern air contributes to the breakup.

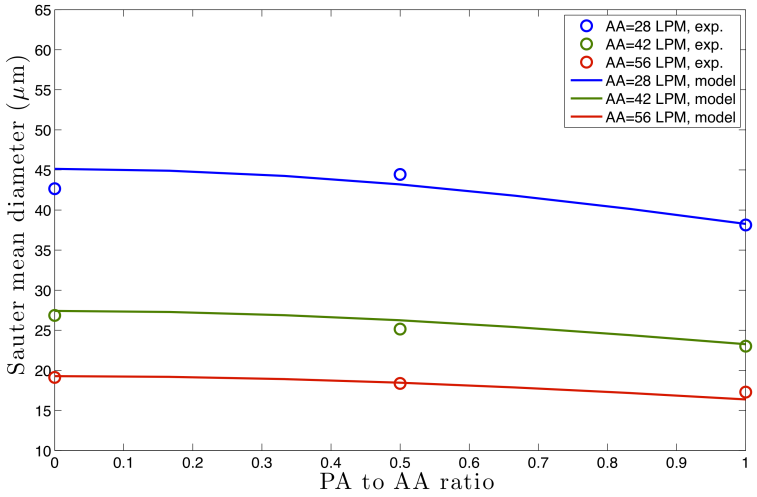

Figure A.11: Comparison between D_{32} prediction and experimental results for all cases.

The probability density function (PDF) of the droplet size at the center of the spray is shown in Figure A.12. Since the center of the spray can be thought of as the "stagnation point" of the two impinging PA streams, there is no transport of drops due to PA. Thus, these results provide another perspective on the influence of PA on the atomization process. In both figures, there is a critical diameter separating two distinct behaviors with the introduction of the pattern air. In Figure A.12a, for example, the critical diameter is located at around 10 μm. Below the critical diameter, the number density increases with an increase of PA. The opposite happens above the critical diameter. The number density is lower for higher PA/AA ratio. Similar behaviors are observed in different flow cases. This is another evidence showing that PA plays a role in the atomization process.

A.5.4 Influence of pattern air on droplets size distribution

The flow rate of PA changes the shape of the spray pattern by relocating some of the drops within the spray and, as a result, the size distribution of the spray changes. Figure A.13 shows that the size distribution is axisymmetric for the no PA case. With the introduction of PA (Figure A.14), not only does the size distribution get elongated along the major axis, there are more large size droplets on the major axis than the minor axis. Figures A.15a and A.15b show the comparison of the Sauter mean diameter for different PA on the minor and major axis, respectively. PA reduces the droplet size throughout the entire minor axis. On the major axis, however, several features are observed. First, the introduction of PA (with $PA/AA = 0.5$) results in smaller D_{32} within 10 mm radial distance from the centerline. Beyond this distance, larger drops are observed with PA. Similarly, smaller drops are observed for $PA/AA = 1$ when comparing to the entire spray region of the no PA case. However, once the radial distance reaches at about 40 mm, the size of the drops is larger than the no PA case at any point of its major axis. Comparing the two non-zero PA cases on the major axis shows that the high PA/AA ratio case has smaller D_{32} throughout the entire radial distance except at the very edge of the spray, where D_{32} is comparable for both cases. Further explanation can be made by looking at the size distribution at specific locations.

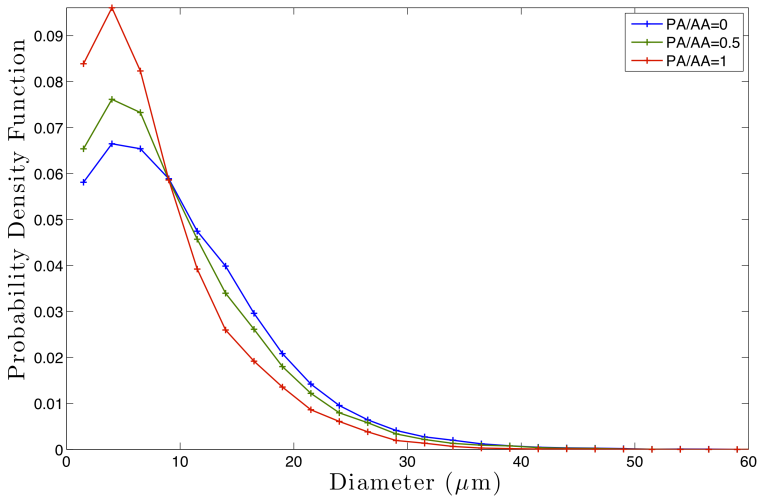

(a) $Q_{AA} = 42\ LPM$, $x/D_o = 32$

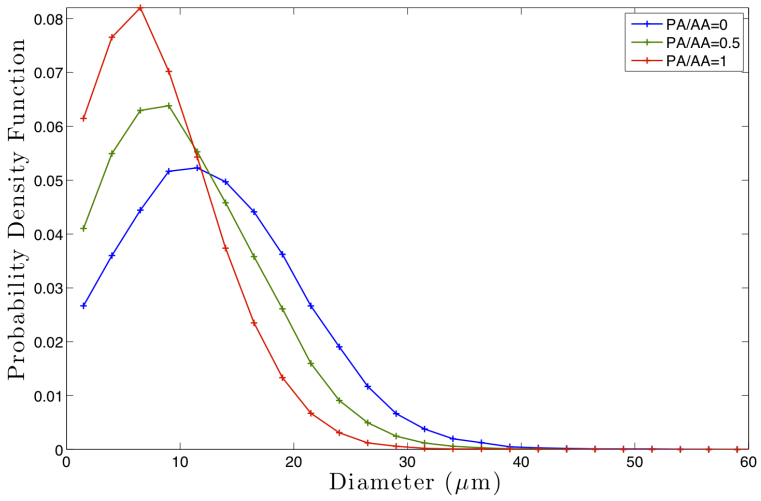

(b) $Q_{AA} = 56\ LPM$, $x/D_o = 48$

Figure A.12: Size distribution at the center of the spray.

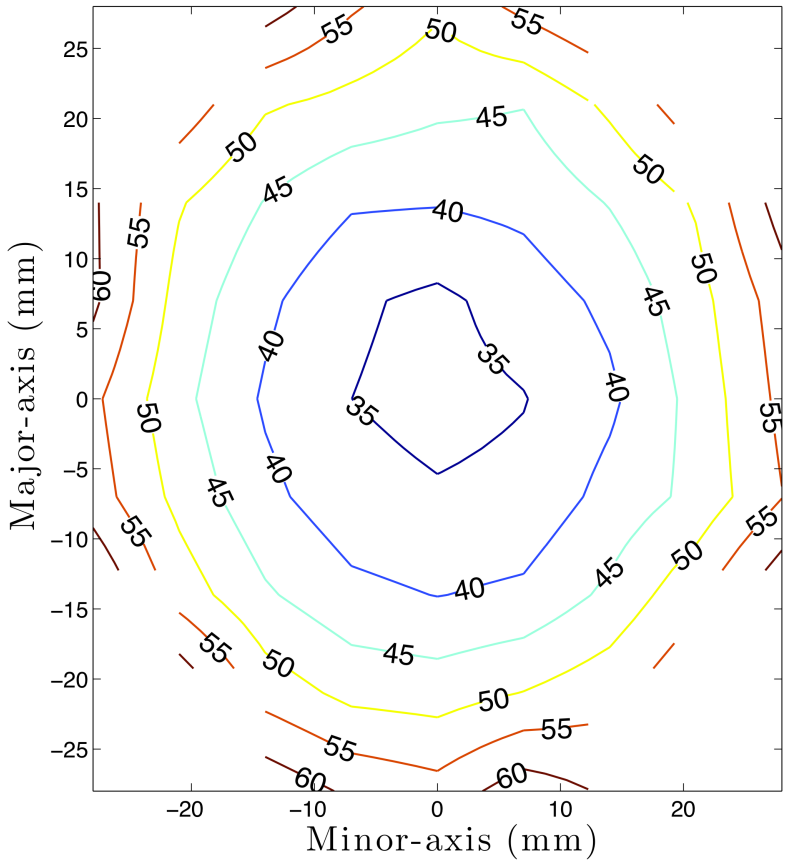

Figure A.13: Size distribution (D_{32}, [μm]) on cross-sections of the spray at $x/D_o = 48$. $Q_{AA} = 28$ LPM and $Q_{PA} = 0$.

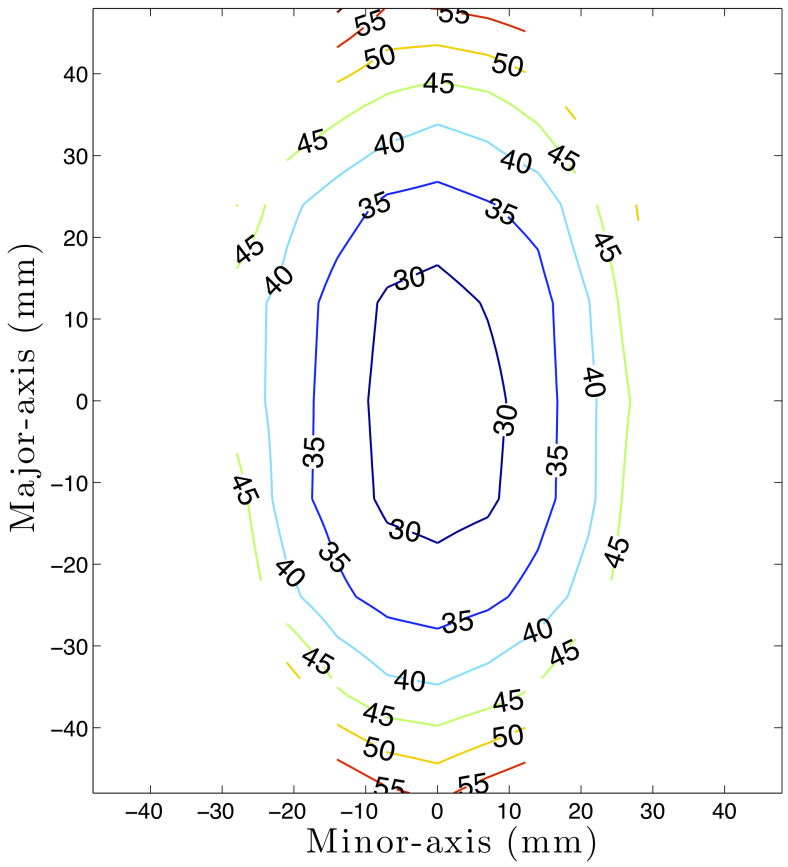

Figure A.14: Size distribution (D_{32}, [μm]) on cross-sections of the spray at $x/D_o = 48$. $Q_{AA} = 28$ LPM and $Q_{PA} = 28$ LPM.

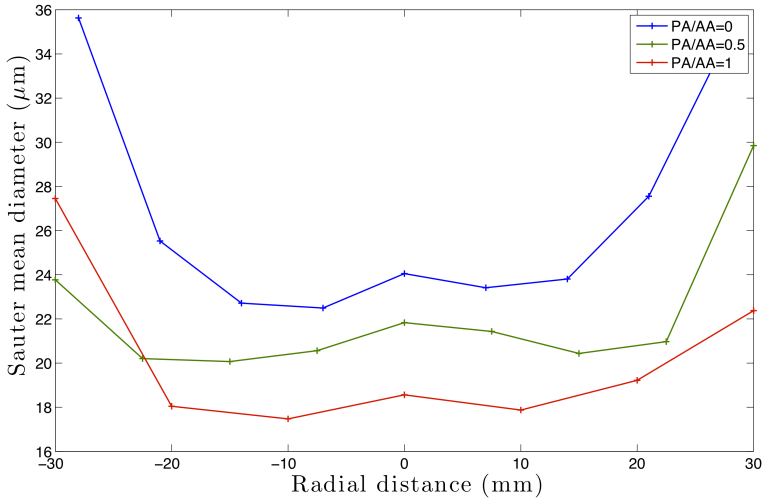

(a) Minor axis

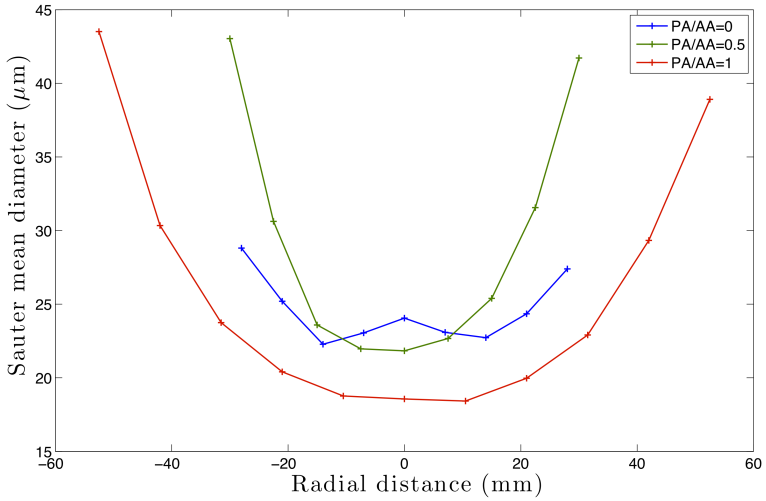

(b) Major axis

Figure A.15: Sauter mean diameter profile of the spray at $x/D_o = 48$. $Q_{AA} = 42$ LPM.

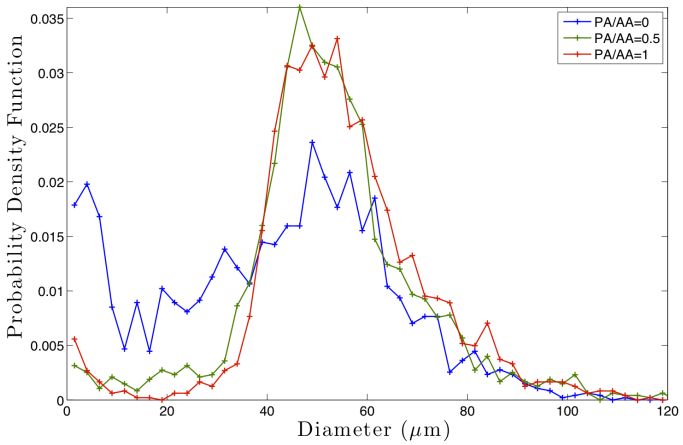

(a) $Q_{AA} = 28$ LPM, Major axis

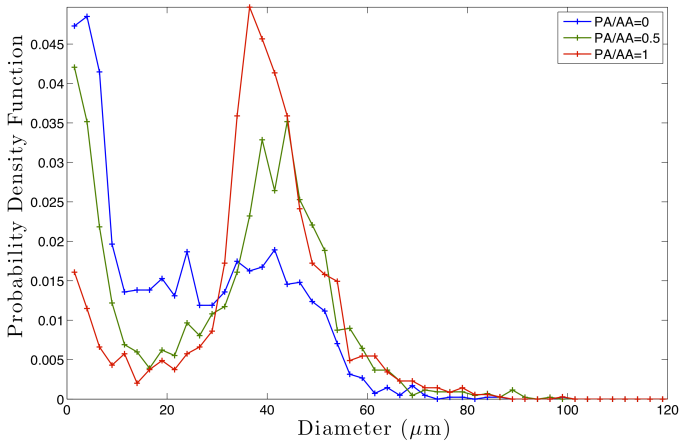

(b) $Q_{AA} = 42$ LPM, Major axis

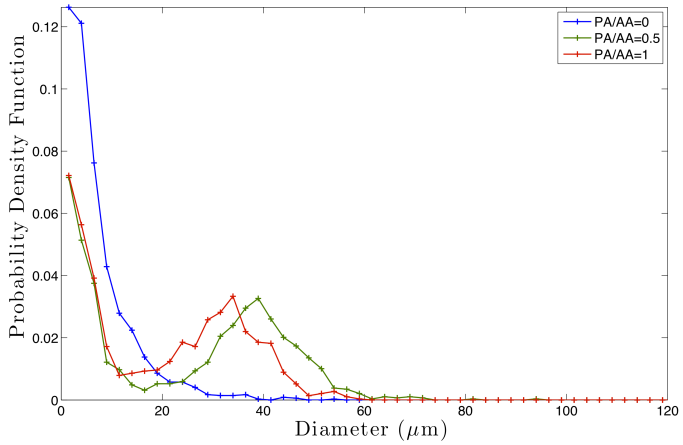

(c) $Q_{AA} = 56$ LPM, Major axis

Figure A.16: Size distribution at the spray rim of the major axis. $x/D_o = 32$.

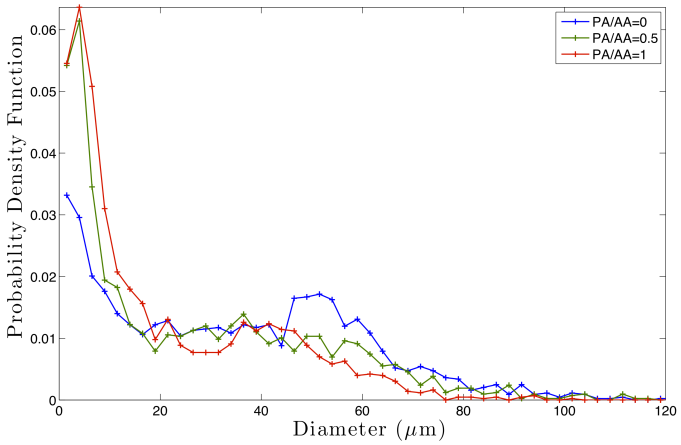

(a) $Q_{AA} = 28$ LPM, Minor axis

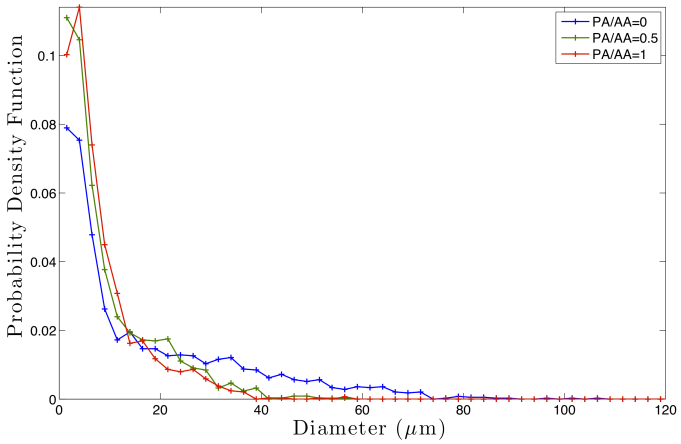

(b) $Q_{AA} = 42$ LPM, Minor axis

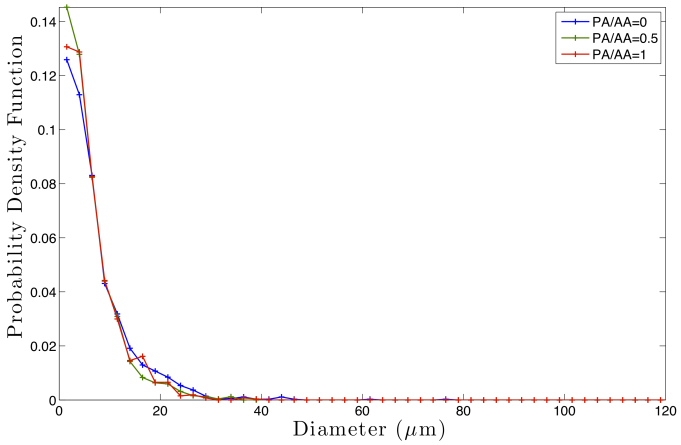

(c) $Q_{AA} = 56$ LPM, Minor axis

Figure A.17: Size distribution at the spray rim of the minor axis. $x/D_o = 32$.

The droplets size distribution at the spray rim on the major axis is shown in Figure A.16. Several important features are observed in this figure. First, a bimodal behavior is observed. In general, the number density of the smaller drops peaks at less than 10 μm and the number density of bigger drops peaks between 40 to 60 μm depending on the AA flow rate. Second, PA changes the number density of these two size ranges. The number density increases for larger size range and decreases for smaller size range with PA. There is a critical diameter that separates the two size ranges. At the axial distance of 3.4 in, the critical diameter is about 40, 30, and 20 μm for the atomization air of 28, 42, and 56 LPM, respectively.

At the spray rim of the minor axis, the double peak feature has either become less prominent (Figure A.17a) or disappeared (Figure A.17c). Because of this, the critical diameter is not as clearly shown in the figures. Nonetheless, the opposite effect on the size distribution is observed compared to the major axis counterpart. The number density decreases for the larger size range and increases for the smaller size range.

While the number density increase of smaller size droplets can be attributed to either atomization or transport, the number density increase of larger droplets is most likely due to the transport of larger size droplets because coalescence is not likely a factor at low droplet density locations, such as the spray rim. Therefore, the contrasting results of the droplets size distribution at the spray rim of the minor and major axis suggest that certain sizes of drops are being transported between these two locations.

The re-distribution of different sizes of drops can be explained by a new flow field created by the pattern air streams (Figure A.18). Pattern air forces the air flow to converge on the minor axis. The impingement of air streams on the centerline causes air to accelerates in both directions on the major axis. The result is the transport of drops from the rim on the minor axis to the rim on the major axis. In addition, the center of the spray becomes a stagnation point (radially) because of the impingement of the pattern air streams. Thus, this confirms that the change in size distribution at the center of the spray discussed in Section A.5.3 is only due to the breakup mechanism, but not the convective transport by this pattern air modified flow field.

This new flow field alone does not fully explain the size-biased droplet transport. Inertia effect also plays an important role in this mechanism. Larger drops tend to travel farther along the PA-modified flow field because of their higher inertia. Once they are accelerated to the speed of the nearby flow field, they carry enough momentum to continue traveling across the flow field with minimal impact by the local velocity fluctuations. On the other hand, the transport of the smaller drops is mostly due to turbulent mixing. Despite these smaller drops are also subjected to the PA-modified flow field, they are as easily affected by the turbulent fluctuations within the spray. Thus, smaller drops tend to be evenly distributed within the spray. This explains why only larger drops migrate from the spray rim of the minor axis to the spray rim of the major axis, as illustrated in Figure A.18.

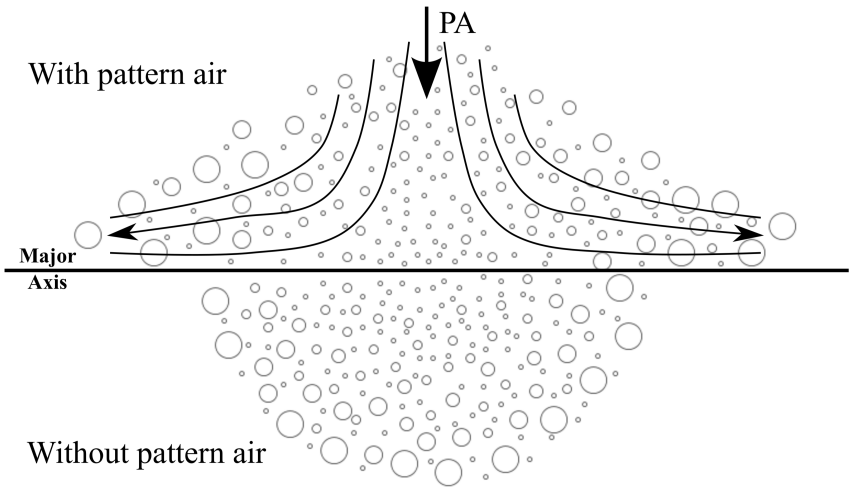

Figure A.18: Illustration of the droplets transport with (top) and without PA-modified flow field (bottom)

A.6 Summary

The effect of PA on the spray characteristic has been examined experimentally using a non-intrusive Phase Doppler Particle Analyzer measurement technique. Unlike in the axisymetric spray where one-dimensional measurements along the radial direction can represent the entire

spray, two-dimensional measurements are needed for sprays where a third fluid stream with a radial component, the pattern air is present. By taking spatial measurement across the cross-sections of the spray and at different axial locations, we were able to show that the introduction of PA changes the spray shape, droplets size, and its spatial distribution.

We have studied, a class of two-fluid injectors, frequently used in industrial applications but not thoroughly studied in the literature where PA impinges on the liquid stream very close to the nozzle exit, as the breakup mechanism is still in process. Thus, similar to the effect of AA, the axial component of PA has high enough velocity to help accelerate the liquid ligaments, which helps in decreasing the wavelength of the Rayleigh-Taylor instability, resulting in smaller droplets size. On the other hand, the change in size distribution is due to the transport of droplets by the PA-modified flow field. Larger droplets are more likely to follow the mean flow because of their inertia and smaller droplets are more likely to be affected by the local velocity fluctuations. As a result, larger droplets migrate from the spray rim of the minor axis to the spray rim of the major axis. This explains the higher number density of larger droplets observed on the spray rim of the major axis compare to the minor axis.

The model presented in this study is based on the two-stage breakup mechanism similar to the models developed by Varga et al. [69] and Aliseda et al. [2]. Unlike previous models, we used the viscous potential theory for the calculation of the Rayleigh-Taylor wavelength and included the effect of PA in the model. Our model compared well with the experimental data and prediction of the Rayleigh-Taylor wavelength from Varga et al. [69] for the low viscosity case (water). Since they ignored the effect of viscosity in their model, we expect our model to work better for viscous liquids. The results from our model also agreed well with our experimental data even with the introduction of PA.

The current model has proved to be adequate for the case of low viscosity liquid, but further investigation with highly viscous or viscoelastic fluids is needed as they are widely used in the tablet coating process and other industrial applications. As of now, the amount of contribution to the breakup due to PA in the model depends on an empirical coefficient,

C_{PA}. This coefficient is believed to depend on the impingement distance from the nozzle and on the geometry of PA ports. Thus, more experimental data with different nozzle designs would help identify the relationship between C_{PA} and the aforementioned parameters.

Appendix B

PHASE DOPPLER PARTICLE ANALYZER

Phase Doppler Particle Analyzer (PDPA) was developed to measured the size and velocity of spherical and transparent particles in fluid flow. It uses the same principle of widely used Laser Doppler Velocimetry (LDV) for velocity measurement. As suggested by their name, Phase PDPA and LDV utilize the Doppler effect of lasers to measure velocity of particles. Since the measurement is done by recording the reflected and refracted light from the laser, it is considered as an non-intrusive measurement technique. The system of PDPA consists of many components, the section below intents to introduce and explain each component by describing how the PDPA works from laser beams generation to converting raw data to useful data such as size and velocity.

B.1 Laser beams generation

The source of the laser is an argon-ion laser. The laser beam is directed into the multicolor beam generator to create two laser beams. Two laser beams is needed because the typical Doppler shift frequency created by the movement of the particles (from a few kHz to 100 MHz) is typically much smaller than the basic light frequency (about 440 GHz). Therefore, by using two lasers, the basic light frequency can be subtracted to enhance the signal from the Doppler shift frequency. The beam splitting mechanism is done by an acousto-optic modulator, also called the Bragg cell. By inducing vibration through a medium where the laser beam passes through, the incoming laser beam is diffracted into two beams. The intensity of the two beams can be equalized by adjusting the angle between the Bragg cell and the incident beam. Another function of the Bragg cell is to create a frequency shift in one of the beam. The purpose of this frequency shift will be discussed later.

While still in the multicolor beam generator, each beam is further separated into three beams of different color: the green laser (514.5 nm), the blue laser (488.0 nm) and the violet laser (476.5 nm). The reason of having three wavelengths is to make velocity measurement in all three components simultaneously. In our system, only the green and the blue laser are used. The four beams (2 greens and 2 blues) leaving the beam generator are focused by the fiber optic couplers in order to minimize power losses. The focused beams are then guided to the transmitter through the fiber optic cable. The lens on the transmitter focuses each pair of beams to its focal point, which is where the desired measurement location take places.

B.2 Size and velocity measurement of particles

When the pair of lasers converges, they creates a fringe pattern (shown in Figure B.1) due to the constructive and destructive interference of the light waves. The spacing between these fringes are called fringe spacing, which is directly related to the wavelength of the laser (Equation (B.1)). When a particle pass through these fringes, light scatter in all directions due to reflection and/or refraction from the particle. Since the particle is moving, the frequency of the scattered light are shifted. The velocity of the particle can be calculated by multiplying the frequency shift with the fringe spacing (Equation (B.2)). However, only the component of the velocity perpendicular to the fringes can be determined. Thus, to obtain all three components of the velocity, three pairs of lasers (in different color) are used.

$$d_f = \frac{\lambda}{2 \sin \kappa} \tag{B.1}$$

where d_f is the fringe spacing, λ is the wavelength of the laser and κ is the angle between the two incoming lasers.

$$U_p = f_d d_f \tag{B.2}$$

where U_p is a component of the particle velocity in the direction perpendicular to the fringes and f_d is the shifted frequency of the scattered light.

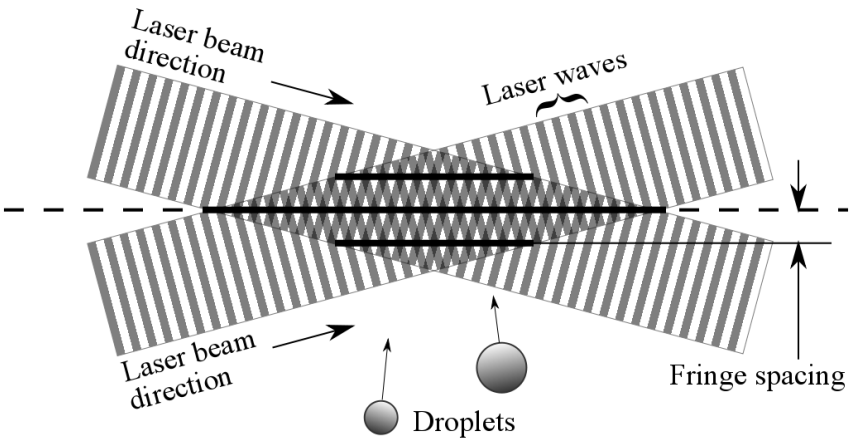

Figure B.1: Illustration of interference pattern (fringes) created by the laser beams.

The intensity of the laser has a Gaussian profile across its cross-section, so the intensity at the intersection between the two lasers, where the fringe pattern is formed, is not constant. At the edge of the intersection, the scattered light is too weak to be detected. Thus, the boundary of the measuring volume is defined as where the light intensity of the fringes is $1/e^2$ of the maximum intensity, which results in a ellipsoidal shaped measuring volume. Its volume is defined in Equation (B.3).

$$V_m = \frac{\pi d_{e^{-2}}^3}{6\cos^2\kappa\sin\kappa} \tag{B.3}$$

$$d_{e^{-2}} = \frac{4f\lambda}{\pi D_{e^{-2}}} \tag{B.4}$$

where $D_{e^{-2}}$ is the diameter of the laser beam.

With no frequency shift between the two lasers, the fringe pattern is stationary. Thus, when two particles pass through the measuring volume with the same speed but opposite direction, the detected frequency is the same for the two particles. This means that the system has no way to determine the direction of the particle motion. By creating a frequency shift in one of the beam by using the Bragg cell discussed in a earlier section, the fringe

pattern is no longer stationary and has a constant frequency shift, f_1. This means that the detected frequency of a particle passing through the measuring volume is $f_1 + U_p/d_f$. For a particle with zero velocity, the detected frequency is f_1. The direction of the particle motion is determined by whether the detected frequency is above or below f_1. Another advantage of the shifted frequency is that it can extend the range of measuring velocity by adjusting the shifting frequency.

The receiver is oriented in a specific angle to maximize the scattered light from the measuring volume. According to the Mie solution, the intensity of the scattered light by a sphere is a function of the scattering angle. Therefore, the optimal orientation of the receiver can be determined by knowing the index of refraction between water and air, which is 1.33. In this case, the receiver is positioned at 70° with respect to the line of the transmitter.

A series of lens in the receiver collect the scatter light and focus them on three photodetectors. One photodetector is capable to obtain light frequency necessary to determine the velocity of particles. With two photodetectors separated at a known distance, the scattered light from a particle will reach each photodetector through different paths. Because of this, there is a phase shift between the measurement from the two photodetectors. According to Bachalo [6], this phase shift is linearly related to the particle size providing the spacing of the photodectors are known. The third photodetector provides two independent set of measurement, which serves as a testing of the signal sensitivity. In addition, it can extend the particle size range.

The light collected by the photodetectors are transmitted to the photodetector module (PDM) for processing. PDM convert the incoming light signals into electrical signals. A sudden jump in the signal implies a particle is detected in the measuring volume. This is referred to a burst. Signal of bursts are then transfered to the FSA signal processor. A couple of processing is done in the FSA. First, a downmixing process is used to subtract a user-defined frequency from the frequency shift created by the Bragg cell. This allows the user to select the range of the frequency shift that is appropriate to the measurement. Another process is the bandpass filtering, which helps improving the signal to noise ratio

(SNR). Once these processes are finished, the FSA sends the doppler frequency and phase difference of each burst to the computer.

Appendix C

SAUTER MEAN DIAMETER

Within a spray, a distribution of droplet sizes is found both locally (at a point of the spray) and globally (at different locations of the spray), thus statistical parameters are often used to characterize the droplet size of a spray. One of such parameters is Sauter Mean Diameter (D_{32}). The formulation of D_{32} suggests that its value represents a drop that has the same volume to surface area ratio as the entire spray. Since this ratio is related to the rate of evaporation, D_{32} is widely used in applications where evaporation of drops is a concern, such as in combustion and spray coating.

$$D_{32} = \frac{\sum N_i D_i^3}{\sum N_i D_i^2} \tag{C.1}$$

where N_i is the number of droplets

The Sauter mean diameter of individual measurement points, such as PDPA measurements, can be calculated using Equation (C.1). However, calculation of the D_{32} across an entire spray cross-section is not as simple. Recall that multiple measurement points are taken at different locations of a spray. The data rate at different locations might be different, so applying Equation (C.1) over all the measurement points bias the resulting D_{32} towards points with higher data rate. Also, each measurement is taken when droplets pass through a probe volume. Since the cross-sectional area of the probe volume, A_{probe}, is small, some scaling of the area is required to represent the actual area of the spray. Moreover, each droplet is traveling at a different velocity, some weighting in velocity is required to prevent bias towards points with higher velocity. Therefore, D_{32} of the entire spray is calculated applying a weighted average of individual D_{32} at different measurement point as shown in Equation (C.2).

$$D_{32,spray} = \left(\frac{\sum D_{32,i}^3 \frac{N_i}{T_i} \frac{A_i}{A_{probe,i}} \frac{1}{U_i}}{\sum \frac{N_i}{T_i} \frac{A_i}{A_{probe,i}} \frac{1}{U_i}} \right)^{\frac{1}{3}} \tag{C.2}$$

where $D_{32,spray}$ is the Sauter mean diameter of the spray, N_i/T_i is the data rate of a measurement point, A_i is the discretized area of a measurement point, and U_i is the average velocity of a measurement point.

Appendix D

STOKES NUMBER

D.1 PIV seeding particles

In the validation study (Chapter 4), the velocity of the interior of the turbulent jet is calculated based on the displacement of the seeding particles between consecutive images. Since the particles need to represent the true velocity of the jet, their response time to the flow must be fast enough that the velocity of the particles are visually the same as the local flow field. Stokes number, equation (D.1) is a metric for how responsive the particles are relative to the flow. It is the ratio of the particle relaxation time to the flow relaxation time.

$$St = \frac{T_p}{T_f} \tag{D.1}$$

where the particle relaxation time is given by Kennedy and Moody [29] as:

$$T_p = \frac{\rho_p D^2}{18 \rho_j \nu_j} \tag{D.2}$$

where ρ_p is the density of the seeding particle of size D and μ_j is the viscosity of the jet liquid.

In a turbulent flow, the Kolmogorov time scale is an appropriate choice for the fluid relaxation time. The Kolmogorov scale is a combination of the fluid kinematic viscosity and the turbulent dissipation, ϵ, as shown below:

$$T_f = \sqrt{\frac{\nu_j}{\epsilon}} \tag{D.3}$$

$$\epsilon = \frac{36 U_j^3}{d_j} \left(\frac{z}{d_j} - \frac{z_o}{d_j} \right)^{-4} \tag{D.4}$$

The maximum turbulent dissipation rate occurs at the centerline, which can be expressed in Equation (D.4) [16]. Substituting this back to Equation (D.3), we obtain:

$$T_f = \left(\frac{\nu_j d_j}{36}\right)^{1/2} \left(\frac{z}{d_j} - \frac{z_o}{d_j}\right)^2 U_j^{-3/2} \tag{D.5}$$

Applying this to Equation (D.1), the Stokes number becomes:

$$St = \frac{D^2}{108}\left(\frac{\rho_p}{\rho_j}\right)\left(\frac{d_j}{\nu_j U_j^3}\right)^{1/2} \left(\frac{z}{d_j} - \frac{z_o}{d_j}\right)^2 \tag{D.6}$$

The density of the seeding particles, lycopodium particles, are similar to the density of the water, so the density ratio is about one. The nominal size of the lycopodium particles is assumed to be approximately 30 μm [46]. For the jet used in the validation study, $d_j = 4$ mm and $U_j \approx 12.6$ m/s. The virtual origin of the jet is obtained empirically, which has a value of $z_o/d_j = 4$. With these values, the Stokes number can be calculated as a function of axial distance, as shown in Figure D.1.

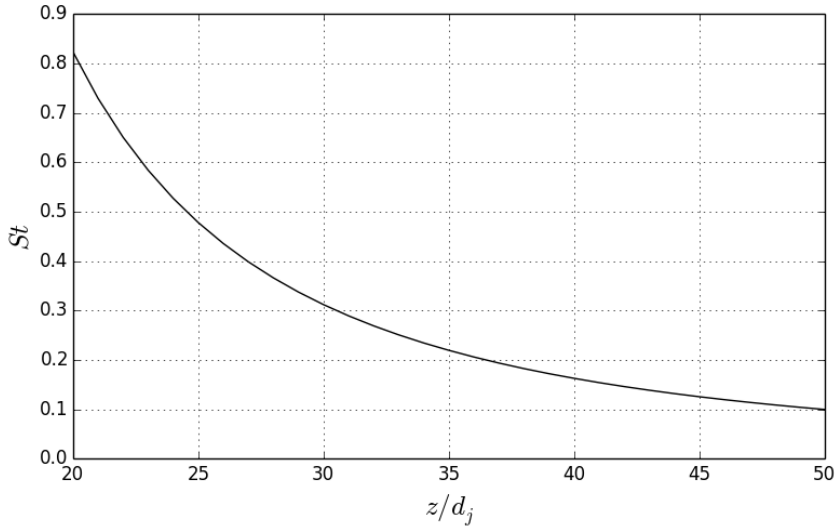

Figure D.1: Stokes number of the seeding particle as a function of axial distance

A particle can be considered as a good flow tracer when $St < 1$ [29]. Figure D.1 shows that this condition is satisfied for $z/d > 20$. However, it is likely that the lycopodium particles are

still capable to be tracers upstream because Equation (D.4) assumed fully developed flow. However, the turbulence in this region is not fully developed, so it is likely that the fluid relaxation time is higher, resulting a lower Stokes number.

D.2 Dispersed phase fluid particles

The study of the breakup of dispersed phase fluids in a turbulent jet assumed that breakup and deformation due to aerodynamic effect (drag force) is negligible. Hence, the relative velocity between the particle and the mean flow is negligible. For this to be true, the particles must response to the mean flow quickly. Again, we will use the Stokes number as a measure of how well the particle response to the change in dynamics of the flow.

The particle relaxation time for the dispersed phase particles uses the same expression (Equation (D.2)) as the analysis of the PIV seeding particles. However, the fluid relaxation time, T_f, is different. In the PIV analysis, the seeding particles must be able to follow the small scale turbulent motions in the flow as their displacements are used for calculating turbulent quantities, such as the velocity fluctuation. In contrast, the small scale turbulent motions are the driving force of the particle deformation/breakup, so they are not expected to be able to response the small scales turbulent motions. Therefore, the flow relaxation time calculated based on the Kolmogorov scale is not applicable here. Instead, a time scale representing the change of the mean flow should be used.

The mean velocity of the jet is continously decreasing over the axial distance. This time scale due to this deceleration can be used to characterize the fluid relaxation time of the mean flow. According to Call and Kennedy [11], this time scale is defined by the velocity gradient in the axial distance, as shown in Equation (D.7).

$$T_f = \left| \frac{dU}{dz} \right|^{-1} \tag{D.7}$$

Using this definition of fluid relaxation time, the Stokes number can be expressed in Equation (D.8). Among all dispersed phase fluids tested, the highest density is $\rho_p = 1060\ kg/m^3$. The particle diameter is chosen to be $D = 1\ mm$, which is the largest spherical particles

that experienced breakup in our experiments. The Stokes numbers of three Reynolds number cases are shown in Figure D.2.

$$St = \frac{\rho_p D^2}{18\rho_j \nu_j} \left| \frac{dU}{dz} \right| \tag{D.8}$$

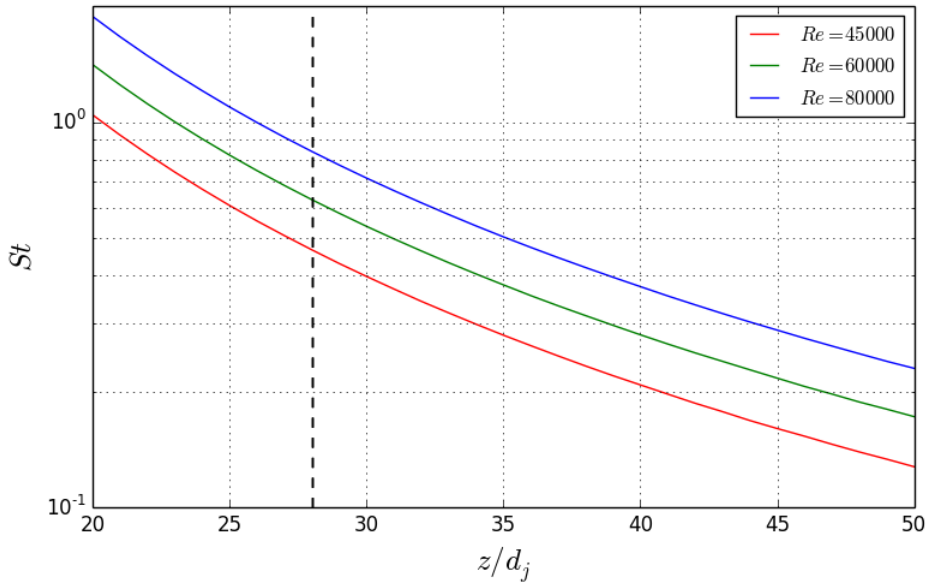

Figure D.2: Stokes number of the dispersed phase particle as a function of axial distance

The vertical black line in the figure represents the start of the field of view for the viscous particle breakup experiments. Prior to entering the field of view, we expect the particles to experience aerodynamic drag, especially near the particle injection location. However, the needle was positioned upstream of the field of view to allow the particles to have sufficient time to reach the local velocity of the mean flow by the time they reached the field of view. Upon entering the field of view (to the right of the vertical black line), the Stokes number stays below 1. This indicates the slip velocity between the particle and the flow is minimal as the particles can response quickly to the flow.

Appendix E

SAMPLE IMAGES OF VISCOUS PARTICLE BREAKUP EXPERIMENTS

This appendix shows the sample images of each experimental set (Table 7.1) used in the particle size analysis of the breakup of viscous particles (Chapter 7). Background subtraction were applied to all images in order to remove artifacts that are not fluid particles. For each experimental set, an image from both camera locations are shown. Also, only the medium flow rate case ($Re = 60000$) is shown for each experimental set.

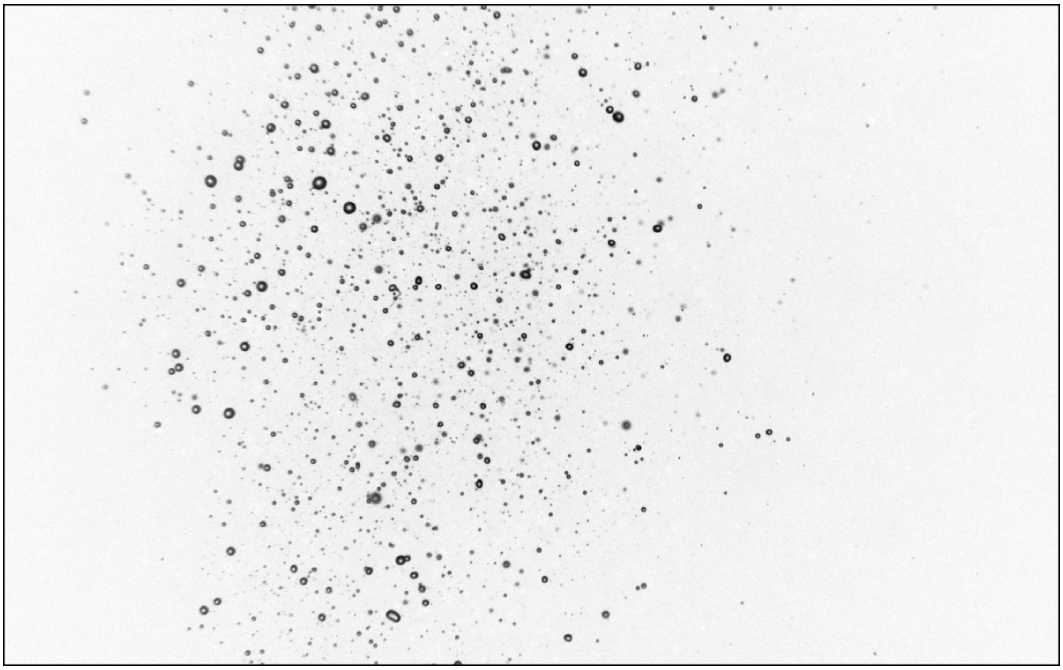

(a) $z/d_j = 28$ to 37

(b) $z/d_j = 39$ to 48

Figure E.1: Sample images of experimental set 1A (Canola oil)

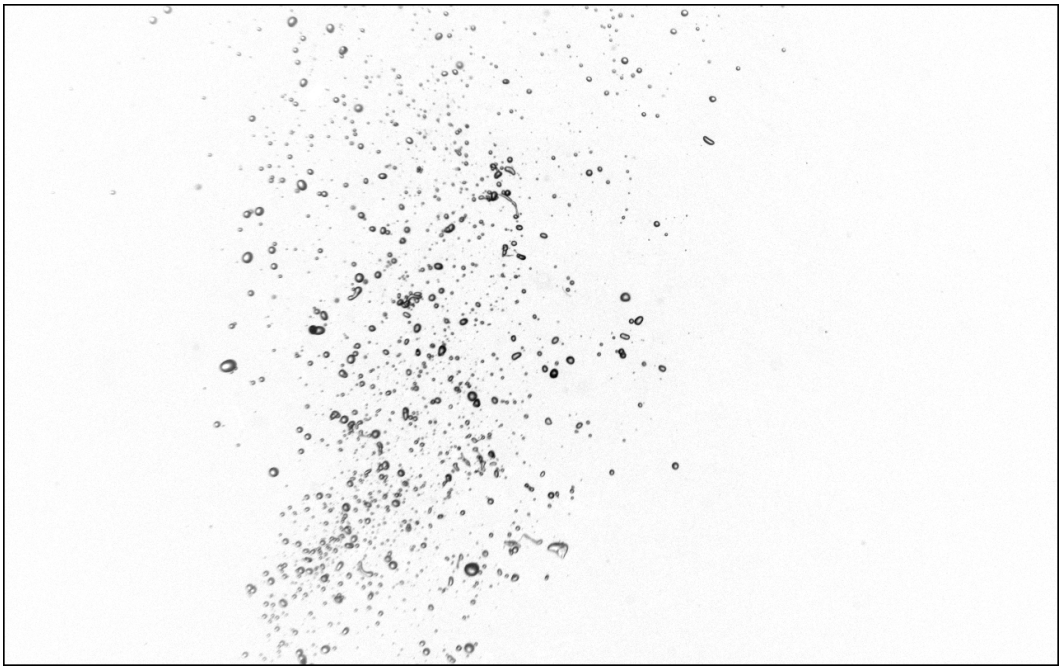

(a) $z/d_j = 28$ to 37

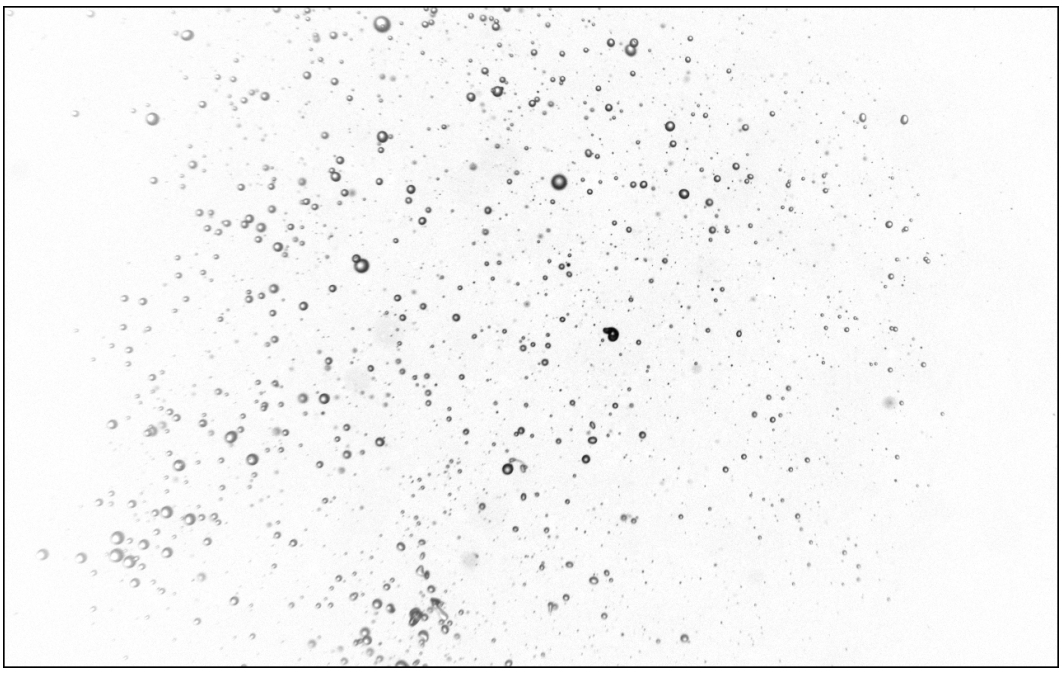

(b) $z/d_j = 39$ to 48

Figure E.2: Sample images of experimental set 1B (10 cSt silicone oil)

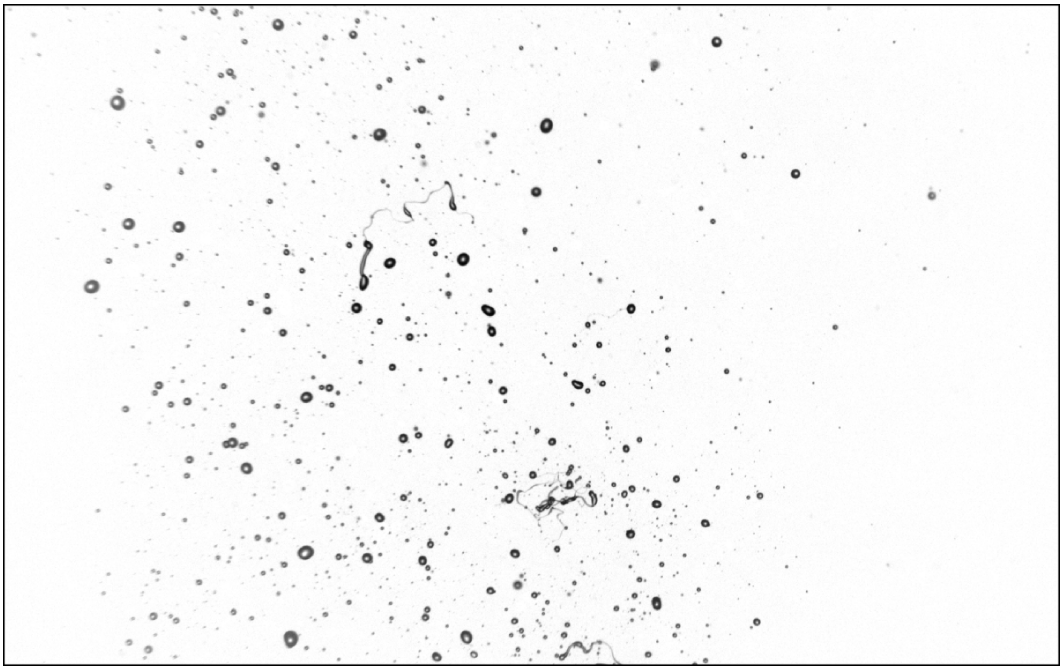

(a) $z/d_j = 28$ to 37

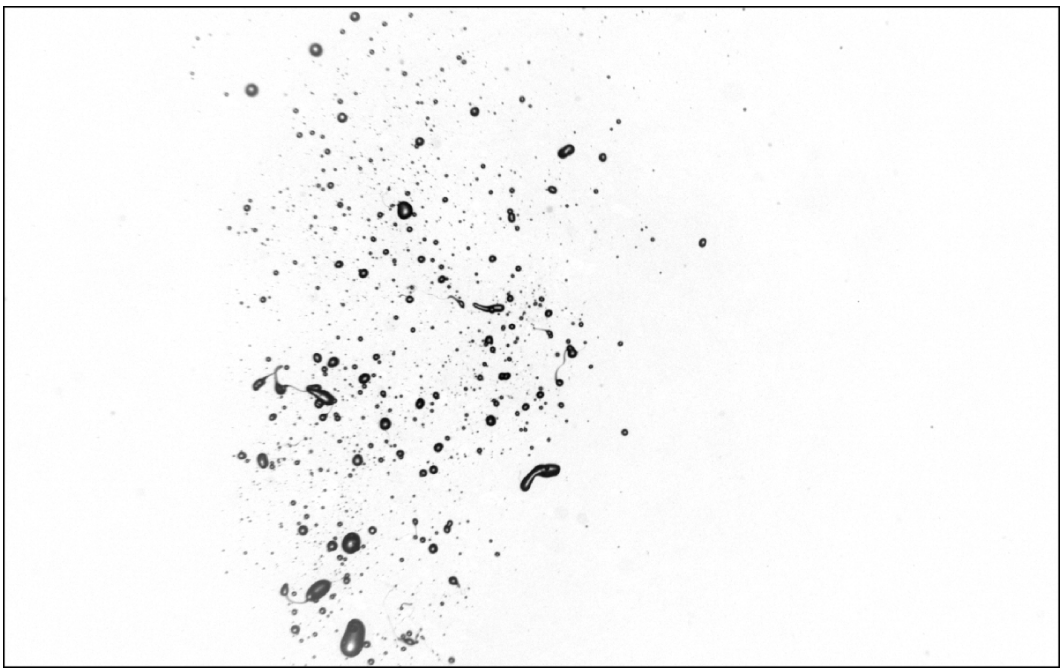

(b) $z/d_j = 39$ to 48

Figure E.3: Sample images of experimental set 1C (100 cSt silicone oil)

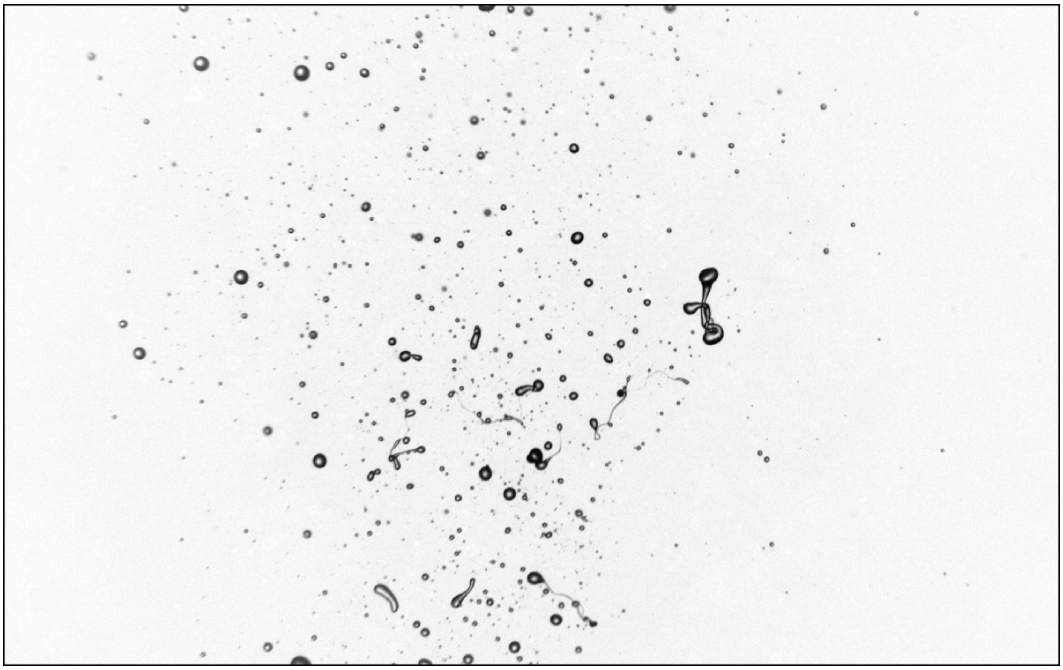

(a) $z/d_j = 28$ to 37

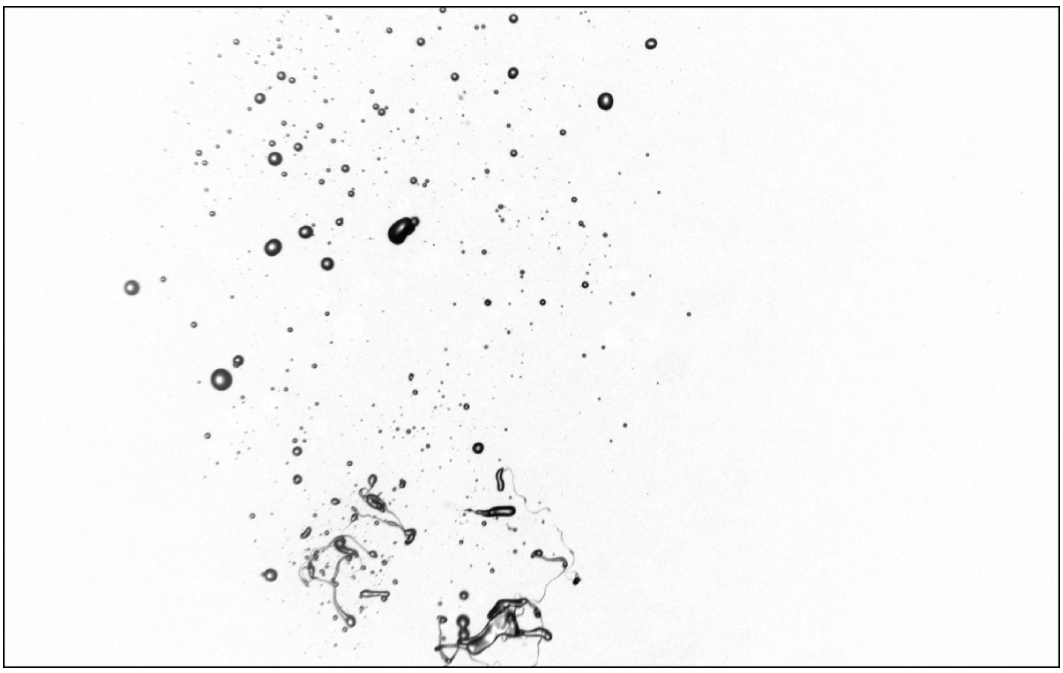

(b) $z/d_j = 39$ to 48

Figure E.4: Sample images of experimental set 1D (200 cSt silicone oil)

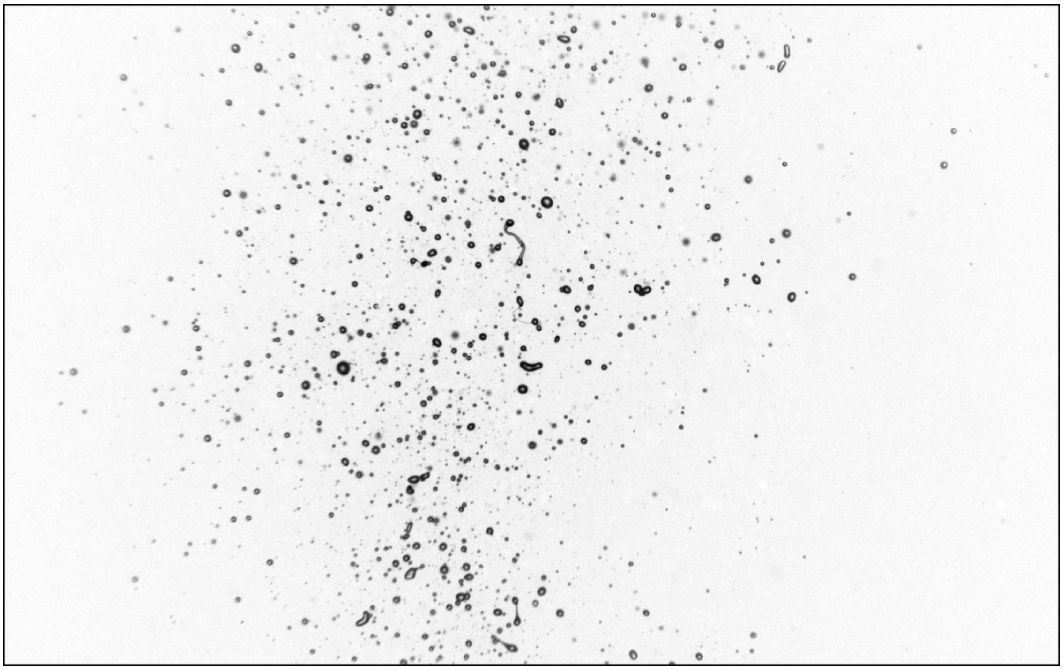

(a) $z/d_j = 28$ to 37

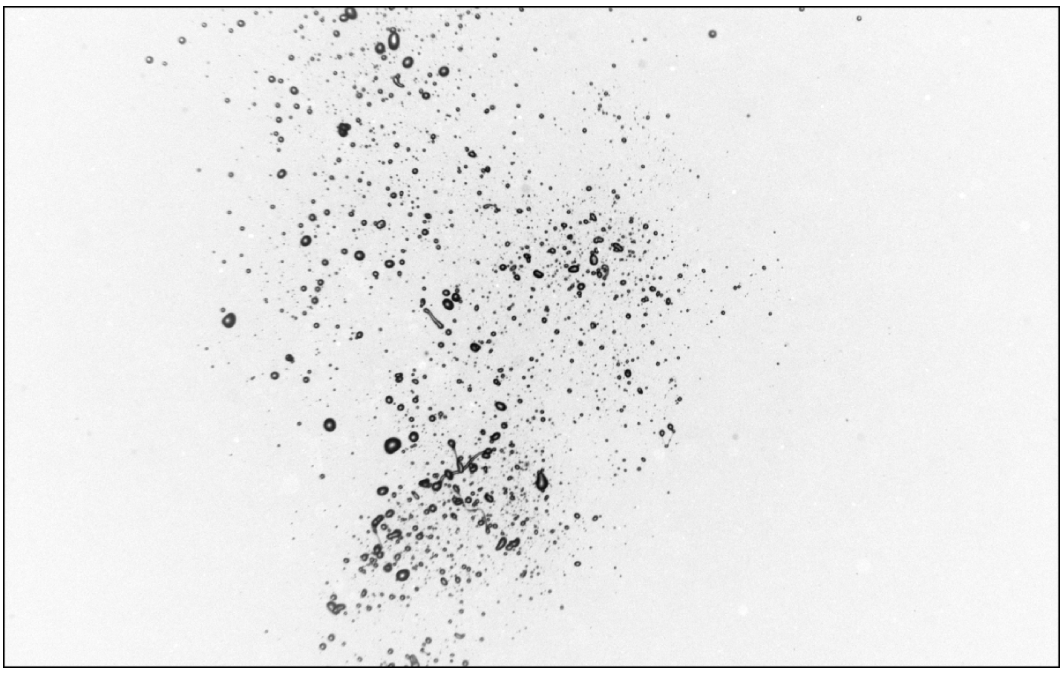

(b) $z/d_j = 39$ to 48

Figure E.5: Sample images of experimental set 2A (Canola oil + 100 ppm Triton X-100)

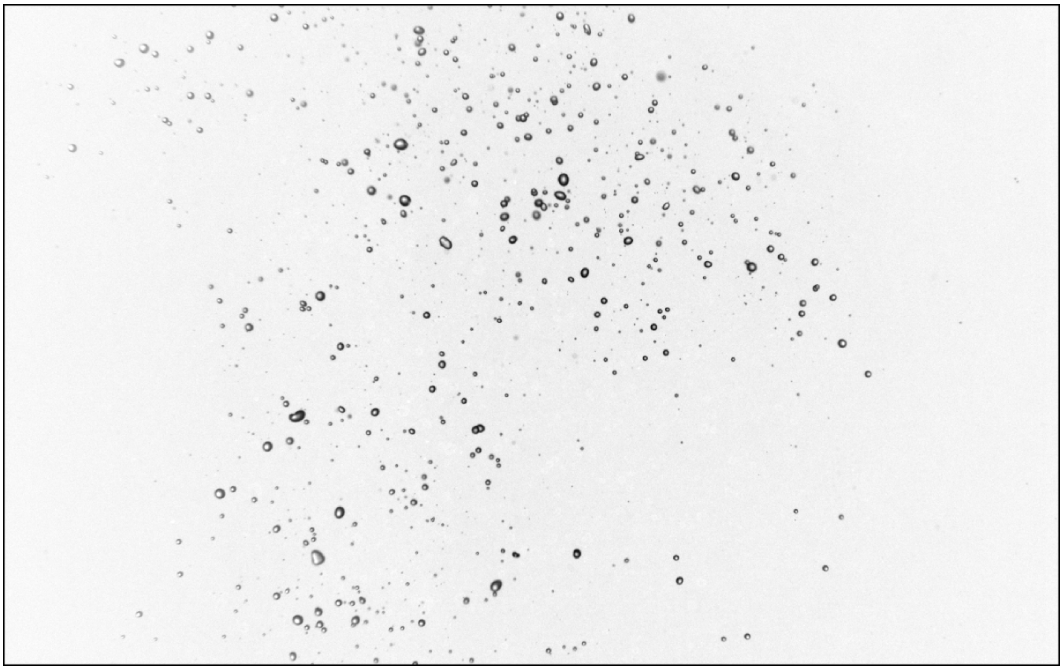

(a) $z/d_j = 28$ to 37

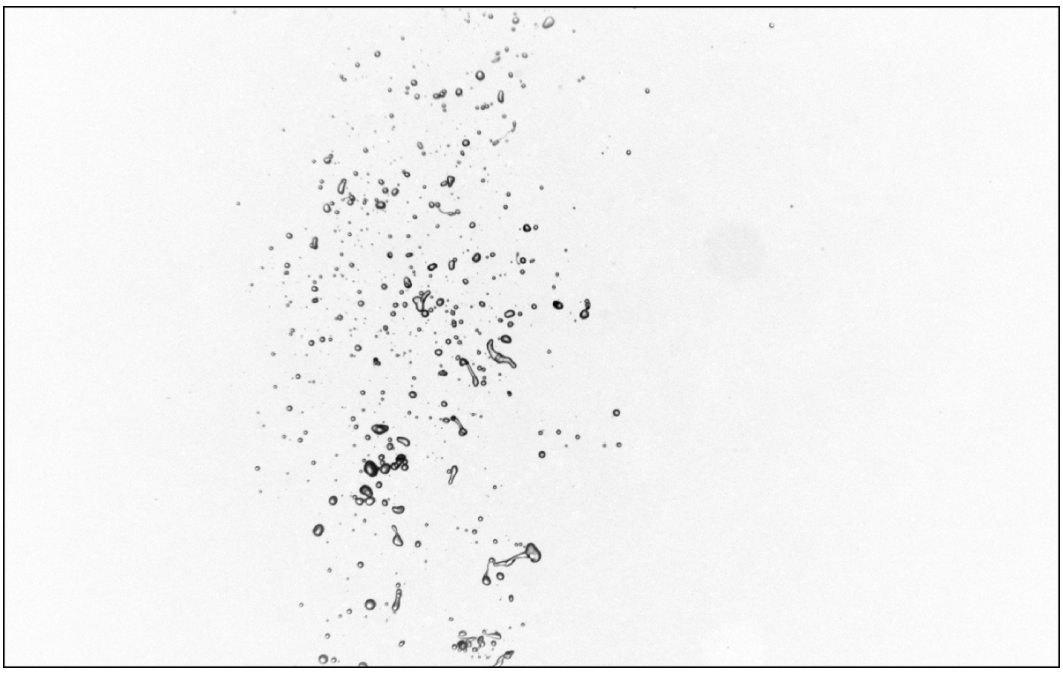

(b) $z/d_j = 39$ to 48

Figure E.6: Sample images of experimental set 2B (10 cSt silicone oil + 100 ppm Triton X-100)

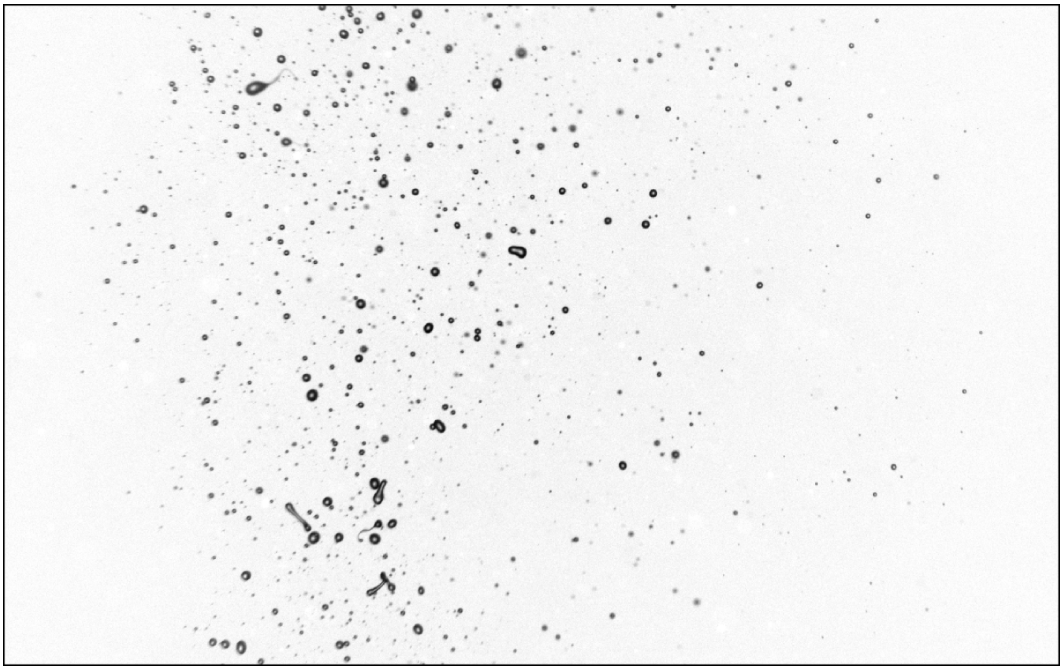

(a) $z/d_j = 28$ to 37

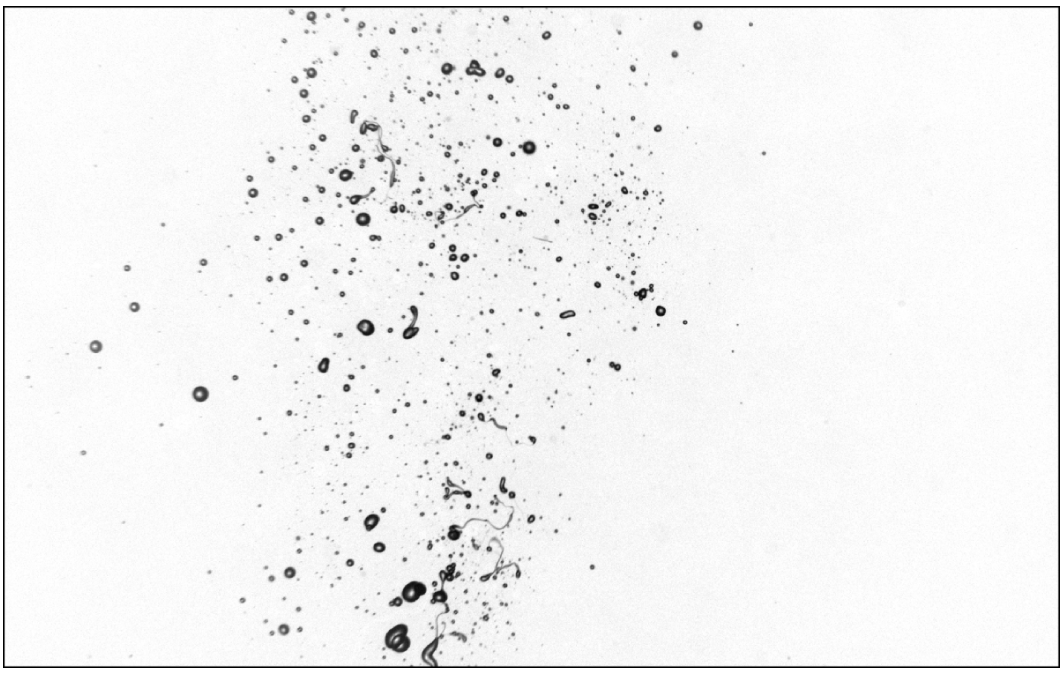

(b) $z/d_j = 39$ to 48

Figure E.7: Sample images of experimental set 2C (100 cSt silicone oil + 100 ppm Triton X-100)

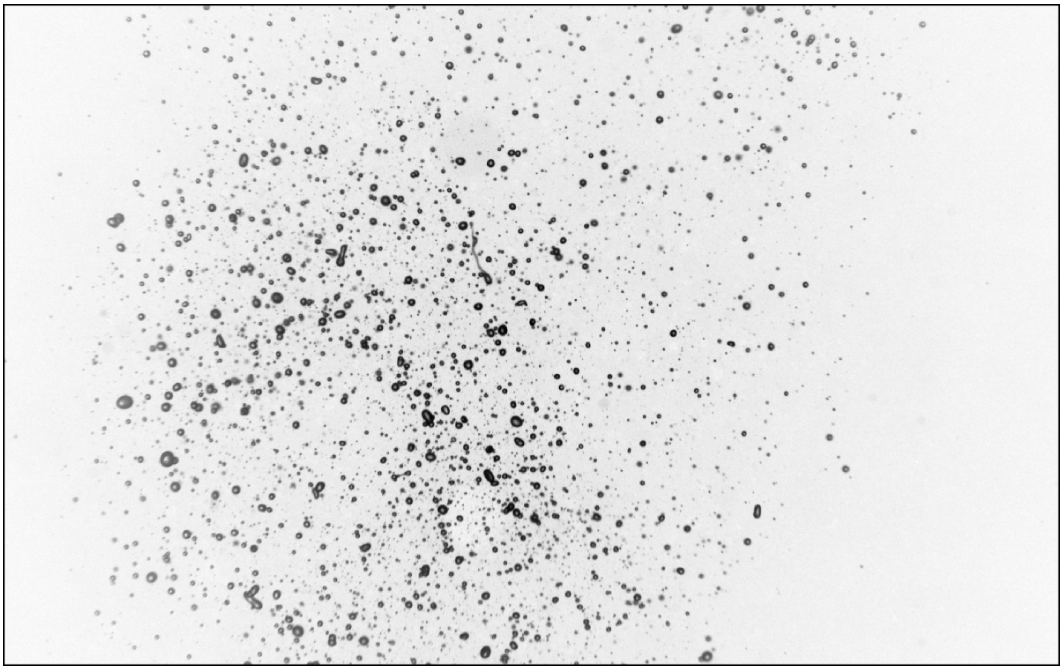

(a) $z/d_j = 28$ to 37

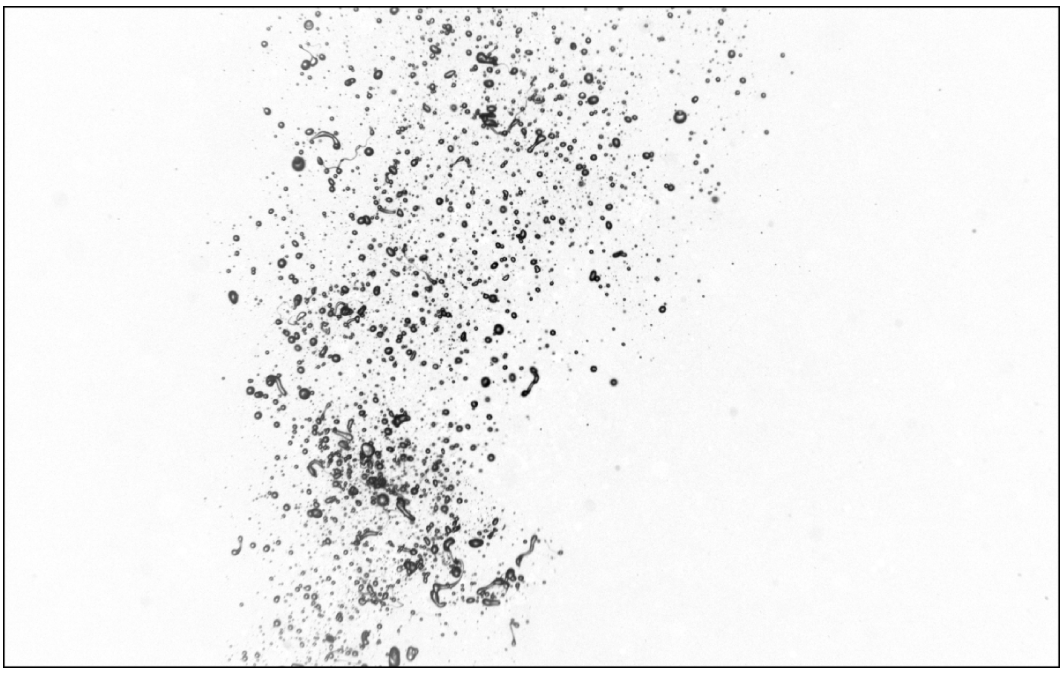

(b) $z/d_j = 39$ to 48

Figure E.8: Sample images of experimental set 3A (Canola oil + 1000 ppm Triton X-100)

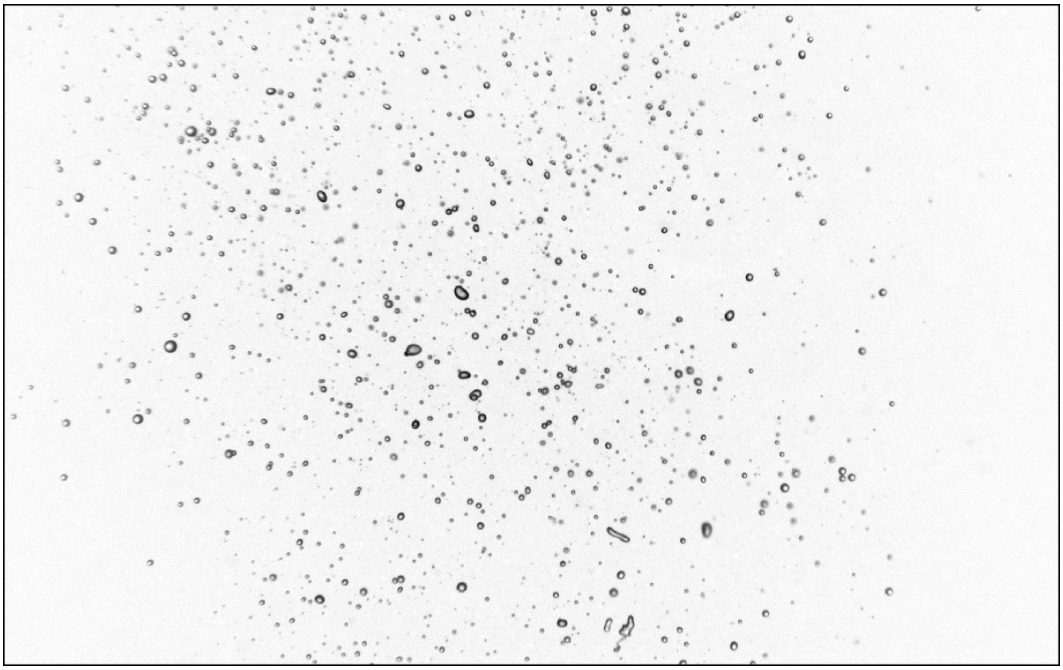

(a) $z/d_j = 28$ to 37

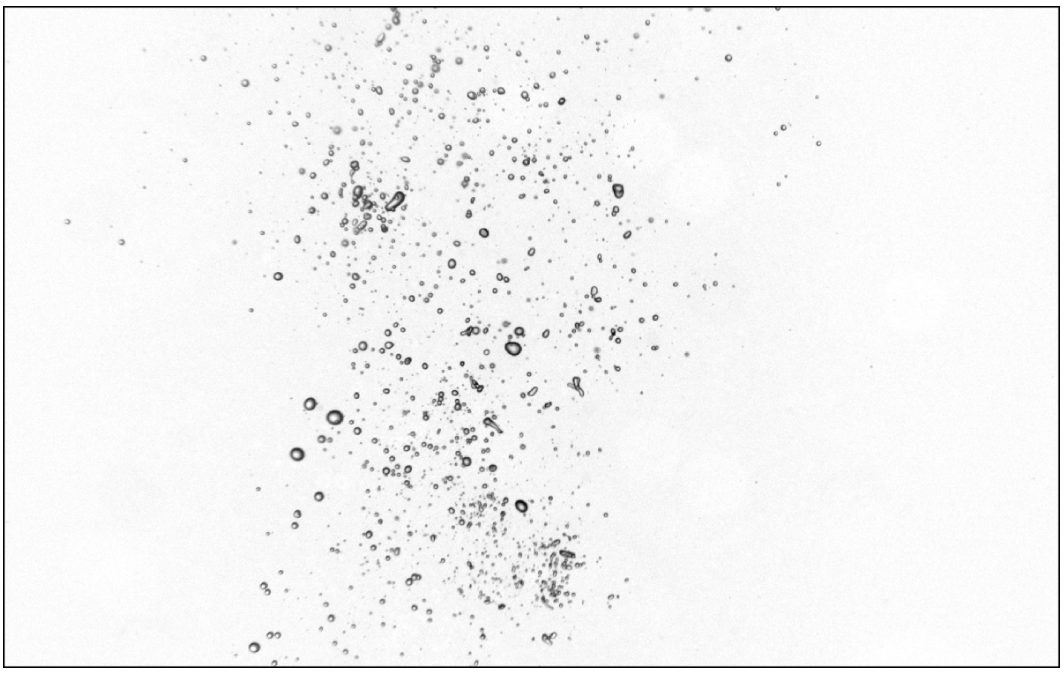

(b) $z/d_j = 39$ to 48

Figure E.9: Sample images of experimental set 3B (10 cSt silicone oil + 1000 ppm Triton X-100)

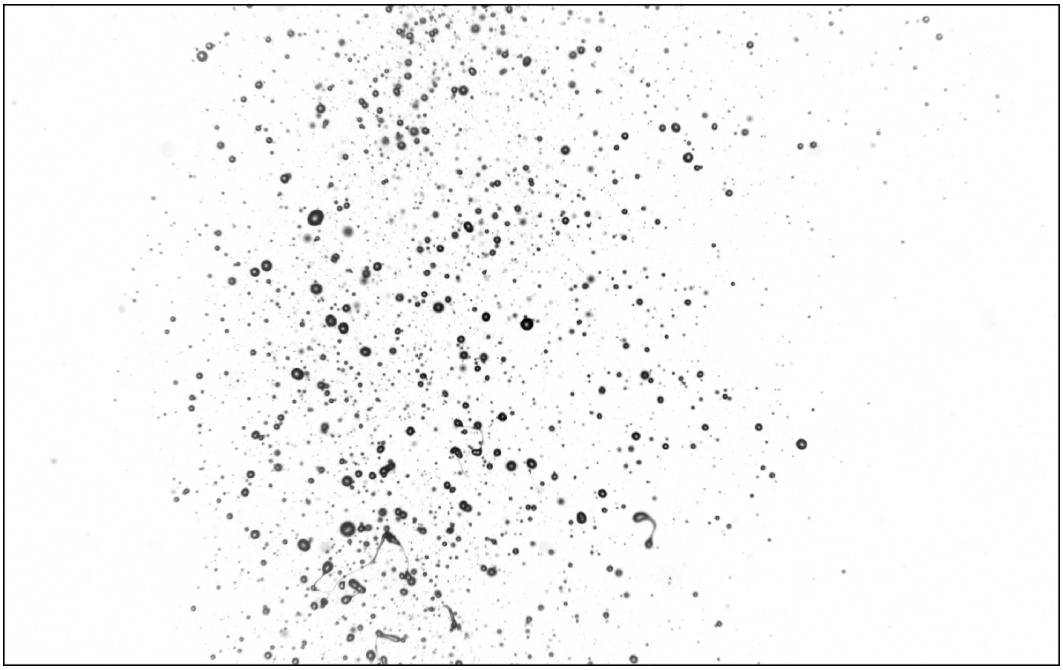

(a) $z/d_j = 28$ to 37

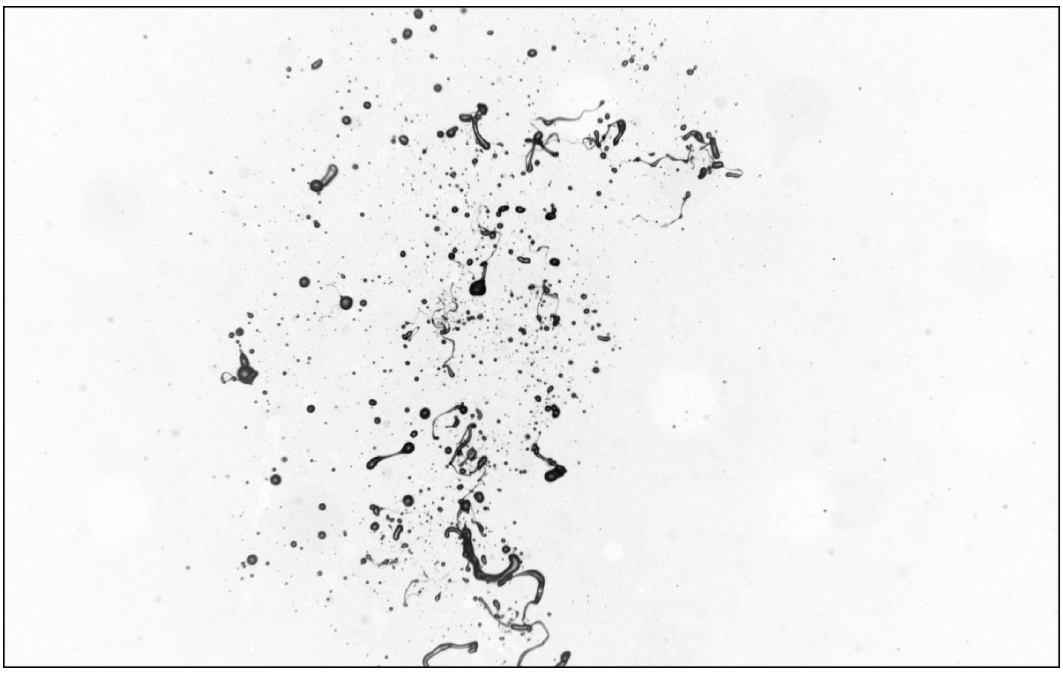

(b) $z/d_j = 39$ to 48

Figure E.10: Sample images of experimental set 3C (100 cSt silicone oil + 1000 ppm Triton X-100)

Appendix F

EQUIVALENT PARTICLE SIZE AND SHAPE

F.1 Equivalent ligament calculation

When studying individual breakup event where the particle get deformed and stretched into different shape, some shape representation metrics are needed. In addition, the breakup happens when the string gets too thin to keep the ligament intact, so the thickness and the length of the ligament are critical in the analysis of the breakup. It would be ideal to have the actual length (length of the thin string) and thickness (thinnest point of the ligament) of the ligaments. Although the viscous particles go through a stretching process prior to breakup, the stretching is one directional. In many cases, the ligaments wrap around to form unique complicated curves. Thus, getting the actual length and thickness for all ligaments at different points of the event would be impractical. Instead, we ultilize the simple size and shape properties, such as the projected area and the circumference, to calculate the equivalent ligament thickness and length.

The equivalent ligament is defined as a rectangle that has the same projected area and perimeter as the ligament. An illustration of the equivalent ligament is shown in Figure F.1. Based on this definition, the equivalent length and thickness can be calculated as:

$$l_{e,rec}, b_{e,rec} = \frac{\frac{P}{2} \pm \sqrt{\left(\frac{P}{2}\right)^2 - 4A}}{2} \tag{F.1}$$

where $l_{e,rec}$ is the equivalent length, $b_{e,rec}$ is the equivalent thickness, P is the perimeter and A is the projected area of the ligament.

For Equation (F.1) to have real results, $\left(\frac{P}{2}\right)^2 - 4A \geq 0$. Another particle shape properties that depends on both the projected area and the perimeter is the circularity, which is defined

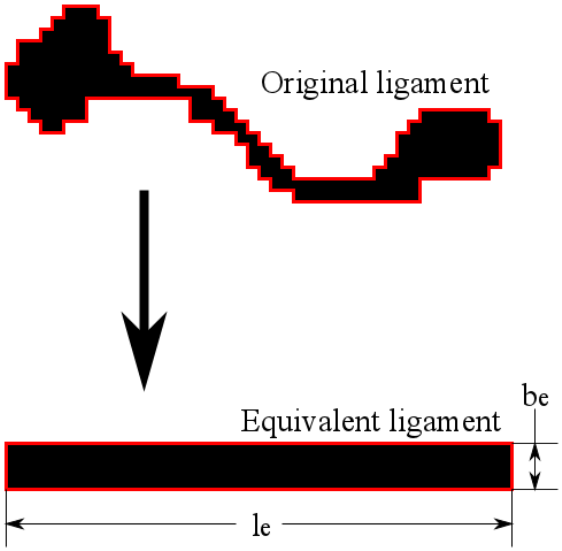

Figure F.1: Illustration of a ligament converted into its equivalent ligament.

as $CC = 4\pi A/P^2$. Combining this with the inequality, we obtained $CC \leq \pi/4 \approx 0.785$. This is the condition where the equivalent ligament calculation is valid.

For reference, particles with $CC > \pi/4$ typically are not stretched enough where thin string is formed. Since these particles resemble more of deformed particles than ligaments, the thickness and length are not important in this range. However, it is beneficial to have the thickness and length information of a particle along its entire breakup path (from circular particle to deformed particles to ligament), so another method is needed to fill the void where $CC > \pi/4$.

Another method is to use a well defined shape to represent the shape of a given ligament. An ellipse is defined by its major and minor axis. By fitting an ellipse to a ligament, the length and the thickness of the ligament can be approximated by the length of the major axis and the minor axis, respectively. Figure F.2 shows the comparison before and after the "fit ellipse" function is applied. Notice that the major and the minor axis approximate the length and thickness of the deformed particles and the slightly stretched ligaments well. Many highly elongated ligaments tend to bend in different direction (e.g. C-shape), an ellipse

would not fit well in these cases. However, this method is only applied to the particles with $CC > \pi/4$, which excludes almost all of the highly stretched/thinned ligaments.

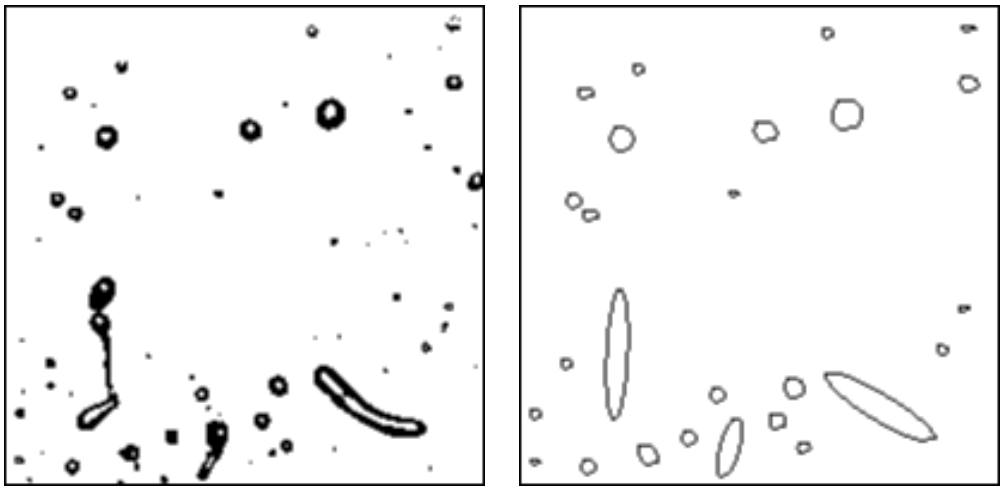

(a) Before "Fit ellipse" (b) After "Fit ellipse"

Figure F.2: Comparison between images before and after "Fit ellipse" is applied.

Combining the equivalent rectangle method ($CC \leq \pi/4$) and the fit ellipse method ($CC > \pi/4$) means there is a possibility of a jump at the transition point.

Figure F.3 shows the ratio of the two methods both in ligament length and thickness. For small circularity value, the two methods differs significantly. This is expected as the fit ellipse method does not work well for low circularity as mentioned above. As the circularity approaches to $\pi/4$, both ratio approach to 1. This means that the transition from the equivalent rectangle method ($CC \leq \pi/4$) to the fit ellipse method ($CC > \pi/4$) should be consistent.

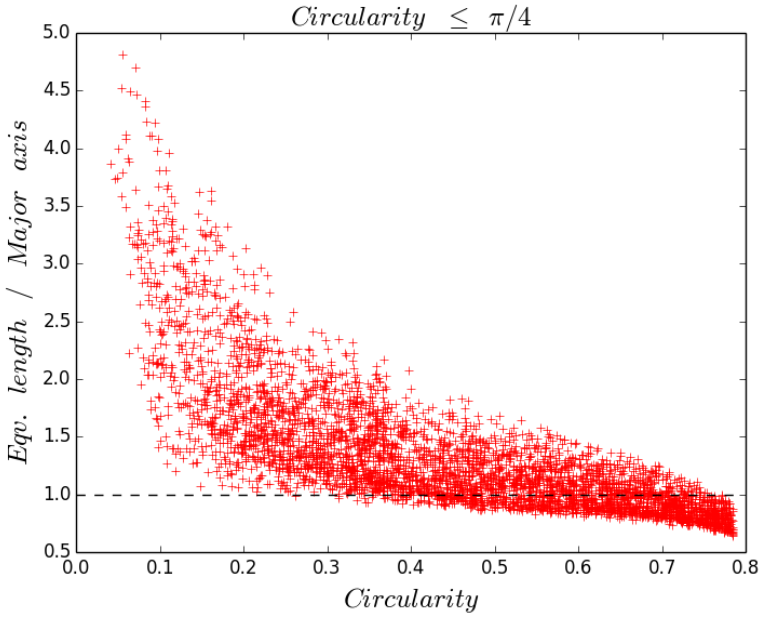

(a) Ligament length ratio

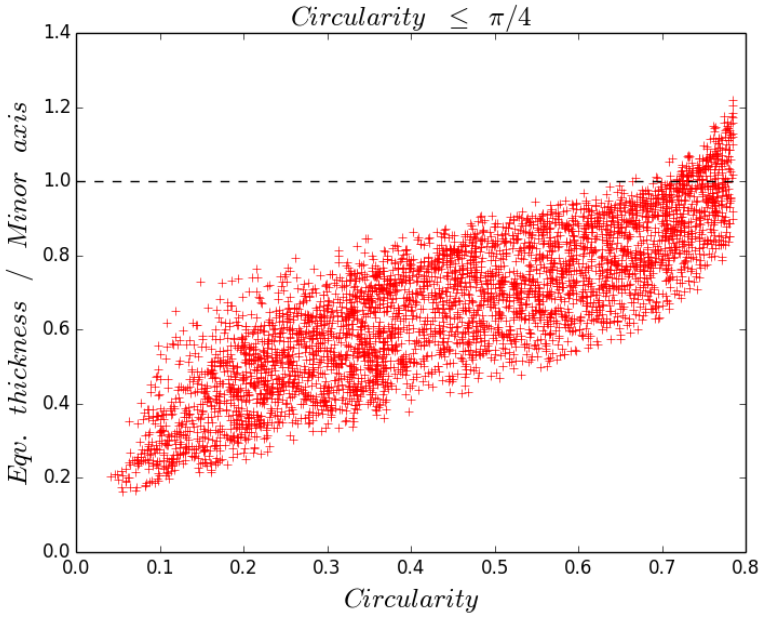

(b) Ligament thickness ratio

Figure F.3: The ligament length/thickness ratio vs circularity (for $CC \leq \pi/4$)

F.2 Equivalent particle diameter calculation

In some previous experiments [39, 16, 61], the particle size was computed based on a equivalent circle using one parameter, the projected area (Equation (F.2)). While this is a good estimation of the particle size for particles that are relatively spherical, it is not a good estimation for highly deformed particles and ligaments.

$$D = \sqrt{\frac{4A}{\pi}} \tag{F.2}$$

The area based (equivalent circle) method only takes into account of the size (projected area), but not the shape of the particle. In the case of a highly deformed particles or a ligament, this method might not accurately represent the particle size. This can be observed by the evolution of the equivalent diameter of particles in their breakup paths (Figure F.4a). Since all breakup paths shown are completed path, meaning they begin with a fairly spherical particle (circularity larger than $\pi(\pi+2)/(\pi+1)^2 \approx 0.94$), the equivalent diameter at the beginning of the paths is fairly accurate. Also, since no breakup or coalescence occurs when a particle is in the path, the particle volume should be constant. However, Figure F.4a shows that the equivalent diameter increases significantly for most breakup paths. This indicates that the equivalent circle method over estimate highly deformed particles or ligaments.

In order to get a more accurate representation of the particle size, we used a volume based method using an equivalent ellipsoid. Assuming the ellipsoid is axisymmetric, we employ two parameters in the calculation: the thickness and length of the particle. Naturally, the thickness and length are taken as the minor and major axis length of the particle obtained from the "fit-ellipse" function in the image processing. However, as the ligament stretches, it forms a thin string, so the minor axis length might not be a good representation of the width. Instead, the $b_{e,rec}$ and $l_{e,rec}$ from the previous section were used as the particle width and length for highly deformed particle ($CC \leq \pi/4$).

In the equivalent ellipsoid method, the equivalent diameter is the diameter of a sphere that have the same volume as the ellipsoid. The formation can be expressed as followed:

$$D = (l_e b_e^2)^{1/3} \tag{F.3}$$

where $l_e = l_{e,rec}$ and $b_e = b_{e,rec}$ for $CC \leq \pi/4$; $l_e = Major$ and $b_e = Minor$ for $CC > \pi/4$.

Figure F.4b shows the evolution of the equivalent diameter calculated using the volume based method for different breakup paths. Although fluctuation of the equivalent diameter is still present, the diameter no longer increase continuously. To quantify the variation in the equivalent diameter for each method, we calculated the standard deviation for each path and created a histogram of the standard deviations. Figure F.5 shows the comparison of the two histograms. In the volume based method, not only does it has significantly more particles with lower standard deviation, but it also has a narrower range of deviation. This suggests a higher confident level for the volume based method to achieve a higher accuracy in the equivalent diameter calculation.

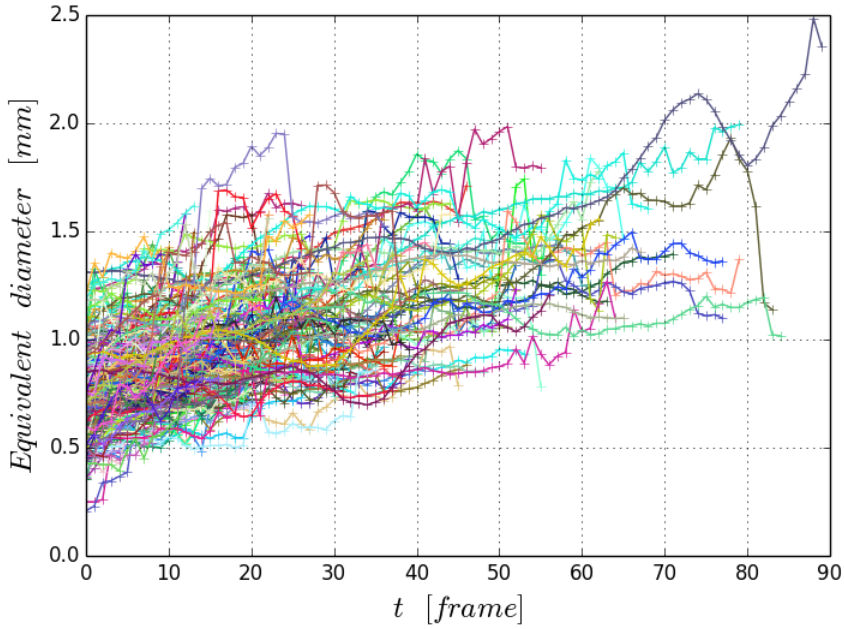

(a) Area based method (equivalent circle)

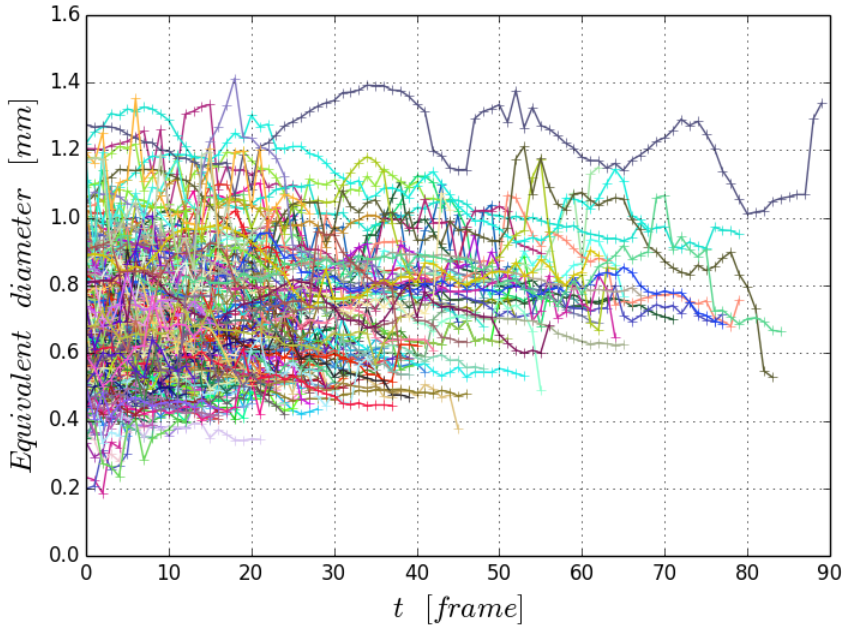

(b) Volume based method (equivalent ellipsoid)

Figure F.4: Evolution of equivalent diameter for different breakup paths.

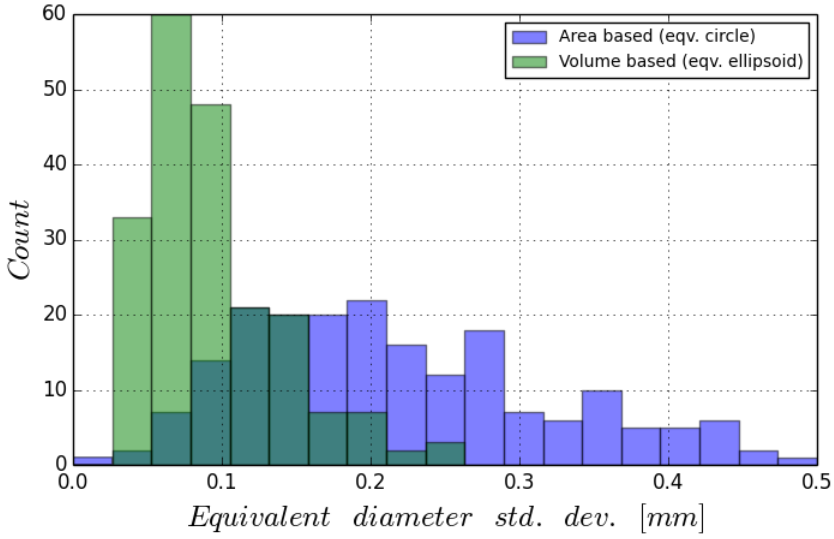

Figure F.5: A comparison of the histograms of equivalent diameter standard deviation between the equivalent circle method and the equivalent ellipsoid method.

Appendix G

SAMPLING RATE AND PHASE SHIFT STUDY

In the size distribution analysis (Chapter 7), all image sequences were captured at 60 fps to ensure the same particle did not appear twice in the same zone so that independent statistics was achieved. The image sequences used in Chapter 8 were recorded at 5000 fps, so we were able to perform a sampling study on the same video by using different frame increment for data analysis.

The sampling rate were chosen to be every 5, 10, 50, 83, and 166 frames, which corresponds to frame rates of 1000, 500, 100, 60, and 30 frame per second, respectively. In this study, we compare the number of particles counted in each frames that are being sampled and in each axial distance (the particles were counted in each zone, see Chapter 3). Because the numbers of frames being sampled are different for different sampling rates, the results were divided by the number of frames (i.e. number of particles per frame). Figure G.1 shows the comparison of the evolution of number of particles for different sampling rate. For all dispersed phase fluids (two are shown here), the trends of different sampling rates collapse on to each other. This indicates the sampling rate has no influence on the counting of the number of particles.

Because of the relatively low interfacial tension, a large lump of dispersed phase fluid was injected to the flow before it detached from the needle (unlike in the air case where smaller bubbles are detached from the needle). This large lump of liquid would disintegrate into a cloud of smaller particles and ligaments before reaching the imaging field of view. Theis cloud of particles came in the field of view in a certain frequency. Thus, we observed a modest pulsation behavior in the particle injection. To ensure our sampling was not biased towards different phase shift, another sampling study was performed. In this study, the sampling

rate is fixed at 60 frame per second (sampling every 83 frames). The starting frame were chosen to be 1, 18, 35, 52, and 69. For example, the first sampling sequence would be [1, 61, 121, etc] and the second sampling sequence would be [18, 78, 138, etc]. The number of particles were counted in each of these phase shifted sampling sequences. Figure G.2 show that there is no significant difference in the number of particles per frame between different phase shifts.

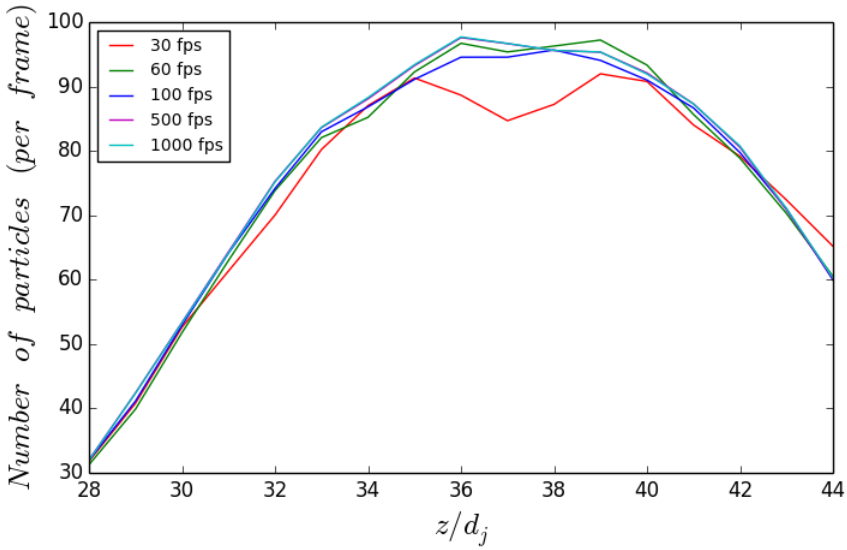

(a) 10 cSt silicone oil

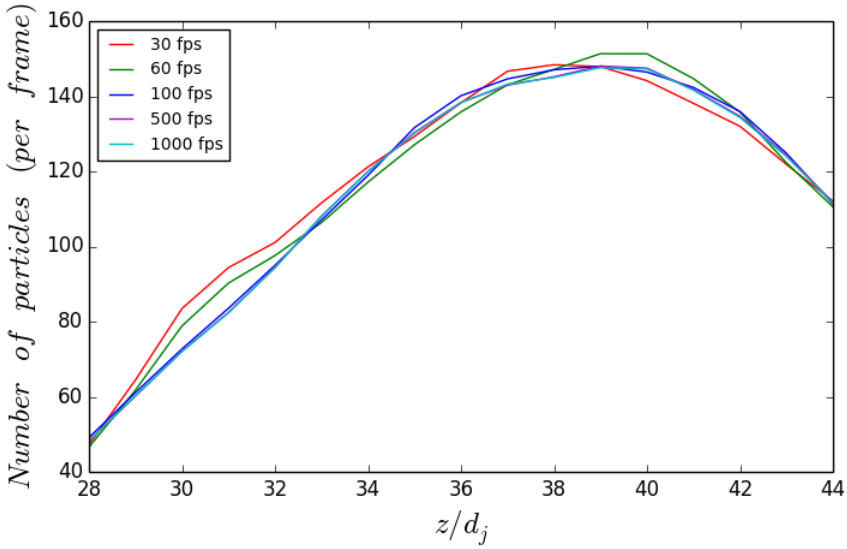

(b) 100 cSt silicone oil

Figure G.1: Comparison of the evolution of the number of particles per frame for different sampling rates.

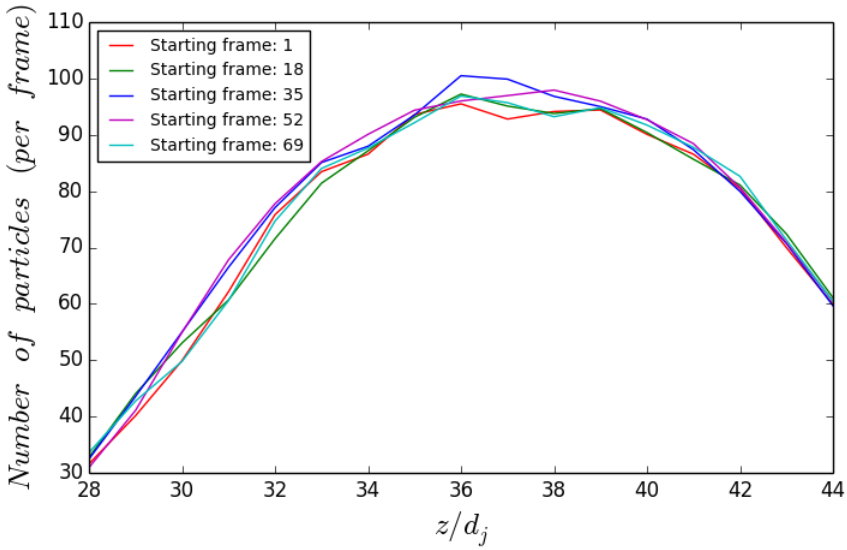

(a) 10 cSt silicone oil

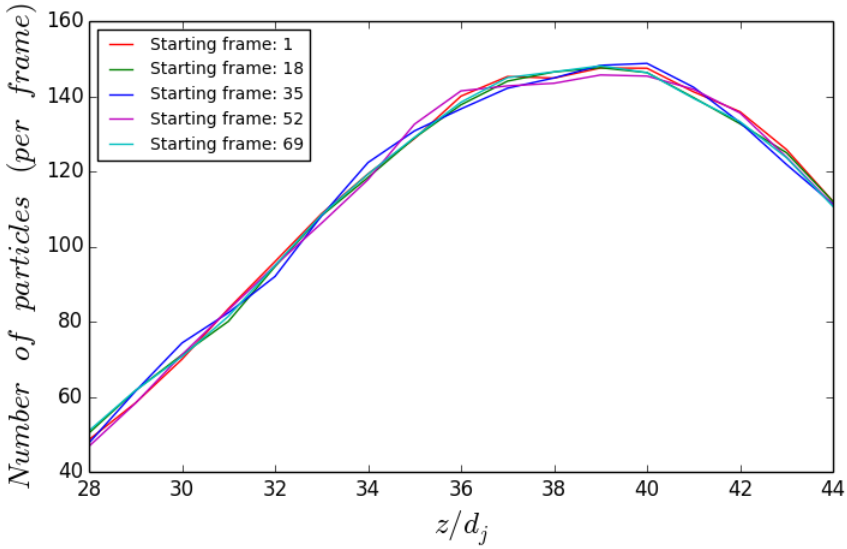

(b) 100 cSt silicone oil

Figure G.2: Comparison of the evolution of the number of particles per frame for different phase shifts.

BIBLIOGRAPHY

[1] R. J. Adrian and J. Westerweel. *Particle image velocimetry*. Cambridge University Press, 2010.

[2] A. Aliseda, E. J. Hopfinger, J. C. Lasheras, D. M. Kremer, A. Berchielli, and E. K. Connolly. Atomization of viscous and non-newtonian liquids by a coaxial, high-speed gas jet. Experiments and droplet size modeling. *International Journal of Multiphase Flow*, 34(2):161–175, Feb. 2008.

[3] R. Andersson and B. Andersson. Modeling the Breakup of Fluid Particles in Turbulent Flows. *AIChE Journal*, 52(6):2031–2038, 2006.

[4] R. Andersson and B. Andersson. On the Breakup of Fluid Particles in Turbulent Flows. *AIChE Journal*, 52(6), 2006.

[5] M. E. Aulton and A. M. Twitchell. Solution properties and atomization in film coating. In *Pharmaceutical Coating Technology*, pages 64–116. CRC Press, 1995.

[6] W. D. Bachalo. Experimental Methods in Multiphase Flows. *International Journal of Multiphase Flow*, 20:261–295, 1994.

[7] G. K. Bachelor. *The Theory of Homogeneous Turbulence*. Cambridge University Press, London, 1956.

[8] B. J. Bentley and L. G. Leal. An experimental investigation of drop deformation and breakup in steady, two-dimensional linear flows. *Journal of Fluid Mechanics*, 167:241–283, Apr. 1986.

[9] P. J. Brandvik, O. i. Johansen, F. Leirvik, U. Farooq, and P. S. Daling. Droplet breakup in subsurface oil releases - Part 1: Experimental study of droplet breakup and effectiveness of dispersant injection. *Marine pollution bulletin*, 73(1):319–26, Aug. 2013.

[10] R. V. Calabrese, T. P. K. Chang, and P. T. Dang. Drop Breakup in Turbulent Stirred-Tank Contactors Part I: Effect of Dispersed-Phase Viscosity. *AIChE Journal*, 32(4):657–666, 1986.

[11] C. J. Call and I. M. Kennedy. Measurements and simulations of particle dispersion in a turbulent flow. *Int. J. Multiphase Flow*, 18(6):891–903, 1992.

[12] G. C. Cole. The coating process. In *Pharmaceutical Coating Technology*, pages 170–204. CRC Press, 1995.

[13] C. A. Coulaloglou and L. L. Tavlarides. Description of interaction processes in agitated liquid-liquid dispersions. *Chemical Engineering Science*, 32:1289–1297, 1977.

[14] G. B. Deane and M. D. Stokes. Scale dependence of bubble creation mechanisms in breaking waves. *Nature*, 418(6900):839–44, Aug. 2002.

[15] P. E. Dimotakis. Two-Dimensional Shear-Layer Entrainment. *AIAA Journal*, pages 1791–1796, 1986.

[16] C. D. Eastwood, L. Armi, and J. C. Lasheras. The breakup of immiscible fluids in turbulent flows. *Journal of Fluid Mechanics*, 502:309–333, Mar. 2004.

[17] M. M. Elkotb, M. A. Mahdy, and M. E. Montaser. Investigation of External-Mixing Air-blast Atomizers. *Proceedings of the 2nd International Conference on Liquid Atomization and Sprays*, pages 107–115, 1982.

[18] H. Eroglu, N. Chigier, and Z. Farago. Coaxial atomizer liquid intact lengths. *Physics of Fluids A: Fluid Dynamics*, 3(2):303, 1991.

[19] B. Gopalan and J. Katz. Turbulent Shearing of Crude Oil Mixed with Dispersants Generates Long Microthreads and Microdroplets. *Physical Review Letters*, 104(5):054501, Feb. 2010.

[20] v. d. Graaf. Gpiv, open soource software for particle image velocimetry. `http://gpiv.sourceforge.net/`, 2012.

[21] F. K. Hansen and G. Rodsrud. Surface Tension by Pendant Drop. *Journal of Colloid and Interface Science*, 141(1), 1991.

[22] J. O. Hinze. Fundamentals of the hydrodynamics mechanisms of splitting in dispersion process. *AIChE J.*, 1:289–295, 1955.

[23] H. M. Hulbert and S. Katz. Some problems in particle technology. A statistical mechanical formulation. *Chemical Engineering Science*, 19:555–574, 1964.

[24] A. K. M. F. Hussain and V. Ramjee. Effects of the Axisymmetric Contraction Shape on Incompressible Turbulent Flow. *Journal of Fluid Engineering*, 98(1):58–68, 1976.

[25] H. J. Hussein, S. P. Capp, and W. K. George. Velocity measurements in a high-Reynolds-number, momentum-conserving, axisymmetric, turbulent jet. *Journal of Fluid Mechanics*, 258:31–75, 1994.

[26] T. Inamura and N. Nagai. The Relative Performance of Externally and Internally-Mixed twin-Fluid Atomizers. *Proceedings of the 3rd International Conference on Liquid Atomization and Sprays*, pages IIC/2/1–11, 1985.

[27] D. D. Joseph, G. S. Beavers, and T. Funada. Rayleigh-Taylor instability of viscoelastic drops at high Weber numbers. *Journal of Fluid Mechanics*, 453:109–132, Mar. 2002.

[28] D. D. Joseph, J. Belanger, and G. S. Beavers. Breakup of a liquid drop suddenly exposed to a high-speed airstream. *International Journal of Multiphase Flow*, 25(6-7):1263–1303, Sept. 1999.

[29] I. M. Kennedy and M. H. Moody. Particle dispersion in a turbulent round jet. *Experimental Thermal and Fluid Science*, 18:11–26, 1998.

[30] A. N. Kolmogorov. The local structure of turbulence in incompressible viscous fluid for very large reynolds numbers. In *Dokl. Akad. Nauk SSSR*, volume 30, pages 299–303, 1941.

[31] A. N. Kolmogorov. On the breakage of drops in a turbulent flow. *Dokl. Akad. Navk. SSSR*, 66(5):825–828, 1949.

[32] J. C. Lasheras, C. Eastwood, C. Martinez-Bazan, and J. L. Montanes. A review of statistical models for the break-up of an immiscible fluid immersed into a fully developed turbulent flow. *International Journal of Multiphase Flow*, 28(2):247–278, Feb. 2002.

[33] J. C. Lasheras and E. J. Hopfinger. Liquid Jet Instability and Atomization in a Coaxial Gas Stream. *Annual Review of Fluid Mechanics*, 32(1):275–308, Jan. 2000.

[34] C. H. Lee, L. E. Erickson, and L. A. Glasgow. Dynamics of Bubble Size Distribution in Turbulent Gas-Liquid Dispersions. *Chemical Engineering Communications*, 16:181–195, 1987.

[35] A. H. Lefebvre. *Atomization and sprays*. CRC press, 1989.

[36] H. Luo and H. F. Svendsen. Theoretical model for drop and bubble breakup in turbulent dispersions. *AIChE Journal*, 42(5):1225–1233, May 1996.

[37] A. Mansour and N. Chigier. Air-blast atomization of non-Newtonian liquids. *Journal of Non-Newtonian Fluid Mechanics*, 58:161–194, July 1995.

[38] P. Marmottant and E. Villermaux. On spray formation. *Journal of Fluid Mechanics*, 498(January 2004):73–111, Jan. 2004.

[39] C. Martínez-Bazán, J. L. Montanes, and J. C. Lasheras. On the breakup of an air bubble injected into a fully developed turbulent flow. Part 1. Breakup frequency. *Journal of Fluid Mechanics*, 401:157–182, 1999.

[40] C. Martínez-Bazán, J. L. Montanes, and J. C. Lasheras. On the breakup of an air bubble injected into a fully developed turbulent flow. Part 2. Size PDF of the resulting daughter bubbles. *Journal of Fluid Mechanics*, 401:183–207, 1999.

[41] W. J. McManamey. Sauter Mean and Maximum Drop Diameters of Liquid-Liquid Dispersions in Turbulent Agitated Vessels at Low Dispersed Phase Hold-up. *Chem. Eng. Sci.*, 34:432, 1979.

[42] S. Middleman. Drop Size Distributions Produced by Turbulent Pipe Flow. *Ind. Eng. Chem., Process Des. Develop.*, 13(1):78–83, 1974.

[43] R. Mueller and P. Kleinebudde. Comparison of a laboratory and a production coating spray gun with respect to scale-up. *AAPS PharmSciTech*, 8(1):3, Jan. 2007.

[44] R. Müller and P. Kleinebudde. Comparison study of laboratory and production spray guns in film coating: effect of pattern air and nozzle diameter. *Pharmaceutical development and technology*, 11(4):425–33, Jan. 2006.

[45] D. K. R. Nambiar, R. Kumar, T. R. Das, and K. S. Gandhi. A new model for the breakage frequency of drops in turbulent stirred dispersions. *Chemical Engineering Science*, 47(12):2989–3002, 1992.

[46] T. Okubo, E. Kokufuta, M. Nakamuro, K. Yoshinaga, M. Mizutani, and A. Tsuchida. Drying dissipative structures of lycopodium spore particles in aqueous dispersion. *Colloids and surfaces. B, Biointerfaces*, 80(2):193–9, Oct. 2010.

[47] N. T. Ouellette, H. Xu, and E. Bodenschatz. A quantitative study of three-dimensional Lagrangian particle tracking algorithms. *Experiments in Fluids*, 40(2):301–313, Nov. 2006.

[48] N. Panchapakesan and J. Lumley. Turbulence measurements in axisymmetric jets of air and helium. Part 1. Air jet. *Journal of Fluid Mechanics*, 246(1):197–223, 1993.

[49] N. Panchapakesan and J. Lumley. Turbulence measurements in axisymmetric jets of air and helium. Part 2. Helium jet. *Journal of Fluid Mechanics*, 246(1):225–247, 1993.

[50] M. Pilch and C. A. Erdman. Use of breakup time data and velocity history data to predict the maximum size of stable fragments for acceleration-induced breakup of a liquid drop. *International Journal of Multiphase Flow*, 13(6):741–757, 1987.

[51] J. A. F. Plateau. *Statique expérimentale et théorique des liquides soumis aux seules forces moléculaires*, volume 2. Gauthier-Villars, 1873.

[52] S. B. Pope. *Turbulent flows*. Cambridge university press, 2000.

[53] M. J. Prince and H. W. Blanch. Bubble Coalescence and Break-up in Air-Sparged bubble Columns. *AIChE Journal*, 36(10):1485–1499, 1990.

[54] M. Raffel, C. E. Willert, J. Kompenhans, et al. *Particle image velocimetry: a practical guide*. Springer, 2007.

[55] J. M. Rallison. THE DEFORMATION OF SMALL VISCOUS DROPS AND BUBBLES IN SHEAR FLOWS. *Annual Review of Fluid Mechanics*, 16:45–66, 1984.

[56] L. Rayleigh. On the capillary phenomenon of jets. *Proc. R. Soc. London*, 29:71–97, 1879.

[57] L. Rayleigh. On the Instability of Jets. *Proc. London Math. Soc.*, 10:4–13, 1879.

[58] L. Rayleigh. On the stability, or instability, of certain fluid motions. *Proc. London Math. Soc.*, 11:57–72, 1880.

[59] R. D. Reitz and F. V. Bracco. Mechanisms of breakup of round liquid jets. *Encyclopedia of fluid mechanics*, 3:233–249, 1986.

[60] A. A. Rizkalla and A. H. Lefebvre. The Influence of Air and Liquid Properties on Airblast Atomization. *Journal of Fluids Engineering*, pages 316–320, 1975.

[61] J. Rodriguez-Rodriguez, C. Martinez-Bazan, and J. L. Montanes. A novel particle tracking and break-up detection algorithm: application to the turbulent break-up of bubbles. *Measurement Science and Technology*, 14(8):1328–1340, Aug. 2003.

[62] J. C. Rotta. *Turbulente Stromungen*. B. G. Teubner, Stuttgart, 1972.

[63] H. C. Simmons. The Prediction of Sauter Mean Diameter for Gas Turbine Fuel Nozzles of Different Types. *Journal of Engineering for Power*, 102(July):646–652, 1980.

[64] K. Sveen. Matpiv, open soource software for particle image velocimetry. `http://www.mn.uio.no/math/english/people/aca/jks/matpiv/`, 2004.

[65] M. Tjahjadi and J. M. Ottino. Stretching and breakup of droplets in chaotic flows. *Journal of Fluid Mechanics*, 232:191–219, Apr. 1991.

[66] C. Tsouris and L. L. Tavlarides. Breakage and Coalescence Models for Drops in Turbulent Dispersions. *AIChE Journal*, 40(3):395–406, 1994.

[67] R. Turton and X. X. Cheng. The scale-up of spray coating processes for granular solids and tablets. *Powder Technology*, 150(2):78–85, Feb. 2005.

[68] K. J. Valentas, O. Bilous, and N. R. Amundson. Analysis of breakage in dispersed phase systems. *Industrial & Engineering Chemistry Fundamentals*, 5(2):271–279, 1966.

[69] C. M. Varga, J. C. Lasheras, and E. J. Hopfinger. Initial breakup of a small-diameter liquid jet by a high-speed gas stream. *Journal of Fluid Mechanics*, 497:405–434, Dec. 2003.

[70] J. Vilcáez, L. Li, and S. S. Hubbard. A new model for the biodegradation kinetics of oil droplets: application to the Deepwater Horizon oil spill in the Gulf of Mexico. *Geochemical transactions*, 14(1):4, Jan. 2013.

[71] I. Wygnanski and H. Fiedler. Some measurements in the self-preserving jet. *Journal of Fluid Mechanics*, 38(3):577–612, 1969.